SAPIENZA
UNIVERSITÀ DI ROMA

Analysis and decomposition of frequency modulated multicomponent signals

Michela Tartaglione

PhD Thesis in Mathematical Models for Engineering

Advisor: Prof. Vittoria Bruni

Department of Basic and Applied Sciences for Engineering

XXXIII Cycle

Contents

Introduction

Many real-life signals are multicomponent and frequency modulated (FM), i.e. they consist of the superposition of oscillating modes having a specific time-dependent frequency content. The list of applications dealing with FM multicomponent signals (MCS) is quite large and it involves geology [1], wireless communication [2], speech processing [3], gravitational waves detection [4], biology [5–7], radar and micro-doppler analysis [8–13] and so on. In the literature, a single FM signal is classified depending on its specific frequency modulation, i.e. the class of its phase function or equivalently, its instantaneous frequency (IF) — the phase time derivative. For example, chirp-like signals are characterized by an increasing (or decreasing) frequency with respect to time and they are widely used to model radar, communication and seismic signals [14]. Sinusoidally modulated signals have periodic frequency, instead and they also appear in several applications involving radar and human gait detection [11].

Independently of the specific frequency modulation, the correct analysis of a MCS requires the separation of its single modes. In other words, an observed signal has to be properly decomposed in order to extract its characteristics (amplitude and IF). It is worth observing that interference between modes generally makes the separation task remarkably hard. As a matter of fact, the current literature does not offer a general solution to the problem of decomposing MCS with interfering modes. Indeed, the existing methods are mostly parametric, i.e. they assume a specific signal class, otherwise they consist of interpolation techniques. In the first case, methods' drawback is to only adapt to specific situations, while the second approach is quite limited as it does not rely on signal's physical properties. Therefore, both are unsatisfactory views and, as a consequence, efficient modes separation still represents a very demanding goal in signal processing.

The aim of the presented thesis is to exhaustively investigate the problem

of FM-MCS decomposition, with particular focus on the pathological case of almost complete interference between individual modes, as well as to propose practical and efficient strategies for signal modes separation. Chapter 1 presents the mathematical tools and the main definitions needed to introduce and formalize the problem. An extended state of the art concerning the topic is then provided. It is worth pointing out that both the classical and the more recent methods for MCS decomposition are revised for a complete background, but focusing on some parts is enough to get a comprehensive understanding of the thesis. In particular, Sections 1.1.1, 1.1.3, 1.1.5 and 1.2 contain classical and fundamental topics. The reader is encouraged to consider reassignment method presented in Section 1.3.2.1 and to focus on methods' pros. and cons. summarized in Section 1.4. The latter are crucial for fully appreciating the original results that will be presented in this work.

Chapters 2 and 3 contain the results achieved during my Phd course. Each chapter is self-contained, as far as possible, to facilitate reading. The two chapters reflect the main strategies adopted in this research, i.e. the iterative one, aimed at enhancing MCS' resolution in the time-frequency (TF) domain and the transform-based approach, whose purpose is to effectively separate individual components, by analyzing signal energy in a proper domain. More specifically, Chapter 2 first introduces a MCS' model in the TF plane and deeply discusses the problem of modes separability. Based on these results, it then presents an iterative reallocation approach for signal resolution improvement, which is compared to one of the most popular reallocation technique, i.e. reassignment method. Chapter 3 addresses MCS decomposition by further processing the signal under analysis. In particular, it will be proved that energy-based transforms, such as Radon Transform, are suitable for characterizing interference between signal modes and, for this reason, they can be adopted for successfully separating individual modes. The presented approach leads to the definition of an effective non-parametric method, whose main advantages as well as limitations will be deeply discussed and compared to existing procedures.

Notice that short proofs can be found below the corresponding proposition, while the more structured ones are listed in the Appendix. Finally, the Conclusions summarize the thesis's main findings, highlighting their contribution to advance the state of the art. Possible future developments are also discussed.

List of abbreviations

ADTFD	Adaptive Directional Time-Frequency Distribution
AM	Amplitude Modulated
BD	B-Distribution
CFCR	Centroid Frequency and Chirp Rate
CWT	Continuous Wavelet Transform
EEG	Electroencephalography
EEMD	Ensemble Empirical Mode Decomposition
EMD	Empirical Mode Decomposition
FIRST	Fast Iterative and Robust Spectrogram Thinning
FM	Frequency Modulated
FT	Fourier Transform
FrFT	Fractional Fourier Transform
IA	Instantaneous Amplitude
ICC	Intrinsic Chirp Components
ICC	Intrinsic Chirp Components Decomposition
IF	Instantaneous Frequency
IMF	Intrinsic Mode Function
IRT	Inverse Radon Transform
LMD	Local Mean Decomposition
LFM	Linearly Frequency Modulated
LO-ADTFD	Locally Adaptive Directional Time-Frequency Distribution
LVD	Lv's Distribution
MAP	Maximum A Posteriori
MCS	Multicomponent Signals
NE	Normalized Energy
PSIAF	Parametric Symmetric Instantaneous Autocorrelation Function
QML	Quasi Maximum Likelihood
RANSAC	Random Sample Consensus
RM	Reassignment Method

RPRM	Ridge Path Regrouping Method
RSD	Radon Spectrogram Distribution
RT	Radon Transform
RW	Radon-Wigner Transform
SM	S-Method
SST	Synchrosqueesing Transform
STFT	Short-time Fourier Transform
TF	Time-Frequency
TFD	Time-Frequency Distribution
WD	Wasserstein Distance
WSC	Weakened Separability Condition
WT	Wavelet Transform
WEF	Windowed Energy Function
WVD	Wigner-Ville Distribution

Chapter 1

Analysis and decomposition of frequency modulated signals: state of the art

Most real-world signals are non-stationary, i.e. they have time-dependent frequency content. Some examples of real-world FM signals are shown in Fig.1.1. Given a superposition of such waveforms, namely a FM-MCS, the decomposition task consists of recovering each individual component. Methods in the literature, designed to this aim, can be grouped into two main classes: the first one refers to strategies that analyze the signal directly in the time domain and the second class is based on TF analysis. The latter is more suitable for IF estimation, which is a fundamental goal in applications. Given a FM-MCS, the problem of estimating its IF is solved if all its IFs, defined as the time derivatives of the phases corresponding to each mode, have been detected. Signal decomposition and IF detection are therefore two closely related concepts, as the former is necessary to separate and detect each IF and, conversely, the latter allows for the recovery of each individual component. TF analysis provides powerful mathematical tools for the correct study of non-stationary signals. Contrary to the classical Fourier transform (FT), TF transforms and TF distributions (TFDs) map a signal into a joint TF domain, which is the suitable space for observing the frequency time-behaviour.

The decomposition problem, as well as IF estimation, is substantially solved for MCS with well separated components in the TF plane and the list of different approaches dealing with the problem is quite large [15–31]. Conversely, the

most challenging problem in FM-MSC analysis is the decomposition of signals affected by interference, i.e. with overlapping or crossing components in the TF plane. The latter is a common scenario in real applications [8, 10]. In this case, methods designed for well separated components are not able to distinguish between modes and therefore they fail in estimating signal IFs.

As presented in this chapter, there exist several methods addressing the problem of overlapped MCS. In most of them, IF estimation relies on specific assumptions on the signal under study (parametric approaches); other methods estimate IF based on image processing techniques aimed at finding the optimal path connecting TFD peaks through minimization, which often involves a high computational cost. As already outlined in the Introduction, existing methods do not fully solve the problem of IFs separation, which is a perspective of the presented work.

The chapter is organized as follows. Section 1.1 introduces the fundamental mathematical tools for TF analysis. In Section 1.2, the main definitions to formally introduce the problem of signals decomposition, as well as IFs separation, are given. A brief review of the main methods dealing with the problem is then provided. Specifically, the various methods for well separated components are described in Section 1.3, as background information. Particular attention is devoted to approaches dealing with overlapping modes, which are reviewed in Section 1.4.

1.1 Linear TF transforms and quadratic distributions

A FM-MCS is non-stationary, i.e. its frequency depends on time, therefore the classical FT is not suitable for signal characterization and a joint TF representation is needed to process the signal. For this reason, linear TF transforms and quadratic distributions have been proposed. They are mainly windowed transforms aimed at localizing the signal FT in time.

A linear TF transform decomposes a signal into a family of waveforms, known as TF atoms, that are well concentrated in time and frequency. Let us denote a family of TF atoms as $\{\varphi_\gamma\}_\gamma$ where γ is a multi-index parameter. Let $\varphi_\gamma \in L^2(\mathbb{R})$ and $||\varphi_\gamma||_{L^2(\mathbb{R})} = 1$. The corresponding TF transform of

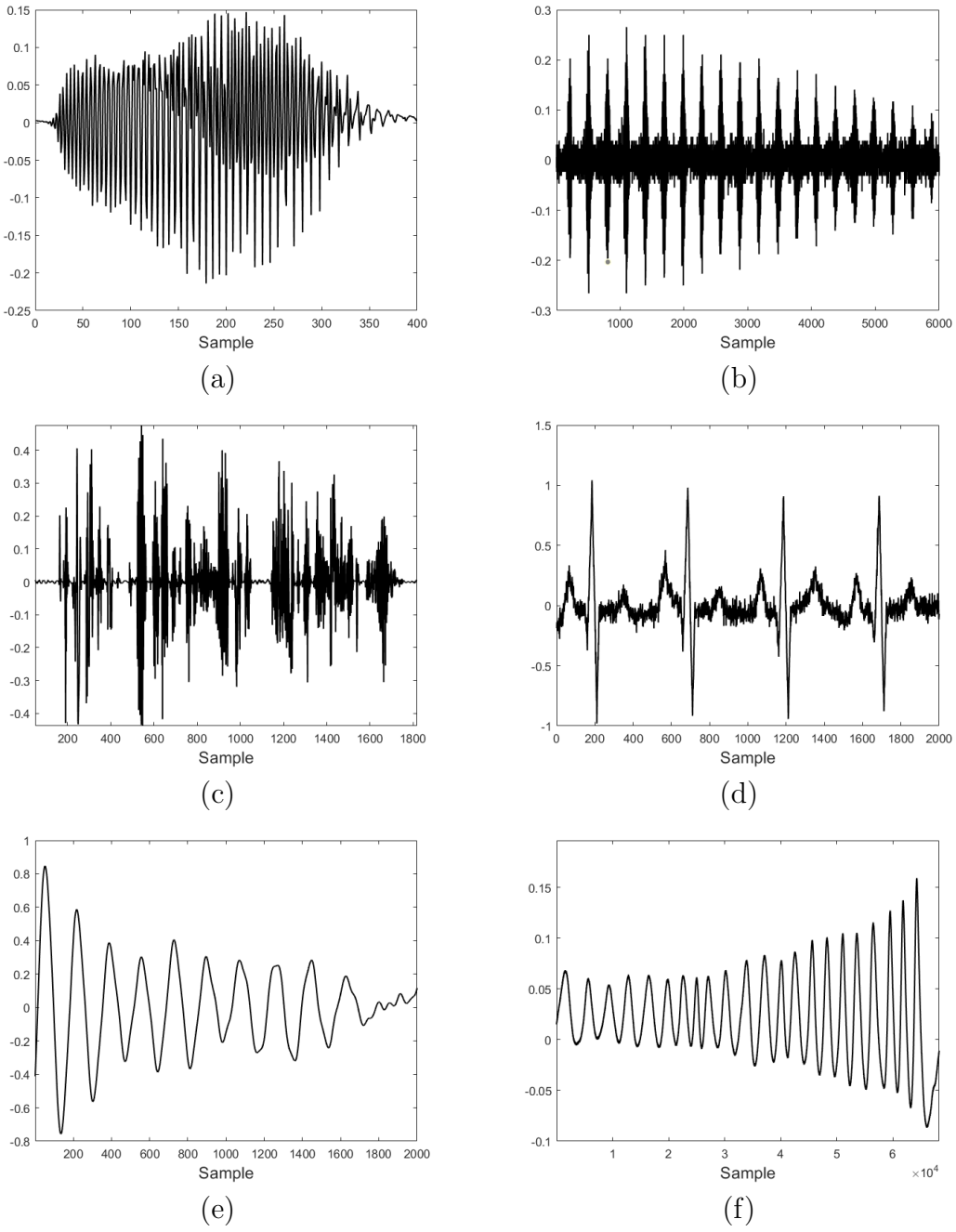

Figure 1.1: Real-world AM-FM signals. (a) Ultrasound signal emitted by a bat [32]; (b) Whale trill [33]; (c) Speech signal [32]; (d) Electrocardiogram (ECG) signal [33]; (e) Seismic signal [33]; (f) Doppler radar signal corresponding to the measurement of a moving hand [34].

$f(t) \in L^2(\mathbb{R})$, at a point γ, is defined as [35]

$$T_f(\gamma) =< f, \varphi_\gamma >_{L^2(\mathbb{R})} = \int_{-\infty}^{+\infty} f(t)\, \varphi_\gamma^*(t)\, dt.$$

Linear transforms' resolution depends on atoms' spread in the TF plane. φ_γ resolution is represented in TF plane by a so-called Heisenberg box which is centered at the point (u_γ, ξ_γ), defined as

$$u_\gamma = \int_{-\infty}^{+\infty} t\,|\varphi_\gamma(t)|^2\,dt,$$

$$\xi_\gamma = \frac{1}{2\pi}\int_{-\infty}^{+\infty} \omega\,|\hat{\varphi}_\gamma(\omega)|^2\,d\omega,$$

and whose widths in time and frequency are respectively given by the variances

$$\sigma_t^2(\gamma) = \int_{-\infty}^{+\infty} (t-u_\gamma)^2|\varphi_\gamma(t)|^2\,dt.$$

$$\sigma_\omega^2(\gamma) = \frac{1}{2\pi}\int_{-\infty}^{+\infty} (\omega-\xi_\gamma)^2|\hat{\varphi}_\gamma(\omega)|^2\,d\omega.$$

Heisenberg boxes are shown in Fig.1.2. As stated by Heisenberg principle, it is not possible to reach arbitrary localization both in time and frequency. Formally, the widths satisfy

$$\sigma_t(\gamma)\sigma_\omega(\gamma) \geq \frac{1}{2},$$

which limits the joint TF resolution.

If for any (u, ξ) there exists a unique atom φ_γ centered at (u, ξ), then each Heisenberg box specifies a TF neighborhood of (u, ξ) where the energy of the analyzed signal f is measured by the energy density $|T_\gamma(u, \xi)|^2$.

1.1.1 STFT and spectrogram

STFT has been introduced in order to localize FT in time, that's why in the literature it is also referred as Windowed FT. Atoms are derived as translated and modulated version of a real, even and smooth window g such that $||g||_{L^2(\mathbb{R})} = 1$, modulated by the frequency ξ, i.e. $\{\varphi(u,\xi)\}_{(u,\xi)} = \{e^{i\xi t}g(t-u)\}_{(u,\xi)}$. More precisely, for any TF point $(u, \xi) \in \mathbb{R} \times \mathbb{R}^+$, the STFT of a function $f \in L^2(\mathbb{R})$ with respect to the analysis window g is [15, 35]

$$S_f^g(u,\xi) = \int_{-\infty}^{+\infty} f(t)g(t-u)e^{-i\xi t}\,dt\,. \tag{1.1}$$

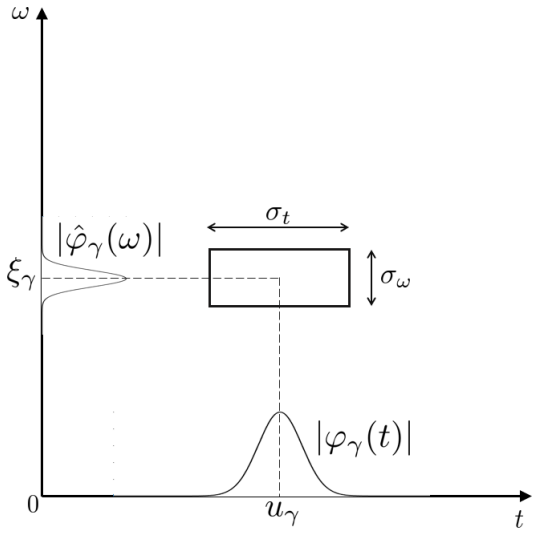

Figure 1.2: Heisenberg boxes in TF plane.

The spectrogram is defined as the squared modulus of the STFT, i.e.

$$P(u,\xi) = |S_f^g(u,\xi)|^2\,, \tag{1.2}$$

and it measures the energy of f in the TF neighborhood of (u,ξ). The spectrogram of a linear chirp, computed by a gaussian window, is depicted in Fig.1.3.

A signal can be recovered by its STFT and the energy is preserved, as stated in the following

Theorem 1. *Let $f \in L^2(\mathbb{R})$ then*

$$f(t) = \frac{1}{2\pi}\int_{-\infty}^{+\infty}\int_{-\infty}^{+\infty} S_f^g(u,\xi)g(t-u)e^{i\xi t}du d\xi$$

and

$$\int_{-\infty}^{+\infty}|f(t)|^2\,dt = \int_{-\infty}^{+\infty}\int_{-\infty}^{+\infty}|S_f^g(u,\xi)|^2\,du\,d\xi.$$

STFT resolution depends on Heisenberg box area and it can be modified, in the constraints of Heisenberg principle, by a scaling of the analysis window g. Indeed, if we consider $g_s(t) = \frac{1}{\sqrt{s}}g\left(\frac{t}{s}\right)$, with $s > 0$, then Heisenberg boxes are dilated by s in time and compressed by s in frequency, but its area is preserved. The parameter s is usually set to better represent the specific analyzed signal; in general, the choice of its optimal value is an independent research topic [36]. In numerical applications, g must be compactly supported. It follows

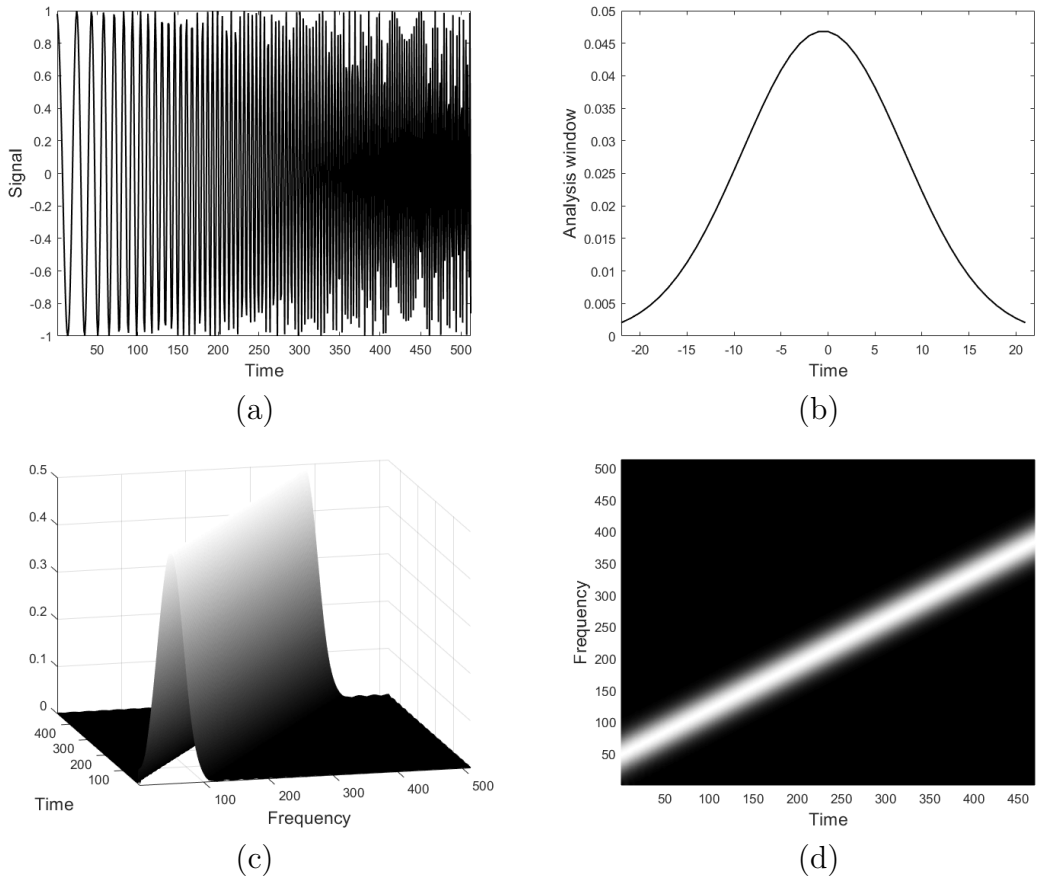

Figure 1.3: Spectrogram of a linear chirp. (a) Signal; (b) Gaussian analysis window for STFT computation; (c) Spectrogram, 3D view; (d) Spectrogram, view from above.

that its FT $\hat{g}$ necessarily has an infinite support. The assumptions on g also ensure that $\hat{g}$ is a symmetric function with a main lobe center at $\omega = 0$, as depicted in Fig.1.4. In order to maximize frequency resolution, it is desirable to concentrate the energy of $\hat{g}$ around $\omega = 0$. The root mean-square bandwidth $\tilde{\Delta}\omega$ is an important parameter to evaluate the spread of $\hat{g}$ and it is defined by

$$\frac{|\hat{g}\left(\frac{\tilde{\Delta}\omega}{2}\right)|^2}{|\hat{g}\,(0)\,|^2} = \frac{1}{2},$$

while the frequency bandwidth of g is defined as the bandwidth of its FT $\hat{g}$ instead, that is $\Delta\omega$ satisfying

$$|\hat{g}(\omega)| \ll 1 \quad \text{for} \quad \omega \geq \Delta\omega.$$

STFT is designed for revealing IF, indeed spectrogram maxima are closely related to IF. For getting a better understanding, let us consider the following

Definition 1. *The local maxima of $P(u,\xi)$ are defined as* ***ridge points****.*

The proposition below provides a spectrogram model directly depending on ridge points and IF.

Proposition 1.1 (Mallat model [35])**.** *Let $f(t) = a(t)\cos\phi(t)$ and let $s > 0$. For each $\xi \geq 0$, the STFT of f can be expressed as*

$$S_f^g(u,\xi) = \frac{\sqrt{s}}{2} a(u) e^{i(\phi(u)-\xi\cdot u)} \left[\hat{g}\left(s(\xi-\phi'(u)) + \epsilon(u,\xi)\right)\right], \tag{1.3}$$

where $\epsilon(u,\xi)$ is a corrective term satisfying

$$|\epsilon(u,\xi)| \leq \epsilon_{a,1} + \epsilon_{a,2} + \epsilon_{\phi,2} + sup_{|\omega|\geq s|\phi'(u)|}|\hat{g}(\omega)|,$$

with

$$\epsilon_{a,1} \leq \frac{s|a'(u)|}{a(u)}, \quad \epsilon_{a,2} \leq \sup_{|t-u|\leq s/2} \frac{s^2|a''(t)|}{a(u)}, \tag{1.4}$$

and if $s\frac{|a'(u)|}{|a(u)|} \leq 1$, then

$$\epsilon_{\phi,2} \leq sup_{|t-u|\leq s/2} s^2|\phi''(u)|. \tag{1.5}$$

In addition, if $\xi = \phi'(u)$, then $\epsilon_{a,1} = \frac{s|a'(u)|}{a(u)}|\hat{g}'(2s\phi'(u))|$.

Remark 1. *Assuming $\epsilon(u,\xi)$ negligible in eq.(1.3) and by taking the absolute value, we obtain the following model for the spectrogram*

$$P(u,\xi) = \frac{s}{4} a^2(u)\hat{g}^2\left(s(\xi-\phi'(u))\right). \tag{1.6}$$

According to the assumptions on the window g, $\hat{g}$ is maximum in $\omega = 0$, then by eq.(1.6) *it follows*

$$\max_{\xi} P(u,\xi) = P(u,\phi'(u)),$$

For this reason, the curve $(u,\phi'(u))$ is denoted as ***ridge curve*** *(or* ***IF curve****).*

The expressions in eqs.(1.4)-(1.5) show that the corrective terms $\epsilon_{a,1}$, $\epsilon_{a,1}$ and $\epsilon_{\phi,2}$ are small if $a(t)$ and $\phi'(t)$ have small relative variations over the support of

the window g. In addition, the term $sup_{|\omega|\geq s|\phi'(u)|}|\hat{g}(\omega)|$ is negligible if $\phi'(u) \geq \frac{\Delta\omega}{s}$. In practical applications, s is chosen in order to meet the above conditions, so that $\epsilon(u,\xi)$ could be neglected.

Eq.(1.3) also shows that ridge points are the phase stationary points. Anyway, the procedures exploiting this property have turned out to be numerically unstable, that's why it is preferable to derive IF from ridge points.

As it can be observed in Fig.1.5, since the FT of a gaussian function is still gaussian, the spectrogram profile is gaussian, according to eq.(1.6)—see Fig.1.5(b). In addition, the local maxima of the spectrogram reveal exactly signal IF, as it can be derived by comparing Fig.1.5(c)-(d).

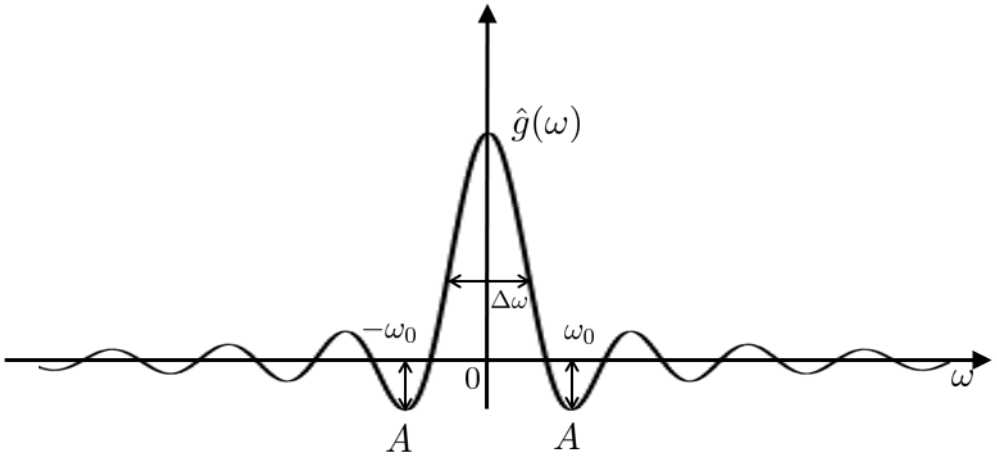

Figure 1.4: A generic analysis window in the Fourier domain and its parameters [35]. The energy spread of $\hat{g}$ is measured by its frequency bandwidth $\Delta\omega$ and by the maximum amplitude A of the first side-lobes located at $\omega = \pm\omega_0$.

1.1.2 Wavelet Transforms

Contrary to STFT, Wavelet transform (WT) decomposes a signal over TF atoms having different time supports. A wavelet is a unitary function $\psi(t) \in L^2(\mathbb{R})$ with zero mean, i.e. $\int_{-\infty}^{+\infty}\psi(t)dt = 0$ and centered at $t = 0$. Atoms are obtained as scaled and translated versions of the "mother" function ψ, i.e.

$$\psi_{u,s}(t) = \frac{1}{\sqrt{s}}\psi\left(\frac{t-u}{s}\right).$$

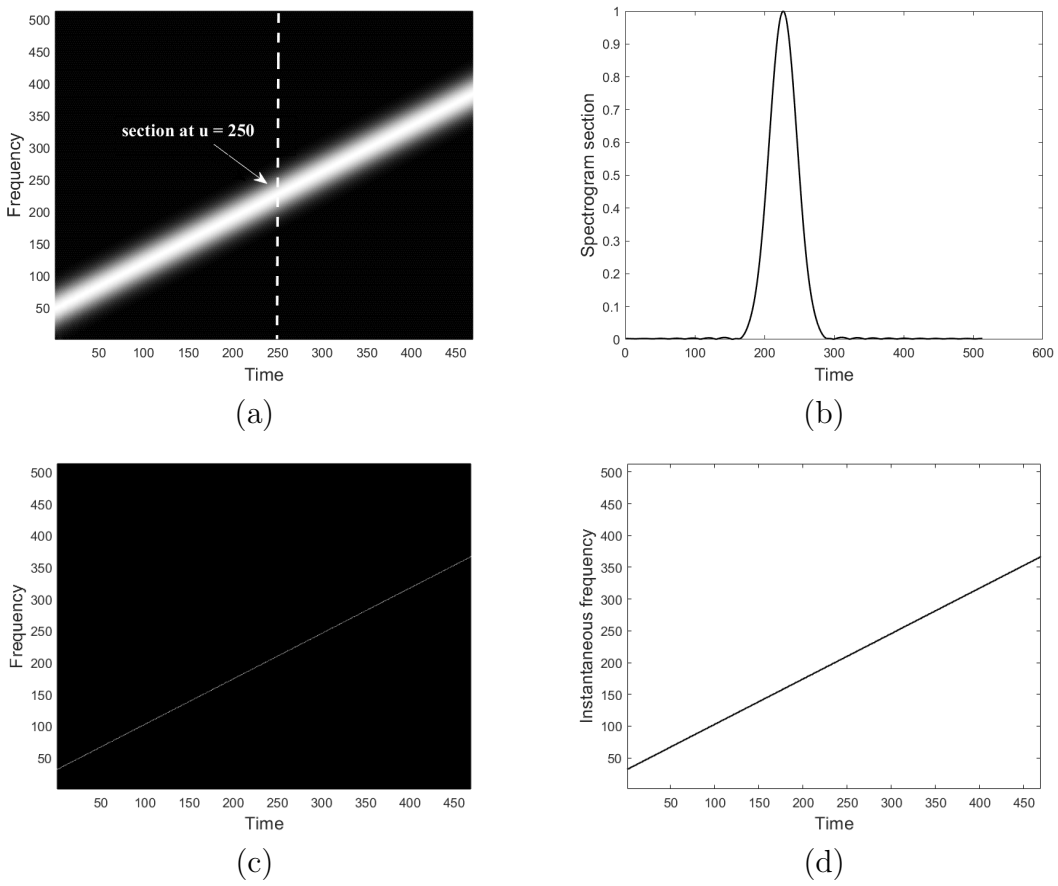

Figure 1.5: Mallat Model. (a) Spectrogram of the linear chirp in Fig. 1.3(a). The section at $u = 250$ is emphasized by the dashed line; (b) Normalized section at $u = 250$. Spectrogram profile is a gaussian; (c) Local maxima in the TF plane; (d) IF.

The continuous WT (CWT) of a function $f \in L^2(\mathbb{R})$ at a point $(u, s) \in \mathbb{R} \times \mathbb{R}^+$ is then defined as

$$W_f(u, s) = \int_{-\infty}^{+\infty} f(t)\psi^*_{u,s}(t)\, dt.$$

In order to measure the frequency time evolution and to separate amplitude and phase components, the analytic WT has been introduced.

Definition 2. *A function $f(t) \in L^2(\mathbb{R})$ is analytic if $\hat{f}(\omega) = 0 \quad \forall\, \omega < 0$. The analytic part of a generic $f \in L^2(\mathbb{R})$ is defined as the inverse FT of*

$$\hat{f}_a(\omega) = \begin{cases} 2\hat{f}(\omega), & \omega \geq 0 \\ 0, & \omega < 0. \end{cases}$$

Contrary to CWT, the analytic WT is computed by considering an analytic wavelet, which is forced to be complex. Thanks to WT adaptivity, WT squared modulus, referred as scalogram, is particularly suitable for detecting IFs that rapidly vary in time. For instance, a hyperbolic chirp $f(t) = \cos\left(\frac{\alpha}{\beta - t}\right)$, $\alpha, \beta \in \mathbb{R}$ is better represented by the scalogram rather than the spectrogram [35].

1.1.3 Wigner Ville distribution

As all linear TF transforms, STFT and WT are computed by correlating a function with families of TF atoms. Therefore, linear TFDs' resolution is limited to Heisenberg principle. Wigner-Ville distribution (WVD) is a quadratic TF energy with high resolution properties, instead. It is defined by correlating a signal $f(t)$ with its TF translations, i.e.

$$WV_f(u,\xi) = \int_{-\infty}^{+\infty} f\left(u + \frac{\tau}{2}\right) f^*\left(u - \frac{\tau}{2}\right) e^{-i\tau\xi}\, dt,\ \forall\, (u,\xi) \in \mathbb{R} \times \mathbb{R}^+.$$

It is worth observing that WVD is real, for each $(u,\xi) \in \mathbb{R} \times \mathbb{R}^+$. In addition, time and frequency have a symmetrical role, as Parseval relation implies

$$WV_f(u,\xi) = \int_{-\infty}^{+\infty} \hat{f}\left(\xi + \frac{\gamma}{2}\right) \hat{f}^*\left(\xi - \frac{\gamma}{2}\right) e^{-i\gamma u}\, d\gamma.$$

Thanks to its high resolution property, WVD is preferred for IF estimation. For a monocomponent signal $f(t) = a(t)e^{i\phi(t)}$, IF can be expressed as local moment of the WVD, as stated in the following

Proposition 1.2. *Let $f_a(t)$ be the analytic part of f, then*

$$\phi'(t) = \frac{\int_{-\infty}^{+\infty} \xi WV_{f_a}(u,\xi)\, d\xi}{\int_{-\infty}^{+\infty} WV_{f_a}(u,\xi)\, d\xi}.$$

Despite of its remarkable localization properties, due to its quadratic nature, WVD is affected by the presence of cross terms, i.e. interference terms between single modes — see Fig.1.6. Indeed, WVD of the composite signal $f(t) =$

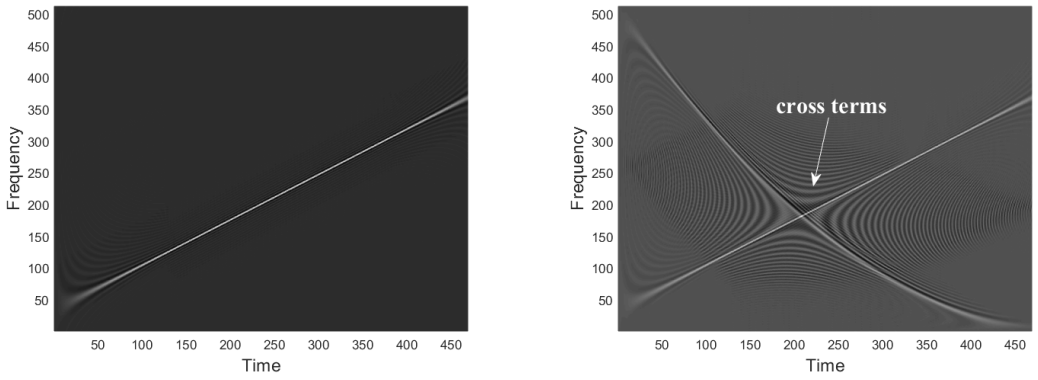

(a) (b)

Figure 1.6: WVD. (a) WVD of a linear chirp; (b) WVD of a two-components signal having overlapping modes.

$\sum_{k=1}^{N} f_k(t)$ can be expressed as

$$WV_f(u,\xi) = \underbrace{\sum_{k=1}^{N} WV_{f_k}(u,\xi)}_{auto-terms} + \underbrace{\sum_{k\neq j} Q[f_k, f_j](u,\xi)}_{cross-terms},$$

where Q denotes the cross WVD, i.e.

$$Q[h,z](u,\xi) = \int_{-\infty}^{+\infty} h\left(u+\frac{\tau}{2}\right) z^*\left(u-\frac{\tau}{2}\right) e^{-i\tau\xi}\, d\tau,\ \ h,z \in L^2(\mathbb{R}).$$

Cross-terms can be attenuated by applying proper TF filtering/averaging but it results in a loss of resolution. Actually, spectrogram, scalogram and all squared TF energy densities can be expressed as WVD smoothing. In particular, the spectrogram is the 2-dimensional convolution, in time and frequency, of the signal WVD with the analysis window WVD, i.e.

$$P_f^g(u,\xi) = \frac{1}{2\pi} WV_f * * WV_g = \frac{1}{2\pi} \iint_{-\infty}^{+\infty} WV_f(t,\omega) WV_g(t-u,\omega-\xi)\, dt\, d\omega. \tag{1.7}$$

More in general, since cross-terms include both positive and negative oscillations, they can be partially removed by applying a smoothing kernel, i.e.

$$WV_f^\theta(u,\xi) = \int_{-\infty}^{+\infty} \int_{-\infty}^{+\infty} WV_f(u',\xi')\, \Theta(u,u',\xi,\xi')\, du'\, d\xi',$$

resulting in the so-called smoothed WVD.

1.1.4 S-method

Spectrogram is the most common tool used in TF analysis, but it suffers from a lack of concentration, especially in case of highly non-stationary signals. On the contrary, WVD provides very concentrated distributions but, in case of MCS, it also produces cross-terms that can deteriorate resolution and make the representation unreadable. Many efforts have been done to propose smoother versions of WVD with attenuated cross-terms [37–39]. Unfortunately, the smoothing also causes auto-terms' degradation. In contrast to these approaches, S-method (SM) is designed for enhancing spectrogram resolution gradually. Based on the following expression of the WVD of a signal $f(t) \in L^2(\mathbb{R})$ [40]

$$WV_f(u,\xi) = 2\int_{-\infty}^{+\infty} S_f^g(u,\xi+\omega)(S_f^g(u,\xi-\omega))^* \, d\omega, \tag{1.8}$$

the TF representation referred as SM is defined as [15, 41]

$$SM_f(u,\xi) = 2\int_{-\infty}^{+\infty} \Theta(\omega) S_f^g(u,\xi+\omega)(S_f^g(u,\xi-\omega))^* \, d\omega, \ \forall\,(u,\xi) \in \mathbb{R}\times\mathbb{R}^+, \tag{1.9}$$

where $\Theta(\omega)$ is a window function. It is worth observing that if $\Theta(\omega) = 1$, then SM coincides to WVD, while $\Theta(\omega) = \delta(\omega)/2$ corresponds to the spectrogram. By changing the width of the window $\Theta(\omega)$ we thus obtain a gradual transition from spectrogram to WVD. If $f(t) = \sum_{k=1}^{N} f_k(t) = \sum_{k=1}^{N} a_k(t)e^{i\phi_k(t)}$ is a composite signal with separated modes in the TF plane, i.e. f_k lies in $D_k(u,\xi) \subset \Pi$, $\forall\, k = 1, ..., N$, with Π is the TF plane and $D_k \cap D_j = \emptyset$, $\forall k \neq j$, then SM provides TF representations having high concentration and cross-terms free. Indeed, in this case, the window length can be chosen so that SM is the sum of the WVDs of each signal components, i.e.

$$SM_f(u,\xi) = \sum_{k=1}^{N} WV_{f_k}(u,\xi). \tag{1.10}$$

The discrete version of eq.(1.9) for a rectangular window and defined on the

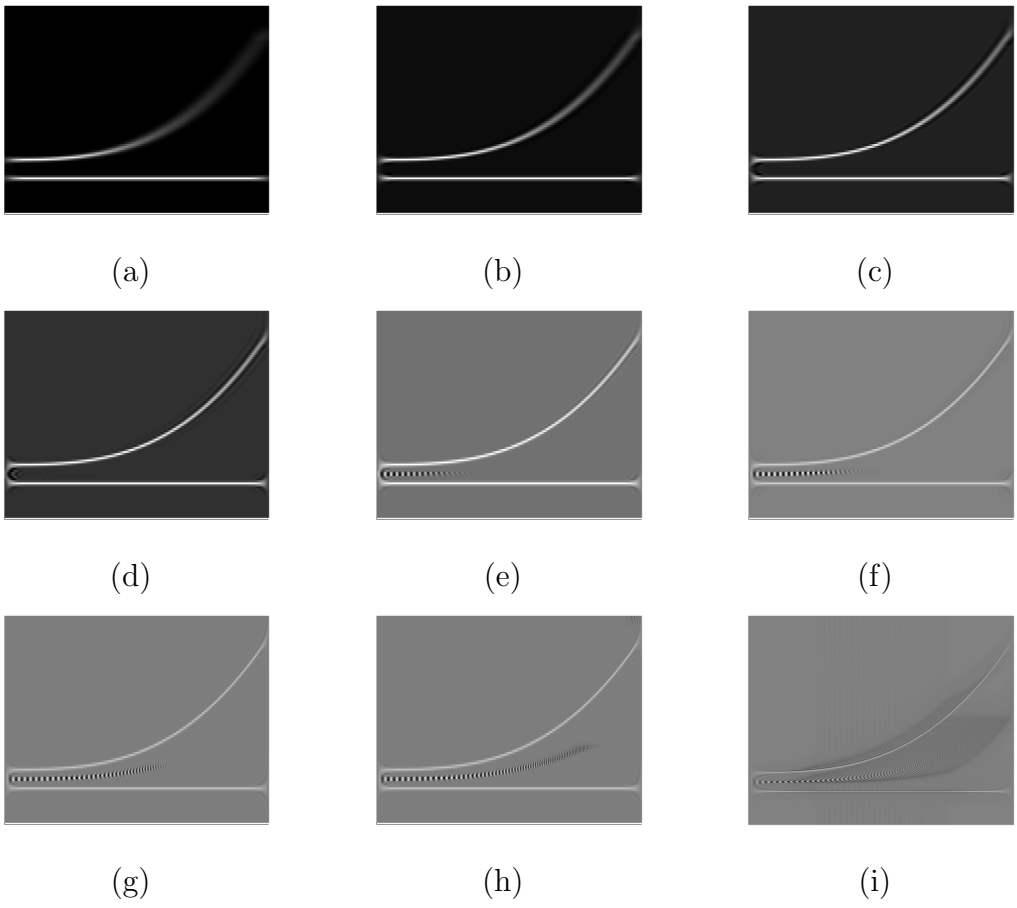

Figure 1.7: Two-components signal with separated modes in the TF plane. SM obtained for an increasing number of correcting terms. (a) $L = 0$, spectrogram; (b) $L = 1$; (c) $L = 2$; (d) $L = 3$; (e) $L = 4$; (f) $L = 5$; (g) $L = 10$; (h) $L = 20$; (i) WVD.

grid $\{(i,j)\}_{i,j} \subset \Pi$ is

$$SM_f(i,j) = P_f^g(i,j) + 2\Re\left\{\sum_{l=1}^{L} S_f^g(i,j+l)(S_f^g(i,j-l))^*\right\}, \qquad (1.11)$$

where $2L+1$ is $\Theta(\omega)$ length. As it can be observed, SM as in eq.(1.11) is the sum of the spectrogram plus corrective terms. The optimal signal length is signal-dependent. Theoretically, for well separated components, eq.(1.11) reduces to eq.(1.10) if $2L$ is equal to the width of the widest auto-term. Fig.1.7 shows the SM applied to a two-components signal whose modes are separated in the TF plane. As it can be noticed, the spectrogram smears the quadratic component. By adding the corrective terms in eq.(1.11), the resolution gradually increases,

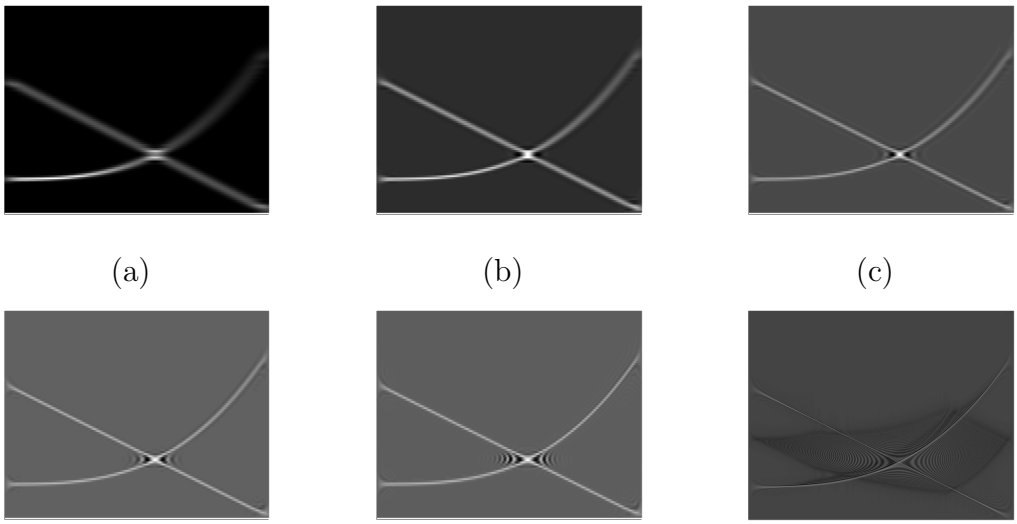

(a) (b) (c)

(d) (e) (f)

Figure 1.8: Two-components signal with crossing modes in the TF plane. SM obtained for an increasing number of correcting terms. (a) $L = 0$, spectrogram; (b) $L = 1$; (c) $L = 2$; (d) $L = 3$; (e) $L = 5$; (f) WVD.

until more concentration is obtained, as shown in Fig.1.7(c). For larger values of L, cross-terms appear in representation, which approaches WVD. Unfortunately, the same result can not be achieved if modes are not separated, as in the case shown in Fig.1.8. Fig.1.8(a) depicts the spectrogram of a signal composed of a quadratic plus a linear component that do cross in the TF plane. Even if SM helps in concentrating distribution at the intersection point, at the same time it introduces cross-terms that degrade the readability.

1.1.5 Radon transform

Radon transform (RT) is widely used in tomography as a tool for the recovery of the internal structure of an object by the knowledge of some projections. Nowadays, RT is adopted in many applications, including signal processing. RT is a non-linear transform which can be combined with WVD, as well as with the spectrogram, resulting in a powerful TF tool.

RT of a smooth function $F(x, y) \in \mathbb{R}^2$ at a point $(r, \theta) \in \mathbb{R}^2$ is defined as the integral of F along the line identified by the parameters r and θ, i.e. [42]

$$R_F(r, \theta) = \int_{\mathbb{R}} F(r\mathbf{n}_\theta + s\mathbf{n}_\theta^\perp)\, ds\,,$$

where $\mathbf{n}_\theta = (\cos\theta, \sin\theta)$ and $\mathbf{n}_\theta^\perp = (-\sin\theta, \cos\theta)$. A rotation of the coordinate system (x, y) by an angle θ gives the new coordinates

$$\begin{bmatrix} x' \\ y' \end{bmatrix} = \begin{bmatrix} \cos\theta & -\sin\theta \\ \sin\theta & \cos\theta \end{bmatrix} \begin{bmatrix} x \\ y \end{bmatrix} ;$$

therefore RT can be rewritten as [42]

$$R_F(r, \theta) = \int_{\mathbb{R}} F(r\cos\theta - s\sin\theta, r\sin\theta + s\cos\theta) ds \, .$$

RT is 2π-periodic with respect to θ. It is worth recalling the equivalent definition making use of delta function, i.e.

$$R_F(r, \theta) = \int_{-\infty}^{+\infty} F(x, y)\delta(r - x\cos\theta - y\sin\theta) \, dx \, dy.$$

According to the notation $R[F(x, y)] = R_F(r, \theta)$, RT main properties are listed below. The proof can be found in [43].

1. **Linearity**
$$R[aF + bG] = aR[F] + bR[G]$$

2. **Similarity**
$$R[F(ax, by)] = \frac{1}{|ab|} R_F\left(r, \frac{\cos\theta}{a}, \frac{\sin\theta}{b}\right)$$

3. **Symmetry**

$$R_F(ar, a\cos\theta, a\sin\theta) = \frac{1}{|a|} R_F(r, \cos\theta, \sin\theta)$$

$$R_F(-r, -\cos\theta, -\sin\theta) = R_F(r, \cos\theta, \sin\theta)$$

$$R_F(r, \rho\cos\theta, \rho\sin\theta) = \frac{1}{|\rho|} R_F\left(\frac{r}{\rho}, \cos\theta, \sin\theta\right)$$

4. **Shifting**

$$R[F(x - a, y - b)] = R_F(r - a\cos\theta - b\sin\theta, \cos\theta, \sin\theta)$$

5. **Differentiation**

$$R\left[\frac{\partial}{\partial x}F(x,y)\right] = \cos\theta\frac{\partial}{\partial r}R_F(r,\theta)$$

$$R\left[\frac{\partial}{\partial y}F(x,y)\right] = \sin\theta\frac{\partial}{\partial r}R_F(r,\theta)$$

$$R\left[\frac{\partial^2}{\partial x^2}F(x,y)\right] = \cos^2\theta\frac{\partial^2}{\partial r^2}R_F(r,\theta)$$

$$R\left[\frac{\partial^2}{\partial y^2}F(x,y)\right] = \sin^2\theta\frac{\partial^2}{\partial r^2}R_F(r,\theta)$$

$$R\left[\frac{\partial^2}{\partial x\partial y}F(x,y)\right] = \cos\theta\sin\theta\frac{\partial^2}{\partial r^2}R_F(r,\theta)$$

6. **Convolution**

$$F**G(x,y) = \int_{-\infty}^{+\infty} F(x',y')G(x-x',y-y')\,dx'\,dy'$$

$$R_{F**G} = R_F * R_G = \int_{-\infty}^{+\infty} R_F(\tau,\cos\theta,\sin\theta)R_G(r-\tau,\cos\theta,\sin\theta)\,d\tau$$

7. **Linear transformation**

$$R[F(A\mathbf{x})] = |\det(A^{-1})|R_F(r,A^{-T}\mathbf{n}_\theta).$$

The Fourier Central-Slice Theorem states that the n-dimensional FT of a function $F(\vec{x})$, $\vec{x}\in\mathbb{R}^n$, evaluated on the slice specified by the angle θ, is the 1-dimensional FT of $R_F(r,\theta)$ with respect the radial coordinate r. The result for $n=2$ is provided by the following

Theorem 2 (Fourier Central-Slice Theorem)**.** *Let us consider the 2-dimensional FT of the function F, i.e. $\hat{F}(q_1,q_2) = \int_{\mathbb{R}^2} F(x,y)e^{-i2\pi(q_1x+q_2y)}\,dx\,dy$, then*

$$\hat{F}(q\cos\theta, q\sin\theta) = \int_{\mathbb{R}} R_F(r,\theta)e^{-i2\pi rq}dr. \tag{1.12}$$

Theorem 2 establishes a fundamental relation between Euclidean, Radon and Fourier domains, that is depicted in Fig.1.9. Equivalently, the following

equality between operators acting on $L^2(\mathbb{R}^2)$ is satisfied

$$\mathcal{S}\mathcal{F}_2 = \mathcal{F}\mathcal{R},$$

where $\mathcal{F}$ and $\mathcal{F}_2$ respectively denote the 1-dimensional and 2-dimensional Fourier operators, $\mathcal{R}$ is the Radon operator and $\mathcal{S}$ is the operator extracting a central slice, i.e. $\mathcal{S}G(q_1, q_2) = G(q\cos\theta, q\sin\theta)$, with $G \in L^2(\mathbb{R}^2)$. In terms of involved variables, instead

$$\mathcal{F}_{2|(q\cos\theta, q\sin\theta)} = \mathcal{F}_{r\to q}\mathcal{R}_{|(r,\theta)},$$

and then

$$\mathcal{F}^{-1}_{q\to r}(\mathcal{F}_2(F))_{|(q\cos\theta, q\sin\theta)} = \mathcal{R}(r,\theta). \tag{1.13}$$

RT is thus equivalent to the inverse FT of the 2-dimensional FT of the signal with respect to the radial variable and eq.(1.13) provides an alternative method for RT computation, known as Fourier direct method and sketched in Fig.1.10.

Theorem 2 allows for the formal definition of the Inverse RT (IRT), whenever the 2-dimensional inverse FT is considered. Indeed, $F(x,y) = \mathcal{F}_2^{-1}\hat{F}(q_1, q_2)$, i.e.

$$\begin{aligned} F(x,y) = &\int_{-\infty}^{+\infty}\int_0^{\pi} \hat{F}(q\cos\theta, q\sin\theta)e^{-iq(x\cos\theta + y\sin\theta)}|q|d\theta dq = \\ &\int_0^{\pi} d\theta \left[\int_{-\infty}^{+\infty} |q|\hat{F}(q\cos\theta, q\sin\theta)e^{-iq\,r}dq\right]\Big| r = x\cos\theta + y\sin\theta \end{aligned}, \tag{1.14}$$

where polar coordinates have been used.

The term in square brackets in eq.(1.14) is the inverse 1-dimensional FT of the product function $|q|\hat{F}(q\cos\theta, q\sin\theta)$ evaluated at $r = x\cos\theta + y\sin\theta$, then by FT properties, the term can be replaced by the convolution of the FTs at the same point. For this reason, by recalling eq.(1.13), we obtain

$$F(x,y) = \int_0^{\pi} d\theta \left[\mathcal{F}^{-1}(|q|) * R(r,\theta)\right]\Big| r = x\cos\theta + y\sin\theta\,.$$

It is possible to prove that [44]

$$\mathcal{F}^{-1}(|q|) = \delta'(r) * \frac{1}{2\pi^2}\mathcal{P}\left(\frac{1}{r}\right),$$

where $\mathcal{P}$ stands for the Cauchy principal value. Finally, by delta function

properties

$$F(x,y) = -\frac{1}{2\pi^2}\int_0^\pi d\theta\ \mathcal{P}\left(\int_{-\infty}^{+\infty}\frac{\frac{\partial R}{\partial r}(r,\theta)}{x\cos\theta + y\sin\theta}\,dr\right)$$
$$= -\frac{1}{2\pi^2}\int_0^\pi \lim_{M\to+\infty}\left(\int_{-M}^{M}\frac{\frac{\partial R}{\partial r}(r,\theta)}{x\cos\theta + y\sin\theta}\,dr\right)\,d\theta,$$

with $\frac{\partial R}{\partial r}$ denoting the derivative of R_F with respect to radial coordinate r.

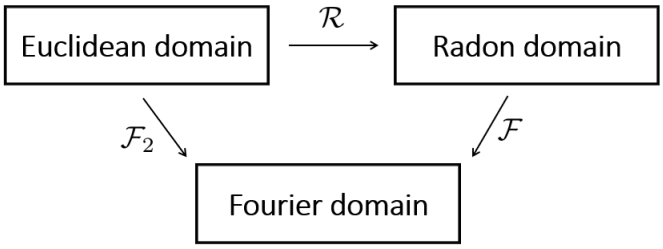

Figure 1.9: Relation between Euclidean, Radon and Fourier domains established by Theorem 2. $\mathcal{R}, \mathcal{F}_2$ and $\mathcal{F}$ respectively denote Radon, 2-dimensional Fourier and Fourier operator.

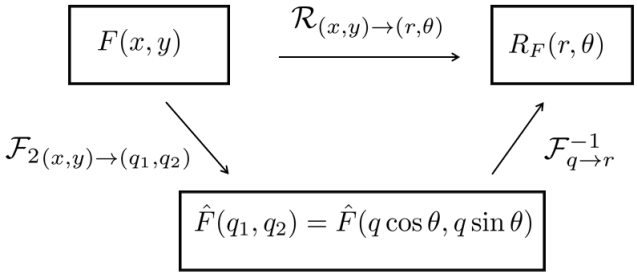

Figure 1.10: Fourier direct method for RT computation. $\mathcal{R}$ and $\mathcal{F}_2$ respectively denote Radon and 2-dimensional Fourier operator, while $\mathcal{F}^{-1}$ stands for the 1-dimensional inverse Fourier operator.

The inversion formula is valid for $\theta \in [0,\pi)$ with continuity. In applied problems, only a discrete set of projections is available, that's why only an approximation of the function F can be recovered. For this reason, the *back-projection formula* below (eventually filtered) is commonly used, i.e.

$$F(x,y) = \frac{1}{\pi}\int_0^\pi R_F((x,y)\cdot\mathbf{n}_\theta)\,d\theta. \tag{1.15}$$

As mentioned before, RT is nowadays a useful tool in signal processing, especially in linear FM signals representation. Indeed, the problem of detecting a linear chirp reduces to peak detection in Radon domain, as shown in Fig.1.11, which respectively depicts the RT of the spectrogram and the WVD of a linear chirp (this last is referred as Radon Wigner in the literature). As it will been shown in Chapter 3, the joint use of RT and TF analysis can be effective also for non-linearly FM signals.

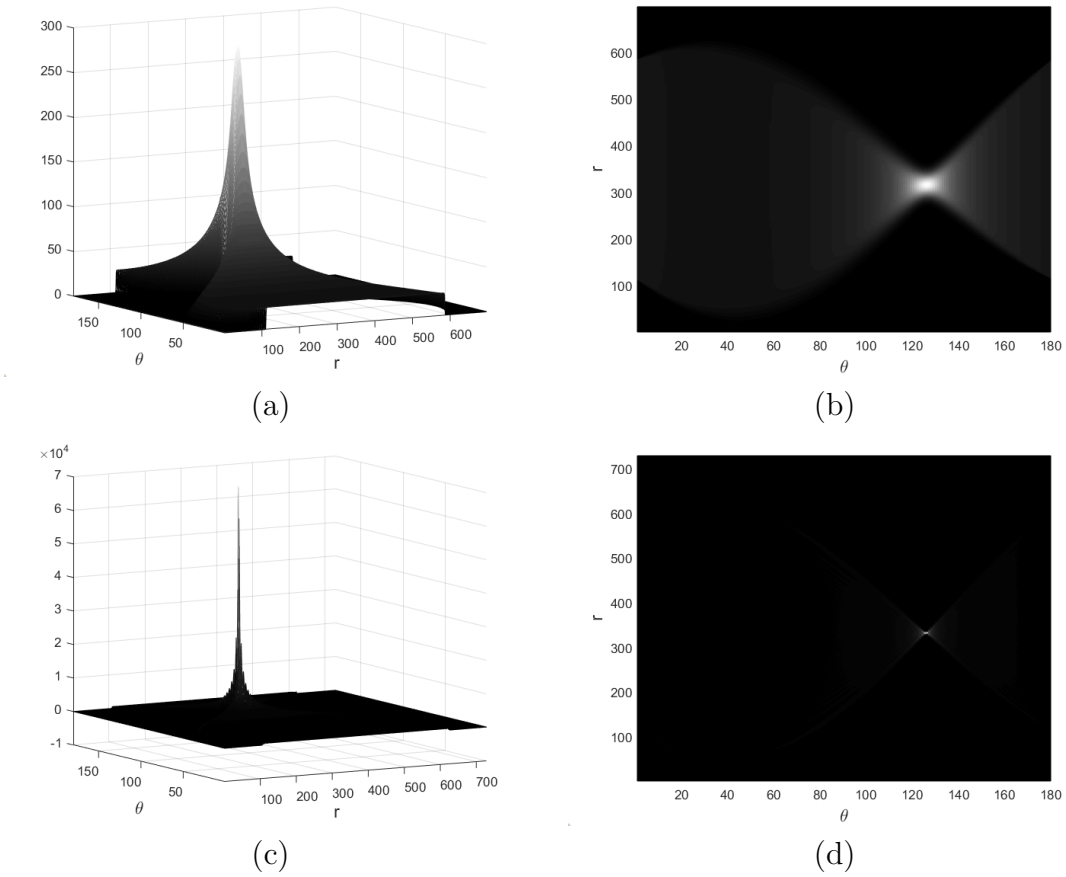

Figure 1.11: Combination of RT and TF signal analysis. (a) RT of the spectrogram in Fig.1.3(d), 3D view; (b) view from above of (a); (c) RT of the WVD in Fig.1.6(a), also known as Radon Wigner, 3D view; (d) view from above of (c).

1.1.6 Fractional Fourier transform

The Fractional Fourier transform (FrFT) belongs to the class of linear TFRs and it can be seen as a generalization of the classical FT. The FrFT of a function

$f \in L^2(\mathbb{R})$ at a point $(r, \theta) \in \mathbb{R}^2$ is defined as [15, 45]

$$\mathbb{F}_f(r, \theta) = \int_{-\infty}^{+\infty} f(t)\, K(\theta, t, r)\, dt, \tag{1.16}$$

where the kernel $K(\theta, t, r)$ is given by

$$K(\theta, t, r) = \frac{e^{i\frac{\theta}{2}}}{\sqrt{i \sin\theta}} e^{i\pi \frac{(t^2+r^2)\cos\theta - 2rt}{\sin\theta}}.$$

It is worth observing that for $\theta = 0$ and $\theta = \pi$, the kernel K reduces to the Dirac delta functions $\delta(x - r)$ and $\delta(x + r)$, respectively. Therefore, $\mathbb{F}_f(r, 0) = f(r)$ and $\mathbb{F}_f(r, \pi) = f(-r)$. In addition, $\mathbb{F}_f(r, \pi/2)$ and $\mathbb{F}_f(r, -\pi/2)$ respectively correspond to the classical FT and the inverse FT. In addition, the following properties hold [46, 47]:

1. **Linearity**
$$\mathbb{F}_{af(t)+bg(t)}(r, \theta) = a\mathbb{F}_f(r, \theta) + b\mathbb{F}_g(r, \theta)$$

2. **Parseval's equality**
$$\int_{-\infty}^{+\infty} f(t) g^*(t)\, dt = \int_{-\infty}^{+\infty} \mathbb{F}_f(r, \theta)\mathbb{F}_g^*(r, \theta)\, dr$$

3. **Shifting**
$$\mathbb{F}_{f(t-\tau)}(r, \theta) = \mathbb{F}_f(r - \tau\cos\theta, \theta) e^{i\pi \sin\theta(\tau^2 \cos\theta - 2r\tau)}, \quad \forall\, \tau \in \mathbb{R}$$

4. **Modulation theorem**
$$\mathbb{F}_{f(t)e^{i2\pi\nu t}}(r, \theta) = \mathbb{F}_f(r - \nu\sin\theta, \theta) e^{i\pi \sin\theta(\nu^2 \sin\theta - 2r\nu)}, \quad \forall\, \nu \in \mathbb{R}$$

5. **Scaling theorem**
$$\mathbb{F}_{f(ct)}(r, \theta) = \sqrt{\frac{\cos\gamma}{\cos\theta}} e^{i\frac{\theta-\gamma}{2}} e^{i\pi r^2 \cot\theta \left(1 - \frac{\cos^2\gamma}{\cos^2\theta}\right)} \mathbb{F}_{f(t)}\left(\frac{r}{c}\frac{\sin\gamma}{\sin\theta}, \gamma\right),$$
$$\forall\, c\, \gamma \in \mathbb{R} : \frac{\tan\gamma}{\tan\theta} = c^2$$

6. **Continuity** $\mathbb{F}_f(r, \theta)$ is a continuous function with respect to θ

7. 2π**-periodicity**

$$\mathbb{F}_f(r, \theta + 2k\pi) = \mathbb{F}_f(r, \theta), \quad \forall\, k \in \mathbb{Z}$$

8. **Additivity**

$$\mathbb{F}_f(r, \theta_1)\mathbb{F}_f(r, \theta_2) = \mathbb{F}_f(r, \theta_1 + \theta_2)$$

9. **Symmetry**

$$\mathbb{F}_f^*(r, \theta) = \{\mathbb{F}_f(r, -\theta)\}^*.$$

From the properties listed above, it follows the inverse formula

$$f(t) = \int_{-\infty}^{+\infty} \mathbb{F}_f(r, \theta)\, K(-\theta, t, r)\, dr.$$

The Hermite-Gauss functions defined as $\Psi_n(t) = \frac{1}{\sqrt{2^{n-\frac{1}{2}}\, n!}} e^{-\pi t^2} H_n(\sqrt{2\pi}t)$, with $H_n(t) = (-1)^n e^{t^2} \frac{d^n}{dt^n} e^{-t^2}$ denoting the Hermite polynomials, are eigenfunctions of the FrFT with eigenvalues $e^{-in\theta}$. Since the family $\{\Psi_n(t)\}_n$ is a complete orthonormal set, then the fractional kernel K can be expressed as

$$K(\theta, t, r) = \sum_{n \geq 0} e^{-in\theta} \Psi_n(t) \Psi_n(r).$$

The variable θ can be interpreted as a rotation angle in the phase plane as it holds

$$W_{\mathbb{F}_f}(u, \xi) = W_f(u\cos\theta - \xi\sin\theta, u\sin\theta + \xi\cos\theta),$$

or equivalently $W_{\mathbb{F}_f}(u', \xi') = W_f(u, \xi)$ where (u', ξ') are the coordinates in the rotated plane, i.e.

$$\begin{bmatrix} u' \\ \xi' \end{bmatrix} = \begin{bmatrix} \cos\theta & \sin\theta \\ -\sin\theta & \cos\theta \end{bmatrix} \begin{bmatrix} u \\ \xi \end{bmatrix}.$$

A similar relation holds for the ambiguity function. The above relations establish a connection between FrFT and WVD. In particular, for each angle θ, the squared modulus of the FrFT, referred as fractional power spectrum, corresponds to the projection of the WVD along the direction identified by θ. More precisely, the fractional power spectrum is

$$|\mathbb{F}_f(u, \theta)|^2 = \int_{-\infty}^{+\infty} W_{\mathbb{F}_f(r,\theta)}(u, \xi) d\xi = \int_{-\infty}^{+\infty} W_f(u\cos\theta - \xi\sin\theta, u\sin\theta + \xi\cos\theta)\, d\xi,$$

with $\theta \in [0, \pi)$. The latter is also called Radon Wigner transform (RW) — the RT of WVD. In signal processing, RW was originally adopted for detecting multicomponent linearly modulated (LFM) signals [48, 49]. Indeed, the FrFT of a linear chirp $f(t) = e^{-i\frac{\pi t^2}{\tan\beta}}$ is

$$e^{i\frac{\theta}{2}}\sqrt{\frac{\sin\beta}{\sin(\beta-\theta)}}e^{-i\pi\frac{r^2}{\tan(\beta-\theta)}},$$

which becomes proportional to a Dirac function $\delta(r)$ for $\theta \to \beta$, thus the constant chirp slope (IF) can be detected as a local maximum of RW.

The following proposition gives the expression of IF in terms of the FrFT.

Proposition 1.3. *[50] Let $f(t) = a(t)e^{i\phi(t)}$ be a monocomponent signal*

$$\begin{aligned}\phi'(t) =& \frac{1}{2|\mathbb{F}_f(r,\pi)|^2}\int_{-\infty}^{+\infty}\left.\frac{\partial|\mathbb{F}_f(r,\beta)|^2}{\partial\beta}\right|_{\beta=\theta} sgn(\tau-t)\,d\tau = \\ & \frac{1}{2RW(r,\theta)}\int_{-\infty}^{+\infty}\left.\frac{\partial RW(r,\beta)}{\partial\beta}\right|_{\beta=\theta} sgn(\tau-t)\,d\tau.\end{aligned}$$

1.2 Main definitions

This section formally defines the most important concepts introduced in the previous section.

Definition 3. *An AM-FM-MCS is defined as*

$$f(t) = \sum_{k=1}^{N} f_k(t) = \sum_{k=1}^{N} a_k(t)e^{i\phi_k(t)}\,, \tag{1.17}$$

where $f_k \in L^2(\mathbb{R})$ is the $k-th$ mode and a_k and ϕ_k are smooth time-varying functions respectively denoting the amplitude and the phase of f_k. N is finally the number of components.

According to Def.3, the decomposition task is achieved if each mode $f_k(t)$ is separated from the mixture signal $f(t)$. The decomposition allows for the estimation of the IFs of the signal, which are defined in the following

Definition 4. *The instantaneous frequencies (IFs) of $f(t)$ as in eq.(1.17) are defined as the phases time derivatives, i.e.*

$$\phi_k'(t), \quad k = 1, ..., N. \tag{1.18}$$

Fig.1.12(a) shows a monocomponent signal having quadratic frequency modulation, whose IF is depicted in Fig.1.12(b).

It is worth pointing out that, in the multicomponent framework, IFs separation enables signal decomposition.

Analysis window and its spread are formally defined in the following

Definition 5. *An analysis window $g(t)$ is a positive and symmetric function, compactly supported or smooth and fast decreasing to zero. The frequency bandwidth of g, denoted as $\Delta\omega$, is defined by the following condition*

$$|\hat{g}(\omega)| \ll 1 \quad for \quad \omega \geq \Delta\omega. \tag{1.19}$$

In the literature, the definition of separable components depends on the adopted analysis window.

Definition 6. *Let f be a AM-FM MCS signal as defined in eq.(1.17) and let f_{k_1} and f_{k_2}, $k_1, k_2 \in \{1, ..., N\}$ be two single modes. f_{k_1} and f_{k_2} are separable in $\Omega \subseteq \mathbb{R}$ by the analysis window g if*

$$|\phi'_{k_1}(t) - \phi'_{k_2}(t)| \geq \Delta\omega, \quad \forall\, t \in \Omega\,, \tag{1.20}$$

where $\Delta\omega$ is the frequency bandwidth of g.

Equivalently speaking, ϕ'_{k_1} and ϕ'_{k_2} satisfy the separability condition in Ω. Otherwise, they are said non-separable in Ω.

On the contrary, the definition of well separated and overlapping components is independent of the specific transforms (the device used to analyze the signal), as they refer to an intrinsic feature of the signal.

Definition 7. *A FM-MCS signal f as defined in eq.(1.17) is composed of well separated components if its IFs can be ordered so that*

$$\phi'_N(t) > \phi'_{N-1}(t) > ... > \phi'_1(t),\ \forall\, t \in supp\{f\}.$$

Definition 8. *Let f be a FM-MCS signal as defined in eq.(1.17) and let f_{k_1} and f_{k_2}, $k_1, k_2 \in \{1, ..., N\}$ be two single modes. f_{k_1} and f_{k_2} are overlapped components if their supports overlap both in time and frequency, i.e.*

$$supp\{f_{k_1}\} \cap supp\{f_{k_1}\} \neq \emptyset \text{ and } supp\{\hat{f}_{k_1}\} \cap supp\{\hat{f}_{k_1}\} \neq \emptyset.$$

Definition 9. *Let f be a FM-MCS signal as defined in eq.(1.17) and let f_{k_1} and f_{k_2}, $k_1, k_2 \in \{1, ..., N\}$ be two single modes. f_{k_1} and f_{k_2} are crossing components in $t_0 \in \mathbb{R}$ if*

$$\phi_1'(t_0) = \phi_2'(t_0)$$

A similar definition has been introduced in [51], i.e.

Definition 10. *Two components f_1 and f_2 are said to be crossing (or overlapping) in the TF domain if there exists a time instant t_0 and a bound $d > 0$ such that*

$$\phi_1'(t_0) = \phi_2'(t_0),$$

$$|\phi_1''(t_0) - \phi_2''(t_0)| \geq d. \tag{1.21}$$

It is worth observing that eq.(1.21) excludes the case of tangent modes at t_0. For this reason, Def.10 is not adopted in this thesis.

Remark 2. *If two modes do cross in the TF plane, then they are overlapping components. The latter are non-separable, as it can not exist a proper window g such that condition in eq.(1.20) holds true. In all these cases, we say that modes interfere with each other.*

Fig.1.13(a) shows the spectrogram of a signal having two well separated components, in the sense of Def.7. In addition, modes are separable, according to Def.6. As a consequence, spectrogram section at each fixed time instant u matches with the single profiles — the sections referred to the spectrogram of the single modes, processed separately — as shown in Fig.1.13(b).

Fig.1.14 provides an example of crossing modes. As it can be noticed in Fig.1.14(b) and (d), spectrogram section does not match the single profiles, even if the window size is changed. In particular, maxima points positions are highly deviated due to interference and spectrogram energy is much lower than the energy of the individual profiles, as depicted in Fig.1.14(b). In addition, only a component is perceived at $u = 170$, see Fig.1.14(d).

1.3 Decomposition of non-overlapping components

The main methods for the decomposition of well separated components are reviewed in this section. Section 1.3.1 briefly presents methods which process the

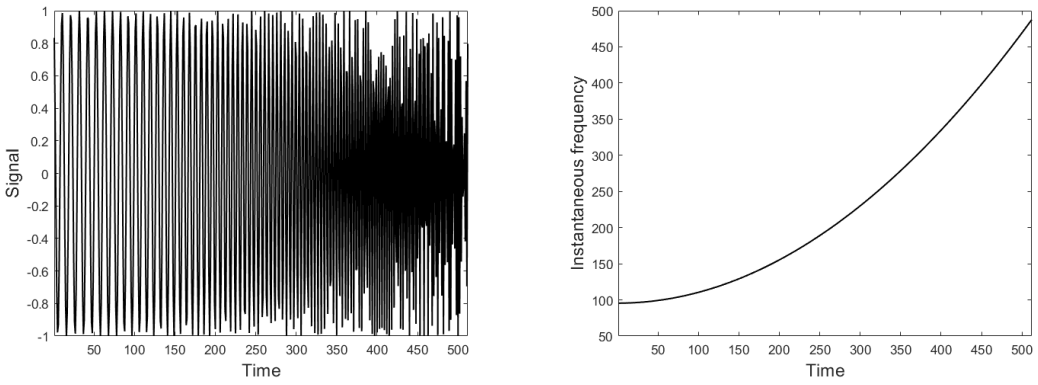

(a) (b)

Figure 1.12: (a) Quadratic chirp; (b) IF profile.

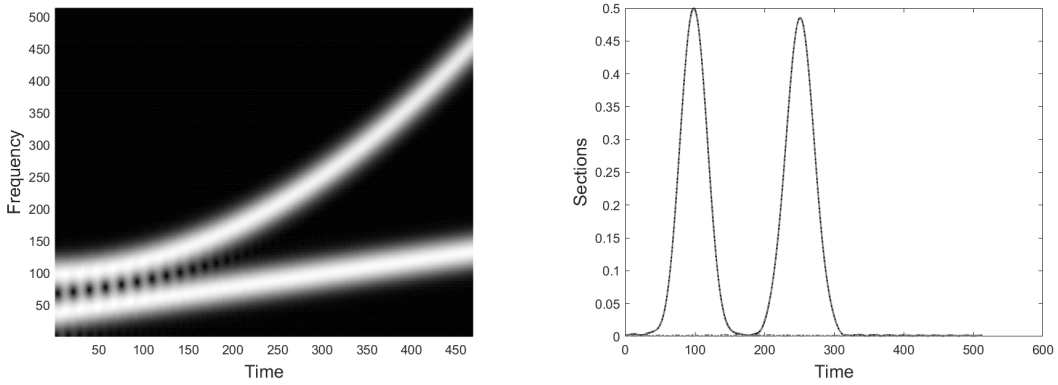

(a) (b)

Figure 1.13: Separable components. (a) Spectrogram; (b) Spectrogram section (solid line) and sections of the spectrogram of the single modes (dotted grey lines).

signal in the time domain while Section 1.3.2 is devoted to TF-based approaches.

1.3.1 Analysis in the time domain: EMD

First introduced in [52], the Empirical Mode Decomposition (EMD) is a non-linear technique aimed at representing non-stationary signals. It decomposes a FM-MCS into a small number of oscillating components, referred as intrinsic mode functions (IMFs), provided they are well separated in the TF plane.

According to [52], a MCS $f(t) = \sum_{k=1}^{N} f_k(t)$ can be decomposed into its IMFs $f_k(t) = a_k(t)\cos\phi_k(t)$, $k = 1, ..., N$ if the following conditions are satisfied:

(i) the number of extrema and the number of zeros crossing of f_k is either

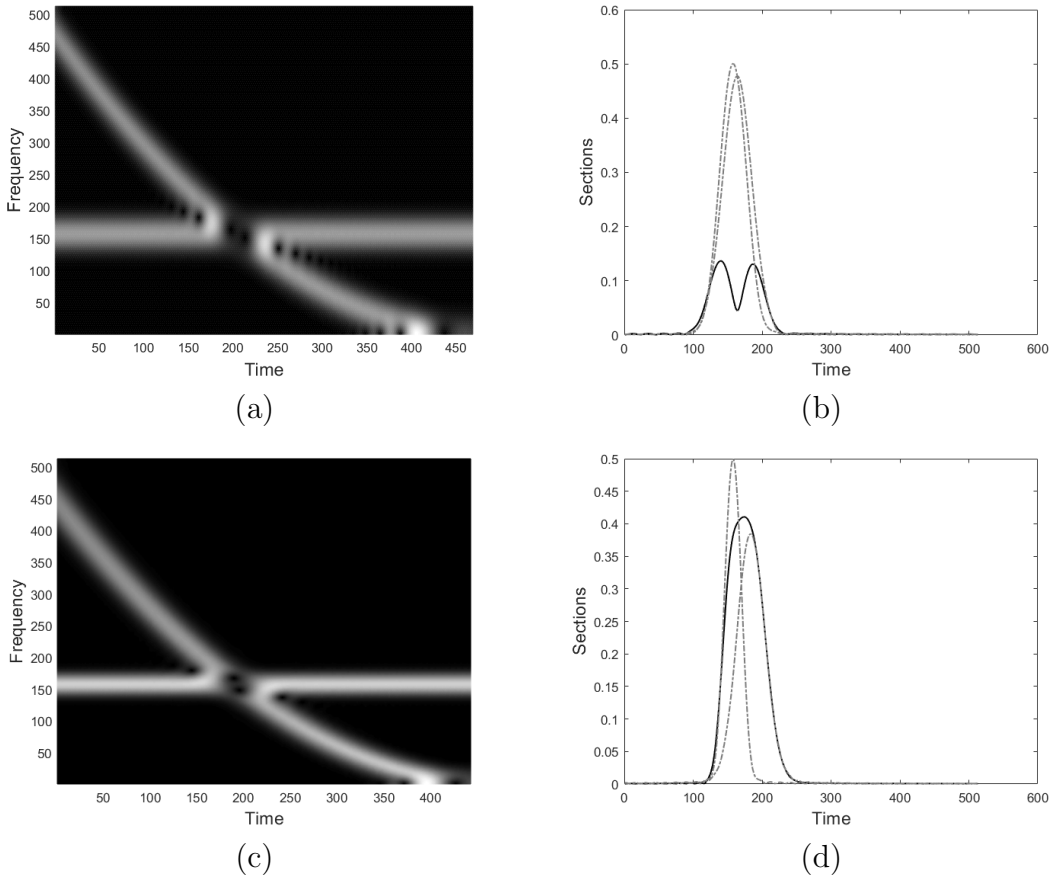

Figure 1.14: Non separable components. (a) Spectrogram, window size = 44; (b) Section of the spectrogram (solid line) and sections of the spectrogram of the single modes (dotted grey lines) at $u = 200$;(c) Spectrogram, window size $s = 70$; (b) Section of the spectrogram (solid line) and sections of the spectrogram of the single modes (dotted grey lines) at $u = 170$.

equal or differs at most by one;

(ii) for any t, the value of a smooth envelope defined by the local minima of f_k is the negative of the corresponding envelope defined by the local maxima.

Notice that IMFs f_k satisfy condition (i) and (ii), but the reverse inclusion does not hold in general.

EMD considers signal oscillations at a very local level. Indeed, it looks at two consecutive extrema and extracts the high-frequency part (or local detail $r(t)$) and the low-frequency part (local trend $m(t)$), so that the signal is decomposed as $f(t) = r(t) + m(t)$.

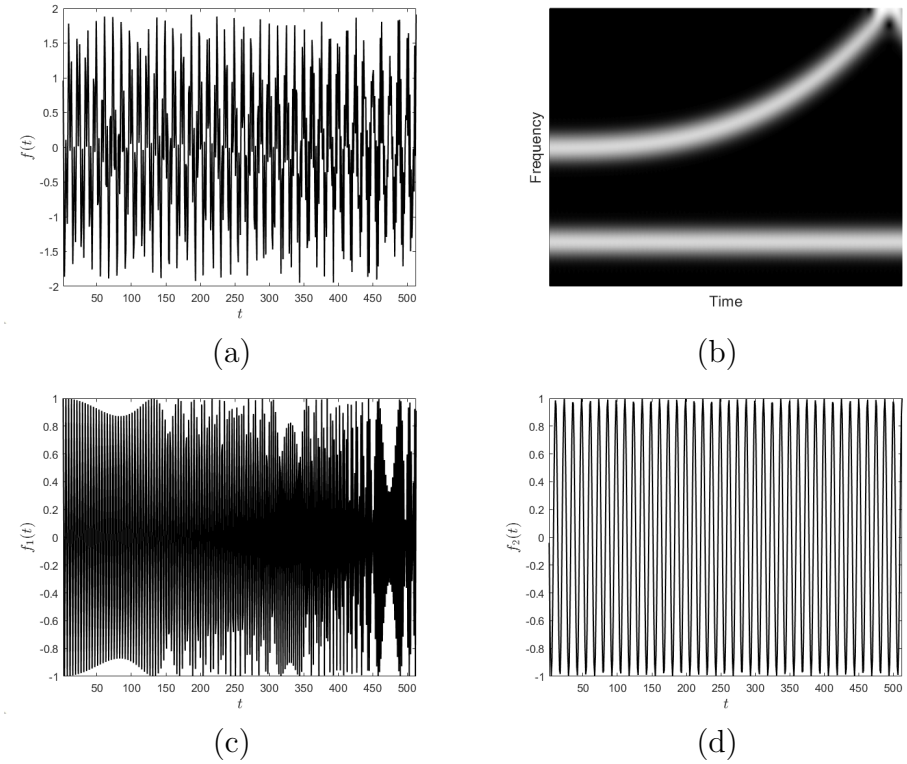

Figure 1.15: Two-components signal $f(t) = f_1(t) + f_2(t)$ with separated modes. (a) Signal in the time domain; (b) Spectrogram; (c) True $f_1(t)$; (d) True $f_2(t)$.

EMD consists of a *sifting* process. At each step, two smooth envelopes are constructed by cubic splines, respectively interpolating the local maxima and the local minima. Then, the mean of the two envelopes is taken and subtracted from the original signal. The latter is the candidate first IMF, i.e. the harmonic function with higher IF. The above procedure is repeated on the residual signal for a fixed number of iterations or, alternatively, until the residual is almost zero-mean, according to some stopping criterion. The desired decomposition is achieved by taking the residuals $\{r_k, k = 1, ..., N\}$ as IMFs.

The whole algorithm can be summarized as follows:

1. identify the extrema of $f(t)$;
2. interpolate the minima and the maxima, ending up with two envelopes $\bar{f}(t)$ and $\underline{f}(t)$;
3. compute the mean $m(t) = \left(\bar{f}(t) + \underline{f}(t)\right)/2$ (local trend);
4. extract the residual $r(t) = f(t) - m(t)$ (local detail);

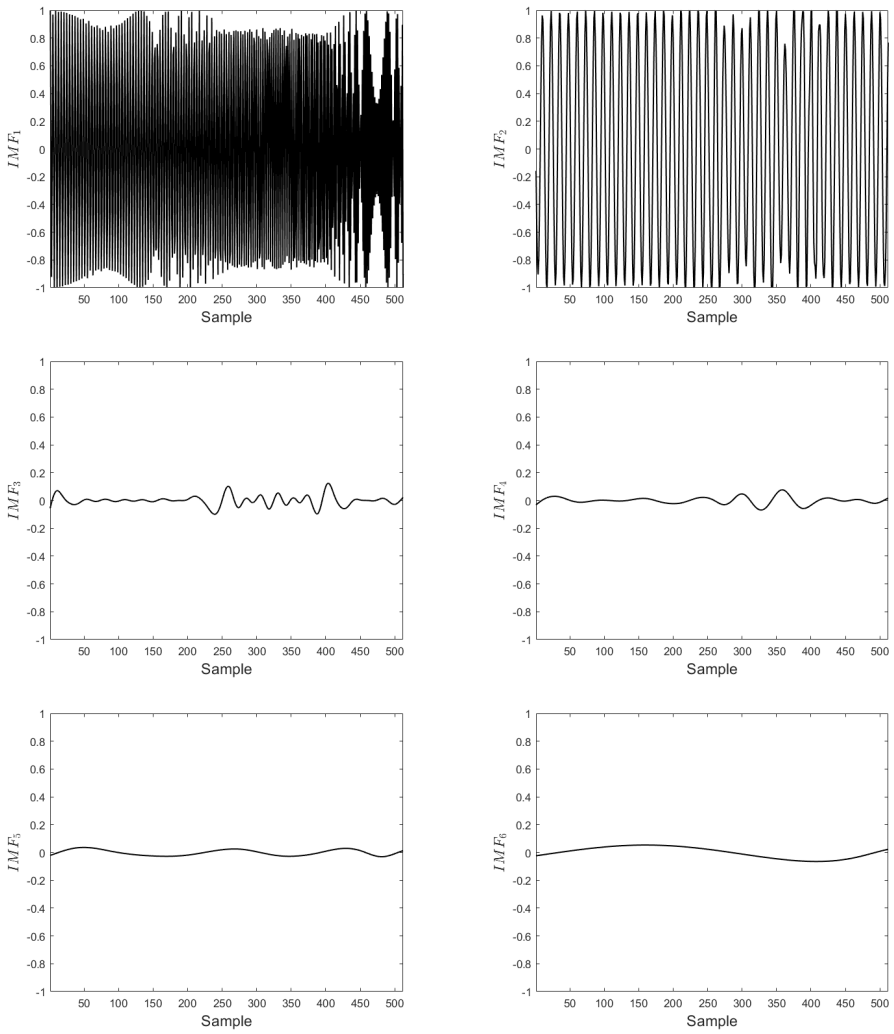

Figure 1.16: IMFs obtained by EMD applied to the signal in Fig.1.15(a).

5. iterate steps 1-4 on the residual $r(t)$.

Fig.1.16 shows EMD output when applied to the two-components signal in Fig.1.15(a). As it can be observed, IMFs in the first line of Fig.1.16(a)-(b) well approximate the true components depicted in Fig.1.15(c)-(d). Unfortunately, the same algorithm is not suitable for analysing overlapped components in the TF plane, as the ones shown in Fig.1.17. In this case, IMFs do not match the true modes at all—compare Fig.1.18 to Fig.1.17(c)-(d).

EMD pros. Linear methods (e.g. STFT) decompose a signal by computing its inner product (or correlation) with a pre-assigned family of functions (atoms).

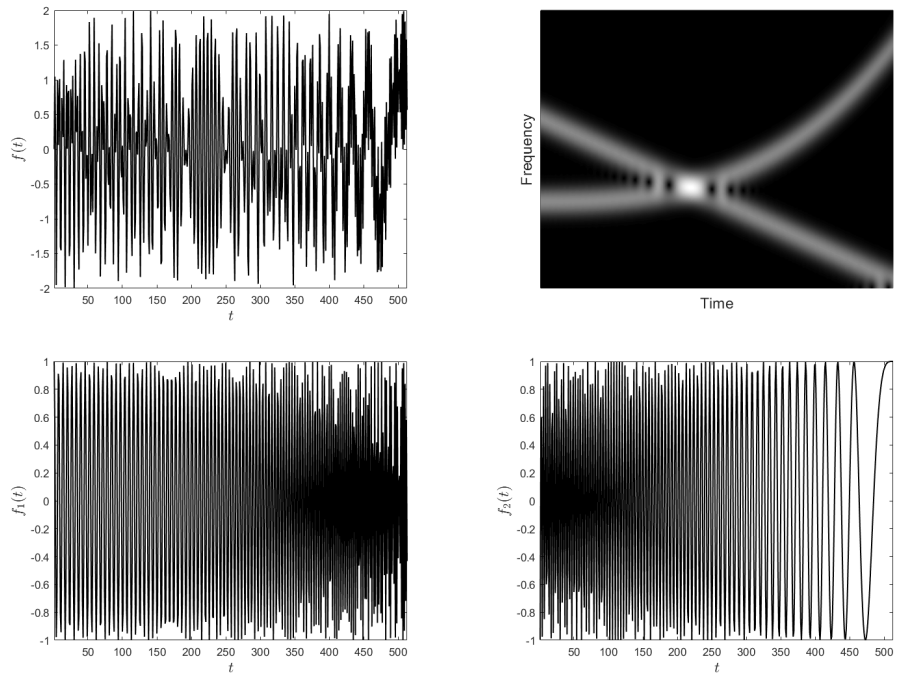

Figure 1.17: Two-components signal $f(t) = f_1(t)+f_2(t)$ with overlapped modes. (a) Signal in the time domain; (b) Spectrogram; (c) True $f_1(t)$; (d) True $f_2(t)$.

This unavoidably results in TF representations that are spread all over the domain and whose readability is affected by the chosen atoms. Furthermore, TF representations are subjected to Heisenberg uncertainty principle which limits the resolution. EMD does not present these drawbacks, as it directly processes the signal in the time domain.

EMD cons. The decomposition into IMFs is not unique. Since the number of components is generally unknown, EMD output depends on the pre-fixed and arbitrary choice of the number of IMFs. As further limitation, EMD technique does not admit any analytical formulation which would allow for its theoretical analysis and rigorous performance evaluation. Finally, EMD is sensitive to noise and limited to well separated components.

EMD modifications. The Ensemble Empirical Mode Decomposition (EEMD) has been introduced in [53] in order to overcome the sensitivity to noise of the original algorithm.

Inspired by EMD, an iterative filtering method has been proposed in [54]. Contrary to EMD and EEMD, in this procedure the mean is computed as a local average of the values of the signal [55]. As a result, in many cases the

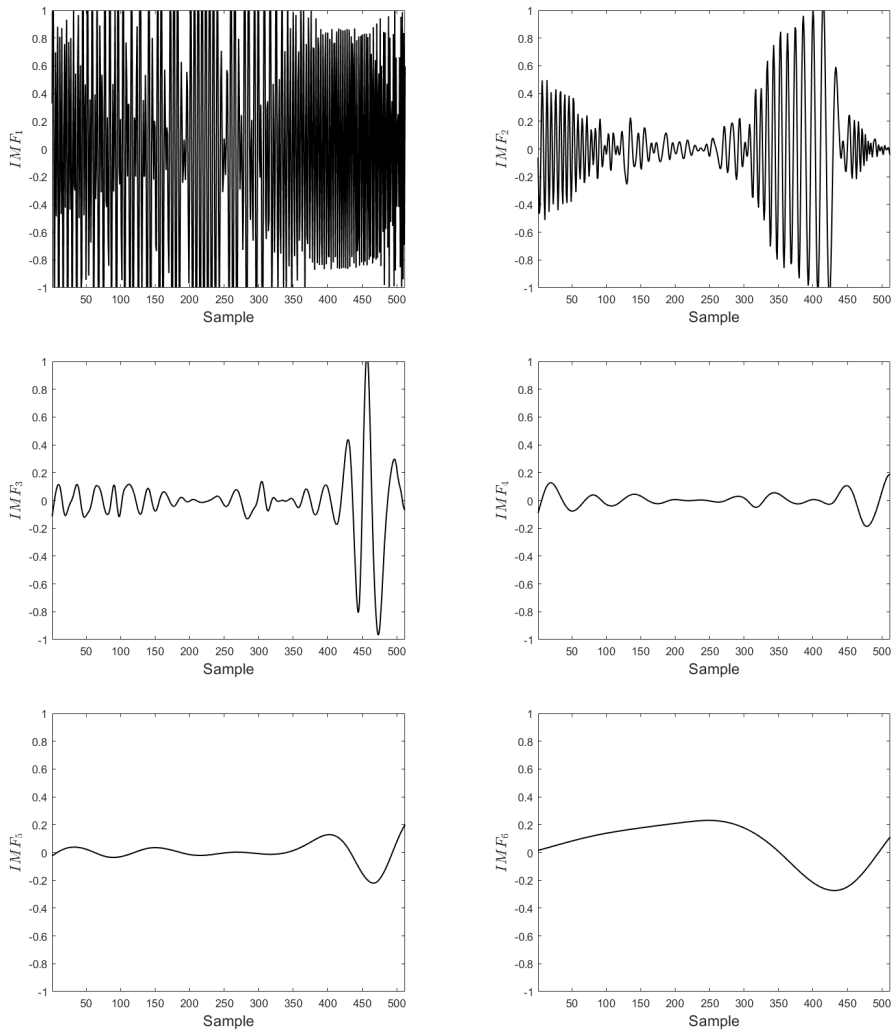

Figure 1.18: IMFs obtained by EMD applied to the signal in Fig.1.17(a).

convergence can be rigorously proved.

Recently, EMD has been extended to multivariate signals [56, 57] and successfully applied for the analysis of real-life signals [6].

Similarly to EMD, the local mean decomposition (LMD) is an iterative approach aimed at demodulating AM-FM signals, such as electrocardiograms, functional magnetic resonance imaging data, and earthquake data. Introduced in [5], LMD decomposes signals into a set of functions, each of which is the product of an envelope signal and a frequency modulated signal. Differently from EMD, LMD of a signal is accomplished by progressively smoothing the signal using moving averaging which is weighted by the distance between the successive extrema of the signal. As a result, a time-varying IF can be derived

by LMD.

1.3.2 TF analysis

TF signal analysis provides an efficient characterization of non-stationary signals. In order to overcome the limitations given by Heisenberg uncertainty principle and to further enhance TF resolution, Reassignment method and Synchrosqueezing transform have been introduced.

Modes separation, as well as IFs estimation, is commonly achieved by the detection of TFD local maxima, e.g. spectrogram, WVD, absolute value of ST or higher-resolution representation such as Adaptive directional TFD or FrFT. A brief review of the above-mentioned transforms and related separation methods is given below.

1.3.2.1 Sparsification approaches (RM and SST)

Reassignment method

Reassignment method (RM) has been proposed for enhancing the readability of TF and time-scale distributions. Specifically, reallocation techniques allow to achieve both concentration of signals components and no misleading interference terms, such as the cross terms arising in WVD. Reassignment principle formalizes and extends the Modified Moving Window Method introduced in [58]. In particular, [59] presented the method in a modern way and proved its efficiency theoretically, opening the way to its application to general bilinear TF and time-scale representations. Reliable algorithms for RM has been then proposed [60], as well as some modifications and extension to multidimensional signals [61]. In this section, without loss of generality, the reassigned spectrogram is presented.

It is well known that spectrogram can be expressed as an averaging of WVD, i.e.

$$P_f^g(u,\xi) = \frac{1}{2\pi} \int \int_{-\infty}^{+\infty} WV_f(t,\omega) WV_g(t-u, \omega-\xi)\, dt\, d\omega,$$

that is the value of the spectrogram at a given point (u, ξ) in the TF plane is the convolution of the signal WVD with the window WVD. In other words, the whole WVD is weighted by the WVD of the window and the resulting sum is assigned to the geometrical center of the domain over which the distribution is considered. In RM, the total mass is conversely assigned to the center of

gravity of the distribution within the domain, i.e. the following quantities are computed

$$\hat{u}_f(u,\xi) = \frac{1}{2\pi P_f^g(u,\xi)} \int\int_{-\infty}^{+\infty} t\, WV_f(t,\omega) WV_g(t-u,\omega-\xi)\, dt\, d\omega, \qquad (1.22)$$

$$\hat{\xi}_f(u,\xi) = \frac{1}{2\pi P_f^g(u,\xi)} \int\int_{-\infty}^{+\infty} \omega\, WV_f(t,\omega) WV_g(t-u,\omega-\xi)\, dt\, d\omega, \qquad (1.23)$$

which define the local centroids of WV_f, as seen through the TF window WV_g centered in (u,ξ). The reassigned spectrogram is then given by

$$\hat{P}(u,\xi) = \int\limits_{\mathbf{R}^2} P(u',\xi')\delta(u'-\hat{u}_f(u',\xi'),\xi'-\hat{\xi}_f(u',\xi'))\frac{du'd\xi'}{2\pi}\,. \qquad (1.24)$$

Denoting by φ the phase of the STFT, it can be proved that quantities in eqs.(1.22) and (1.23) are equivalent to [58]

$$\hat{u}_f(u,\xi) = \frac{u}{2} - \frac{\partial}{\partial\omega}\varphi(u,\xi),$$

$$\hat{\xi}_f(u,\xi) = \frac{\omega}{2} + \frac{\partial}{\partial u}\varphi(u,\xi),$$

which can be interpreted as the local IF and group delay (GD) of the analyzed signal. Unfortunately, the computation of phase derivatives suffers from the phase unwrapping problem. A more reliable algorithm is based on the following expressions for the centroids, i.e.

$$\hat{u}_f(u,\xi) = u + \Re\left(\frac{S_f^{tg}(u,\xi)}{S_f^g(u,\xi)}\right), \quad \hat{\xi}_f(u,\xi) = \xi - \Im\left(\frac{S_f^{g'}(u,\xi)}{S_f^g(u,\xi)}\right), \qquad (1.25)$$

where $\Re(z)$ and $\Im(z)$ respectively denote the real and the imaginary part of $z \in \mathbb{C}$. Notice that eqs.(1.25) require the computation of the STFT of f with respect to three windows: g, tg (its product by t) and its derivative g'.

Reassignment operators are shown in Fig.1.20(a). When applied to a TFD of a signal having well separated components, RM gives a representation which is sparse and well-concentrated on the single IF curves, allowing for IFs estimation, as shown in Fig.1.20(b). On the contrary, if two modes do not satisfy the separability condition as in Def.6, then the interference between modes can highly affect maxima positions, resulting in a loss of resolution in the region of

non-separability, see Fig.1.20.

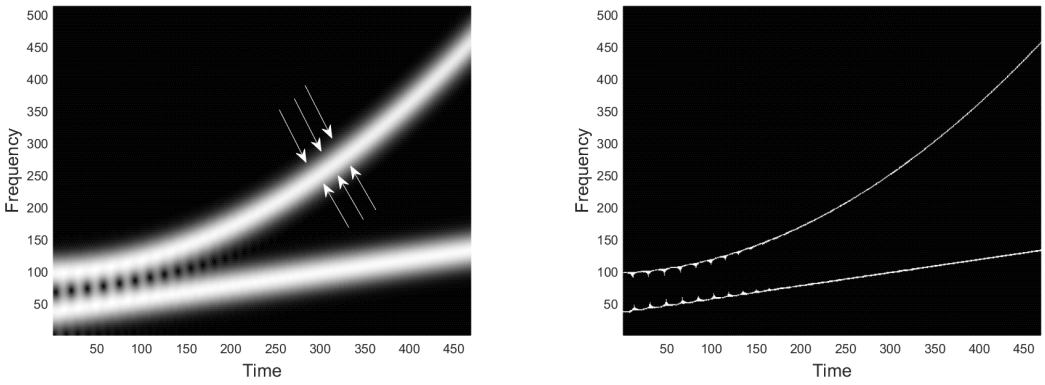

(a) (b)

Figure 1.19: RM applied to separable components. (a) Spectrogram of two well separated components. White arrows indicate the reassignment operators; (b) Reassigned spectrogram.

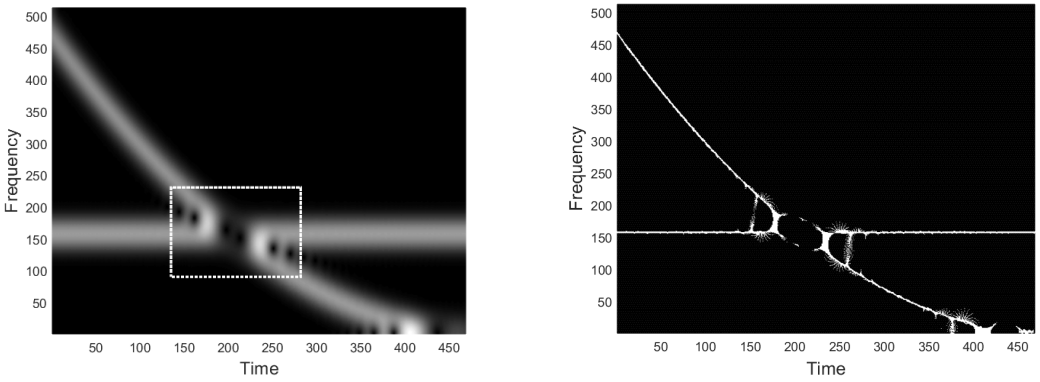

(a) (b)

Figure 1.20: RM applied to non-separable components. (a) Spectrogram of two crossing components. White box indicates the non-separability region; (b) Reassigned spectrogram.

Syncrosqueezing Transform

Syncrosqueezing transform (SST) was originally introduced for analyzing auditory signals [62] and then formalized in [31]. It belongs to the class of reallocation methods. Contrary to RM, it operates directly on the transform (and not on the related distribution); therefore, it allows for signal reconstruction.

Moreover, TF points are moved only along the frequency direction, that is the considered local centroid does not depend on time.

To motivate the idea behind SST, let us consider a purely harmonic signal (constant chirp), i.e.

$$f_0(t) = A\,\cos(\Omega t) \tag{1.26}$$

and its analytic WT defined as [35]

$$W_{f_0}(u,s) = \int f_0(t)\frac{1}{\sqrt{s}}\psi^*\left(\frac{t-u}{s}\right)dt, \tag{1.27}$$

where ψ is an analytic wavelet mother, i.e. $\hat{\psi}(\omega) = 0, \forall\,\omega < 0$. By Parseval Theorem, eq.(1.27) can be rewritten as

$$\begin{aligned} W_{f_0}(u,s) &= \frac{1}{2\pi}\int \hat{f}_0(\omega)\frac{1}{\sqrt{s}}\hat{\psi}^*(s\omega)e^{iu\omega}\,d\omega \\ &= \frac{A}{2\pi}\int[\delta(\omega-\Omega)+\delta(\omega+\Omega)]\frac{1}{\sqrt{s}}\hat{\psi}^*(s\omega)e^{iu\omega}\,d\omega \\ &= \frac{A}{2\pi}\frac{1}{\sqrt{s}}\hat{\psi}^*(s\Omega)e^{iu\Omega}. \end{aligned}$$

If $\hat{\psi}^*$ is well concentrated around ω_0, then $W_{f_0}(u,s)$ will be well concentrated around ω_0/Ω.

As observed in [62], $W_{f_0}(u,s)$ spreads out over the time-scale plane around the horizontal line $s = \omega_0/\Omega$, but its oscillatory behaviour with respect to time u points to the original frequency Ω, independently on the value of s. For this reason, for a generic real signal $f(t) = A\cos\phi(t)$ and for each (u,s) s.t. $W_f(u,s) \neq 0$, IF is approximated by

$$\hat{\omega}_f(u,s) = -i\frac{\frac{\partial}{\partial u}W_f(u,s)}{W_f(u,s)}, \tag{1.28}$$

that gives exactly $\hat{\omega}_f(u,s) = \Omega$ in the case $f(t) = f_0(t)$ as in eq. (1.26).

SST essentially consists in applying the map $(u,s) \longrightarrow (u, \hat{\omega}_f(u,s))$. By considering a uniform discretization of W_f in the scale variable (i.e. W_f is computed only at discrete points s_k, with $s_k - s_{k-1} = (\Delta s)_k$), then the SST is defined only at centers ω_l of the successive bins $[\omega_l - \frac{1}{2}\Delta\omega, \omega_l + \frac{1}{2}\Delta\omega]$, with

$\Delta\omega = \omega_l - \omega_{l-1}$, as

$$T_f(u,\omega_l) = \frac{1}{\Delta\omega} \sum_{s_k:|\hat{\omega}(u,s_k)-\omega_l|\leq\Delta\omega/2} \frac{1}{s\sqrt{s}} W_f(u,s_k)(\Delta s)_k. \tag{1.29}$$

If u and ω are continuous variables, the analogous of eq.(1.29) is

$$T_f(u,\omega) = \int_{\{s\,:\,W_f(u,s)\neq 0\}} W_f(u,s) \frac{1}{s\sqrt{s}} \delta(\hat{\omega}-\omega)\, ds.$$

The signal can be recovered by its SST. Indeed, if f is real, $\hat{f}(\omega) = \hat{f}^*(-\omega)$ and it holds

$$\begin{aligned}\int_0^{+\infty} W_f(u,s)\frac{1}{s\sqrt{s}} ds &= \frac{1}{2\pi}\int_{-\infty}^{+\infty} \frac{\hat{f}(\omega)}{\sqrt{s}} \hat{\psi}^*(s\omega) e^{iu\omega} ds d\omega \\ &= \int_0^{+\infty} \frac{\hat{\psi}^*(\omega)}{\omega} d\omega \cdot \int_0^{+\infty} \hat{f}(\zeta) e^{iu\zeta}\, d\zeta;\end{aligned}$$

thus, by setting $C_\psi = \frac{1}{2}\int_0^{+\infty} \frac{\hat{\psi}^*(\omega)}{\omega} d\omega$, it follows

$$f(t) = \Re\left[\frac{1}{C_\psi}\int_0^{+\infty} W_f(u,s)\frac{1}{s\sqrt{s}}\, ds\right]. \tag{1.30}$$

By considering a piecewise constant approximation according to the binning in s, eq.(1.30) becomes

$$f(t) \approx \Re\left[\frac{1}{C_\psi}\sum_l T_f(u,\omega_l)\,\Delta\omega\right].$$

Syncrosqueezing operator can be defined for a generic TF transform. In the case of the STFT, the SST is closely related to the synthesis formula

$$f(t) = \frac{1}{2\pi g(0)}\int S_f^g(u,\xi) e^{i\xi t} d\xi,$$

and it can be expressed as [63]

$$T_f(u,\xi) = \frac{1}{2\pi g(0)}\int S_f^g(u,\xi) e^{i\xi t}\delta(\xi - \hat{\xi}_f) d\xi,$$

where $\hat{\xi}_f$ is the local centroid referred to RM as defined in eq.(1.25). It follows

that SST can be understood as a frequency reassignment.

If $f(t) = \sum_k a_k f_k(t)$ is a superposition of well separated components, then the k-th mode can be recovered by integrating T_f^g in the vicinity of the corresponding ridge, i.e.

$$f_k(t) = \int_{\{\xi\,:\,|\xi-\phi_k'(t)|<d\}} T_f(u,\xi)d\xi,$$

for some small parameter $d > 0$.

Recently, SST has been improved by the introduction of higher-order approximation in eq.(1.28) [4, 64, 65].

RM and SST pros. They are completely automatic and apply to general TF representations. In addition, SST enables signal modes recovery.
RM and SST cons. Their applicability is limited to well separated components.

1.3.2.2 Adaptive signal representations

Adaptive directional TFD

WVD distribution has ideal energy concentration for monocomponent LFM signals. For MCS, it suffers from cross-term interference which can significantly affect signal readability in the TF domain. Cross-terms reduction is possible by applying a low-pass filter in TF domain [15], i.e.

$$\rho(u,\xi) = WV_f(u,\xi) * *\gamma(u,\xi),$$

where γ is a smoothing kernel depending on some parameters. The resulting TFD ρ is a smoothed version of WVD. Unfortunately, the smoothing also deteriorates signal resolution. In particular, close components could appear merged in the TF domain, not allowing for correct IF estimation. A high-resolution TFD can be obtained by adapting the direction of the smoothing kernel, as proposed in [18]. The adaptive directional TF distribution (ADTFD) is defined as

$$\rho_{AD}(u,\xi) = WV_f(u,\xi) * *\gamma_\theta(u,\xi),$$

where the shape adjustment of γ_θ is based on the following characteristics of cross-terms and auto-terms in quadratic TFDs [66]:

1. cross-terms oscillate along their major axis and they have high pass characteristics in the frequency domain; therefore, cross-terms can be suppressed by smoothing them along their major axis;

2. the amplitude of auto-terms changes slowly along their major axis and the most of them lies in a low frequency band; as a consequence, low pass filtering along the major axis of auto-terms will not deteriorate their energy concentration.

For these reasons, the direction of a smoothing kernel should remain aligned with the major axis of auto-terms and cross-terms. The oscillatory characteristics of cross-terms can be avoided by taking the modulus of a quadratic TFD. For absolute values of a TFD, both auto-terms and cross-terms appear as ridges. Therefore, the direction of γ_θ is chosen as the one which maximizes the correlation of the kernel with the modulus of a quadratic TFD, i.e.

$$\theta(u,\xi) = \arg\max_{\theta} \left| |\rho(u,\xi)| *_u *_\xi \gamma_\theta(u,\xi) \right|. \tag{1.31}$$

In the ideal case, the smoothing kernel should have maximum output when it is parallel to the ridge and it should be zero otherwise, so that eq.(1.31) gives the correct local IF direction. The even derivatives of the Gaussian filter (DGF) satisfy the above conditions, thus the proposed filter in [18] is

$$\gamma_\theta(u,\xi) = \frac{ab}{2\pi}\frac{\partial^2}{\partial\xi_\theta^2} e^{-(a^2u_\theta^2+b^2\xi_\theta^2)},$$

where $u_\theta = u\cos\theta+\xi\sin\theta$, $\xi_\theta = -u\sin\theta+\xi\cos\theta$, $\theta \in [-\pi/2, \pi/2)$ is the rotation angle with respect to the time axis, while a and b respectively control the spread and the smoothing along the time and frequency axis. DGF performs smoothing along its major axis, i.e. $e^{-a^2u_\theta^2}$ and performs second-order differentiation along its minor axis, i.e. $\frac{\partial^2}{\partial\xi_\theta^2}e^{-b^2\xi_\theta^2}$. Therefore, the filter output reduces to zero as the direction of filter is made orthogonal to the major axis of ridges.

The basic principle behind the choice of parameters is that the rate of oscillation of cross-terms decreases as signal components are getting closer in the TF domain [66]. In order to avoid merging components, a long filter (with sharp cuttoff) should be applied along the major axis of ridges for suppressing cross-terms, whereas a short filter should be applied in the direction orthogonal to the major axis of ridges. Thus, the value of the parameter a should be small

(i.e. around 2) to ensure a long filter while a large value should be assigned to b to ensure a short filter (i.e. b around 30).

Global parameters optimization should fail to provide the desired results when the signal presents close or short-duration components. To address this issue, a two-stage algorithm for parameter automatic tuning is proposed in [67]. First, the length of the smoothing kernel is optimized globally. In the second stage, the parameters which control the shape of the selected smoothing window are optimized, locally. Given a set of possible values for a and b $\{(a_i, b_i), i = 1, ..., I\}$, the ADTFD at each TF point (u, ξ) is defined as

$$\rho_{AD} = \min_i WV_f(u, \xi) * *\gamma_{a_i,b_i}(u, \xi).$$

ADTFD pros. Resolution of close components is enhanced.
ADTFD cons. ADTFD is not suitable for estimating the IF of crossing components, as it does not achieve energy concentration at the intersection point.

1.3.2.3 Peaks detection and tracking algorithm

Image processing techniques
Image processing techniques for IF estimation exploit local connectivity of peaks detected by a TFD [19]. These methods are computationally efficient and suitable for real-life signals such as EEG seizure signals and heart rate variability signals, as shown in [68, 69].

The key steps of the IF estimation procedure in [19] are the following:

- detect all peaks along the frequency axis at each time instant u of the considered TFD $\rho(u, \xi)$ as the points satisfying

$$\frac{d}{d\xi}\rho(u, \xi) = 0 \quad \text{and} \quad \frac{d^2}{d\xi^2}\rho(u, \xi) < 0$$

- define $B(u, \xi)$ as a binary image having ones at each peak location and zeros otherwise and assume that the detected peaks correspond to the signal components IFs.

- discriminate peaks between modes accordingly to the 10-connectivity criterion, which states that a detected peak belongs to a signal component if it has at least one other peak in its 10-neighborhood of the same signal

component and it does not have any peak of any other component in its 10-neighborhood.

Specifically, given a pixel (x, y), the set of its 10-neighborhood is defined as $\{x + i, y + j, i = -1, 1, j = -2, ..., 2\}$. In practical implementations, IF curve with a duration longer than a predetermined threshold are retained to improve the robustness of the algorithm against noise.

Generalized Viterbi Algorithm for IF estimation

For monocomponent signals, IF can be derived at each time instant by the locations of TFDs peaks detected along the frequency direction. The same technique can be adapted to MCS having well separated modes by exploiting IF slow variation between consecutive time instants. Unfortunately, high noise can significantly affects peaks positions resulting in inaccurate IF estimation [70]. A Viterbi-based IF estimation method has been proposed in [20] to face this issue.

The basic assumptions taken into account are: (i) if a peak is deviated, with high probability the correct IF is at a point having one of the largest TFD values; (ii) IF variations between two consecutive points are not abrupt. In other words, (i*) IF curve should maximize the number of high energy TF points; (ii*) given a discrete time interval $[n_1, n_2]$, the IF curve should minimize the function $\sum_{n=n_1}^{n_2} |\hat{\omega}(n) - \hat{\omega}(n-1)|$, where $\hat{\omega}(n)$ is the estimated IF at discrete time n.

Formally, let us assume that all paths between time n_1 and n_2 take only discrete frequency values and belong to a set $\mathbf{K}$. IF estimation can be thus formulated as the optimization problem

$$\hat{\omega}(n) = \arg \min_{k(n) \in \mathbf{K}} \underbrace{\left[\sum_{n=n_1}^{n_2-1} g\left(k(n), k(n+1)\right) + \sum_{n=n_1}^{n_2} h(\rho(n, k(n))) \right]}_{:= p(k(n); n_1, n_2),\ \text{penalty function}}, \tag{1.32}$$

where ρ is the considered TFD, n_1, n_2 are two ending points, $g(x, y) = g(|x - y|)$ is a non-increasing function with respect to the absolute difference between variables x and y and $h(\cdot)$ is inversely related to the amplitude of the signal energy. In [71], without loss of generality, WVD is considered as underlying

TFD. A linear form for the function g is assumed, i.e.

$$g(x,y) = \begin{cases} 0, & |x-y| \leq \Delta \\ c(|x-y| - \Delta), & |x-y| > \Delta \end{cases}, \quad c, \Delta > 0$$

and the function h is implemented, for a given time instant n, by sorting the WVD coefficients with respect to the available M frequencies $\{\omega_j\}_{j=1,...,M}$, i.e.

$$WVD(n,\omega_1) \geq WVD(n,\omega_2) \geq ... \geq WVD(n,\omega_M),$$

and by setting $h(WVD(n,\omega_j)) = j-1$, $\forall\, j$.

If the TF domain is discretized into $T = \{(n_i,\omega_j), i \in [1,N], j \in [1,M]\}$, the total number of path between two ending points is M^N, making the direct computation of the optimal curve minimizing functional in eq.(1.32) computationally infeasible. The problem can be recursively solved by using the Viterbi Algorithm, as follows.

(a) Let the optimal paths connecting a given time instant n_1 to n_i are determined and denote them with $\pi(n;\omega_j)$, $n \in [n_1, n_i]$ for $j \in [1,M]$. By defining with $\mathbf{K}_{ij}$ the set of all paths between the instant n_1 and the point (n_i,ω_j), we have

$$\pi(n;\omega_j) = \arg \min_{k(n) \in \mathbf{K}_{ij}} p(k(n); n_1, (n_i,\omega_j)),\ j \in [1,M]. \tag{1.33}$$

According to Viterbi algorithm terminology, paths in eq.(1.33) are referred as partial best paths. IF estimation within the interval $[n_1, n_i]$ is then

$$\hat{\omega}_{(i)}(n) = \arg \min_{\pi(n;\omega_j), j \in [1,M]} p(\pi(n;\omega_j); n_1, (n_i,\omega_j)).$$

(b) The partial best paths referred to the next instant n_{i+1} are represented as concatenation of paths in eq.(1.33) with the points at the new instant $\pi_{i+1}(n;\omega_l), (n_{i+1},\omega_j)$, $j \in [1,M]$ that minimize

$$p(\pi_i(n,\omega_l); n_1, (n_i,\omega_l)) + g(\omega_l,\omega_j) + h(WVD(n_{i+1},\omega_j)) \tag{1.34}$$

for each ω_j. The function h is constant for considered partial best path. Taking advantage of the increasing monotonicity of g, it is possible to

further reduce the searching space for minimizing the function in eq.(1.34).

Peaks detection and tracking algorithms pros. Their formulation is very simple.
Peaks detection and tracking algorithms cons. They are essentially interpolation and searching techniques, thus generally computationally expensive. Even if Viterbi algorithm heavily reduces the computation effort, method effectiveness strongly depends on the predetermined set of candidate parameters. Finally, the presented methods are not able to correctly track intersecting components.

1.4 Decomposition of overlapping components

The separation of components whose domains overlap both in time and frequency is a very challenging task in MCS analysis. Most of the TF tools are limited to well separated components. Many IF estimators based on the TFDs peaks extraction and tracking have been extended to overlapping components. The latter have the main advantage to be non-parametric, but on the other hand, they present a high computational cost. The other existing procedures are mostly signal-dependent. Indeed, they either assume a specific class for the phase/IF function or they consist of adaptive, parametric and local refinements of already existing approaches and/or transforms. Unfortunately, parametric methods are likely to only adapt to specific situations.

A brief presentation of the state of the art techniques is given below.

1.4.1 Non-parametric methods

1.4.1.1 Peaks detection and tracking algorithm

Modified Viterbi algorithms
In order to avoid the so-called "switch problem", that is the assignment of a ridge point to the wrong component, extensions of the Viterbi algorithm to MCS having non-separable components have been recently proposed. In particular, in [72] the penalty function is modified in order to promote the local direction of the estimated ridge, while the local monotonicity is considered in [73]. A similar peak-detection and tracking procedure promoting the direction of the estimated IF is proposed in [74]. As illustrative example, let us focus on the method in [72]. It relies on two fundamental steps: (i) ADTFD is adopted to enhance TF resolution; (ii) a variant of the Viterbi algorithm taking into

account the direction of the ridge is introduced. The latter is exploited to track signal modes and correctly estimate IF curves, even when they intersect with each other in the TF plane. The number of signal modes is assumed. First, the strongest component is detected and removed from the original TFD, which is iteratively processed until all the components are recovered. The new constraint introduced in [72] takes into account ridge direction, by assuming IF curve has small variation along two consecutive points. A similar iterative technique, making use of a tracking algorithm instead of the Modified Viterbi algorithm, has been proposed in [74]. In this work, a local version of ADTFD, denoted as LO-ADTFD, is adopted as high-resolution TF distribution. IF of the strongest signal component is estimated by a peak detection algorithm, that takes into account both the amplitude and the direction of peaks in the TF domain. The procedure is then repeated until all the components are recovered.

Ridge path regrouping method

Ridge path regrouping method (RPRM) is a peak tracking method aimed at identifying overlapped components from a TFD. RPRM consists of two main steps [75]: (i) detection of the peaks/ridges from the considered TFD; (ii) regrouping of the detected ridge points according to their variation rates at the intersection point.

RPRM can be summarized as follows:

1. compute the signal TFD and detect all its peaks;
2. find all the intersection intervals, according to a thresholding operation implementing Def.9;
3. merge intersection intervals which are close to each other;
4. regroup ridge in each intersection interval. Specifically, the detected ridge curve as a whole is broken first and then reconnected according to the slopes of the ridges at the boundary of the intersection interval, by linear interpolation. (The slope of the ridge is also considered in [73] to define a new penalty function to be minimized by means of Viterbi algorithm).

RPRM is computationally efficient, but on the other hand it has proved to be sensitive to noise. Furthermore, the basic assumption in RPRM is that the set

of the detected peaks from a TFD (ridge estimation) as a whole can reflect the global TF patterns of a MCS. This is exploited for assigning the detected peaks to the correct IF curve. It is worth observing that the above assumption immediately fails to be satisfied if two modes interfere in a destructive way. In this critical case, TFD can present much lower energy at the interference region and then the detected ridge curve can appear so deviated to not correlate at all with the global TF pattern.

Image processing techniques

An IF detector which combines TF analysis and image processing technique is proposed in [76] in order to deal with MCS having mixed continuous and stepped FM components overlapping components. The traditional IF estimation problem is here rephrased as a line detection problem from the image processing point of view, under the assumption that realistic IF curves have certain specific geometric properties. In particular, the algorithm exploits the property that for each TF point, the direction of the ridge (IF) is orthonormal to the gradient of the TFD. The line detector algorithm is defined as follows:

1. compute the B-distribution (BD) of the signal [15];
2. compute the gradient image of BD (a local least-squared fitting method is adopted);
3. modify the gradient image to adjust the gradient direction of each pixel point along IFs trajectory. Specifically, the pixel gradient vectors belonging to the first or second quadrant of the 2-D Cartesian coordinates are rotated by 90 deg clockwise around the origin, while gradient vectors is in the third or fourth quadrant are rotated by 90 deg counterclockwise;
4. based on the two gradient images computed in the previous steps, compute the mean gradient ratio image by using an adaptive window around each TF point. Mean gradient images allow for the detection of discontinuities (IF information) in the BD image, which generally appear when two modes intersect with each other.

After the line segments are determined, IF estimation is carried out iteratively. First, a graph by linking the detected line segments is formed by linking segments which are closely located. Then, a Markov random field is defined on

the constructed graph by using the geometric information of IFs, and the IF detection process is modelled as the extraction of the best graph labelling. The regions of discontinuity between line segments are recovered via MAP minimization and the procedure is repeated on the new gradient ratio image defined by setting zero in the region around the detected IFs of continuous components. The procedure is repeated until all the segments have been grouped.

Non-parametric methods pros. The presented procedures do not require any specific assumption on IF class.
Non-parametric methods cons. They are computationally expensive, as the optimal path determination requires an exhaustive search. It is worth pointing out that these methods recover the missing information in the non-separability region by interpolation and, since peaks can be highly deviated by interference, the interpolation result may be meaningless.

1.4.2 Parametric methods

Parametric methods are usually based on a predefined model to characterize the IF of the signal, such as polynomial [12, 77–79], piecewise polynomial [7, 80–82] and sinusoidally models [83, 84]; otherwise they are referred as parametric because they adopt analysis devices which are signal-dependent, i.e. whose parameters strongly depend on the specific signal under analysis.

1.4.2.1 Intrinsic chirp component decomposition

In [85], an iterative and parametric technique for IF estimation in the overlapping framework is introduced. A noisy MCS is modelled as the superposition of Intrinsic Chirp Components (ICC), i.e.

$$f(t) = \sum_{k=1}^{N} f_k(t) + r(t) = \sum_{k=1}^{N} a_k(t) \cos\left(2\pi \int_0^t \varphi_k(\tau) d\tau + \theta_{k0}\right) + r(t), \quad (1.35)$$

where N is the number of components, $r(t)$ consists of the decomposition error and zero-mean Gaussian noise, f_k is an ICC with instantaneous amplitude a_k,

phase $\theta_{k0} \in [0, 2\pi)$ and IF φ_k, which satisfy the following conditions

$$\begin{aligned}
&a_k \in \mathbf{C}^1(\mathbb{R}) \cap \mathbf{L}^\infty(\mathbb{R}),\ \varphi_k \in \mathbf{C}^\infty(\mathbb{R}),\\
&\inf_{t\in\mathbf{R}} a_k(t),\ \inf_{t\in\mathbf{R}} \varphi_k(t) > 0,\\
&\sup_{t\in\mathbf{R}} a_k(t),\ \sup_{t\in\mathbf{R}} \varphi_k(t),\ \sup_{t\in\mathbf{R}} |a_k'(t)|,\ \sup_{t\in\mathbf{R}} |\varphi_k'(t)| < +\infty.
\end{aligned}$$

ICC decomposition (ICCD) first removes the non-linear dependence of the phase in eq.(1.35), which is rewritten as

$$f(t) = \sum_{k=1}^{N} A_k(t) \cos\left(2\pi \int_0^t \varphi_k(\tau)d\tau\right) + B_k(t) \sin\left(2\pi \int_0^t \varphi_k(\tau)d\tau\right) + r(t), \tag{1.36}$$

where $A_k(t) = a_k(t)\cos(\theta_{k0})$ and $B_k(t) = -a_k(t)\sin\theta_{k0}$. Instantaneous amplitudes $A_k(t)$ (IA) and IF $\varphi_k(t)$ are then modelled as redundant Fourier series, i.e.

$$\begin{aligned}
A_k(t) &= A_{k0} + \sum_{j=1}^{L} (A_{kj}\cos(2\pi j F_0 t) + \bar{A_{kj}}\sin(2\pi j F_0 t)),\\
B_k(t) &= B_{k0} + \sum_{j=1}^{L} (B_{kj}\cos(2\pi j F_0 t) + \bar{B_{kj}}\sin(2\pi j F_0 t)),\\
\varphi_k(t) &= \varphi_{k0} + \sum_{j=1}^{M} (\varphi_{kj}\cos(2\pi j F_0 t) + \bar{\varphi_{kj}}\sin(2\pi j F_0 t)),
\end{aligned}$$

where L and M respectively stand for the Fourier order of the amplitude and frequency, $F_0 = f_s/N$, with f_s the sampling frequency. The Fourier coefficients $\{A_{k0}, ..., A_{kL}, \bar{A}_{k0}, ..., \bar{A}_{kL}\}$, $\{B_{k0}, ..., B_{kL}, \bar{B}_{k0}, ..., \bar{B}_{kL}\}$, $\{\varphi_{k0}, ..., \varphi_{kM}, \bar{\varphi}_{k0}, ..., \bar{\varphi}_{kM}\}$ are the parameters to be determined.

Let us focus on a monocomponent signal f, whose analytic form can be obtained by the Hilbert transform [15] and expressed as

$$z(t) = a(t)e^{i(2\pi\theta(t)+\theta_0)},$$

with

$$\theta(t) = \varphi_0\, t + \sum_{j=1}^{M} \left(\frac{\varphi_j}{2\pi j F_0}\sin(2\pi j F_0 t) - \frac{\bar{\varphi_j}}{2\pi j F_0}\cos(2\pi j F_0 t)\right), \tag{1.37}$$

IF estimation can be performed by means of the General Parametrized TF transform (GPTFT) whose kernel is adapted to the phase model in eq.(1.37). More precisely, GPTFT is defined as

$$GP(u,\xi,\alpha;\sigma) = \int_{\mathbb{R}} z(t)\Phi_{\alpha}^{D}(t)\Phi_{u,\alpha}^{C} g_{\sigma}(t-u)e^{-i2\pi\xi t}\,dt,$$

with

$$\begin{aligned}
\Phi_{\alpha}^{D}(t) &= e^{-i2\pi\sum_{j=1}^{M}\left(\frac{\alpha_j}{2\pi jF_0}\sin(2\pi jF_0t)-\frac{\bar{\alpha_j}}{2\pi jF_0}\cos(2\pi jF_0t)\right)},\\
\Phi_{u,\alpha}^{C} &= e^{i2\pi\sum_{j=1}^{M}(\alpha_j\cos(2\pi jF_0t)+\bar{\alpha_j}\sin(2\pi jF_0t))},\\
g_{\sigma}(t) &= \frac{1}{\sqrt{2\pi\sigma}}e^{-\frac{t^2}{2\sigma^2}}.
\end{aligned}$$

Note that the above transform reduces to STFT if the multi-parameter

$$\alpha = (\alpha_1,...,\alpha_M,\bar{\alpha}_1,...,\bar{\alpha}_M)$$

is the null vector. Basically, Φ_{α}^{D} is a demodulation operator which reduces IF variation degree. If α is close to the Fourier coefficients of φ, then the demodulation operator applied to the analyzed signal will output a nearly stationary chirp, with constant frequency φ_0. $\Phi_{u,\alpha}^{C}$ is compensator operator for the error introduced by Φ_{α}.

The discrete counterpart of eq.(1.36) is

$$f = \sum_{k=1}^{N}\mathbf{H}_k\mathbf{y}_k + \mathbf{r}, \tag{1.38}$$

where $f = [f(t_0),...f(t_{l-1})]$, $\mathbf{r} = [r(t_0),...r(t_{l-1})]$, l is the signal length, $\mathbf{y}_k = \left[\mathbf{y}_{kA}^T\mathbf{y}_{kB}^T\right]^T$, with $\mathbf{y}_{kA} = [A_{k0},...,A_{kM},\bar{A}_{k0},...,\bar{A}_{kM}]$ and

$$\mathbf{y}_{kB} = [B_{k0},...,B_{kM},\bar{B}_{k0},...,\bar{B}_{kM}].$$

The kernel matrix H_k is given by $\mathbf{H}_k = [c_k,\mathbf{S}_k]$ with

$$\begin{aligned}
c_k &= diag[\cos\theta_k(t_0),...,\cos\theta_k(t_{l-1}))]\mathbf{K},\\
\mathbf{S}_k &= diag[\sin\theta_k(t_0),...,\sin\theta_k(t_{l-1}))]\mathbf{K},
\end{aligned}$$

where $\theta_k = \int_0^t\varphi_k(\tau)d\tau$ and $\mathbf{K}$ is a $N\times(2l+1)$ matrix containing the model

information of IA, defined for $i \in [1, N]$ as

$$K_{i,j} = \begin{cases} \cos(2\pi(i-1)F_0 t_{j-1}),\ i \in [1, l+1] \\ \sin(2\pi(i-l-1)F_0 t_{i-1}),\ i \in [l+2, 2l+1] \end{cases}.$$

According to eq.(1.38), the estimation of the Fourier coefficient of the IA and IF requires to solve a linear system. Since this inverse problem is ill-posed, Tikhonov regularization is adopted to get a stable solution, by solving

$$\min_y \left(||f - H_k y_k||_2^2 + \lambda_1 ||y_k||_2^2 \right),$$

where λ_1 is a regularization parameter which controls a trade-off between the data fidelity and the perturbation sensitivity. Matrix H is constructed based on the detected ridge points from the TFD.

For MCS, the strongest component IF is estimated first and then the procedure is iterated on the residual. The residual energy is examined to define a stopping criterion. A joint-refinement step consisting in an additional but different Tikhonov regularization is considered to get high-resolution component recovery also for overlapping/crossing modes. It is conducted by the minimization of

$$\min_y \left(||f - H y_k||_2^2 + \lambda_2 ||y_k||_2^2 \right),$$

where H is the assembled kernel matrix, i.e. $H = [H_1, ..., H_N]$.

ICCD pros. Linearity is one of the main advantages. In addition, ICCD allows for the characterization of signal having highly oscillating IF and IA.
ICCD cons. A theoretical analysis is not available yet.
ICCD modifications. An extension of ICCD suitable for complex valued signals has been proposed in [51] and applied to overlapped MCS.

1.4.2.2 Dechirping-based methods

The principle of de-chirping is to remove the "non-stationary term" of a chirp signal so that a narrowband filter can be used for extracting the target component [78, 86, 87]. Given a MCS $f(t) = \sum_{j=1}^{N} a_j(t) e^{i\phi_j(t)}$, de-chirping algorithm consists of the following steps:

1. determine the strongest component IF $\hat{\xi}(u)$, $\forall\, u$ and estimate the corresponding instantaneous phase $\phi_k(t) = \int_0^t \hat{\xi}(\tau)d\tau$;

2. compute the de-chirped signal

$$f_C(t) = f(t)e^{-i\phi_k(t)} = a_k(t) + \sum_{j\neq k} a_j(t)e^{i(\phi_j(t)-\phi_k(t))};$$

3. extract the amplitude $a_k(t)$ by applying a low-pass filter;

4. recover the component $f_k(t) = a_k(t)e^{i\phi_k(t)}$;

5. remove the synthesized signal from the mixture, that is set $f(t) = f(t) - f_k(t)$ and repeat the procedure on the residual.

Generally, de-chirping is not suitable for overlapping components. To deal with the problem, the method proposed in [79] combines parametrized de-chirping and band-pass filter, avoiding the analysis of the considered signal through TF transform. It is worth observing that in [78] authors state that the estimation of the number of modes, needed in [79], requires TF analysis, since a processing in the time domain generally does not allow for it. Thus, the procedure in [79] is not TF analysis-free. Coming back to the description of the method, discrete-time polynomial model for the signal phases is adopted. The parameters describing the target component are estimated by maximizing a concentration measure. Then, the original signal is de-chirped, that is the target mode is reduced to a stationary signal with constant frequency corresponding to its initial frequency. This results in a straight line in the TF plane, while the noise is dispersed across the entire domain. The de-chirped signal is then band-pass filtered and its center frequency is detected as the peak amplitude. Finally, the target component is recovered by the knowledge of its parameters and the entire procedure is repeated iteratively on the residual signal.

De-chirping pros. All methods dealing with WVD and its modifications share the necessity to balance resolution and cross-terms reduction. On the contrary, de-chirping approach simply removes the non-stationary part of a signal.
De-chirping cons. It is based on specific assumptions on IF class.

1.4.2.3 Locally adaptive directional TFDs

In [74] an iterative method for IF estimation of overlapping components with time varying amplitudes has been proposed. As a starting point, the locally ADTFD (LO-ADTFD) introduced in [67] is adopted to promote energy concentration for MCS having time varying amplitudes. Then, the strongest component is detected by tracking the TFD peaks and removed from the mixture signal. The switch problem is avoided by taking into account both the amplitude and the direction of the detected peaks. Instead of assuming the number of components, the above procedure is repeated until the energy falls below a preselected threshold.

The following peak detection and tracking algorithm is used to estimate the strongest component IF:

1. compute LO-ADTFD $\rho(u, \xi)$ of the input signal;
2. detect a point (u_0, ξ_0) of larger energy in TF domain and estimate the IF at u_0 as ξ_0;
3. set $u = u_0 + 1$;
4. detect the peak in the neighborhood of u_0 as $\hat{\xi} = \arg\max_u |\rho(u, \xi)|$, where $f \in [\xi_0 - \Delta, \xi_0 + \Delta]$ and Δ is a prefixed threshold based on bandwidth;
5. compare the detected peaks direction with the principal direction of the peak detected at the previous iteration. If $|\theta(u, \hat{\xi}) - \theta(u, \xi_0))| < T$, then the directions of the peaks are close and the detected peak is assigned to IF curve of the strongest component. Otherwise, the IF is estimated by extrapolation as
$$\hat{\xi} = \xi_0 + \tan\left(\theta(u_0, \xi_0)\right);$$
6. set $u_0 = u$ and $\xi_0 = \hat{\xi}$ and repeat the whole procedure until u_0 belongs to the domain.

Once the strongest component is detected, it is removed from the mixture signal by de-chirping.

LO-ADTFD pros. Resolution is significantly enhanced.
LO-ADTFD cons. It is parametric and its definition implicitly relies on IF local estimate.

1.4.2.4 Quasi maximum likelihood random sample consensus-based IF estimators

The quasi maximum likelihood (QML) algorithm has been originally introduced for monocomponent signals as a powerful polynomial phase estimator [88] and then generalized to MCS with generic non-linear polynomial FM [89]. In order to extend it to MCS having overlapped components, it is assumed that modes present similar amplitudes in the TF plane, as in most existing methods. In addition, amplitudes are assumed to be constant. Higher anti-noise performances have been obtained by adopting the QML random sample consensus (QML-RANSAC) [90]. It performs multiple random selections of the IF estimates samples and reconstructs IF by interpolation. For each overlapped component, the final IF estimate is based on a maximum likelihood-based criterion. QML-RAMSAC algorithm is performed iteratively until all the modes are recovered, according to the following steps:

1. given a MCS $f(t)$, compute its STFT;
2. estimate IF from the spectrogram local maxima;
3. select random samples of IF estimate;
4. estimate the signal parameters from the IF, for each random selection, by maximum likelihood;
5. remove the estimated component from the signal mixture;
6. iterate the procedure on the STFT of the residual signal.

The main drawback of the above procedure is the large number of required STFTs that is proportional to ΛQ, where Q is number of components and Λ is number of random selections. For large Λ, complexity becomes unacceptable. That is why, the elements that are close to the estimated component are removed and random sampling is applied only to remaining IF samples. In this way, STFT is computed only once, but the application of the method is limited to signals with a small number of components and simple signatures, i.e. IF depending on a small number of parameters. The work in [91] overcomes some these drawbacks, only requiring Q STFTs evaluations.

QML-RANSAC pros. The method is simple, as based on random sampling and maximum likelihood estimation.
QML-RANSAC cons. It is parametric and IF is essentially recovered by interpolation.

1.4.2.5 Signal reconstruction from two RW projections

In [92], Prop.1.3 is exploited in order to recover signal overlapped modes, up to a constant phase shift. Let us recall the relation between RW angular derivative and the IF of a monocomponent signal $f(t) = a(t)\cos\phi(t)$, i.e.,

$$\phi'(t) = \frac{1}{2RW(r,\theta)} \int_{-\infty}^{+\infty} \left.\frac{\partial RW(r,\beta)}{\partial \beta}\right|_{\beta=\theta} sgn(\tau - t)\, d\tau. \tag{1.39}$$

The method proposed in [92] is based on the observation that RW angular derivative satisfies

$$\left.\frac{\partial RW(r,\beta)}{\partial \beta}\right|_{\beta=\theta} \approx \lim_{\beta\to 0} \frac{RW(r,\theta+\beta) - RW(r,\theta-\beta)}{2\beta};$$

therefore, the discrete version of the above relation is considered to approximate RW angular derivative. Precisely, a "small" angle $\beta \approx 1^\circ$ and the two close projections $RW(r,\theta+\beta)$ and $R(r,\theta-\beta)$ are considered for implementing eq.(1.39). Phase retrieval can be achieved up to a constant and thus the signal can be recovered.

Method pros. Close components' resolution is enhanced.
Method cons. The procedure works for MCS with overlapped modes only for specific cases. Some a priori knowledge concerning the signal behaviour has to be assumed, such as constant amplitude and polynomial modulation for the phase.

1.4.2.6 Detection of LFM signals

The literature concerning LFM is essentially boundless. LFM are actually of great importance in radar and micro-doppler analysis. In many applications, LFM are also assumed to have constant amplitude [93, 94]. The most efficient LFM detectors dealing with overlapping components are based on RT [48, 95]

as well as FrFT [49]. These latter map the signal into a domain where the problem of signal detection reduces to peak detection.

As an alternative representation of LFM signals, Lv's distribution (LVD) has been proposed in [96]. Differently from FrFT, LVD is free of searching and does not introduce any non-physical attribute such as the order of rotation angles in FrFT. It introduces a time delay into the time-lag instantaneous autocorrelation function and rescales the time axis to eliminate the so-called linearly frequency migration, i.e. each LFM signal is turned into horizontal line in the TF plane, reducing to a constant chirp in the scaled domain (de-chirping). Given a multicomponent LFM signal

$$f(t) = \sum_{k=0}^{K-1} f_k(t) = \sum_{k=0}^{K-1} A_k e^{i2\pi\omega_k t + i\pi\gamma_k t^2},$$

where ω_k and γ_k respectively denote the centroid frequency and the chirp rate (CFCR), the continuous-time parametric symmetric instantaneous autocorrelation function (PSIAF) is defined as

$$R_f(t,\tau) = f\left(t + \frac{\tau + a}{2}\right) f^*\left(t - \frac{\tau + a}{2}\right).$$

LVD is defined as the 2D FT of the PSIAF after removing the couple of variable t and τ in the exponential phase — which allows for integration. Indeed, by direct computation, it follows

$$\begin{aligned} R_f(t,\tau) = &\sum_{k=0}^{K-1} A_k^2 \exp\left[i2\pi\omega_k(\tau + a) + i2\pi\gamma_k \underbrace{(\tau + a)t}_{t \text{ and } \tau \text{ coupled}}\right] \\ &+ \sum_{k=0}^{K-2} \sum_{j=k+1}^{K-1} R_{f_k f_j}(t,\tau) + R_{f_j f_k}(t,\tau), \end{aligned}$$

with

$$R_{f_k f_j}(t,\tau) = f_k\left(t + \frac{\tau + a}{2}\right) f_j^*\left(t - \frac{\tau + a}{2}\right).$$

The couple is removed by rescaling time axis for each time-lag τ. Formally, a scaling operator Γ is defined for a generic phase function G as

$$G(t,\tau) \xrightarrow{\Gamma} G\left(\frac{t_n}{h(\tau + a)}, \tau\right),$$

with $ah = 1$ to guarantee $t_n = t$ if $\tau = 0$.

Geometrically, the scaling operation corresponds to a change of variables which maps lines in the plane $\Pi_1(t, \tau)$ into constant lines into $\Pi_2(t_n, \tau)$. As an example, if $a = h = 1$, the change of variable is

$$t = \frac{t_n}{\tau + 1},$$

and a line in Π_1 can be parametrized as

$$\tau_1(t) = mt + q;$$

then, in Π_2

$$\tau(t_n) = m\frac{t_n}{\tau_1(t) + 1} + q = \underbrace{\frac{m}{\tau_1(t) + 1}}_{m'} t_n + q$$

$$\tau_1(t_n) = m't_n + q = m\frac{t}{\tau + 1} + q.$$

The application of the scaling to the PSIAF then gives

$$\Gamma(R_f(t, \tau)) = \sum_{k=0}^{K-1} A_k^2 e^{i2\pi\omega_k(\tau+a)+i2\pi\gamma_k t_n} + \sum_{k=0}^{K-2}\sum_{j=k+1}^{K-1} \Gamma(R_{f_k f_j}(t, \tau) + R_{f_j f_k}(t, \tau)).$$

Finally, LVD is obtained by computing 2D FT, i.e.

$$L_f(\omega, \gamma) = \mathcal{F}_\tau \left(\mathcal{F}_{t_n} \Gamma(R_f(t, \tau))\right) = \underbrace{\sum_{k=0}^{K-1} L_{f_k}(\omega, \gamma)}_{auto\, terms} + \underbrace{\sum_{k=0}^{K-2}\sum_{j=k+1}^{K-1} L_{f_k f_j}(\omega, \gamma)}_{cross\, terms}.$$

LVD can also be interpreted as the FT of the scaled WV with respect to time-lag τ or the FT of the scaled ambiguity function with respect to the scaled time t_n.

By direct computation, it is possible to prove that the auto terms can be written as

$$L_{f_k}(\omega, \gamma) = A_k^2 e^{i2\pi\omega_k a} \delta\left(\gamma - \frac{\gamma_k}{h}\right) \delta(\omega - \omega_k),$$

thus they peak in CFCR if $h = 1$. In addition, it is possible to prove that $L_f \to \sum_{k=0}^{K-1} \delta\left(\gamma - \frac{\gamma_k}{h}\right) \delta(\omega - \omega_k)$ while the signal time duration T goes to infinity.

Explicit expressions of the cross terms are also provided in [96]. As expected, cross terms present cosine oscillations depending on CFCRs. LVD allows for relative suppression of cross-terms, in the sense that it greatly strengthens the energy of auto terms, so that the energy of cross-terms becomes negligible.

Parameters a and h are both set equal to 1 if $N_{all} \geq +\frac{1}{T_s}$, where N_{all} is the signal length, T_s is the sampling interval and N is the given number if time sampling points of PSIAF. In the case of a short-time signal, i.e. the total sampling time is very short or the frequency varies quickly with time, $h = \frac{1}{(N_{all}-N)T_s}$. This results in a loss in terms of resolution of the chirp rate as $h < 1$. Complexity and properties of LVD (coming from FT properties) can be also found in [96].

LVD pros. It significantly improves WV resolution and it is based on a theoretical analysis.
LVD cons. LVD does not apply to non-linear frequency modulations.

1.4.2.7 Separation of sinusoidally modulated signals

A sinusoidally frequency modulated signal $f(t)$ can be written as

$$f(t) = Ae^{i\frac{A_m}{\omega_m}\sin(2\pi\omega_m t+\theta_m)} \tag{1.40}$$

and its IF is $\omega(t) = 2\pi A_m \cos(2\pi\omega_m t + \theta_m)$.

These signals appear in radars and communications. In [83], sinusoidally FM signals are detected by the inverse RT (IRT). The key idea of the paper is that RT of a delta function is a sinusoid and then the IRT of a sinusoid is a delta function. Therefore, a sinusoidally FM signal can be detected by simply applying the IRT to a TF representation of the signal. In other words, a sinusoidally FM signal is mapped by IRT into a single point whose expression in polar coordinates gives exactly the parameters A_m and θ_m in eq.(1.40). The following procedure is proposed to estimate the modulation parameters A_m, θ_m and ω_m:

1. assume $\omega_m \in [\omega_{min}, \omega_{max}]$;
2. compute a TF representation $T(u, \xi)$ of $f(t)$ (e.g. the spectrogram);
3. consider a set of candidate slopes α uniformly spaced in $[2\pi\omega_{min}, 2\pi\omega_{max}]$;

4. for each α

   (a) introduce coordinate change $\varphi = \alpha t$ and compute the IRT of $T\left(\frac{\varphi}{\alpha}, \xi\right)$;

   (b) calculate the concentration measure μ_α of the obtained IRT;

5. detect $\hat{\alpha}$ providing the higher concentration measure, i.e. $\hat{\alpha} = \arg\max_\alpha \mu_\alpha$;

6. estimate the modulation frequency as $\hat{\omega}_m = \hat{\alpha}/2\pi$;

7. find (x_m, y_m) in the TF plane providing $\max T\left(\frac{\varphi}{\hat{\alpha}}, \xi\right)$;

8. estimate the modulation amplitude as $\hat{A}_m = \sqrt{x_m^2 + y_m^2}$;

9. estimate the modulation phase as $\hat{\theta}_m = \arctan \frac{y_m}{x_m}$.

The method has been successfully applied to MCS that include one or more overlapping sinusoidal patterns as well as to non-period patterns embedded in noise.

Method pros. Based on a theoretical analysis and robust to noise.
Method cons. The procedure involves multi-dimensional searches in the parameter space, which are generally time consuming. As a main drawback, it is limited to sinusoidally modulated signals.

1.4.2.8 Multivariate concept

A new solution in overlapping modes decomposition has been recently proposed in the context of multivariate and multichannel signals [97]. The latter are essentially multi-measurements of a specific signal, which are now available as a result of new developments in the sensor technology. The decomposition procedure is based on the analysis of signal autocorrelation matrix eigenvalues and the separation task is pursued by concentration measure minimization (L^p-norm based measures are adopted). Given a MCS composed of P modes, the procedure proposed in [97] requires at least $S \geq P$ measurements (number of channels/sensors). A larger number of channels is needed in the noisy case. A discrete multivariate signal can be modelled as [97]

$$\mathbf{f}(n) = \begin{pmatrix} f^{(1)}(n) \\ \vdots \\ f^{(p)}(n) \end{pmatrix} = \begin{pmatrix} \sum_{p=1}^{P} \alpha_{1,p} f_p(n) e^{i\phi_{1,p}} \\ \vdots \\ \sum_{p=1}^{P} \alpha_{S,p} f_p(n) e^{i\phi_{S,p}} \end{pmatrix},$$

or equivalently

$$\mathbf{f}(n) = \begin{pmatrix} a_{11} \cdots a_{1P} \\ \vdots \ddots \vdots \\ a_{S1} \cdots a_{SP} \end{pmatrix} \begin{pmatrix} f_1(n) \\ \vdots \\ f_P(n) \end{pmatrix}, \alpha_{m,p} e^{i\phi_{mp}} = a_{mp}.$$

In matrix form, assuming $n = 1 = 1, \cdots, N$, we can write

$$\begin{pmatrix} f^{(1)}(1) \cdots f^{(1)}(N) \\ \vdots \quad \vdots \\ f^{(S)}(1) \cdots f^{(S)}(N) \end{pmatrix} = \begin{pmatrix} a_{11} \cdots a_{1P} \\ \vdots \ddots \vdots \\ a_{S1} \cdots a_{SP} \end{pmatrix} \begin{pmatrix} f_1(1) \cdots f_1(N) \\ \vdots \ddots \vdots \\ f_P(1) \cdots f_P(N) \end{pmatrix}$$

and more compactly

$$F_{sensors} = A \cdot F_{components},$$

where $A = F_{sensors}^H \cdot F_{sensors}$ is the autocorrelation matrix of the sensed signal.

Let $\{q_j\}$, $j = 1, ..., P$ be the orthonormal eigenvectors of A (under the assumption of independent measurements, $rg(A) = P$), then the model for a single component is

$$f_p(n) = \eta_{1p} q_1(n) + \cdots \eta_{Pp} q_P(n), n = 1, \cdots, N,$$

which can be rewritten in vectorial form as

$$\mathbf{f_p} = \eta_{1p} \mathbf{q_1} + \cdots \eta_{Pp} \mathbf{q_P},$$

where the coefficients are determined by concentration measure minimization, i.e.

$$[\eta_{11}, \cdots, \eta_{P1}] = \arg \min_{\beta_1, ..., \beta_P} ||P_f^g(u, \xi)||_0,$$

where $P_f^g(u, \xi)$ is the spectrogram of the signal $\mathbf{y} = \beta_1 \mathbf{q_1} + \cdots + \beta_P \mathbf{q_P}$.

Method pros. It is able to separate overlapping components in high noise environment, provided a sufficient number of measurements.
Method cons. The procedure requires a large amount of information. In addition, it is computationally expensive, as it requires the computation of the spectrogram with respect to $(\beta_0, ...\beta_P)$ for each step in the minimization.

Chapter 2

Improving the resolution of overlapping modes in TF domain: an iterative approach

Reassignment method (RM) is an effective non-linear technique providing a sparse TF representation of a FM signal. The resolution limit established by Heisenberg uncertainty principle is overcome in reassigned representations of a monocomponent signal as they allow for the localization of IF curve both in time and frequency. In addition, RM is completely automatic and suitable for amplitude modulated signals. On the other hand, its applicability is limited to MCS having separable components. Indeed, the reassigned distribution generally presents a poor resolution in those regions where the signal components do overlap, especially in the critical case of crossing modes. Actually, the main advantage of RM is also its main drawback: the procedure is automatically and blindly applied to all points of the distribution support, regardless of their location. On the contrary, RM—as well as all methods designed for separable modes—could be reasonably adapted to the non-separable case if additional information is available, for instance if the partition of TF plane into regions of separability and non-separability would be known in advance. Unfortunately, the automatic detection of the interference/non-separability region is an open problem—the latter will be addressed in Chapter 2. However, we will prove that the information in TF domain can be properly selected so that the interference effects are somehow attenuated. To this aim, a general spectrogram evolution law will be introduced and discussed and, based on this result, TF

points *weakly* separated will be characterized and involved in order to improve resolution at the interference region. As a result, robust iterative reallocation techniques are introduced and their convergence is studied and used for guiding reassignment in the non-separability region. As a result, IFs curves are better localized in the TF domain and the readability of the reassigned spectrogram is improved. Being non-parametric, the proposed methods also lead to significant gain from the computational point of view. The presented results have been partly published in [98–100].

This chapter consists of three parts: Section 2.1 illustrates the motivations of the study; Section 2.2 contains some original theoretical results, it introduces the concept of weak separability, and it presents some practical applications. Finally, Section 2.3 draws the conclusions of the chapter.

2.1 Motivations

Let us consider a monocomponent FM signal $f(t) = a(t)\cos\phi(t)\,, t \in \mathbb{R}$ and let $S_f^g(u,\xi)$ be its STFT as defined in eq.(1.1). STFT squared modulus is referred as spectrogram and denoted by $P(u,\xi)$, whose reassigned version as is defined in eq.(1.24). The latter is obtained by reallocating each point on its local centroid as defined in eq.(1.25), according to the map $(u,\xi) \mapsto (\hat{u}_f(u,\xi), \hat{\omega}_f(u,\xi))$, resulting in a TF representation well concentrated on the ridge curve.

RM effectiveness is guaranteed also for a MCS $f(t) = \sum_{k=1}^{N} a_k(t)e^{i\phi_k(t)}$ having well separated modes, i.e. signal IFs satisfy the *strong* separability condition in Def. 6, i.e.

$$|\phi_k'(t) - \phi_j'(t)| \geq \Delta\omega,\ \forall\, k \neq j \in \{1,...,N\}, \forall\, t \in\ supp\{f\}.$$

In this case, it is always possible to select a proper analysis window such that the local centroids are correctly estimated and then the signal modes are globally well discriminated in the reassigned spectrogram, as shown in Fig.1.19. On the contrary, two overlapping modes in TF domain can not be disentangled by RM, as shown in Fig.2.1(b), that clearly shows the resolution loss at the non-separability region.

The main reason explaining the non-applicability of RM to overlapping modes is that ridge points can be highly deviated by the interference between modes. Precisely, at the non-separability region, the observed position of spec-

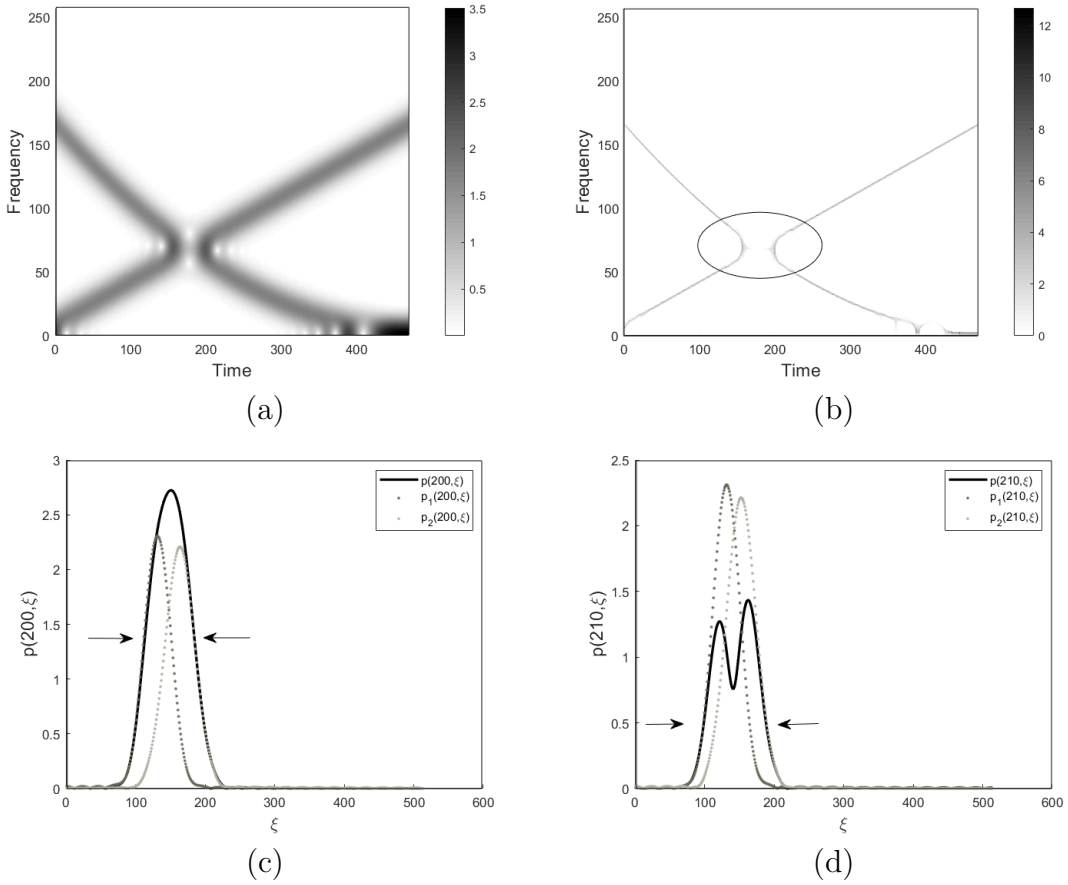

Figure 2.1: Two-components signal whose IFs do not satisfy the separability condition. (a) Spectrogram; (b) Reassigned spectrogram: the non-separability region is emphasized by the ellipse; (c)-(d) Spectrogram sections at u belonging to the non-separability region. As it can be observed, there are several frequency points that satisfy the separability condition —i.e., points where signal spectrogram (solid line) coincides with the spectrogram of one single mode (dotted line) [98].

trogram maxima points does not coincide with the position of single components maxima, in general. To better understand this point, let us consider the spectrogram of a constant amplitude two-components signal $f(t) = f_1(t) + f_2(t)$, i.e.

$$P(u,\xi) = |S^g_{f_1}(u,\xi)+S^g_{f_2}(u,\xi)|^2 = P_1(u,\xi)+P_2(u,\xi)+2\sqrt{P_1P_2}\cos(\phi_2(u)-\phi_1(u)), \tag{2.1}$$

where $P_i(u,\xi) = |S^g_{f_i}(u,\xi)|^2 = \frac{s\,a_i(u)^2}{4}\hat{g}^2(s(\xi-\phi_i'(u)))$ $i = 1,2$, according to eq.(1.6). For a fixed u, the single profiles P_i, $i = 1,2$ have overlapping sup-

ports if $|\phi_1'(u) - \phi_2'(u)| < \Delta\omega$. It means that they interfere with each other. In addition, their interaction also depends on the cosine term and, in particular, on its argument $\phi_2(u) - \phi_1(u)$. As a consequence, spectrogram is interested by a loss (destructive interference) or an increase (constructive energy) of energy, with respect to the energy observed at the separability region — this point will be further discussed later. It follows that, in general $\max_\xi P(u,\xi) \neq P(u,\phi_i'(u))$, $i = 1, 2$. As a result, IF curves $(u, \phi_i'(u))$ can not be detected by simply computing spectrogram maxima. The local centroids definition in RM relies on the assumption that the center of gravity of the distribution reflects the local IF, i.e. the local maximum, which is certainly true for monocomponent signals. If the observed maxima are deviated, local centroids computation is incorrect and TF points belonging to the non-separability are misallocated. Ridge points deviation also explains why the methods described in Chapter 1, that derive IF from the knowledge of TFDs peaks, are unreliable in case of non-separable modes.

Actually, there exist some points lying on the external sides of spectrogram sections which are considerably less affected by interference and, at the same time, keep IF information [101], see Fig.2.1(c)-(d). Therefore, it is convenient to take advantage from those points in order to define a more robust reallocation technique. As it will be shown in the next section, this goal can be reached by the introduction of a spectrogram evolution law that allows us to relax the definition of separability.

2.2 Weak separability

The following proposition provides a model for the spectrogram of a generic AM-FM signal.

Proposition 2.1. *Let $f(t)$ be a MCS as defined in eq.*(1.17) *and let $S_f^g(u,\xi)$ be its STFT. Then, the spectrogram $P(u,\xi)$ satisfies the following evolution laws*

$$(i) : s^2 \Delta_u \frac{\partial P}{\partial u} - \Delta_\xi \frac{\partial P}{\partial \xi} = -2sP \cdot Re\left(\frac{S_f^{g'}}{S_f^g}\frac{S_f^{tg}}{S_f^g}\right), \tag{2.2}$$

where $s > 0$ is the window length and

$$\Delta_u(u,\xi) = \frac{Re(S_f^{tg}(S_f^g)^*)}{P(u,\xi)},$$
$$\Delta_\xi(u,\xi) = \frac{Im(S_f^{g'}(S_f^g)^*)}{P(u,\xi)};$$

$$(ii) : s^2 Im(S_f^{tg}(S_f^g)^*)\frac{\partial}{\partial u}P(u,\xi) + Re(S_f^{g'}(S_f^g)^*)\frac{\partial}{\partial \xi}P(u,\xi) = 0. \tag{2.3}$$

Proof. Proof can be found in Appendix A. □

Remark 3. *The quantities Δ_u and Δ_ξ coincide with the shifts applied in RM, indeed in reference to eq.*(1.25)

$$|\hat{u}_f(u,\xi) - u| = \left|\Re\left(\frac{S_f^{tg}}{S_f^g}\right)\right| = \left|\Re\left(\frac{S_f^{tg}(S_f^g)^*}{S_f^g(S_f^g)^*}\right)\right| = \Delta_u,$$

and similarly $|\hat{\xi}_f(u,\xi) - \xi| = \Delta_\xi$.

Eq.(2.2) is composed of two diffusion terms and a source term and, because of its generality, it could result in a powerful tool in MCS analysis. In the special case of a two-components signal, it is possible to explicit the pde coefficients in eq.(2.3), as stated below.

Proposition 2.2. *Let $f(t) = a_1(t)\cos\phi_1(t) + a_2(t)\cos\phi_2(t)$ be a two-components signal and let set $\hat{g}_i = \hat{g}(s(\xi - \phi_i'(u)))$, where g is the analysis window with length $s > 0$, $a_i = a_i(u)$ and $\phi_i = \phi_i(u)$, $i = 1, 2$. Then, the spectrogram $P(u,\xi)$ satisfies the following evolution law*

$$\frac{\partial P(u,\xi)}{\partial u} + \phi_1''\frac{\partial P(u,\xi)}{\partial \xi} - \frac{s}{2}\Big[a_1 a_1'\hat{g}_1^2 + a_2 a_2'\hat{g}_2^2 + \hat{g}_1\hat{g}_2\cos\Delta\phi(a_1'a_2 + a_2'a_1)\Big]$$
$$+ \frac{s}{2}a_1 a_2\hat{g}_1\hat{g}_2\sin\Delta\phi\Delta\phi' + \frac{s^2}{2}\Delta\phi''\hat{g}_2'\Big[a_2\hat{g}_2^2 - a_1 a_2\cos\Delta\phi\hat{g}_1\Big] = 0 \tag{2.4}$$

Proof. Proof is in Appendix A. □

Remark 4. *The evolution law in eq.*(2.4) *formalizes ridge points deviation described in Section 2.1 proving that the curve $(u, \phi_1'(u))$ is not the curve of maxima, as the spectrogram total differential is non zero.*

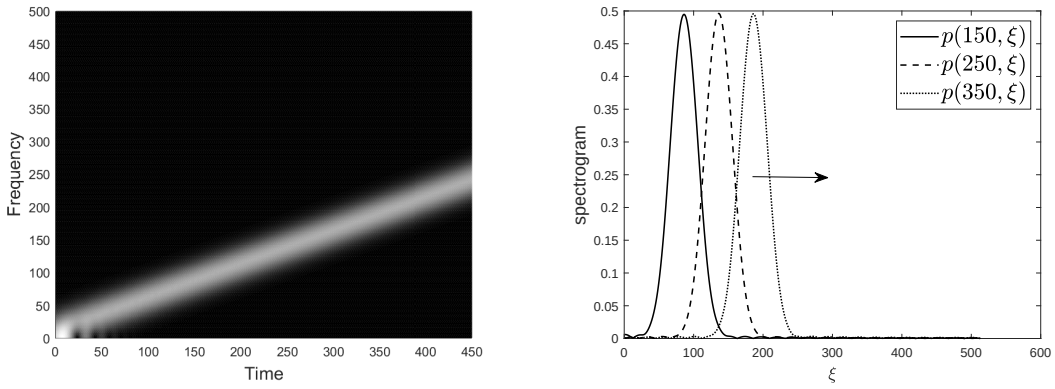

(a) (b)

Figure 2.2: Spectrogram of a linear chirp; (b) Spectrogram section for increasing values of time u. The window profile is translated in the direction indicated by the arrow [100].

Eq.(2.4) consists of two diffusion terms, a source term depending on the amplitudes' variation and an interference term due to the interaction between modes. If $a_2 = 0$, it reduces to the transport equation

Corollary 1. *The spectrogram $P(u,\xi)$ of a monocomponent signal $f(t) = a(t)\cos\phi(t)$ satisfies*

$$\frac{\partial P(u,\xi)}{\partial u} + \phi''(u)\frac{\partial P(u,\xi)}{\partial \xi} - \frac{2a'(u)}{a(u)}P(u,\xi) = 0. \tag{2.5}$$

Proof. The proof follows by setting $a_2(u) = 0$ in eq.(2.4) and by observing that $\frac{s}{2}a_1 a_1' \hat{g}_1^2 = \frac{2a_1'}{a_1}\frac{s}{4}a_1^2\hat{g}_1^2 = \frac{2a_1'}{a_1}P(u,\xi)$. Finally, set $a_1(u) = a(u)$ and $\phi_1(u) = \phi(u)$, $\forall\, u \in supp\{f\}$. □

In addition, in case of constant amplitude monocomponent signals the homogeneous transport equation holds true.

Corollary 2. *The spectrogram $P(u,\xi)$ of $f(t) = a\cos\phi(t)$ satisfies the following evolution law*

$$\frac{\partial P(u,\xi)}{\partial u} + \phi''(u)\frac{\partial P(u,\xi)}{\partial \xi} = 0. \tag{2.6}$$

Proof. The proof trivially follows by eq.(2.5) observing that $a'(u) = 0$. □

According to eq.(2.6), the spectrogram of a monocomponent signal having constant amplitude consists of shifted copies of the window profile, as shown

in Fig. 2.2. Furthermore, eq.(2.6) allows for a further characterization of ridge points, as stated in the following

Proposition 2.3. *Let $f(t) = a\cos\phi(t)$ and let assume $\phi''(u) \neq 0 \; \forall\, u$, then the ridge points $(u, \phi'(u))$ are the solutions of the equation $\frac{\partial P(u,\xi)}{\partial \xi} = 0$.*

Proof. By eq.(2.6), $\frac{\partial P(u,\xi)}{\partial u} = -\phi''(u)\frac{\partial P(u,\xi)}{\partial \xi}$. Since

$$\frac{\partial^2 P(u,\xi)}{\partial^2 \xi}|_{\xi=\phi'(u)} = \frac{s^3}{4}a^2\hat{g}''(0) < 0,$$

and $\phi''(u) \neq 0 \; \forall\, u$, it follows that ridge points are the maxima points along the frequency direction. □

The following proposition shows the fundamental relation between eq.(2.6) and IF.

Proposition 2.4. *The characteristic curves $\mathcal{C}_{c,\phi}$ of the partial differential equation in eq.(2.6) are*

$$\xi(u) = \phi'(u) + c, \tag{2.7}$$

with $c = \xi_0 - \phi'(u_0)$ and (u_0, ξ_0) is a point in the TF plane.

Proof. Proof can be found in Appendix A. □

As a consequence, the following proposition holds true.

Proposition 2.5. *The spectrogram is a constant function along each characteristic curve.*

Proof. By eq,(2.6), the total differential of the spectrogram, evaluated at each characteristic curve, is zero and then the thesis holds true— See eq.(3.52) in Appendix A. □

Prop.2.5 implies that, in the monocomponent case, a simple threshold of spectrogram provides the characteristic curves, as shown in Fig.2.3. In addition, Propositions 2.4-2.5 give a new characterization of IF curve as a specific characteristic curve of eq.(2.6) and state that IF information is available at special TF points different from the maxima, i.e. the characteristic curves. Even if Propositions 2.4-2.5 are formulated for monocomponent signals, they are crucial for MCS analysis. As discussed in Section 2.1, it is not always convenient

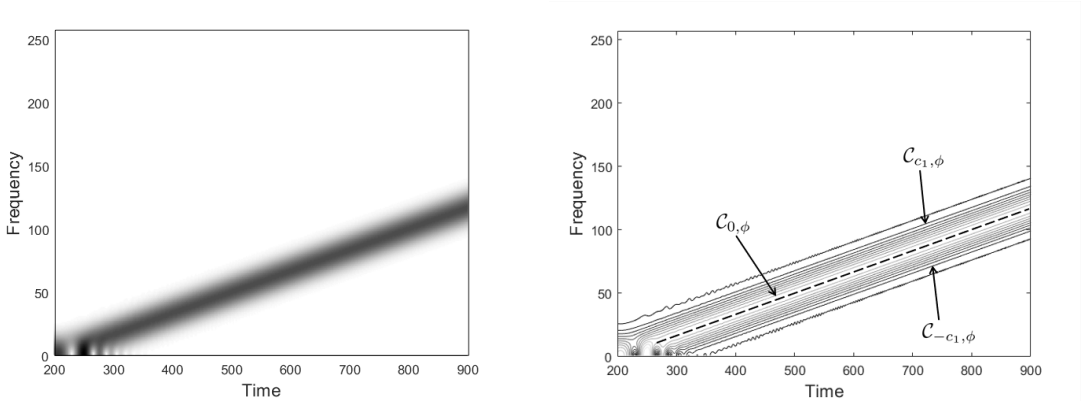

(a) (b)

Figure 2.3: (a) Spectrogram of a linear chirp and (b) its isolevel curves that coincide with the characteristic curves in eq.(2.7).

to involve spectrogram maxima points for estimating IF, as they can be highly deviated. Fortunately, Propositions 2.4-2.5 provide the "good" points to be involved. More precisely, the current study can be generalized to MCS as follows. The evolution law in eq.(2.4) reduces to eq.(2.6) also if $\hat{g}(s(\xi - \phi_2'(u))) << 1$, or equivalently $\hat{g}(s(\xi - \phi_2'(u))) \approx 0$. This happens if the two components are separated, in the sense specified by the following

Definition 11 (Weakened separability condition (**WSC**))**.** *Two modes with IFs $\phi_1'(u)$ and $\phi_2'(u)$ are separated at time location u if there exists at least one curve in $\mathcal{C}_{c_1,\phi_1}$, i.e., $\xi_1(u) = \phi_1'(u) + c_1$, such that $|\xi_1(u) - \phi_2'(u)| \geq \Delta\omega$; or viceversa.*

Remark 5. *It is worth observing that, for example, if $\xi < \phi_1'(u) < \phi_2'(u)$, $|\phi_1'(u) - \phi_2'(u)| = \varepsilon \leq \Delta\omega$, and $\xi \in \xi_1(u) \in \mathcal{C}_{c_1,\phi_1}$, then $\exists\ c_1 \in \mathbf{R}$, $c_1 < 0$ such that $\xi = \phi_1'(u) + c_1$. As a consequence, $|\xi - \phi_2'(u)| = |\phi_1'(u) + c_1 - \phi_2'(u)| = |-\varepsilon + c_1| \geq \Delta\omega \Leftrightarrow -c_1 \geq \Delta\omega - \varepsilon$.*

Definition 11 formally defines those points lying on the external sides of the spectrogram which are less influenced by interference effects. The latter can be operatively selected by means of the following proposition.

Proposition 2.6. *Let consider $f(t) = a_1 \cos\phi_1(t) + a_2 \cos\phi_2(t)$ and let $P(u,\xi)$ be the corresponding spectrogram. Then, TF points (u,ξ) such that the ratio*

$$\frac{P(u,\xi)}{max_\xi P(u,\xi)} << \frac{1}{2}, \tag{2.8}$$

with high probability satisfy the WSC, as in Definition 11.

Proof. Proof can be found in Appendix A. □

Remark 6. *Prop.2.6 also implies that for MCS having constant amplitudes, a proper threshold of the spectrogram provides TF points which are less affected by interference effects, as depicted in Fig.2.4. For this reason, the definition of an effective reallocation technique should involve those points, instead of the maxima, which are deviated with high probability.*

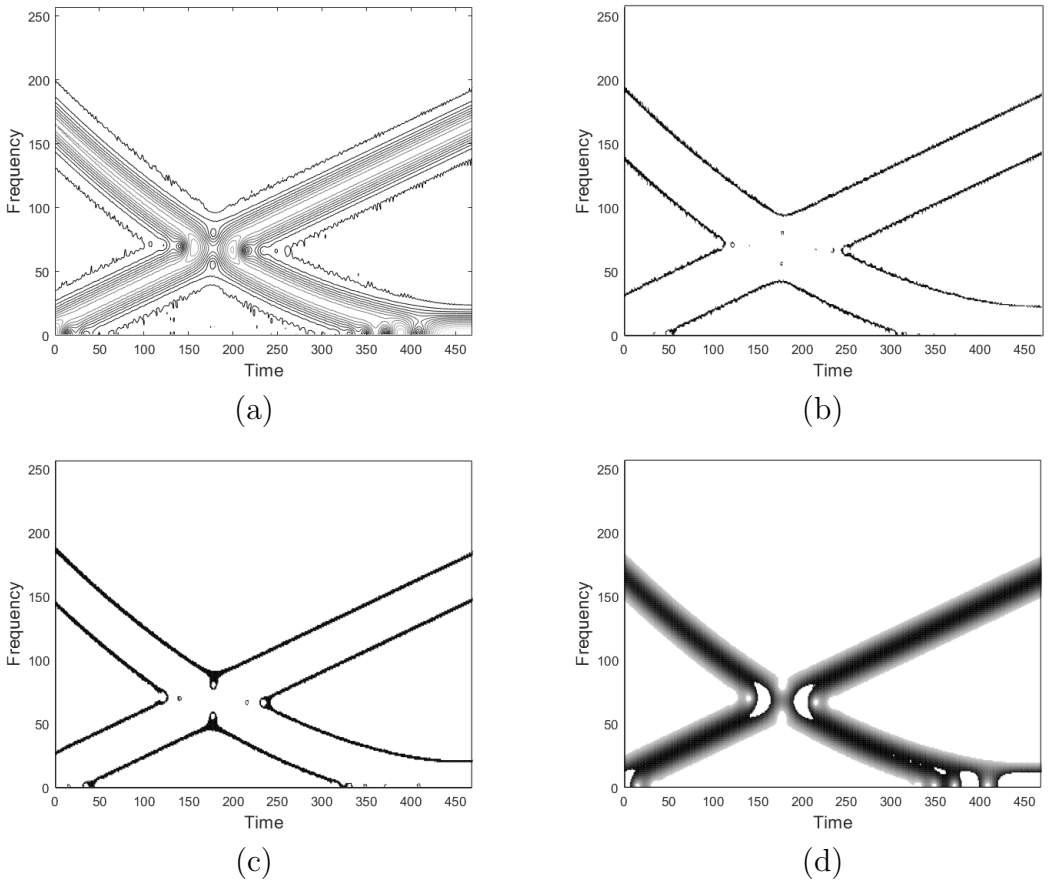

Figure 2.4: Isolevel curves of the spectrogram in Fig.2.1(a). (a) Characteristic curves closer to the ridge are highly deviated at the interference region; (b) Levels in $[0.0004, 0.0012]$ identify those characteristic curves less affected by interference and then better preserving IFs information; (c) Levels in $[0.0025, 0.01]$; (d) Levels in $[0.01, 0.25]$.

Furthermore, the following proposition holds true.

Proposition 2.7. *If $\xi_1(u) \in \mathcal{C}_{c_1,\phi_1}$ and if it satisfies the separability condition with respect to ϕ_2', as in Definition 11, then $\hat{g}(|\xi_1 - \phi_2'(u)|) << 1$.*

Proof. By setting $\omega = \xi_1 - \phi_2'(u)$, the proof directly derives from the definition of window bandwidth, i.e., $\hat{g}(\omega) << 1 \quad \text{for} \quad |\omega| \geq \Delta\omega$, when applied to the mode with $\phi_2'(u)$ as IF. □

As a result, the evolution law in eq.(2.4) evaluated on the characteristic curves satisfying the WSC reduces to eq.(2.6). Actually, as it can be observed in Fig.2.4(a), not all the characteristic curves are deviated in the same way. In particular, the very external sides in Fig.2.4(a) correctly reveal IFs curves, i.e. each TF point detected by thresholding satisfies the WSC. Unfortunately, too low thresholds are unreliable in case of real signals due to the presence of noise. However, higher threshold levels also provide characteristic curves sufficiently weakly separated, as depicted in Fig.2.4(c)-(d).

In case of constant amplitude signals, it is convenient to consider a normalization of the spectrogram instead of the spectrogram, according to the following

Definition 12. *The normalized spectrogram of* $f(t) = \sum_{k=1}^{N} a_k e^{i\phi_k(t)}$ *with respect to the i-th mode is defined as*

$$p(u,\xi) = \frac{\sqrt{P(u,\xi)}}{\frac{\sqrt{s}}{2} a_i \hat{g}(0)}, \forall (u,\xi) \in \mathbb{R} \times \mathbb{R}^+. \tag{2.9}$$

Remark 7. *It is worth observing that if* $f(t) = a\cos\phi(t)$*, then from eq.*(1.6) *it follows*

$$p(u,\xi) = \sqrt{\frac{P(u,\xi)}{P(u,\phi'(u))}} = \frac{\hat{g}(s(\xi - \phi'(u)))}{\hat{g}(0)}. \tag{2.10}$$

It is straightforward to prove that the normalized spectrogram $p(u,\xi)$ *as in eq.*(2.10) *satisfies the evolution law in eq.*(2.6) *and Prop.2.3, Prop.2.4 and Prop.2.5 also remain true. In addition,* $p(u,\xi)$ *as in eq.*(2.9) *satisfies a special case of eq.*(2.4)*, i.e.*

$$\begin{aligned} &\phi_1'' \frac{\partial p(u,\xi)}{\partial \xi} + \frac{\partial p(u,\xi)}{\partial u} + \frac{a_2}{a_1 \hat{g}^2(0)\, p(u,\xi)} \hat{g}_1 \hat{g}_2 \sin(\phi_2 - \phi_1)\,(\phi_1' - \phi_2') \\ &\quad + \frac{s\ (\phi_1'' - \phi_2'')\, \hat{g}_2'}{a_1^2 \hat{g}^2(0)\, p(u,\xi)} \Big[a_2^2 \hat{g}_2 + a_1 a_2 \cos(\phi_2 - \phi_1) \hat{g}_1 \Big] = 0. \end{aligned} \tag{2.11}$$

As a consequence, Prop.2.6 can be rephrased in terms of normalized spectrogram, by replacing the condition in eq.(2.8) *with* $p(u,\xi) << \frac{1}{\sqrt{2}}$*. It is worth noticing*

that thresholding $p(u,\xi)$ at level Θ corresponds to select the characteristic curves at the rate Θ with respect the ridge.

The discussion in Remark 6 can be extended to the normalized spectrogram, as well. For these reasons, without loss of generality, in the sequel we will equivalently refer to spectrogram or normalized spectrogram.

The proof of eq.(2.11) can be found in Appendix A.

2.3 Iterative spectrogram reassignment

Some of the theoretical results presented in the previous section have been applied to define efficient iterative reassignment techniques. The basic idea is to concentrate spectrogram distribution on the ridge curve iteratively and pointwise, that is by moving each selected TF point step by step and independently of the others. Contrary to classical RM, that computes both time and frequency shifts, the proposed approach considers fixed u and reassigns only in the frequency direction, resulting in a frequency reallocation technique, see Fig.2.5. This is mainly justified by the characterization of ridge points as maxima along the frequency direction, provided by Prop.2.3. Furthermore, the procedure is iterative so that we are able to adapt it to regions of non-separability, as it will better explained later. The outline of the proposed iterative methods for a monocomponent signal $f(t) = a\cos\phi(t)$ can be drawn as follows.

Let us consider a fixed u and $\xi_R = \phi'(u) \in \mathcal{C}_{0,\phi}$ the corresponding ridge point. A threshold of the spectrogram at level Θ provides two characteristic curves of eq.(2.6). Since u is fixed, two frequency point ξ_0^+, ξ_0^- are intercepted, as shown in Fig.2.6(b). According to a fixed-point scheme M, each point is then moved as follows

$$M : \xi_{n+1} = \xi_n + \mu\,\Delta_n,\ n \geq 0, \tag{2.12}$$

where $\mu = sign(\xi_R - \xi_0)$, $\Delta_n = \Delta_n(g, p(u,\xi_n))$ is a positive frequency shift only depending on the analysis window and the value of the spectrogram at ξ_n. The latter is estimated by the observed data, at each iteration. The sequence converges to the ridge, i.e. $\xi_n \to \xi_R \in \mathcal{C}_{0,\phi}$. For instance, if we consider the frequency point ξ_0^+ in Fig.2.6(c), then $\mu = -1$. As depicted in Fig.2.6(d), at the first iteration ξ_0 moves to $\xi_1 = \xi_0 - \Delta_0$, which is closer to the ridge. Then, the

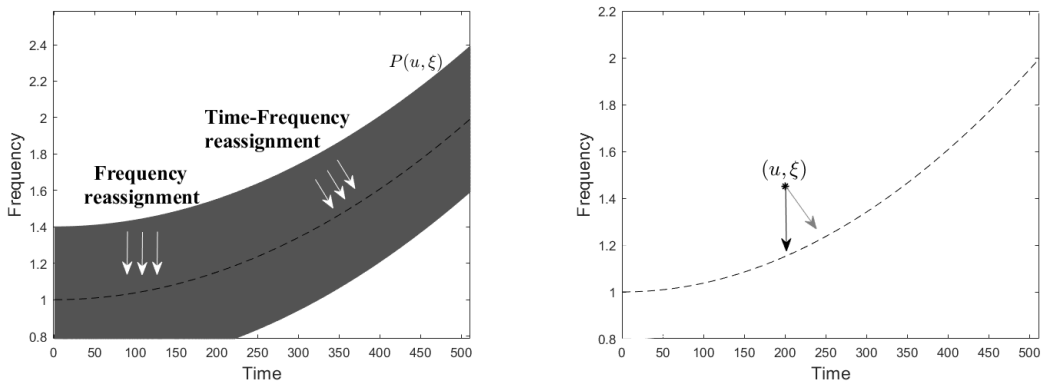

(a) (b)

Figure 2.5: (a) Spectrogram of a FM signal and ridge curve (dashed line). The arrows indicate reassignment operators direction. Classic RM is a TF reallocation method, while the proposed one is a frequency reassignment; (b) Classical RM shifts a point (u, ξ) to its local centroid $(\hat{u}, \hat{\xi})$, according to eq.(1.25) (gray arrow), while the proposed approach moves points only in the frequency direction (black arrow).

new shift Δ_1 is computed and applied to obtain $\xi_2 = \xi_1 - \Delta_1$, as in Fig.2.6(e). The scheme is iterated until ξ_n approaches $\mathcal{C}_{0,\phi}$, i.e. the distance to the ridge is less than a prefixed tolerance, as shown in Fig.2.6(f).

The reallocation is completed by assigning the value of the spectrogram at the starting point, i.e. $P(u, \xi_0^+)$, to the frequency point ξ_n. Formally, we set $\hat{P}(u, \xi_n) = P(u, \xi_0^+)$, where $\hat{P}$ denotes the reassigned spectrogram.

The procedure is repeated on the symmetric point ξ_0^- and on each characteristic curve obtained by a different spectrogram threshold, at the same fixed u. The value of reassigned spectrogram at frequency ξ is the result of the overall contributions $P(u, \xi')$ such that ξ' has been moved to ξ. More formally,

$$\hat{P}_M(u, \xi) = \int_{\mathbb{R}^2} P(u, \xi')\, \delta(\xi' - \xi_M(\xi')\, d\xi' \,, \tag{2.13}$$

where $\xi_M(*)$ denotes the point obtained by applying method M using $*$ as initial point. Finally, the whole algorithm has to be repeated on each u in the spectrogram support. The result of the method restricted to a specific characteristic curve is sketched in Fig.2.7.

In the ideal case, the application of the procedure to all TF points, i.e. to all characteristics, is expected to provide a TF representation perfectly located

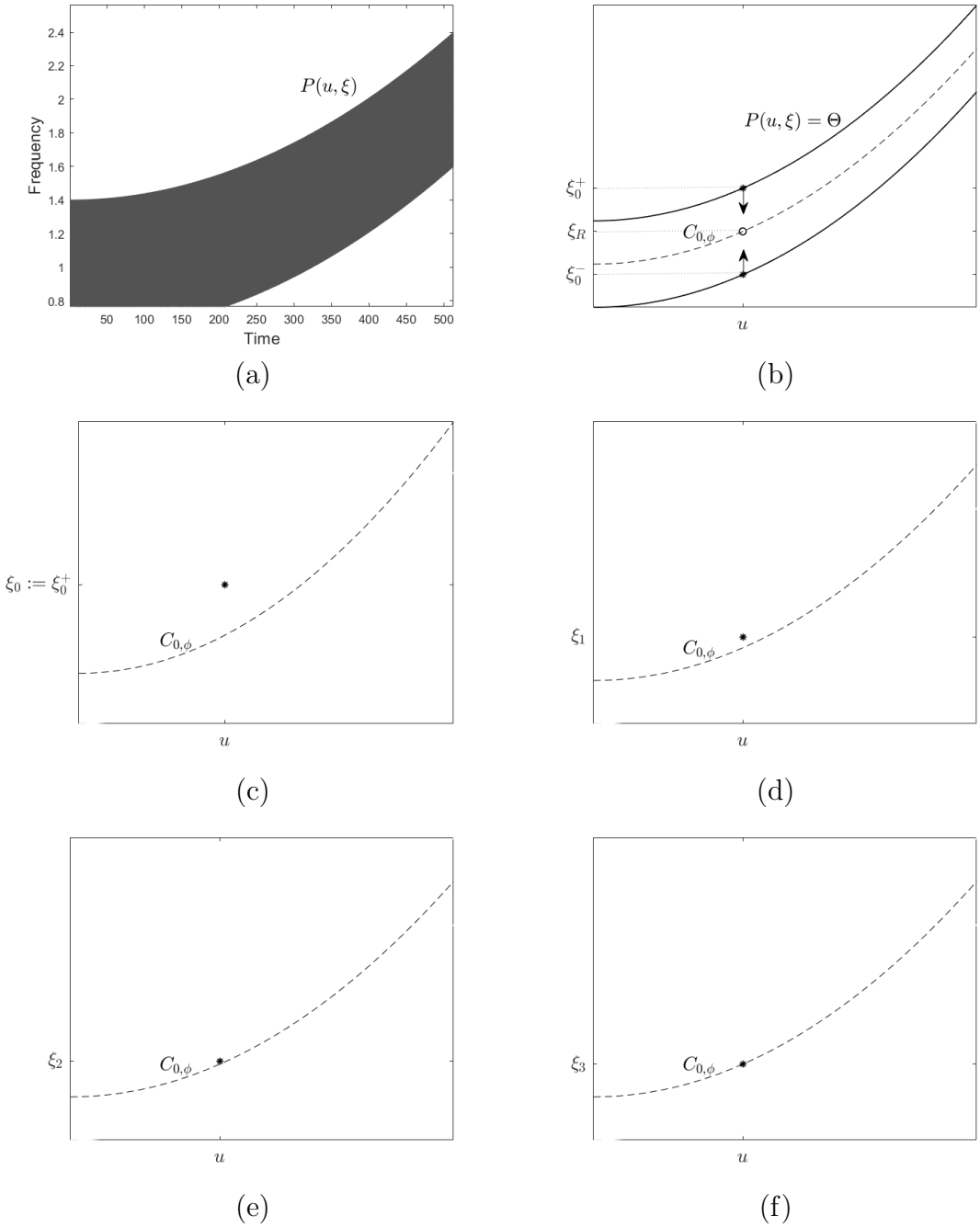

Figure 2.6: Sketch of the iterative procedure at fixed u . (a) Spectrogram; (b) Ridge curve $C_{0,\phi}$ (dashed line) and characteristic curves obtained by thresholding the spectrogram at level Θ, i.e. the set $\{(u,\xi) : P(u,\xi) = \Theta\}$ (solid line). ξ_0^+ belongs to the characteristic curve located above the ridge $C_{0,\phi}$, then it has to be shifted downwards. (c) $\xi_0 = \xi_0^+$ is the starting point that is moved towards the ridge (d)-(e). The convergence is met (f).

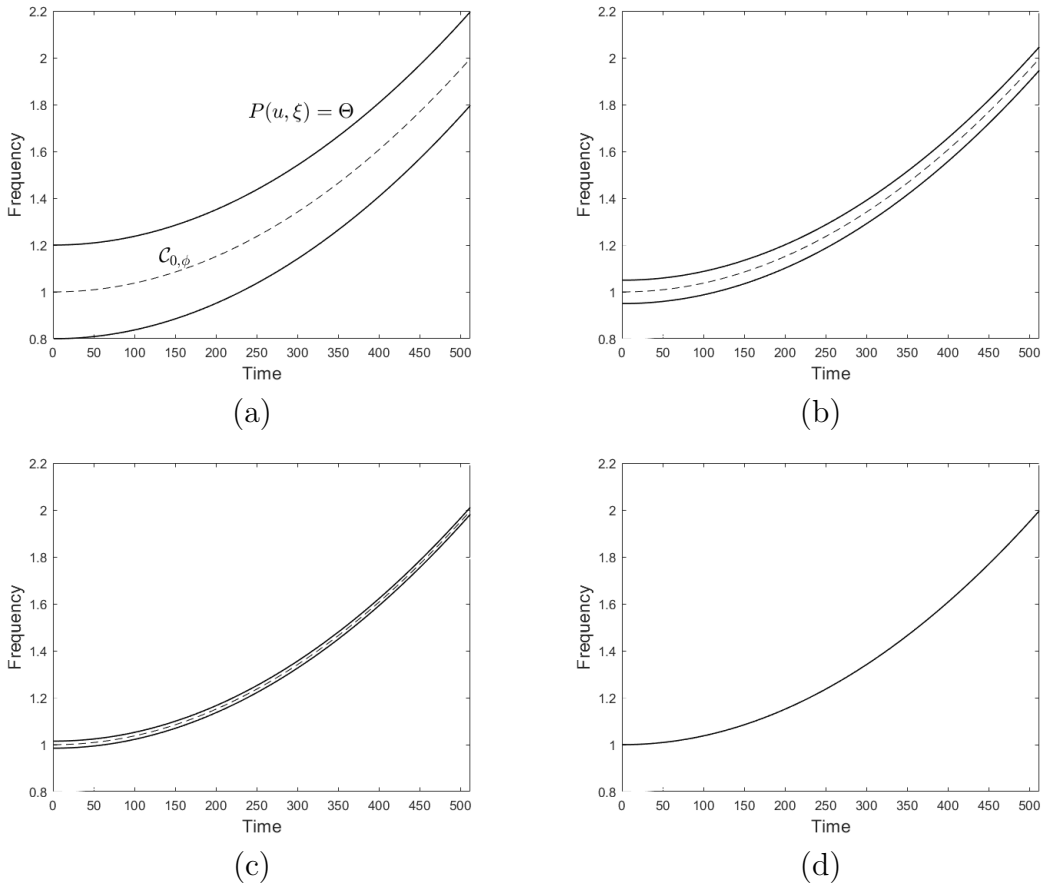

Figure 2.7: Iterative procedure applied to characteristics. (a) Ridge curve $C_{0,\phi}$ (dashed line) and characteristic curves obtained by thresholding the spectrogram at level Θ, that is by selecting the set $\{(u,\xi) : P(u,\xi) = \Theta\}$ (solid line). At each iteration, the characteristic curves are moved towards the ridge (b)-(c). The convergence is met (d).

on the ridge curve, i.e.

$$\hat{P}(u,\xi) = K\,\delta(\xi - \phi'(u)),$$

where K is the energy of the spectrogram profile. It is worth observing that $K = \frac{\pi}{2} s\, a^2 ||g||_{L^2(\mathbb{R})}$ by eq.(1.6).

The methods we are going to present in details in the next section are all fixed-point procedures, that formally differ accordingly to how the shift is calculated. The latter also determines the type of convergence and global effectiveness. In particular, ***FIRST*** and **Method I** are essentially Newton-like methods with fixed tangent. In the first case, the iterations depend on

spectrogram value, while the second method depends on spectrogram frequency derivative. As main advantage, *FIRST* convergence interval is large, but the convergence is linear. On the contrary, Method I is a third order method, but on the other hand it requires functional evaluations, that are computationally expensive. However, **Method II** is a predictor-corrector procedure representing a good trade-off: it is fast, as the convergence is at least quadratic and a large convergence interval can be achieved by its combination with *FIRST*.

It is worth pointing out that not all TF points in spectrogram support will be involved in the procedure. Indeed, according to the discussion provided in Section 2.2, the characteristic curves satisfying the WSC are less influenced by interference and then they better preserve original IFs information. Finally, the convergence properties will be exploited to define a more advanced reallocation technique, namely **Improved Method II**, which attempts to distinguish between separable and non-separable TF points. In the latter case a relaxed scheme is used in order to prevent misallocations. As a result, IFs curves are better localized also at the interference region.

2.3.1 Fast Iterative and Robust Spectrogram Thinning (*FIRST*)

From now on and without loss of generality we set $s = 1$ in eq.(1.6).

The window function can be used for a direct estimation of the reassignment shift as in eq.(2.12). By considering the regularity of the window function, for a fixed u, we can compute the Taylor expansion around the ridge point, i.e.,

$$P(u,\xi) = P(u,\phi'(u)) + \frac{P''(u,\phi'(u))}{2}(\xi - \phi'(u))^2 + o((\xi - \phi'(u))^4). \tag{2.14}$$

By neglecting the error term, we get

$$(\xi - \phi'(u))^2 \approx 2\frac{P(u,\xi) - P(u,\phi'(u))}{P''(u,\phi'(u))} \tag{2.15}$$

and, by multiplying the second member by $\frac{P(u,\phi'(u))}{P(u,\phi'(u))}$, we have

$$(\xi - \phi'(u))^2 \approx 2\left(\frac{P(u,\xi)}{P(u,\phi'(u))} - 1\right)\frac{P(u,\phi'(u))}{P''(u,\phi'(u))}, \tag{2.16}$$

and recalling eq.(2.10), we obtain

$$|\xi - \phi'(u)| \approx \sqrt{\frac{2\,(p(u,\xi)-1)}{\hat{g}''(0)}}. \tag{2.17}$$

It is worth noting that $\hat{g}''(0) < 0$, because the window $\hat{g}$ is commonly a concave function and $p(u,\xi) = \sqrt{\frac{P(u,\xi)}{P(u,\phi'(u))}} \leq 1$, so that the square root is well defined.

Based on Taylor approximation, the previous estimation is almost acceptable whenever ξ approaches $\phi'(u)$, while for points far from $\phi'(u)$, i.e., $\frac{P(u,\xi)}{P(u,\phi'(u))} << 1$, it does not provide a good approximation of the distance from the ridge.

By setting $\tau_n = \xi_n - \phi'(u)$ we can define the following sequence

$$\tau_{n+1} = \tau_n - sign(\tau_n)\Delta\tau_n, \quad \text{with} \tag{2.18}$$

$$\Delta\tau_n = \sqrt{\frac{\alpha\,[p(u,\tau_n+\phi'(u))-1]}{p''(u,\phi'(u))}} = \sqrt{\frac{\alpha\,(1-p(u,\tau_n+\phi'(u)))}{|\hat{g}''(0)|}} \tag{2.19}$$

that directly derives from eqs.(2.16)–(2.17), where $\alpha \leq 2$ is a positive real parameter.

As stated in the following proposition, the sequence τ_n monotonically converges to 0, i.e., $\xi_n \to \phi'(u)$, and then it provides a reassignment method.

Proposition 2.8 (*FIRST*). *Let $\hat{g}(\omega)$ denote the modulus of the FT of a real, positive and symmetric analysis window and let $p(u,\xi) = \sqrt{\frac{P(u,\xi)}{P(u,\phi'(u))}}$ the normalized spectrogram of a monocomponent signal; then, for fixed u the sequence*

$$\tau_{n+1} = \varphi(\tau_n), \quad n \geq 0$$

where $\varphi(\tau) = \tau - sign(\tau)\Delta\tau$, with $\Delta\tau = \sqrt{\frac{\alpha\,(1-p(u,\tau_n+\phi'(u)))}{|\hat{g}''(0)|}}$, $\alpha \in (0,2]$ monotonically converges to 0.

Proof. Proof can be found in Appendix A. □

Eq.(2.18) defines an iterative spectrogram reassignment, referred as *FIRST* [98], whose corresponding reassigned spectrogram is defined as in eq.(2.13), where $\xi_M(*)$ denotes the point obtained by applying *FIRST* method using $*$ as initial point. The whole procedure is sketched in Fig.2.8.

Remark 8. *The computation of the shift in eq.*(2.19) *does not require any functional evaluations, as the quantity $|\hat{g}''(0)|$ is a priori known and the value of the*

spectrogram is estimated by the data, at each iteration.

For monocomponent signals, *FIRST* provides comparable results to classical RM, with a computational gain and a fast convergence, as it will be proved in the sequel. On the contrary, in case of MCS, it actually overcomes RM effectiveness because it contributes to reduce the region of incorrectly reassigned points thanks to the use of the WSC. Only a limited set of points is involved in the reallocation and each of them is forced to converge to the ridge point of the mode it belongs to, i.e., the one with a dominant contribution at the considered location. As a result, reassigned spectrogram resolution is improved at the non-separability region, as it will be shown in the experimental results.

Input: MCS $f(t)$, $\alpha \in (0, 2]$, niter
Output: Reassigned spectrogram $\hat{p}(u, \xi)$
compute the STFT of f and its normalized spectrogram $p(u, \xi)$ as in eq.(2.9)
initialize $\hat{p}$
select all (u, ξ) such that $p(u, \xi) \in [0.1, 0.5]$
for *all selected* u **do**
  for *all selected* ξ **do**
    set $count = 1$ and $\xi_0 = \xi$
    while $count \leq niter$ **do**
      let $\mu = sign(p_\xi(u, \xi_0))$
      let $p = p(u, \xi_0)$
      compute the frequency shift $\Delta\tau_0 = \sqrt{\frac{\alpha(1-p)}{|\hat{g}''(0)|}}$ as in eq.(2.18)
      set $\xi_1 = \xi_0 - \mu\Delta\tau_0$
      set $\xi_0 = \xi_1$
      increment *count*
    end
    let $\xi_M(\xi) = \xi_1$
    for *all selected* ξ **do**
      reassign contribution, i.e. set $\hat{p}(u, \xi_M(\xi)) = \hat{p}(u, \xi_M(\xi)) + p(u, \xi)$
    end
  end
end

Figure 2.8: Algorithm implementing reassignment with *FIRST*.

Even if *FIRST* is more robust to lack of separability, in the critical case of crossing modes there exists a region where the WSC in Definition 11 is not satisfied, either — close to the crossing point— resulting in possible wrong reallocations. Indeed, at each iteration, the spectrogram value at ξ_n, $P(u, \xi_n)$, is not

computed by using the spectrogram functional model. The value is estimated by the observed data, instead. As a consequence, the estimated $P(u, \xi_n)$ does not correspond to the value of the spectrogram of the single mode—the latter is unknown whenever the point ξ_n does not satisfy the WSC. The corresponding shift is then incorrect. However, the lower $P(u, \xi_n)$ the higher the shift and the higher the probability to be far from the interference region. Hence, for MCS, in correspondence to the non-separability region, a correct reallocation is expected for the very first iterations while convergence is not assured as n increases. In order to prevent wrong reallocations and to force the convergence to the ridge point of each component, we should avoid spectrogram evaluations at the non-separability region. More precisely, the following argument can be adopted. The contraction property implies

$$|\tau_{n+1}-\tau_n| = |\xi_{n+1}-\xi_n| = |\varphi'(\theta_n)||\xi_n-\xi_{n-1}| = |\varphi'(\theta_n)||\tau_n-\tau_{n-1}|, \quad \theta_n \in [\tau_{n-1}, \tau_n],$$

By denoting with $K = max_\tau|\varphi'(\tau)| = max\left\{1 - \sqrt{\frac{\alpha\hat{g}''(\bar{\tau})}{2|\hat{g}''(0)|}}, 1 - \sqrt{\frac{\alpha}{2}}\right\}$ the contraction constant of φ, we have

$$|\xi_{n+1} - \xi_n| \leq K|\xi_n - \xi_{n-1}|, \quad \forall\, n \geq 1.$$

As a result, in case of MCS, $\forall\, n \geq 1$ we can modify eq.(2.18) as follows

$$\begin{cases} \tau_1 = \tau_0 - sign(\tau_0)\Delta\tau_0 & n = 0 \\ \tau_{n+1} = \tau_n + K(\tau_n - \tau_{n-1}) & n > 0 \end{cases} \tag{2.20}$$

with τ_0 the initial point. The use of K instead of the spectrogram value for determining the elements of the sequence, except for the first one, can be seen as a regularization. The shift is corrected so that each point is forced to move as if it is a point satisfying the separability condition with respect to another mode, resulting in a more accurate reallocation on the ridge curve—as it will be shown in the experimental results. The reallocation method as in eq.(2.20) is referred as *FIRST_K* [98].

Even if K characterizes the analysis window ($\bar{\tau}$ satisfies eq.(3.59)), its computation could be not trivial, as non-linear iterative methods should be required. Since the closer τ_n to 0 the more $|\varphi'(\theta_n)| \approx |\varphi'(0)| = 1 - \sqrt{\frac{\alpha}{2}}$, a more simple

reassignment scheme can be performed by simply setting $K = 1 - \sqrt{\frac{\alpha}{2}}$, i.e.

$$\begin{cases} \tau_1 = \tau_0 - sign(\tau_0)\Delta\tau_0, & n = 0 \\ \tau_{n+1} = \tau_n + \left(1 - \sqrt{\frac{\alpha}{2}}\right) \cdot (\tau_n - \tau_{n-1}), & n > 0 \end{cases} \tag{2.21}$$

with τ_0 the initial point, and applying the first few iterations.

2.3.2 Improved iterative reassignment

FIRST can be combined with a faster method, resulting in a more robust reallocation technique, as discussed in details in the sequel.

According to Prop.2.3, for each fixed u, the ridge point is the solution of the non-linear equation $\frac{\partial p(u,\xi)}{\partial \xi} = 0$, that can be numerically solved by Newton method, as stated in the following

Proposition 2.9 (Method I)**.** *Let $f(t) = a\cos\phi(t)$ and let $p(u,\xi)$ be its normalized spectrogram as in eq.(2.9). Assuming $\phi''(u) \neq 0 \; \forall\, u$, let us define $p_\xi(\xi) := \frac{\partial p(u,\xi)}{\partial \xi}$, with u fixed. Then, the iterative method*

$$\xi_{k+1} = \xi_k - \frac{p_\xi(\xi_k)}{\hat{g}''(0)}, \quad k \geq 0 \tag{2.22}$$

(i) converges to $\xi_R = \phi'(u)$ for all ξ_0 s.t.

$$0 < \frac{\hat{g}''(\xi_0 - \xi_R)}{\hat{g}''(0)} < 2; \tag{2.23}$$

(ii) is a third order method, with convergence constant equal to $\frac{1}{6}\left|\frac{\hat{g}^{(4)}(0)}{\hat{g}^{(2)}(0)}\right|$.

Proof. Proof is in Appendix A. □

The method in Prop.2.9 will be denoted as Method I in the sequel.

As a corollary, in the gaussian case, it holds the following

Proposition 2.10. *Let $g(t) = \frac{1}{\sqrt{2\pi\sigma^2}} e^{-\frac{1}{2}\frac{t^2}{\sigma^2}}$ be the analysis window, then Method I monotonically converges to the ridge point $\xi_R = \phi'(u)$ $\forall \xi_0 : |\xi_0 - \xi_R| < 1/\sigma$.*

Proof. If g is a gaussian window, $\bar{\xi} \in \arg\max_\xi |\hat{g}''(\xi - \xi_R)| \Leftrightarrow \bar{\xi} = \xi_R$ and $\hat{g}''(\xi - \xi_R) < 0 \Leftrightarrow |\xi - \xi_R| < 1/\sigma$. Hence, $0 < \frac{\hat{g}''(\xi - \xi_R)}{\hat{g}''(0)} < 1 \, \forall\, \xi : |\xi - \xi_R| < 1/\sigma$, i.e. the convergence is monotone. □

Method I is a third order method but the convergence is guaranteed only for an initial point ξ_0 satisfying condition in eq.(2.23), i.e. "close" to the ridge. Once again, even if the proposed method is defined for monocomponent signals, the final goal is to apply it to MCS satisfying the WSC. For this reason, in order to involve points in spectrogram support less affected by interference, few iterations of a slower but convergent method having a larger convergence region can be applied, so that the constraint in eq.(2.23) is satisfied. For instance, the linear method *FIRST* in Prop.2.8 can be adopted. For a gaussian analysis window $g(t) = \frac{1}{\sqrt{2\pi\sigma^2}} e^{-\frac{1}{2}\frac{t^2}{\sigma^2}}$ and setting $\alpha = 1$ in eq.(2.19), it holds

Proposition 2.11. *The sequence*

$$\xi_{k+1} = \xi_k + sign(p_\xi(\xi_k)) \frac{1}{\sigma} \sqrt{1 - p(\xi_k)}, \quad k \geq 0 \tag{2.24}$$

linearly and monotonically converges to the ridge point $\xi_R = \phi'(u)$, with u fixed, $\forall \xi_0 : |\xi_0 - \xi_R| \leq \frac{2}{\sigma}$. Moreover, ξ_1 belongs to the convergence region of Method I.

Proof. Proof is in Appendix A. □

Method I implementation is sketched in Fig.2.9.

Even though Method I is fast, it requires the evaluation of spectrogram derivatives, that is unreliable in case of non-separable modes, as it depends on the unknown IFs. As expected, the experimental results will show that a direct estimation of the derivatives in the interfering case leads to significant numerical instabilities and wrong reallocations. This happens because the value of the spectrogram at the non-separability region does not correspond to the spectrogram of a single mode and the same holds true for its derivatives. A method not requiring functional evaluations is considerably convenient in order to both promote accuracy and to gain from the computational point of view. For this reason, by neglecting the error introduced by Taylor approximation, the forward finite differences is considered for $p_\xi(\xi)$ estimation, i.e. $p_\xi(\xi) = \frac{p(\xi+h)-p(\xi)}{h}$ and the following iterative procedure, referred as Method II, is proposed.

Proposition 2.12 (Method II)**.** *Let us consider $f(t) = a\cos\phi(t)$ and its normalized spectrogram $p(u,\xi)$, as in eq.(2.9). In addition, let us consider ξ_0 s.t. $\hat{g}''(\xi_0 - \xi_R) < 0$, with $\xi_R := \phi'(u)$, and let define $\varphi(\xi) = \xi + sign(p_\xi(\xi))\sqrt{\frac{1-p(\xi)}{|\hat{g}''(0)|}}$*

and the sequence

$$\xi_{k+1} = \xi_k + \alpha\, sign(p_\xi(\xi_k))\sqrt{\frac{p(\varphi(\xi_k)) - p(\xi_k)}{|\hat{g}''(0)|}}, \quad k \geq 0, \tag{2.25}$$

with $\alpha \in (0, 2\sqrt{1-\varphi'^2(\tau)})$, $\tau \in (\xi_0, \varphi(\xi_0))$. *Then the sequence* $\{\xi_k\}_k$ *converges to the ridge point* ξ_R.

Moreover, if $\alpha = \left(\frac{1}{\sqrt{2}} - \frac{1}{4}\right)^{-\frac{1}{2}}$ *the convergence is at least quadratic.*

Proof. Proof can be found in Appendix A. □

Method II is a predictor-corrector method only involving the function p while preserving fast convergence to ξ_R. Since Method I and II share the same convergence interval, even in this case, it is convenient to first apply few iterations of the linear method *FIRST* in eq.(2.24).

Method I and II consist of reassignment methods as, for each fixed u, they converge to the ridge point $\xi_R = \phi'(u)$. The reassigned spectrogram is formally given by eq.(2.13), where M is the adopted iterative method and $\xi_M(*)$ denotes the point obtained applying M using $*$ as initial point. It is worth observing that *FIRST*, Method I and II have the advantage to be pointwise, i.e. each point is moved independently of the others. Furthermore, Method II does not require any functional evaluation, resulting computationally advantageous and effective also in the non-separability region, as it will be shown in the experimental results.

2.3.2.1 Sensitivity to initial point in the non-separable case

Because of the lack of separability in the sense of Definition 11, the frequency shift given by Method II will be not accurate. More in details, given an initial point ξ_0, Method II consists of first computing $\omega_1 = \varphi(\xi_0)$ and then $\xi_1 = \xi_0 + \frac{\alpha sign(p_\xi(\xi_0))}{\sqrt{|\hat{g}''(0)|}}\sqrt{p(\omega_1) - p(\xi_0)}$. If the initial data is corrupted by interference, i.e. the observed spectrogram value is $\tilde{p}(\xi_0) = p(\xi_0) + \epsilon_0$, then, the method will produce the perturbed points $\tilde{\omega_1} = \omega_1 + \delta_1$ and $\tilde{\xi_1} = \xi_0 + \frac{\alpha sign(p_\xi(\xi_0))}{\sqrt{|\hat{g}''(0)|}}\sqrt{\tilde{p}(\tilde{\omega_1}) - \tilde{p}(\xi_0)}$. Let set $\epsilon_1 = \tilde{p}(\tilde{\omega_1}) - p(\tilde{\omega_1})$, then the following proposition provides a bound for the global error $|\tilde{\xi_1} - \xi_1|$.

Proposition 2.13. *Let consider a fixed* u *and let define* $p(\xi) := p(u, \xi)$ *the normalized spectrogram of the two-components signal* $f(t) = a_1 \cos\phi_1(t) + a_2 \cos\phi_2(t)$,

as in eq.(2.9). *The error in the first iteration of Method II satisfies*

$$|\tilde{\xi_1} - \xi_1| \leq \frac{\alpha^2}{|\hat{g}''(0)|} \frac{|\delta_1 p'(\tau_1) + \epsilon_1 - \epsilon_0|}{2|\xi_1 - \xi_0|}, \tag{2.26}$$

where ξ_0 *is the initial point,* ϵ_0 *denotes the initial error on the data,* $\tau_1 \in (\varphi(\xi_0), \varphi(\xi_0) + \delta_1)$, $|\delta_1| < \frac{\epsilon_0}{\Delta\omega}$ *and* $|\epsilon_1| \leq \frac{a_2}{a_1}(1 + |\phi_2'(u) - \phi_1'(u)| \cdot \max_\xi |\hat{g}'(\xi)|)$.

Proof. Proof can be found in Appendix A. □

It is important to notice that the error $|\tilde{\xi_1} - \xi_1|$ in eq.(2.26) can be zero even if ϵ_0, ϵ_1, and δ_1 are non zero, since the quantity $\delta_1 p'(\tau_1) + \epsilon_1 - \epsilon_0$ can sum up to zero. It means that, in principle, it is possible to achieve a compensation of the single errors and then a reduction of interference effects.

Convergence properties can be exploited in order to make Method II more stable in the non-separability region. More precisely, *FIRST* method in eq.(2.24) applied to points belonging to the separability region is expected to converge linearly and provide a growing sequence $p(\xi_k)$. In other words, if ξ_0, ξ_1 and ξ_2 respectively denote the initial point and the first two elements of the sequence in eq.(2.24), we expect $p(\xi_2) > p(\xi_1) > p(\xi_0)$ and $\frac{|\xi_2 - \xi_1|}{|\xi_1 - \xi_0|} < C$, where C is a constant depending on the convergence constant of the linear method in Prop.2.11. A different behaviour proves that the initial point belongs to the non-separability region. In this case, spectrogram values can be highly affected by interference and one iteration of Method II could result less precise. Hence, for the same reason leading to eq.(2.21), the adoption of a relaxed version of eq.(2.24) can be more efficient, i.e.

$$\xi_{k+1} = \xi_k + sign(p_\xi(\xi_k)) \left(1 - \frac{1}{\sqrt{2}}\right) \frac{1}{\sigma} \sqrt{1 - p(\xi_k)}, \quad k \geq 0. \tag{2.27}$$

The procedure described above will be referred as Improved Method II, whose implementation is sketched in Fig.2.10. As it will be shown in the experimental results, even in this case one iteration is sufficient to accurately recover IFs curves.

2.3.3 Computational Complexity

This section provides the number of operations per pixel required by the reassignment methods *FIRST_K* and Method II, presented in the previous sections.

Input: MCS $f(t)$
Output: Reassigned spectrogram $\hat{p}(u,\xi)$
compute the STFT and the normalized spectrogram p as in eq.(2.9)
initialize $\hat{p}$
select all (u,ξ) such that $p(u,\xi) \in [0.2, 0.5]$
set $niter = 9$;
for *all selected* u **do**
  for *all selected* ξ **do**
    compute 1 iteration of the method in eq.(2.24)$\rightarrow \xi_0$;
    compute $niter$ iterations according to eq.(2.22) and using ξ_0 as initial point$\rightarrow \bar{\xi}$;
  end
  let $\xi_M(\xi) = \bar{\xi}$
  for *all selected* ξ **do**
    reallocate ξ to $\xi_M(\xi)$, i.e. set $\hat{p}(u, \xi_M(\xi)) = \hat{p}(u, \xi_M(\xi)) + p(u,\xi)$
  end
end

Figure 2.9: Pseudocode of the algorithm implementing Method I.

Only multiplications, divisions, and comparisons will be considered. The estimated complexity is then compared with the one required by the standard RM in [59]. To this aim we will focus on the number of operations required by the computation of the centroid for each TF point in eq.(1.25), as it represents the actual difference with respect to the standard method. Let us consider eq.(2.20) (*FIRST_K*).

L denotes the signal length, $L \times F$ is the TF dimension of the STFT, N is the number of adopted iterations, $p(u,\xi)$ the normalized spectrogram as in eq.(2.9) and we consider the sets

$$\Omega = \bigcup_{0.1 \leq \Theta \leq 0.5} \Omega_\Theta, \quad \text{with} \quad \Omega_\Theta = \{(u,\xi) : \xi = argmin_\xi \, (p(u,\xi) = \Theta)\} \tag{2.28}$$

and

$$\Omega' = \bigcup_{0.2 \leq \Theta \leq 0.5} \Omega_\Theta, \quad \text{with} \quad \Omega_\Theta = \{(u,\xi) : \xi = argmin_\xi \, (p(u,\xi) = \Theta)\} \subset \Omega. \tag{2.29}$$

According to this notation, the following proposition holds true.

Proposition 2.14. FIRST_K *and* Improved Method II *are computationally*

Input: MCS $f(t)$
Output: Reassigned spectrogram $\hat{p}(u, \xi)$

compute the STFT and the normalized spectrogram p as in eq.(2.9)
initialize $\hat{p}$
select all (u, ξ) such that $p(u, \xi) \in [0.2, 0.5]$
for *all selected* u **do**
    for *all selected* ξ **do**
        set $\mu = sign(p_\xi(\xi))$;
        set $\xi_0 = \xi$;
        compute 2 iterations of the method in eq.(2.24) $\rightarrow \xi_1, \xi_2$;
        set $\Delta\xi = |\xi_1 - \xi|$ and $\Delta\xi_2 = |\xi_2 - \xi_1|$;
        if NOT$((p(\xi_1) > p(\xi)) \,\&\, ((p(\xi_2) > p(\xi_1)) \,\&\, (\Delta\xi_2/\Delta\xi < C))$
            compute 2 iterations of eq.(2.27) using ξ_0 as initial point $\rightarrow \bar{\xi}$;
        else
            compute 1 iteration of the method in eq.(2.25) using ξ_1 as inital point $\rightarrow \bar{\xi}$;
        end
    end
    let $\xi_M(\xi) = \bar{\xi}$
    for *all selected* ξ **do**
        reallocate ξ to $\xi_M(\xi)$, i.e. set $\hat{p}(u, \xi_M(\xi)) = \hat{p}(u, \xi_M(\xi)) + p(u, \xi)$
    end
end

Figure 2.10: Pseudocode of the algorithm implementing improved Method II.

more convenient than RM if

$$\frac{|\Omega|}{F} < \frac{5 + 3log_2(F)}{N + \beta} L. \tag{2.30}$$

Proof. The estimation of the frequency shifts using *FIRST_K* requires:

- the computation of one STFT, i.e., $(2\,F\,log_2(F) + F)$ for each signal sample;
- $F\,log_2(F)$ comparisons of each u for the construction of the set Ω;
- 1 multiplication for each iteration and each point in the TF domain belonging to the set Ω and 1 square root for the first iteration.

Hence, *FIRST_K* requires $C_{proposed} = |\Omega|N + |\Omega|\beta + (2\,F\,log_2(F) + F)L + L\,F\,log_2(F)$ operations, where β is the number of operations required for the computation of the square root.

In RM, the estimation of the centroids requires:

- 2 multiplications and 1 division for each equation in eq.(1.25) each point in the TF domain;
- the computation of three STFTs, i.e., $3(2\,F\,log_2(F) + F)$ for each signal sample.

Hence, the standard reassignment requires $C_{stdreass} = 3LF + 3(2\,F\,log_2(F) + F)L$ operations.

As a result, *FIRST_K* is computationally advantageous with respect to RM if

$$|\Omega|N + |\Omega|\beta + (2Flog_2(F) + F)L + LFlog_2(F) < 3LF + 3(2Flog_2(F) + F)L.$$

By dividing both members by LF, we get the relation in terms of operations per pixel (spectrogram image), i.e.,

$$\frac{(N+\beta)|\Omega|}{LF} + (3log_2(F) + 1) < 3 + 3(2log_2(F) + 1),$$

and then eq.(2.30) holds true.

With regard to Improved Method II, the computation of the frequency shift requires

- the computation of one STFT, i.e., $(2\,F\,log_2(F) + F)$ for each signal sample;
- $F\,log_2(F)$ comparisons of each u for the construction of the set Ω';
- two iterations of *FIRST* in eq.(2.24), i.e. 2 multiplications for each point in the TF domain belonging to the set Ω' and 2 square roots
- 1 division and three comparisons to check the sequence behaviour for each point in Ω'
- two iterations of *FIRST* in eq.(2.27) or 1 iteration according to eq.(2.25), that in both cases require 2 multiplications and 2 square roots for each TF point in Ω'

Therefore, the improved Method II requires

$$C_{improved} = 5|\Omega'| + 4|\Omega'|\beta + (2\,F\,log_2(F) + F)L + L\,F\,log_2(F)$$

operations, where β is the number of operations required for the computation of the square root. By observing $|\Omega'| \leq |\Omega|$, the same argument used for *FIRST_K* implies that Improved Method II is computationally advantageous with respect to RM. □

It is worth observing that $|\Omega| \leq |\Delta\omega| \leq F$, where $|\Delta\omega|$ is the support of the analysis window in the frequency domain. By replacing in eq(2.30), it turns out that *FIRST_K* and Improved Method II are computationally convenient if

$$\frac{5 + 3log_2(F)}{N + \beta} L > 1 \Leftrightarrow (N + \beta) < (5 + 3log_2(F))L. \tag{2.31}$$

Remark 9. *By considering that $F \leq L$, $\beta = 16$ and $N \leq 4$, eq.(2.31) always holds for non-trivial signal lengths. In addition, $(N + \beta) << (5 + 3log_2(F))L$, for $L \geq 512$, which represents a standard signal length.*

2.3.4 Experimental results

The iterative reassignment methods presented in this chapter have been tested on several synthetic MCS signals having different IF functions. In particular, chirp signals having polynomial phases have been considered, as they well model many real-life signals, such as radar signals with Doppler modulation that are used to reveal information concerning human motion in video surveillance. For instance, the problem of human gait classification is addressed in [11], where the motion of a single target (human or object to detect/track) is captured by a Doppler radar. The received signal is modelled as

$$r(t) = A\cos\left(2\pi f\left(t - \frac{2R(t)}{c}\right)\right),$$

where A and f respectively denote a reflection and a frequency coefficient, c is the speed of light and $R(t)$ is the position of the moving target with respect to the receiver. In this context, IF represents the velocity of the moving target. In a more realistic scenario, multiple targets can be present in a scene, i.e. a MCS has to be analyzed, and separation of the signal components is necessary, as in [10].

Linear combinations of the following modes have been considered

$$g_1(t) = \cos\left(n\frac{\pi}{3}(t-1)^2 + 300(t-1)\right),\ g_2(t) = \cos\left(n\frac{\pi}{3}0.49(t-1)^3 + 500(t-1)\right),$$
$$t \in [0,2],$$
$$g_3(t) = \cos\left(n\frac{\pi}{3}t^2 + \pi t + 5\right),\ g_4(t) = \cos\left(n\frac{0.7\pi}{3}(1-t)^3\right),\ t \in [0,1]$$
$$f_1(t) = \sin\left(n\pi 0.6808t\right),\ f_2(t) = \sin\left(n\pi\frac{\pi}{4}(1-t)^2\right),\ t \in [0,1]$$
$$f_3(t) = \cos\left(n\frac{\pi}{3}(1-t)^3\right),\ f_4(t) = \sin\left(n\frac{\pi}{3}(1-t)^2\right),\ t \in [0,1], \tag{2.32}$$

where $n = 512$ and $\frac{1}{n}$ is the sampling frequency.

A gaussian window function with length $s = 44$ and $\sigma = \frac{s-1}{10\pi}$ has been used for STFT computation in all tests. The results have been directly compared to standard RM to appreciate and evaluate the step forward provided by the proposed approach in terms of improved spectrogram readability and computational gain.

FIRST. In all tests, TF points belonging to the set Ω defined in eq.(2.28) and depicted in Fig.2.4(d) have been considered—the left bound is aimed at preventing eventual distortions due to numerical approximations in the computation of the spectrogram; the right bound has been fixed to meet the condition in eq.(2.8).

The first test is oriented to evaluate the reassignment result in the case of a two components signal $g_3 + g_4$ defined in eq.(2.32) and shown in Fig.2.1, where only points satisfying condition in eq.(2.8) are considered. Results are shown in Fig.2.11. As it can be observed, the two results are the same whenever the two modes satisfy the separability condition; on the contrary, in the interference region, the selection of a reduced number of points, i.e., the ones satisfying the WSC in Definition 11, allows for a considerable reduction of the region where RM fails in the separation of the two modes.

The second test aims at evaluating the reassigned distribution obtained using *FIRST*. Figs.2.12 and 2.13 depict the results for the signals $g_1 + g_2$ and $g_3 + g_4$ defined in eq.(2.32). Reassignment results using an increasing number of iterations have been shown using $\alpha = 2$. As it can be observed, the method approaches the solution after very few iterations. The same figures show reassigned distributions obtained by applying two iterations of *FIRST*, where the value of the normalized spectrogram p is used at each iteration. As it can be

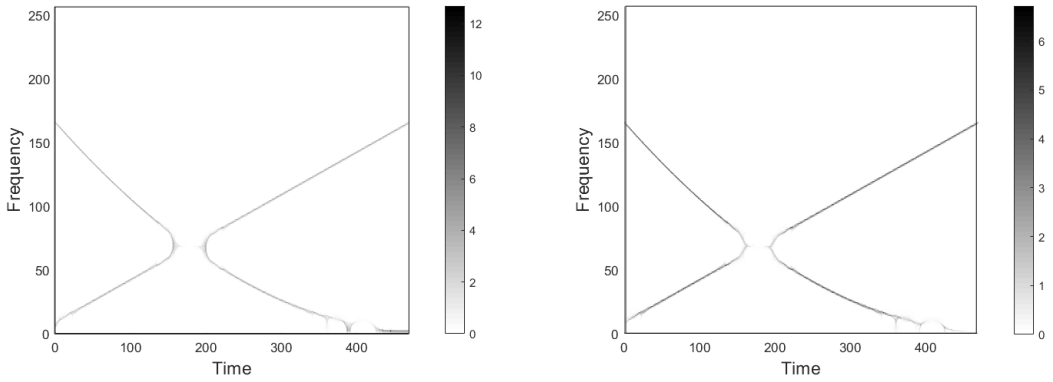

(a) (b)

Figure 2.11: (a) Reassigned spectrogram of the two-components signal in Fig.2.1(a) using the standard RM, i.e. the algorithm computing TF shifts according to eq.(1.25); (b) Reassigned spectrogram of the same signal: only TF points in Ω, as in eq.(2.28) have been considered—the not reassigned region reduces of nearly 30% [98].

observed, *FIRST* has a fast convergence to the ridge curve in correspondence to separable regions; in addition, the method is able to reassign correctly even in the interference region, except for a small region close to the intersection point, i.e., the one where the weak separability condition is not satisfied. The same considerations are valid whenever *FIRST_K* is used. In this case, one iteration allows us to reach the final solution and to provide better results in the interference region and for points very close to modes intersection. Even though reassignment is not correct for these points, estimated reassignment locations are closer to the correct ones with respect to the ones provided by *FIRST*. The main reason is the fact that *FIRST_K* is not influenced by incorrect spectrogram values since it does not employ those values except for the initial point. It is also worth observing that *FIRST_K* is less accurate than *FIRST* in correspondence to interference region since the sequence in eq.(2.20) converges but its limit is not the ridge point of the signal mode. Results do not change if *FIRST_K* is used by setting $K = 1 - \frac{1}{\sqrt{2}}$, independently of the adopted analysis window. However, in this case the sequence converges to a point which can be closer to the ridge point.

Fig.2.14 shows reassignment results provided by the proposed iterative procedure for the spectrogram in Fig.2.12(a) and 2.13(a) where the number of iterations N has been adaptively estimated for value of $p(u, \xi)$ and requiring

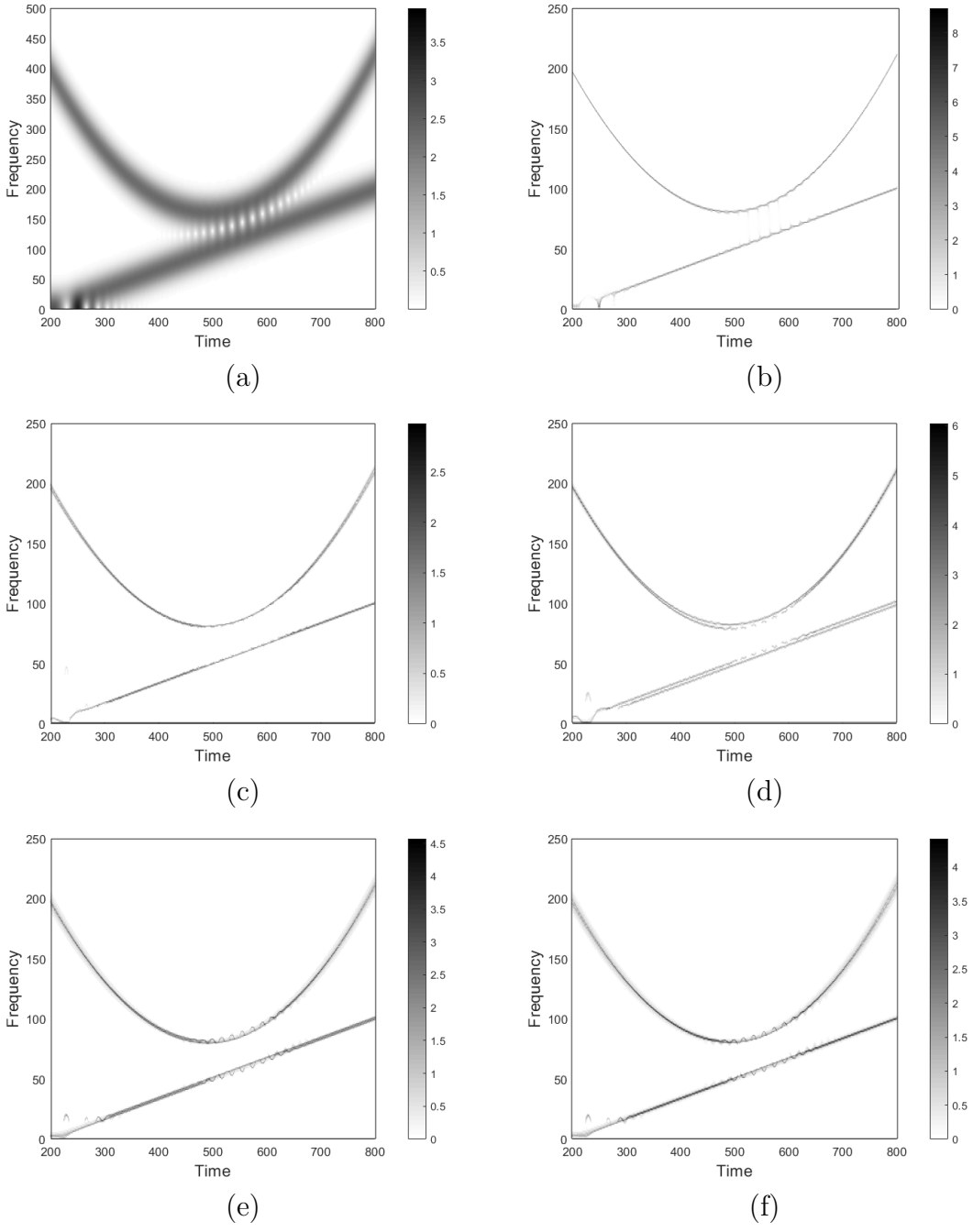

Figure 2.12: Well separated components. (a) Spectrogram; (b) Standard reassigned spectrogram; (c) Reassigned spectrogram using 4 iterations of *FIRST*; (d) Reassigned spectrogram using two iterations of *FIRST*; (e) Reassigned spectrogram using one iteration of *FIRST_K*; (f) Reassigned spectrogram using two iterations of *FIRST_K* with $K = 1 - \frac{1}{\sqrt{2}}$. Reassignment results provided by the proposed method are equivalent to the standard reassignment one since the separability condition is satisfied [98].

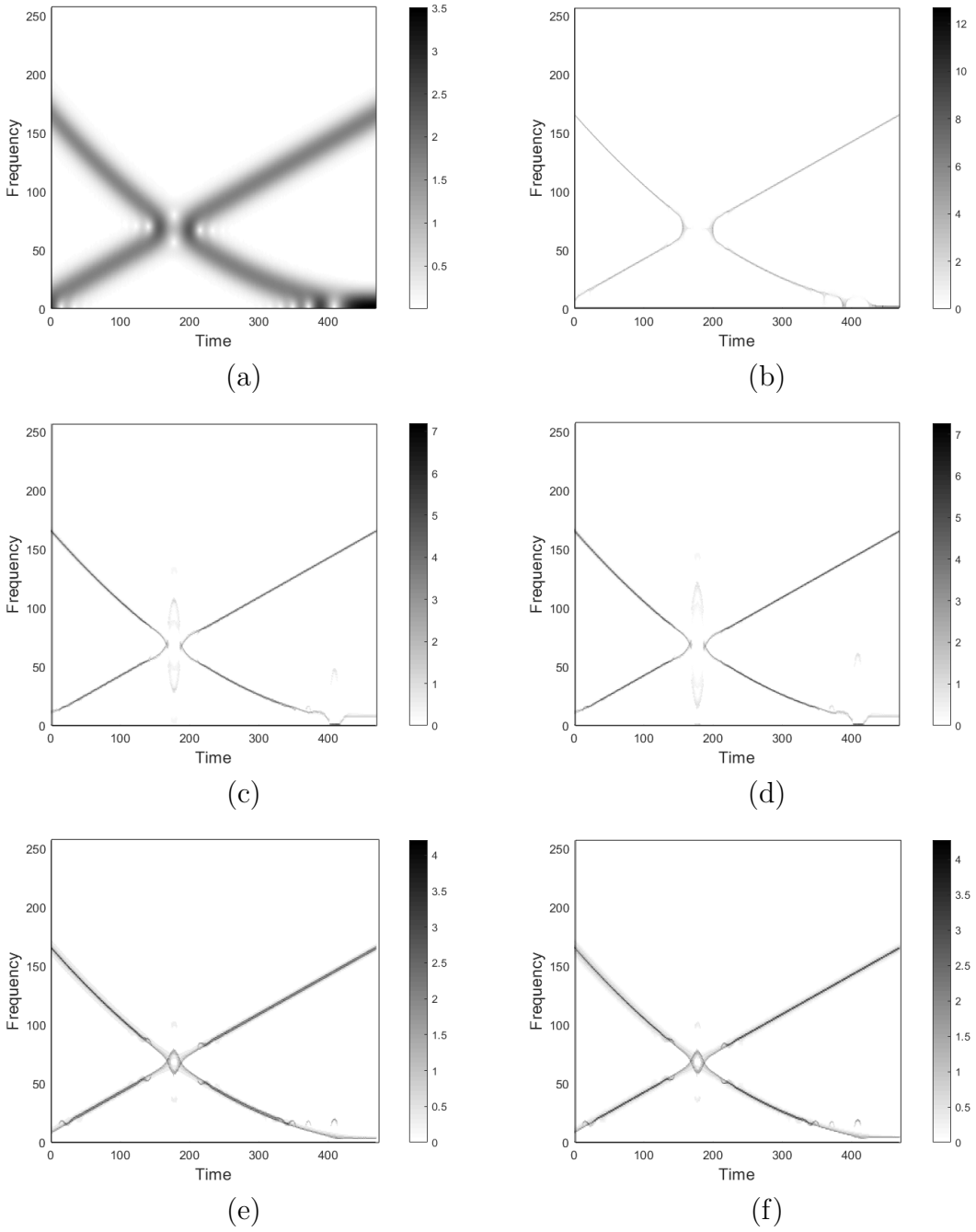

Figure 2.13: Non-separable components. (a) Spectrogram; (b) Standard reassigned spectrogram; (c) Reassigned spectrogram using 4 iterations of *FIRST*—the region of incorrect or missing reassignment is smaller than the one of standard reassignment (about 50%); (d) Reassigned spectrogram using two iterations of *FIRST*—reassignment result does not change within the adopted frequency sampling step; (e) Reassigned spectrogram using one iteration of *FIRST_K*—reassignment result is comparable to the one in (c,d); (f) Reassigned spectrogram using two iterations of *FIRST_K* with $K = 1 - \frac{1}{\sqrt{2}}$—reassignment result is comparable to the one in (d,e) [98].

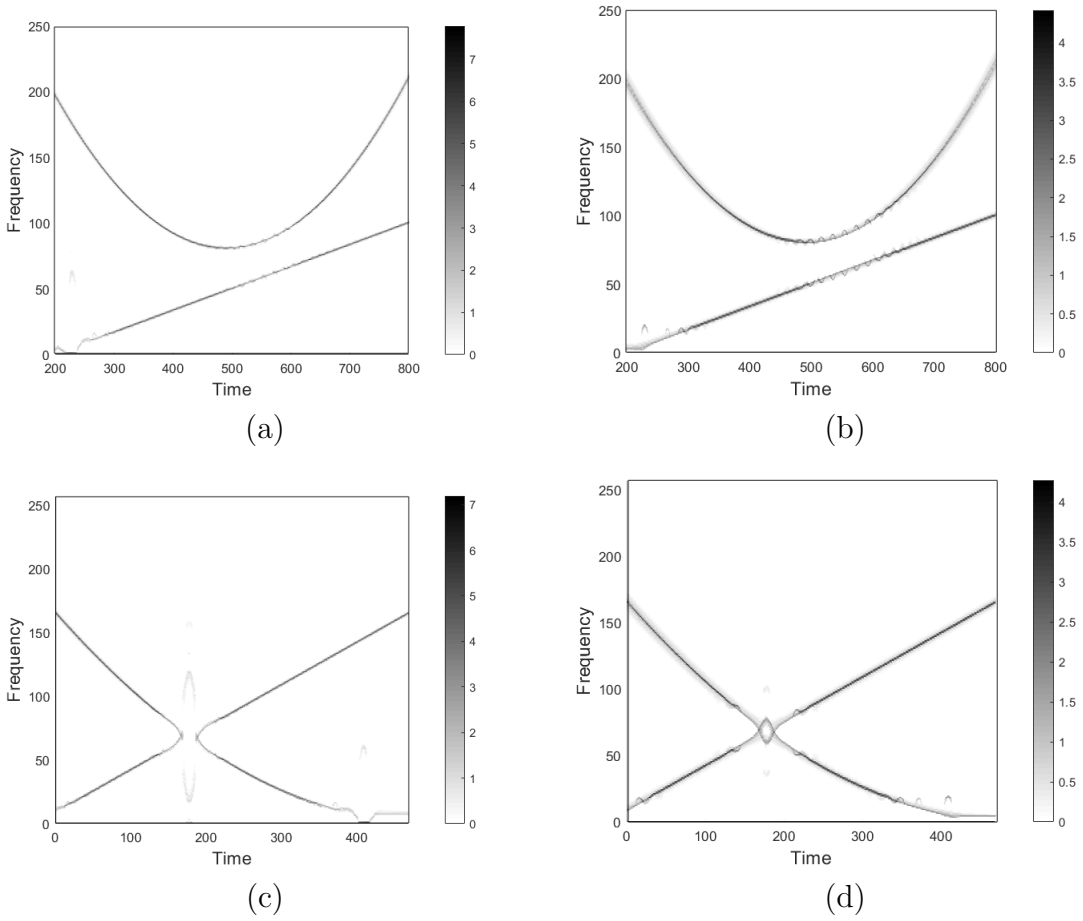

Figure 2.14: (a) Reassigned spectrogram referred to Fig.2.12(a) using *FIRST*, where the number of iterations depends on the value of the spectrogram at the initial point; (b) Reassigned spectrogram of the same signal using *FIRST_K*; (c) Reassigned spectrogram referred to Fig.2.13(a) using *FIRST*, where the number of iterations depends on the value of the spectrogram at the initial point; (d) Reassigned spectrogram of the same signal using *FIRST_K*. As it can be observed, except for the central part, points in the interference regions are correctly reassigned even by *FIRST_K*, which is a less refined iterative method [98].

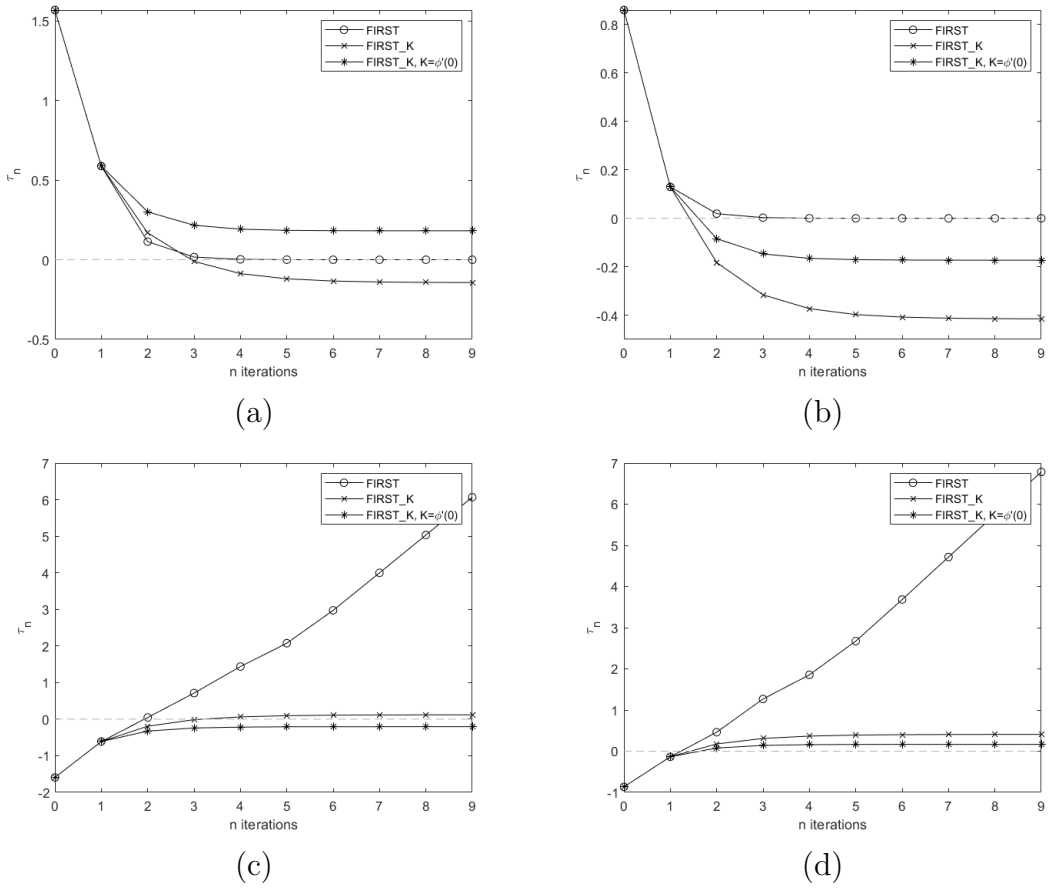

Figure 2.15: (a) Convergence of the sequence τ_n for the spectrogram in Fig.2.12(a): τ_0: $\Theta = 0.10$; (b) Convergence of the sequence τ_n for the spectrogram in Fig.2.13(a): τ_0: $\Theta = 0.10$. For fixed u, all points satisfy WSC as in Definition 11—*FIRST_K* converges to a point close to the ridge; *FIRST* correctly converges to the ridge; (c) Convergence of the sequence τ_n for the spectrogram in Fig.2.12(a): τ_0: $\Theta = 0.50$; (d) Convergence of the sequence τ_n for the signal in Fig.2.13(a): τ_0: $\Theta = 0.50$. For a fixed u, not all points satisfy the separability condition as in Definition 11. In this case, *FIRST* does not converge to the ridge since $Q(u, \xi_n)$ values are not correct in the interference region; on the contrary, *FIRST_K* still converges close to the ridge as it does not depend on values in the interference region, except for the initial point [98].

a tolerance ε corresponding to the discretization step of the frequency axis adopted in the numerical computation of the STFT, i.e., $N = \left\lceil \frac{log\left(\frac{(1-K)\varepsilon}{\Delta\tau_1}\right)}{log(K)} \right\rceil$. As it can be observed, the use of a different number of iterations for points with a different spectrogram value, allows us to correctly reassign points outside and inside the interference region. The same figure shows the reassignment result which has been obtained using one iteration of the sequence in eq.(2.20); results are almost equivalent, making *FIRST_K* a robust and computable version of *FIRST* in the case of lack of both weak and strong separability condition.

Fig.2.15 depicts the convergence rate for two different points in the spectrogram ($\Theta = 0.10$ and $\Theta = 0.50$—see eq. (2.28)). As it can be observed, for the signal with two separated modes, the proposed method is able to correctly reassign each point since the value of the spectrogram at τ_0 is exact. For the signal with two non-separated modes, the convergence is slightly altered (especially for points closer to the ridge, i.e., the ones for which the separability condition does not hold). It is due to the error on the spectrogram value caused by the interference of the two modes. In this case, *FIRST_K* provides a more robust solution since it only depends on the analysis window while it does not depend on the value of the spectrogram except for the initial point.

Finally, it is worth underlying that *FIRST_K* is more computationally efficient than the standard reassignment as it just requires the computation of one spectrogram; in addition, for points with the same spectrogram value, the sequence τ_n in eq.(2.20) is the same—this allows us to drastically reduce the number of operations and the computing time.

Improved iterative reassignment. TF points belonging to the set Ω' defined in eq.(2.28), with $\Theta \in [0.2, 0.5]$, have been employed for Method I and II application. The lower bound of Ω' is chosen to meet the convergence condition of the methods. It is worth observing that, for a gaussian analysis window with variance σ^2, eq.(2.23) holds true $\forall\, \xi : |\xi - \xi_R| < 1/\sigma$, i.e. $p > 0.6$. The latter represents a criterion for the selection of the initial point ξ_0 and it also allows us to determine the number of iterations that guarantees a prefixed accuracy $\epsilon > 0$ [102], i.e.

$$j = \left\lceil \frac{\log(\frac{2(1-Q)\epsilon}{\sigma})}{\log(Q)} \right\rceil, \text{ where } Q = 1 - p(\xi).$$

In the numerical tests ϵ has been fixed equal to the discretization frequency

step, i.e. 0.041, so that $j = 9$. Results are compared to the standard reassigned spectrogram given by RM in [59].

Figs. 2.16–2.18 show that standard RM and Method I give equivalent results if applied to monocomponent signal, as well as to MCS in regions where the separability condition holds.

For MCS, (Figs.2.17–2.18), TF points at the interference region are misallocated by both methods: RM is subjected to the limitation of window sensitivity, while Method I strongly depends on spectrogram values, which can be highly deviated due to interference. Nevertheless, Method I is able to separate the single components for a larger set of points, as proven in Figs.2.17(e)-(f). The eventual oscillations at the beginning (or at the end) of TF representation are due to boundary effects in STFT numerical computation.

Figs.2.19–2.25 refer to Method II. We further stress that it does not require any functional evaluations, expect for the sign of spectrogram derivative. In order to prevent numerical instabilities, the latter is assumed to be constant and equal to the one of the point to be reassigned. The initial point ξ_0 is selected as for Method I. As Fig.2.19 shows, whenever the separability condition is satisfied, convergence to the ridge points is guaranteed after very few iterations. As expected, results of Method II are comparable to standard RM whenever the separability condition is satisfied — see Figs.2.20–2.24. Conversely, as depicted in Fig.2.21(b), Method II successfully reallocates TF points on the two ridge curves in the non-separability region, although some numerical and negligible instabilities. Furthermore, it is important to notice that Method II greatly improves and corrects the result given by the linear method *FIRST_K*, as shown in Fig.2.22.

It is worth observing that in case of constructive interference, as in Fig.2.23(b), reassignment is less accurate, even though better than RM. In fact, in this case the assumption of derivative with constant sign should be weakened. Finally, results provided by Method II do not change in case of higher number of signal components (see Fig.2.24), while Fig.2.25 gives evidence of the robustness to the analysis window size.

2.3.4.1 Quantitative performance evaluation

The accuracy of Method I and II and the quality of the corresponding reassigned spectrograms in terms of concentration property are evaluated by means of

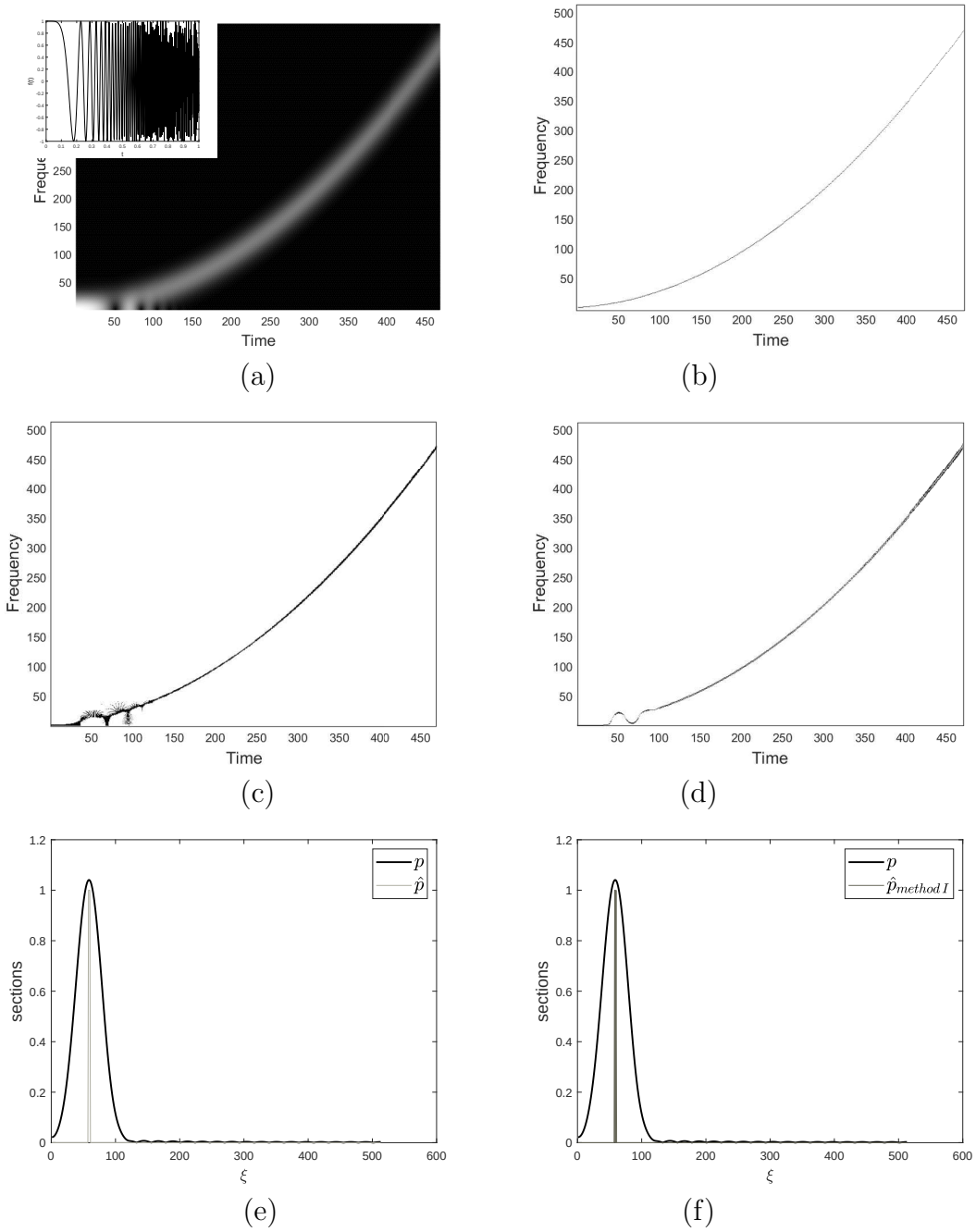

Figure 2.16: (a) Quadratic chirp f_3 in eq.(2.32) and spectrogram; (b) Ideal TF representation perfectly localized on the ridge curve; (c) Standard reassigned spectrogram; (d) Reassigned spectrogram using Method I; (e) Normalized section of the standard reassigned spectrogram in (c) at time $u = 150$; (f) Normalized section of the reassigned spectrogram in (d) at time $u = 150$ [100]
.

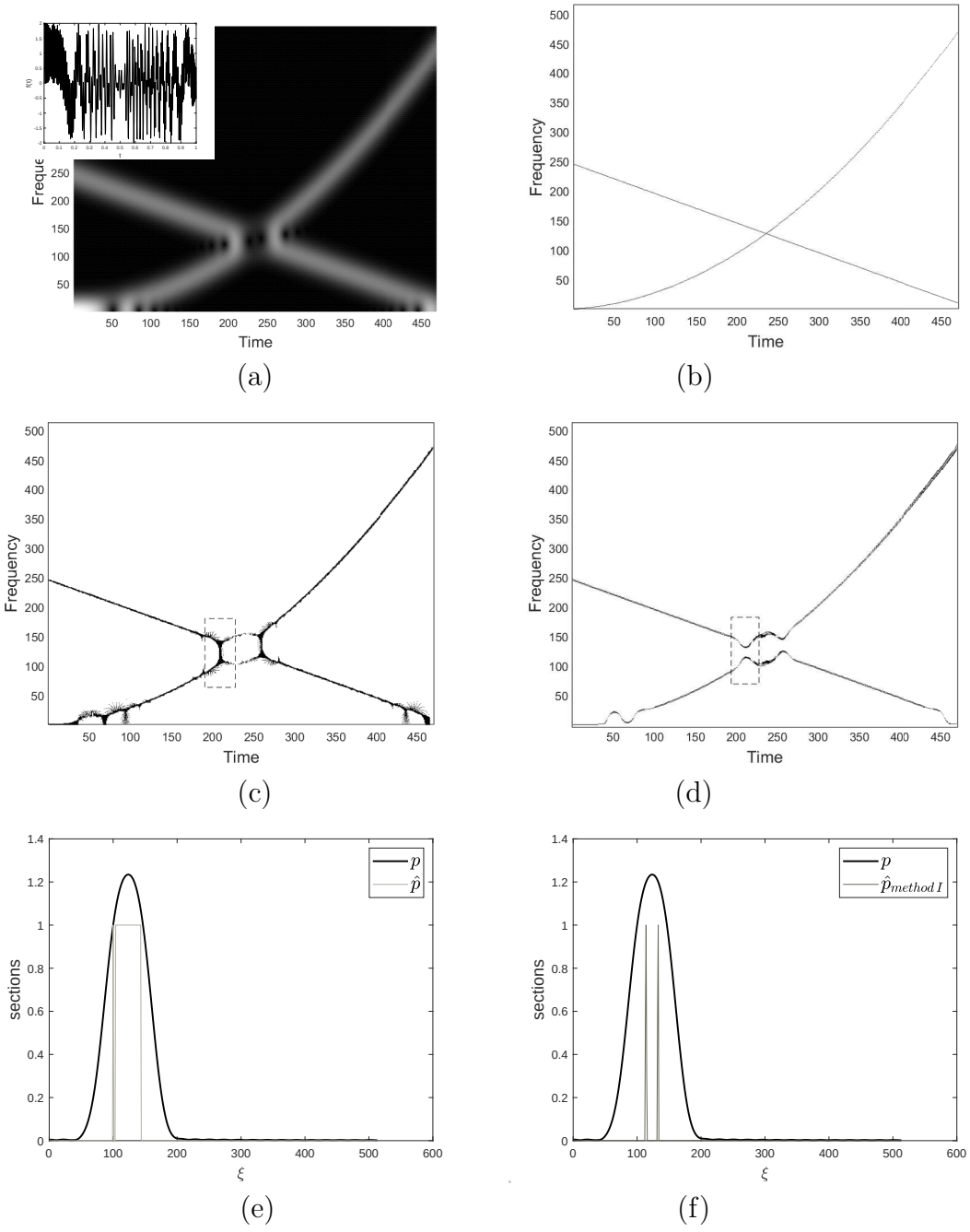

Figure 2.17: (a) Sum of the quadratic and the linear chirps in eq.(2.32), $f = f_3 + f_2$ and spectrogram; (b) Ideal TF representation perfectly localized on the ridge curves; (c) Standard reassigned spectrogram. Ridge curves are not disclosed in the region emphasized by the dashed rectangle; (d) Reassigned spectrogram using Method I. Ridge curves are separated in the region emphasized by the dashed rectangle; (e) Normalized section of the standard reassigned spectrogram in (c) at time $u = 210$; (f) Normalized section of the reassigned spectrogram in (d) at time $u = 210$ [100].

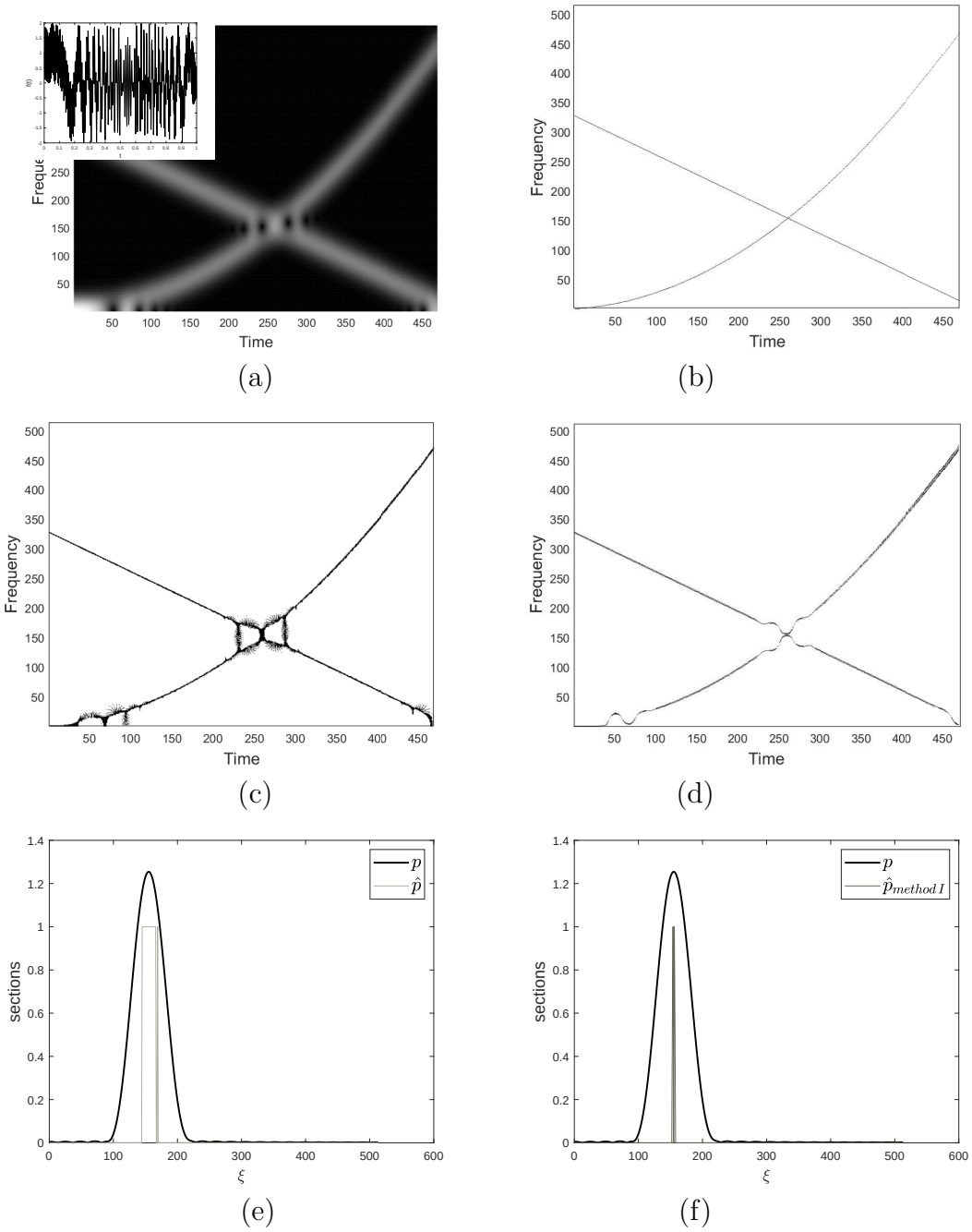

Figure 2.18: (a) Sum of the quadratic and the linear chirps in eq.(2.32), $f = f_3 + f_4$ and spectrogram; (b) Ideal TF representation perfectly localized on the ridge curves; (c) Standard reassigned spectrogram; (d) Reassigned spectrogram using Method I; (e) Normalized section of the standard reassigned spectrogram in (c) at time $u = 260$; (f) Normalized section of the reassigned spectrogram in (d) at time $u = 260$ [100].

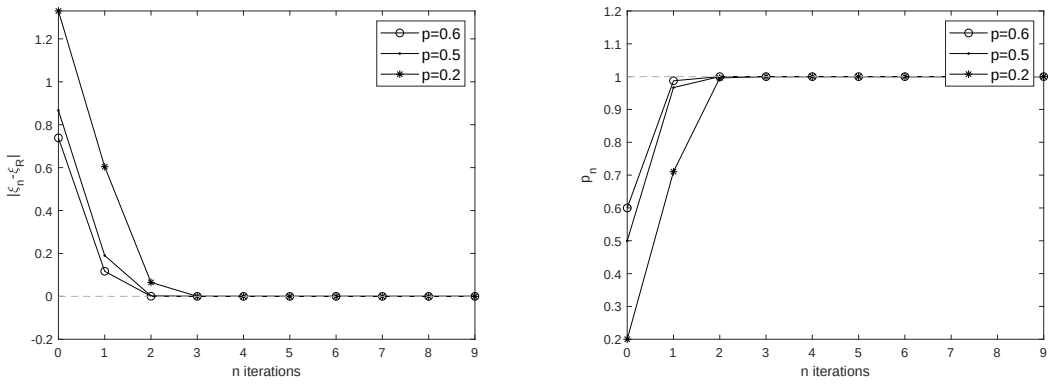

(a) (b)

Figure 2.19: Convergence of Method II in regions where the separability condition, as in Def.6, holds. Characteristic curves at rate $p = 0.2$, $p = 0.5$ and $p = 0.6$ have been selected. (a) Error; (b) Sequence of rates $p(\xi_n)$. The error rapidly goes to zero and the rate of points given by eq.(2.25) reaches one [100].

Normalized Energy (NE) and Earth mover's distance [4, 103]. NE measures the sharpness of the representation, while Earth mover's distance enables to deliver the accuracy of the localization of the ridges of each single mode. More precisely, NE is computed as the cumulative sum of the sorted coefficients of the representation. The faster its growth towards 1, the sharper the representation [4]. Fig.2.26 depicts NE for the presented experimental results. In all cases, Method I provides very concentrated representations, while NE of Method II presents a slower growth with respect to RM in the first part but it reaches the global energy earlier, especially in case of MCS.

Earth mover's distance enables to compare two probability measures defined on the same set, providing the amount of "work" needed to "deform" one into the other [103]. In mathematics, Earth mover's distance is referred as the Wasserstein distance (WD) [104] and it is formally defined as follows.

Definition 13. *Given a complete and separable metric space $(\mathcal{X}, \mathcal{D})$, the WD between two probability distributions q_1, q_2 over $\mathcal{X}$ is defined as*

$$W(q_1, q_2) = \inf_{\gamma \in \Gamma(q_1, q_2)} \int_{\Omega} \mathcal{D}(x, y) d\gamma(x, y),$$

where $\Gamma(q_1, q_2)$ is the set of all joint distributions having marginals q_1 and q_2.

An explicit formula for WD can be derived if $\mathcal{X} = \mathbb{R}$ with the euclidean

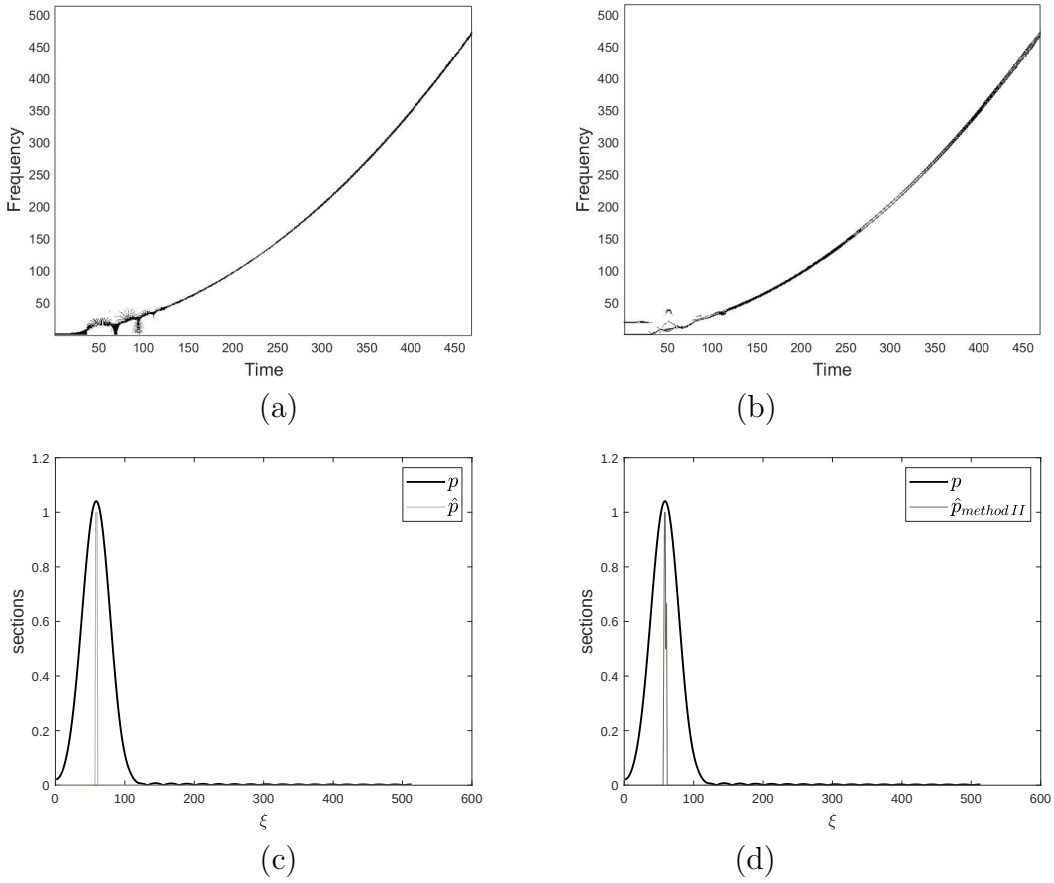

Figure 2.20: (a) Standard reassigned spectrogram of the quadratic chirp in Fig.2.16(a); (b) Reassigned spectrogram using Method II; (c) Normalized section of the reassigned spectrogram in (a) at time $u = 150$; (d) Normalized section of the reassigned spectrogram in (b) at time $u = 150$ [100].

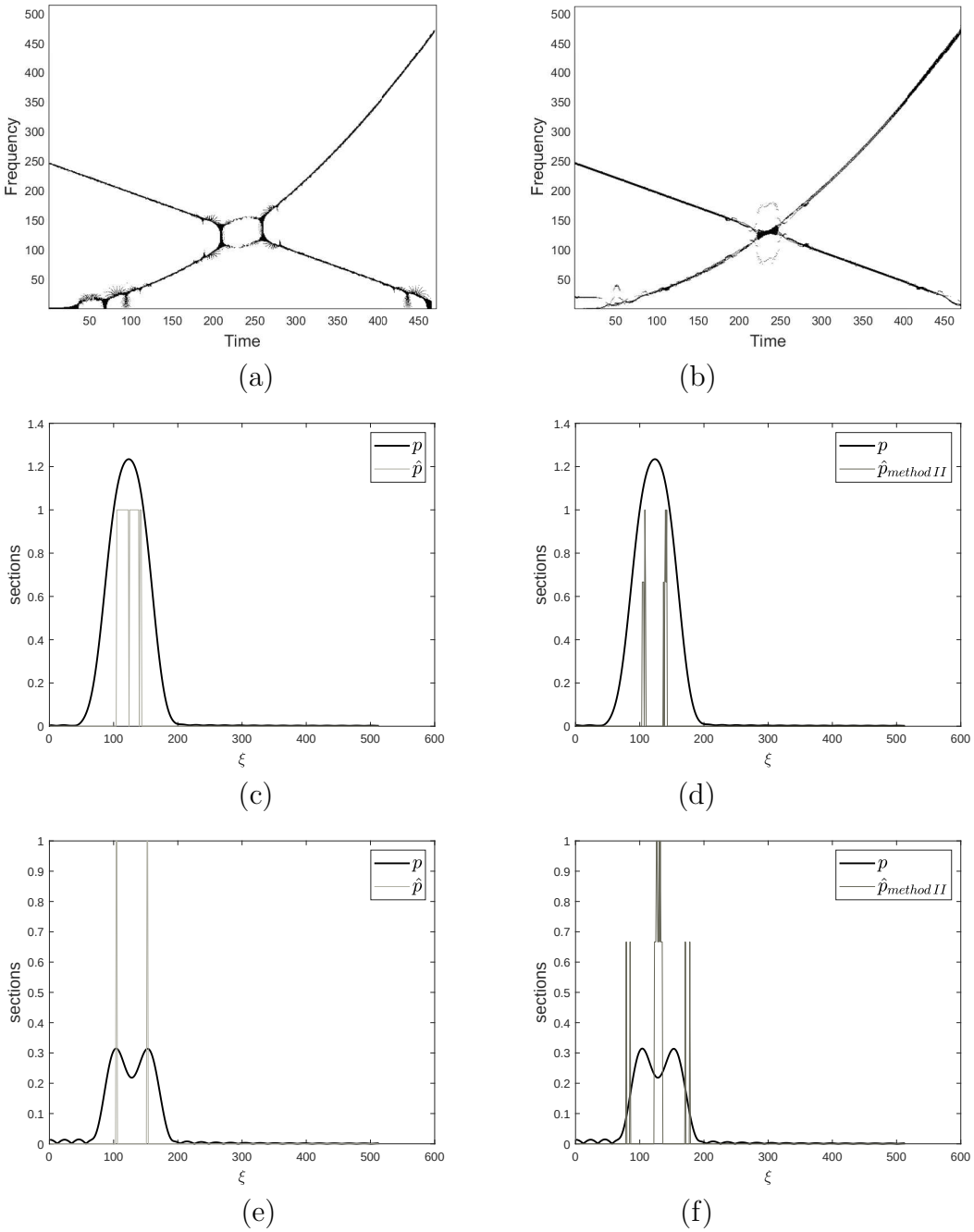

Figure 2.21: (a) Standard reassigned spectrogram of the signal $f = f_3 + f_2$ in Fig.2.17(a); (b) Reassigned spectrogram using Improved Method II; (c)-(e) Normalized section of the standard reassigned spectrogram in (a) at time $u = 210$ (c) and $u = 234$ (e); (d)-(f) Normalized section of the reassigned spectrogram in (b) at time $u = 210$ (d) and $u = 234$ (f) [100].

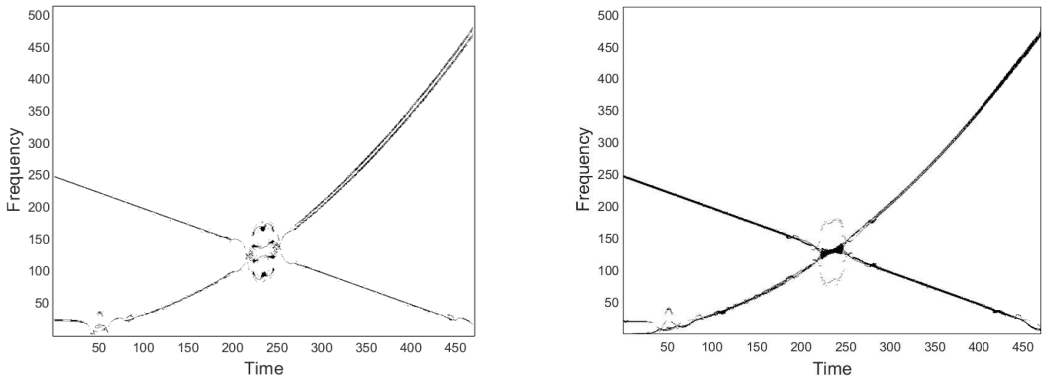

(a) (b)

Figure 2.22: (a) Reassigned spectrogram of the signal $f = f_3 + f_2$ in Fig.2.17(a) given by *FIRST*; (b) Reassigned spectrogram using Method II.

distance $\mathcal{D}(x, y) = |x - y|$, so that

$$W(q_1, q_2) = \int_{\mathbb{R}} |F_{q_1}(y) - F_{q_2}(y)| dy, \tag{2.33}$$

where F_* denotes the cumulative distribution function of $*$. A comprehensive discussion concerning WD can be found in [104, 105].

Following the same approach adopted in [103], Earth mover's distance is computed by first considering the WD between the considered TF representation and the ideal one—i.e. the one perfectly localized on the ridge curves—for each fixed $u \in [0, U]$ and then by taking the mean value over u. Without loss of generality, let us consider the ideal TF representation of a single mode, i.e. $\rho_1 = \delta(\xi - \phi'(u))$ and let denote by ρ_2 the reassigned distribution. Then, the corresponding probability densities are given by

$$q_i(u, \xi) = \frac{\rho_i(u, \xi)}{\int_0^{+\infty} \rho_i(u, \xi)\, d\xi}, \; i = 1, 2,$$

whose cumulative distributions are

$$F_{q_i}(u, \xi) = \int_0^{\xi} q_i(u, \omega)\, d\omega, \; i = 1, 2,$$

so that Earth mover's distance is computed as

$$\mathcal{EMD}(q_1, q_2) = \frac{1}{U} \int_0^U \int_0^{+\infty} |F_{q_1}(u, \xi) - F_{q_2}(u, \xi)|\, d\xi\, du.$$

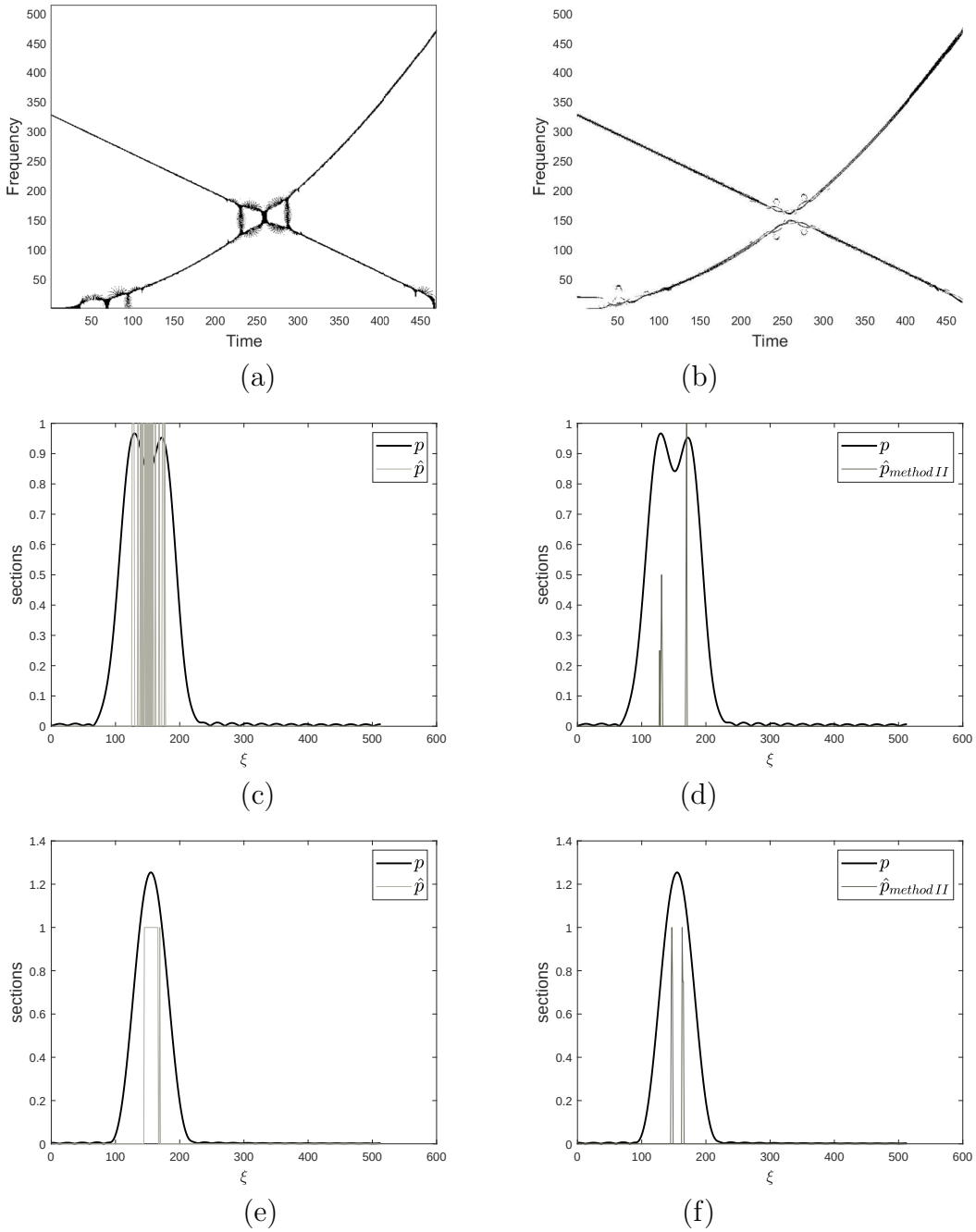

Figure 2.23: (a) Standard reassigned spectrogram of the signal $f = f_4 + f_3$ in Fig.2.18(a); (b) Reassigned spectrogram using Improved Method II; (c)-(e) Normalized section of the standard reassigned spectrogram in (a) at time $u = 234$ (c) and $u = 260$ (e); (d)-(f) Normalized section of the reassigned spectrogram in (b) at time $u = 234$ (d) and $u = 260$ (f) [100].

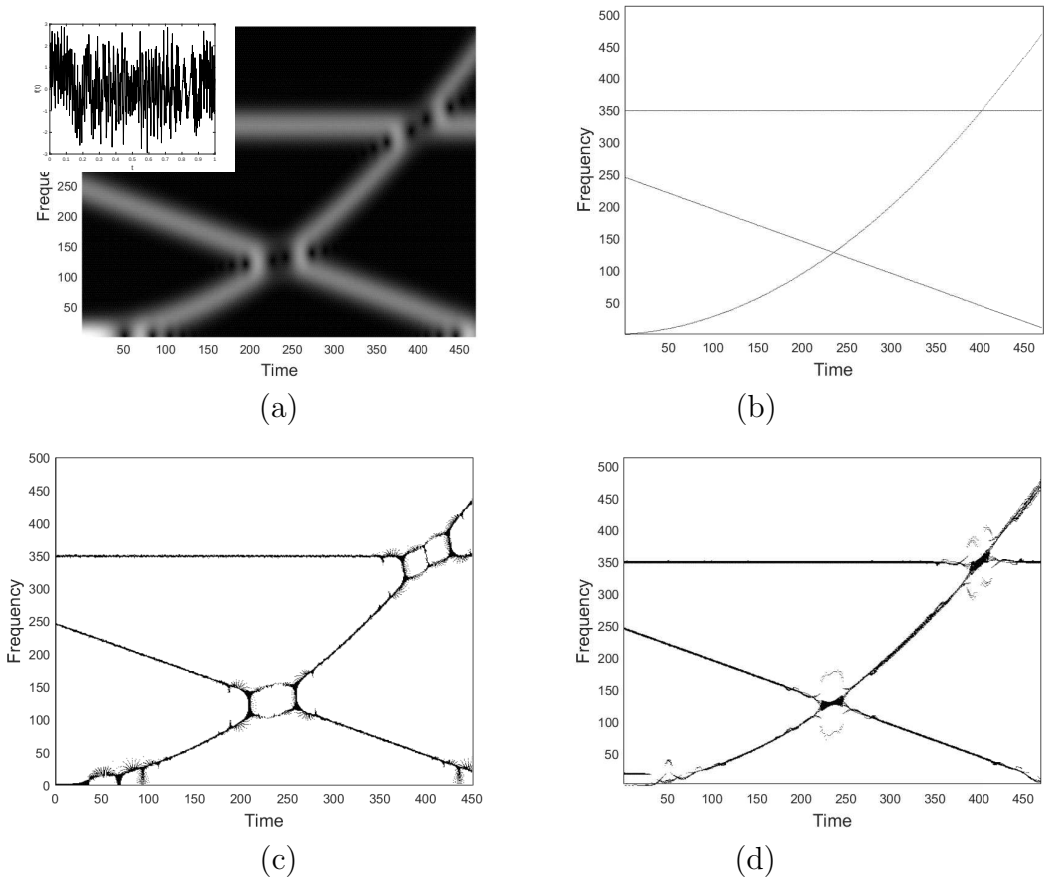

Figure 2.24: (a) Superposition of the quadratic, linear and constant chirps in eq.(2.32), $f = f_1 + f_2 + f_3$ and spectrogram; (b) Ideal TF representation perfectly localized on the ridge curves; (c) Standard reassigned spectrogram; (d) Reassigned spectrogram using Improved Method II [100].

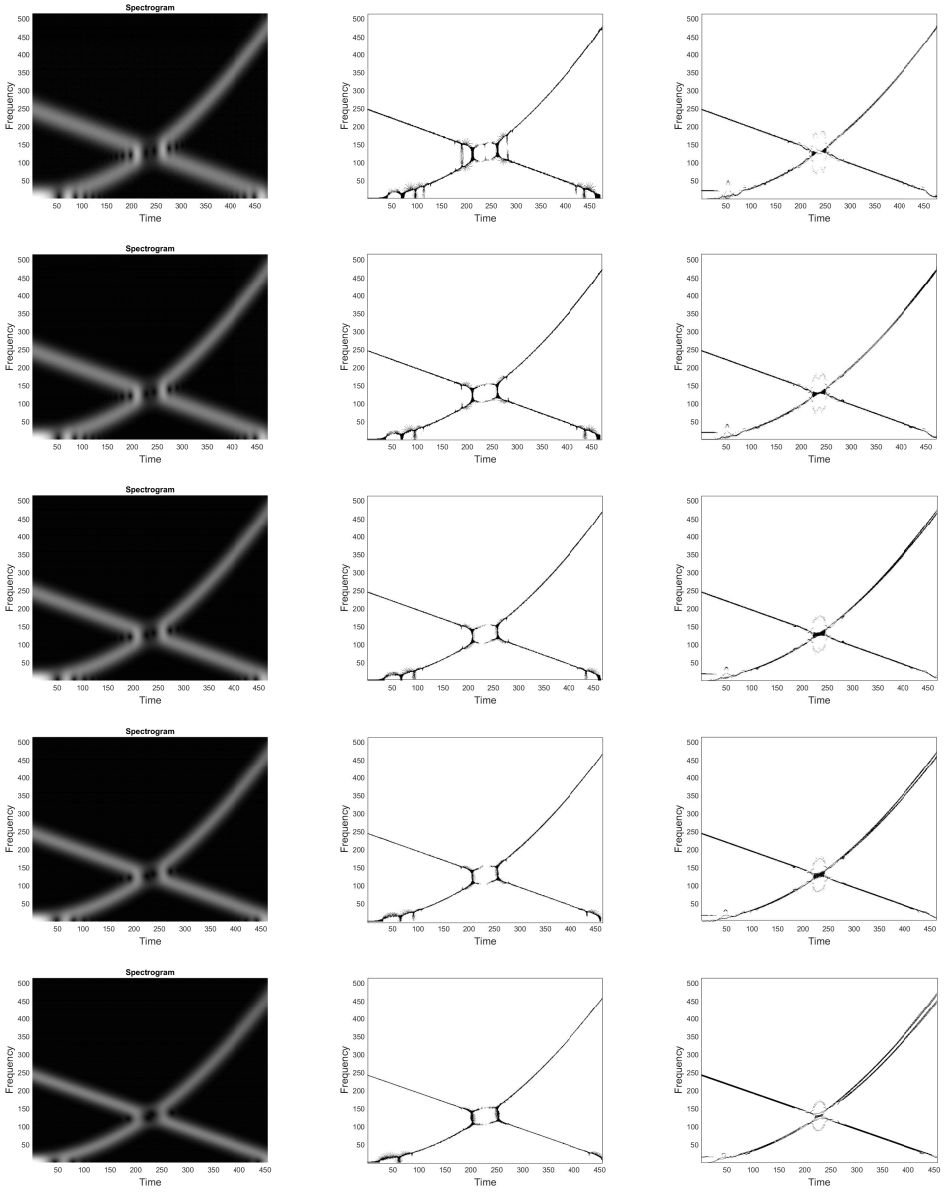

Figure 2.25: Results for the signal $f = f_3 + f_2$ for different values of the analysis window dimension s. *From top to bottom:* $s = 38, 42, 46, 50, 58$. (a) Spectrogram; (b) Standard reassigned spectrogram; (c) Reassigned spectrogram using Improved Method II [100].

Both standard [59] and proposed reassigned spectrograms have been considered—i.e. the ones given by Method I and Improved Method II. Table 2.1 contains Earth mover's distance mean values referred to presented reassignment results, where boundary points are excluded in the computation. In absence of interference (line 1) or in case of moderate interference (line 2,3), RM gives a TF representation which is very close to the ideal one. Actually, our goal is to enhance spectrogram readability whenever the separability condition does not hold true. That is why Table 2.2 provides Earth mover's distance mean values restricted to the non-separability region Ω_{int}. In this case, both Method I and Improved Method II greatly outperform standard RM. Finally, Table 2.3 refers to Fig.2.25 and quantifies the robustness to the size of the analysis window.

MCS	RM	Method I	Method II
f_3	1.70	**1.69**	1.94
$f_3 + f_2$	**5.28**	9.02	7.79
$f_3 + f_4$	**4.90**	10.52	6.84
$f_1 + f_2 + f_3$	38.49	18.29	**17.58**

Table 2.1: Earth mover's distance mean values computed with respect to the ideal reassigned spectrogram.

MCS	RM (Ω_{int})	Method I (Ω_{int})	Method II (Ω_{int})
$f_3 + f_2$	10.06	9.51	**5.52**
$f_3 + f_4$	5.68	**4.24**	4.68
$f_1 + f_2 + f_3$ (1st region)	66.79	27.03	**25.45**
$f_1 + f_2 + f_3$ (2nd region)	74.71	31.05	**27.53**

Table 2.2: Earth mover's distance mean values restricted to the non-separability region Ω_{int}.

2.4 Conclusions

This chapter introduced a TF spectrogram evolution law that applies to generic AM-FM MCS signals. In the special case of constant amplitude MCS, the latter allows to formalize the concept of weakened separability between modes. As a result, we formally characterized TF points which are less affected by interference with respect to spectrogram maxima and, at the same time, keeping

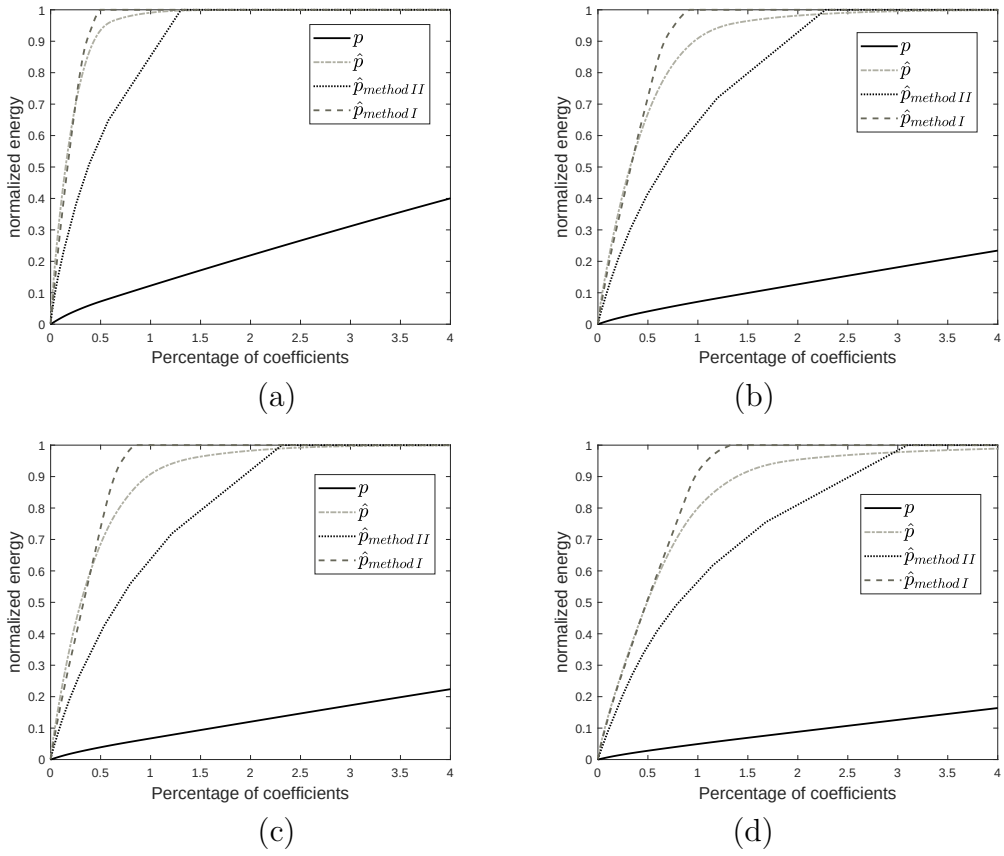

Figure 2.26: Normalized energy (NE) as a function of the percentage of coefficients. Comparison between the TF representations: spectrogram p, standard reassigned spectrogram $\hat{p}$, result given by Method I $\hat{p}_{methodI}$, result given by Improved Method II $\hat{p}_{methodII}$. (a) Signal f_3 in Fig.2.16(a); (b) Signal $f_3 + f_2$ in Fig.2.17(a); (c) Signal $f_3 + f_4$ in Fig.2.18(a); (d) Signal $f_3 + f_2 + f_1$ in Fig.2.24(a) [100].

MCS: $f_3 + f_2$	RM	Method II	RM (Ω_{int})	Method II (Ω_{int})
s=38	**6.59**	7.76	10.67	**6.87**
s=42	**5.34**	7.49	10.30	**5.71**
s=46	**4.99**	7.86	9.98	**5.04**
s=50	**4.85**	8.89	9.86	**5.00**
s=58	**4.79**	11.38	9.14	**7.04**

Table 2.3: Earth mover's distance mean values for the standard reassigned spectrogram and the result given by the proposed method with respect to the ideal representation, for different values of the analysis window length s. Ω_{int} denotes the non-separability region.

IF information. Based on these theoretical results, robust iterative reallocation techniques have been introduced and extensively discussed, including methods' convergence, conditioning and complexity. Numerical studies showed that the proposed approach is convenient with respect to standard RM, as more robustness and sparsity is achieved in the case of MCS with non-separable modes, especially in regions of the TF plane where the modes strongly interfere. In addition, the proposed methods proved to be computationally advantageous.

As future perspectives, the presented study could be extended to noisy data as well as non-constant amplitude modes and, finally, to scalogram reassignment.

Chapter 3

An energy-based approach for the separation of overlapping components

In the literature, methods dealing with overlapping components generally attempt to compensate for the missing information at the non-separability region essentially by interpolation. Actually, peaks detection and tracking procedures, such as Viterbi algorithm and ridge path regrouping, recover IF curve by the optimization of a proper cost function. Adaptive TF distribution-based approaches also extrapolate the local IF by optimization. On the contrary, the iterative approach introduced in Chapter 2 is based on the selection of some "good points" preserving IF information and thus it contributes to reduce the non-separability region and to improve IF curves readability. Nevertheless, the effectiveness is limited to the region of weakened separability, in the sense specified by Definition 11. For crossing modes, the latter can not be satisfied in the neighborhood of the intersection point. As a result, the reassigned distribution does not accurately localize IF curve globally. The loss of resolution can be addressed by changing the usual perspective: instead of recovering the missing information by the knowledge of the observed peaks (interpolation) or iteratively concentrating distribution, the information available should be further analysed. Actually, this is possible by studying the behaviour of MCS energy, as it will shown in this chapter. In particular, in Section 3.1 the lack of separability is addressed by introducing an energy-based approach for MCS analysis. We will prove that the energy of a constant amplitude MCS is also a MCS, whose

IFs are differences in pairs of the original IFs. As a result, the STFT of the energy signal can be used for extracting the original IFs in the non-separability region. In addition, the introduction of a two-dimensional spectrogram energy function allows us to define a procedure for the automatic interference region detection, as it will be discussed in Section 3.2.

Since TF representations alone are not sufficient to fully address the problem of MCS decomposition, Section 3.3 introduces the combination of spectrogram and Radon Transform (RT), namely Radon Spectrogram Distribution. The latter provides a spectrogram multi-level energy and it maps crossing modes into a domain where components look separated, as it will be explained in details. Some results presented in this chapter have been published in [106–108]. Finally, Section 3.4 draws the conclusions of the chapter.

3.1 Energy-based analysis of interference

As extensively discussed in Section 2.1, non-separability between components could cause a significant deviation of ridge points, resulting in non accurate reassigned distributions. It is possible to measure the interaction between signal modes by analysing spectrogram energy in a specific direction, which is introduced in the following

Definition 14. *Given $f \in L^2(\mathbb{R})$, let $S_f^g(u,\xi)$ be its STFT. The spectrogram integral along frequency is defined as the* ***energy function****, i.e.*

$$\mathcal{E}_g(u) = \int_{-\infty}^{+\infty} |S_f^g(u,\xi)|^2 \, d\xi. \tag{3.1}$$

The energy function in Definition 14 is the L^2-norm of the STFT profile, with u varying in time. From now on, we will consider MCS satisfying the condition specified in the following Definition.

Definition 15. *Let f a AM-FM MCS as in eq.*(1.17)*. Let $\Omega_{k_1k_2}, \Omega_{k_3k_4} \subset \mathbb{R}^+ \times \mathbb{R}^+$ be two non-separability regions, respectively between modes f_{k_1}, f_{k_2} and f_{k_3}, f_{k_4}, composing $f(t)$, i.e.*

$$|\phi'_{k_1}(u) - \phi'_{k_2}(u)| < \Delta\omega, \, \forall\, u \in \Omega_{k_1k_2} \text{ and } |\phi'_{k_3}(u) - \phi'_{k_4}(u)| < \Delta\omega, \, \forall\, u \in \Omega_{k_3k_4}.$$

Then, $\Omega_{k_1k_2}$ and $\Omega_{k_3k_4}$ are ***solvable*** *if $\Omega_{k_1k_2} \cap \Omega_{k_3k_4} = \emptyset$.*

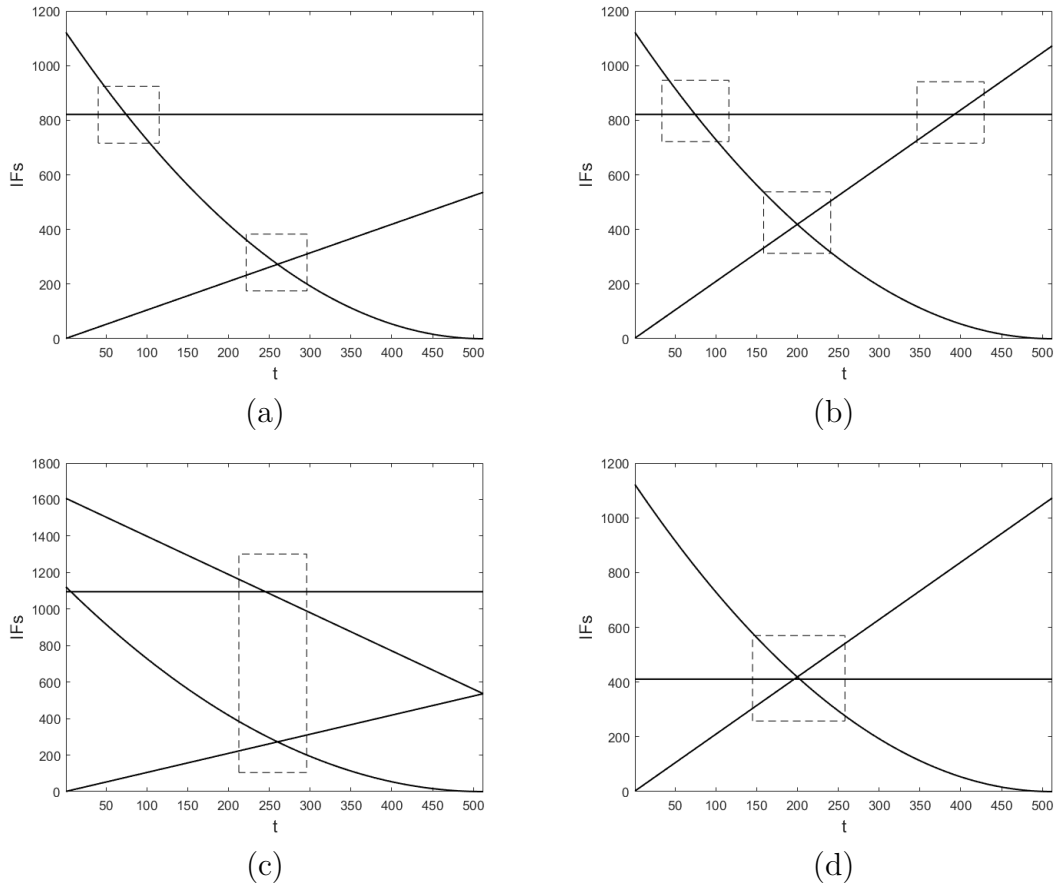

Figure 3.1: IF curves of non-separable MCS. The interference regions are emphasized by dashed rectangles. Solvable case: (a) and (b); Non solvable case: (c) regions overlap in time, (d) regions overlap in time and frequency.

In other words, interference regions are solvable if they do not have the same time supports—Fig.3.1 shows some illustrative examples. Under this assumption, the energy function of a MCS has a nice representation, as stated below.

Proposition 3.1. *The energy function $\mathcal{E}_g(u)$ of a constant amplitude MCS can be expressed as*

$$\mathcal{E}_g(u) = K(u) + \sum_{k \neq j} A_{k,j}(u) \cos \theta_{k,j}(u), \tag{3.2}$$

$$\textit{with} \quad A_{k,j}(u) = \frac{a_k(u) a_j(u)}{2} \int_{-\infty}^{+\infty} \hat{g}(\xi - \phi_k'(u)) \hat{g}(\xi - \phi_j'(u))\, d\xi, \tag{3.3}$$

$$\theta_{k,j}(u) = \phi_k(u) - \phi_j(u) \quad \textit{and} \quad K(u) = \frac{\pi}{2} \sum_k a_k^2(u) \int_{-\infty}^{+\infty} g^2(t)\, dt. \tag{3.4}$$

Proof. Proof can be found in Appendix B. □

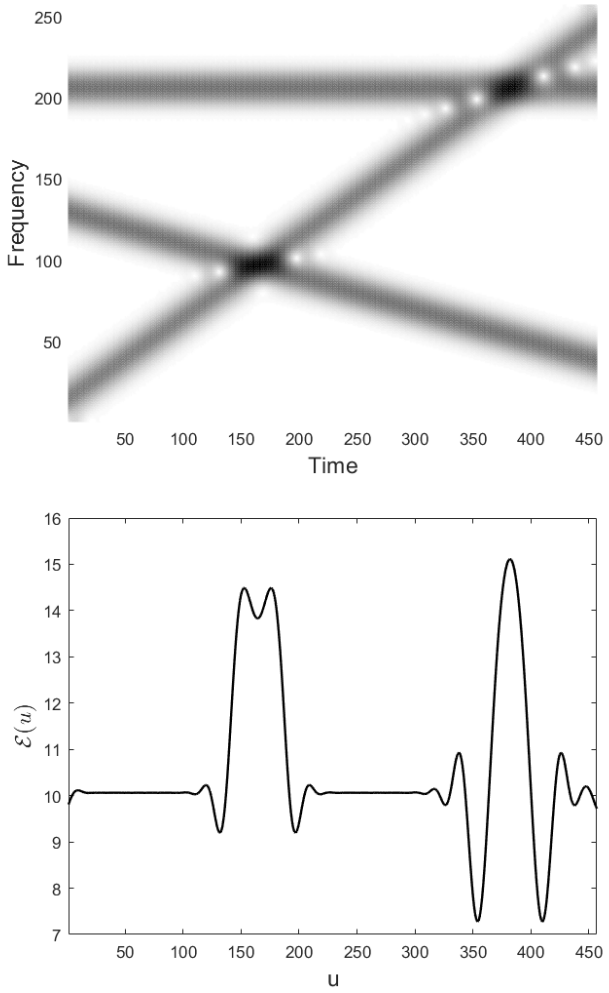

Figure 3.2: A three-components signal having constant amplitudes and solvable separability regions. Top): Spectrogram; Bottom) Energy function as defined in eq.(3.1).

Remark 10. *Prop.3.1 states that the shifted energy function* $f_{int}(u) := \mathcal{E}_g(u) - K(u)$ *is a MCS. Furthermore, its IFs are differences in pairs of the original IFs and its amplitudes vanish for well separated components. Indeed, according to Definition 6, let suppose* $|\phi'_{k_1}(u) - \phi'_{k_2}(u)| \geq \Delta\omega$, $\forall\, u$, $k_1, k_2 \in \{1, ..., N\}$. *As a consequence,* $\hat{g}(\xi - \phi'_{k_1}(u)) \ll 1$, $\forall\, \xi : |\xi - \phi'_{k_2}(u)| < \Delta\omega/2$, *that is the integral*

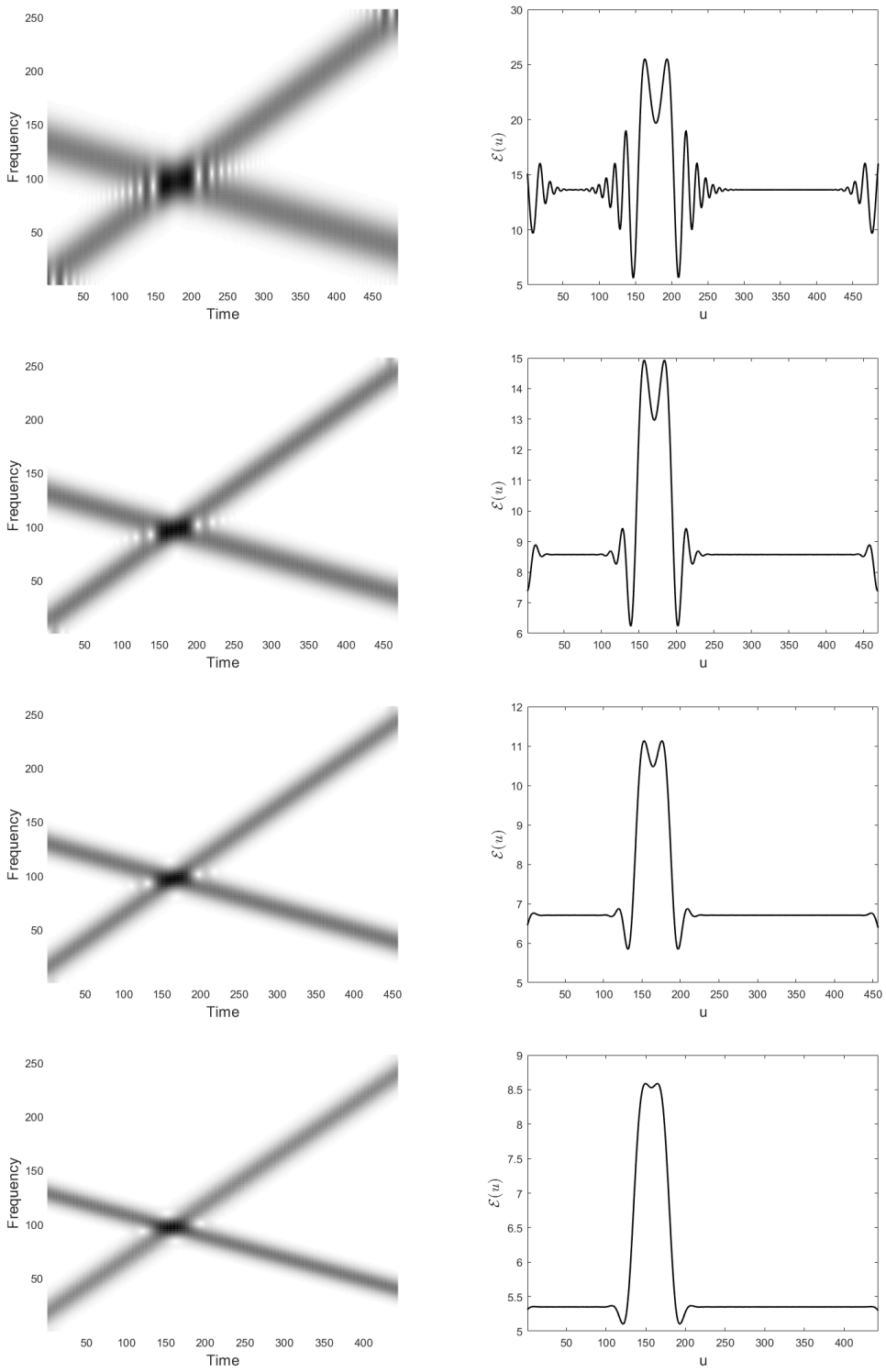

Figure 3.3: Dependence of the energy function on the analysis window. (a) Spectrogram obtained by considering different window sizes; (b) Energy function as defined in eq.(3.1).

functions in eq.(3.3) have disjoint supports, resulting in $A_{k_1,k_2} \approx 0$. *On the contrary, if the separability condition is not satisfied, then* $A_{k_1,k_2}(u) \neq 0$ *as the supports of* $\hat{g}(\xi - \phi'_{k_i}(u))$, $i = 1, 2$ *do overlap and then the integral in eq.*(3.3) *is non zero. It follows that* $\mathcal{E}_g(u) - K(u)$ *oscillates where modes interfere, as shown in Fig.3.2, measuring the interaction between modes.*

The amplitudes in eq.(3.3) can be expressed in terms of the ambiguity function of the analysis window.

Proposition 3.2. *For each* $k, j \in \{1, ...N\}$ *let consider the amplitude* $A_{k,j}(u)$ *in eq.*(3.3) *and let* $Ag(\tau, \gamma) = \int_{-\infty}^{+\infty} \hat{g}\left(\omega + \frac{\gamma}{2}\right) \hat{g}\left(\omega - \frac{\gamma}{2}\right) e^{i\tau\omega}\, d\omega$ *be the ambiguity function of the analysis window* g. *Then, it holds*

$$A_{k,j}(u) = \frac{a_k(u)a_j(u)}{2} Ag\left(0, \phi'_k(u) - \phi'_j(u)\right). \tag{3.5}$$

Proof. For each fixed u, let consider the change of variable $\omega = \xi - \frac{\phi'_k(u)+\phi'_j(u)}{2}$, then eq.(3.3) can be rewritten as

$$\begin{aligned} A_{k,j}(u) =& \frac{a_k a_j}{2} \int_{-\infty}^{+\infty} \hat{g}\left(\omega + \frac{\phi'_k(u) - \phi'_j(u)}{2}\right) \hat{g}\left(\omega - \frac{\phi'_k(u) - \phi'_j(u)}{2}\right) d\omega \\ =& \frac{a_k a_j}{2} Ag\left(0, \phi'_k(u) - \phi'_j(u)\right). \end{aligned}$$

□

It is worth observing that, even if $\mathcal{E}_g(u)$ depends on the adopted analysis window, its localization property only depends on the window support. Fig.3.3 depicts the energy function of a two-components signal having overlapped modes. As it can be observed, the non-separability region is identified by $\mathcal{E}_g(u)$ oscillations, while the window length is varying.

The proposition below gives the expression of the amplitude $A_{k,j}$ in the gaussian case.

Proposition 3.3. *If the STFT is computed with a gaussian window* $g(t) = \frac{1}{\sqrt{2\pi\sigma^2}} e^{-\frac{t^2}{2\sigma^2}}$, *then for each* $k, j \in \{1, ...N\}$, $A_{k,j}(u)$ *in eq.*(3.3) *can be expressed as*

$$A_{k,j}(u) = \frac{\sqrt{\pi} a_k(u)a_j(u)}{2\sigma} e^{-\frac{\sigma^2}{4}(\phi'_k(u) - \phi'_j(u))^2}. \tag{3.6}$$

Proof. Proof is in Appendix B. □

If $f(t)$ in eq.(1.17) is a constant amplitude MCS, then special properties can be derived.

Corollary 3. *If the amplitudes a_k and a_j in eq.*(1.17) *are constant, then $A_{k,j}(u)$ is still gaussian.*

Proof. The proof straightforwardly follows from eq.(3.6). □

Furthermore, if modes have constant amplitudes and they are well separated, Prop.3.1 implies that spectrogram energy is constant along u and equal to K as in eq.(3.4), while if two components do interfere, the energy function oscillates exactly in correspondence to the TF region interested by the overlapping, with specific IF depending on the original IFs. Locally around the crossing point, $\mathcal{E}_g(u)$ can be larger than K, as in the Fig.3.4(b), or significantly smaller, as it happens in Fig.3.4(d). Since the cosine sign in eq.(3.2) distinguishes between the two cases, we consider the following

Definition 16. *Let f_k and f_j be crossing modes at u_0, i.e. $\phi_k'(u_0) = \phi_j'(u_0)$ and let define $\Delta\phi_{k,j} = \phi_k(u) - \phi_j(u)$. Then, the interference is said to be constructive if $\cos \Delta\phi_{k,j}(u_0) \geq 0$, otherwise it is said to be destructive.*

It is important to notice that the destructive case corresponds to the most critical scenario in existing methods dealing with overlapped modes as the more the loss of energy, the more the missing information.

Remark 11. *The computation of STFT can be avoided and $\mathcal{E}_g(u)$ can be understood as the a localized signal energy, as stated in the following proposition.*

Proposition 3.4. *The energy function $\mathcal{E}_g(u)$ of the signal f as defined in eq.*(1.17) *is equivalent to*

$$\mathcal{E}_g(u) = 2\pi \int_{-\infty}^{+\infty} |f(t)|^2 \, |g(t-u)|^2 \, dt. \tag{3.7}$$

Proof. By definition,

$$\mathcal{E}_g(u) = \int_{-\infty}^{+\infty} S_f(u,\xi)\, S_f^*(u,\xi)\, d\xi = \int_{-\infty}^{+\infty} \mathcal{F}\left(f(t)g(t-u)\right) \mathcal{F}^*\left(f(t)g(t-u)\right) d\xi,$$

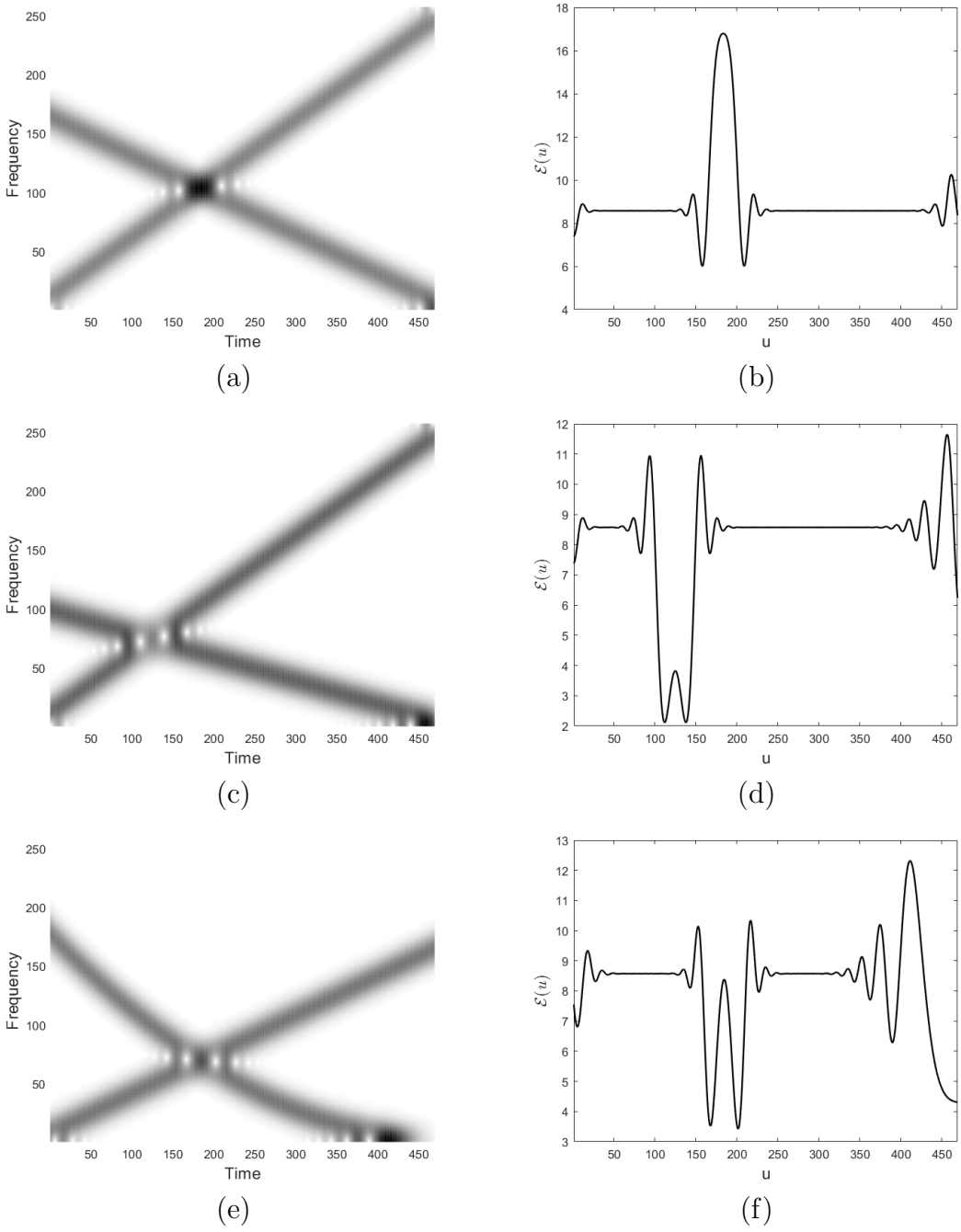

Figure 3.4: Example of non-separable MCS. Left) Spectrogram; Right) Energy function as defined in eq.(3.1). The energy is constructive in (b) and destructive in (d), while a critical limit case is observed in (f), according to Definition 16.

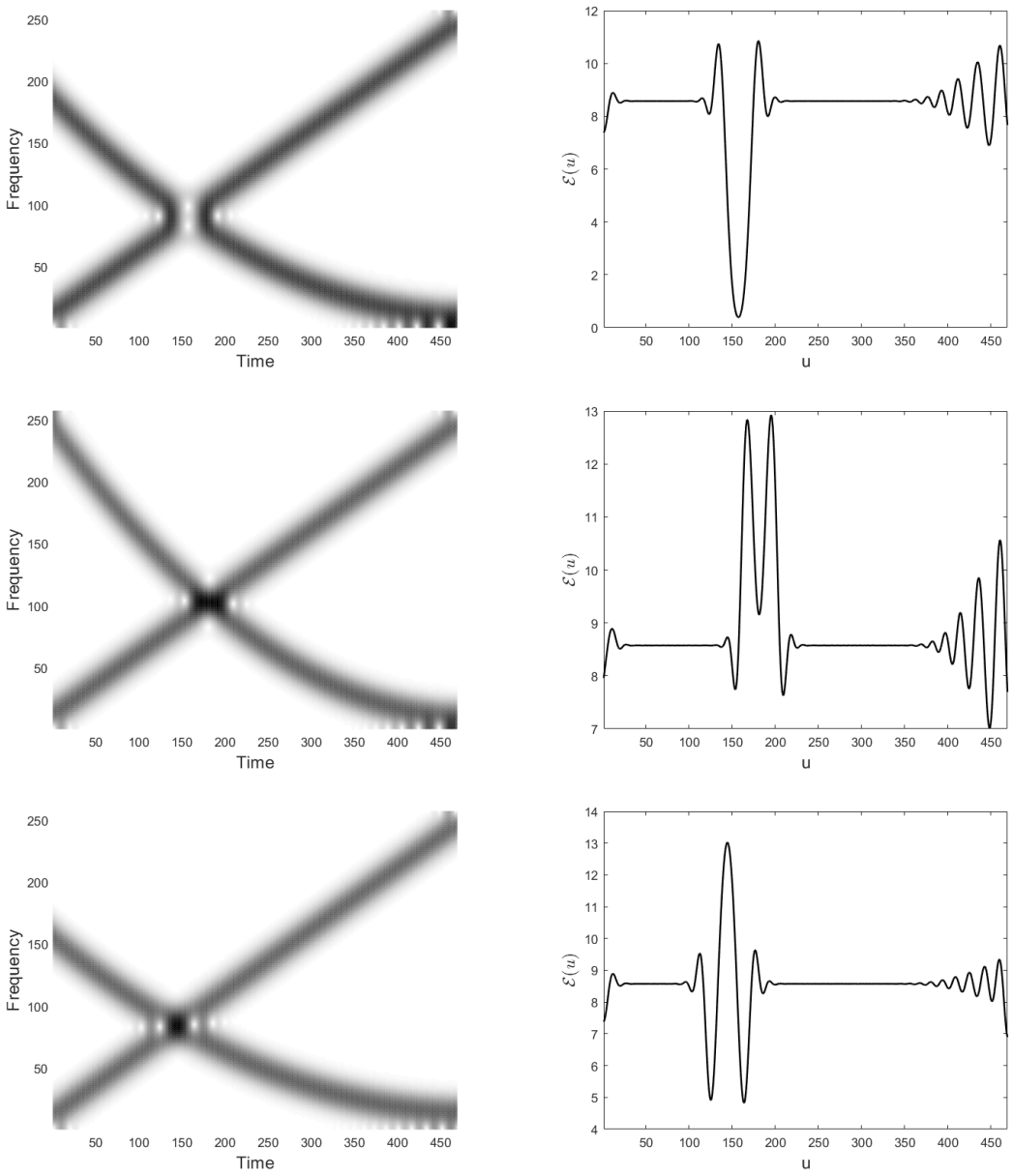

Figure 3.5: Example of non-separable MCS. Left) Spectrogram; Right) Energy function as defined in eq.(3.1).

where $\mathcal{F}(\cdot)$ stands for the Fourier transform of $(\cdot)$ and $*$ denotes the conjugate operator. By applying Parseval theorem [35], it follows

$$\mathcal{E}_g(u) = 2\pi \int_{-\infty}^{+\infty} f(t)g(t-u)\, f^*(t)g^*(t-u)\, dt,$$

and then eq.(3.7) holds true. □

3.1.1 STFT-based method for the recovery of IFs curves

The signal $\mathcal{E}_g$ can be analysed to estimate $|\Delta\phi'_{k,j}(u)| = |\phi'_k(u) - \phi'_j(u)|$, under the hypothesis of separated interference regions with respect to ξ—see Fig.3.1. As a preliminary study, the simple case of a FM signal having two components, f_1 and f_2, with constant amplitude $a = 1$ is considered in this section. The following proposition provides an estimate of the difference between IFs.

Proposition 3.5. *Let $S^g_f(u,\xi)$ be the STFT of $f(t) = \cos\phi_1(t) + \cos\phi_2(t)$ computed by a gaussian unitary window $g(t) = \frac{1}{\sqrt{2\pi\sigma^2}} e^{-\frac{t^2}{2\sigma^2}}$. Set $f_{int}(u) = \mathcal{E}_g(u) - K$ according to eq.(3.2) and let $S^g_{f_{int}}(u,\xi)$ be the corresponding STFT computed using the same window g. By denoting $\Delta\phi'(u) = \phi'_2(u) - \phi'_1(u)$, it holds*

$$|\Delta\phi'(u)| = \sqrt{\ln\left[\left(\frac{2\Re(S^g_{f_{int}}(u,0))}{f_{int}(u)}\right)^{-\frac{2}{\sigma^2}}\right]}, \forall\, u \in supp\{f_{int}\} : \frac{2\Re(S^g_{f_{int}}(u,0))}{f_{int}(u)} \leq 1. \tag{3.8}$$

Proof. Proof can be found in Appendix B. □

The estimate in eq.(3.8) can be used to partially reconstruct IF curves at the non-separability region. To this aim, let us denote by G the center of mass of the spectrogram distribution, along the frequency direction, i.e.

$$G(u) = \frac{1}{\mathcal{E}_g(u)} \int_{-\infty}^{+\infty} \xi \cdot P(u,\xi)\, d\xi. \tag{3.9}$$

Intuition suggests that for separable components having comparable amplitudes, spectrogram center of mass lies on the ridge curves center of gravity. Actually, the latter holds true also for overlapping components, even if ridge curves can be highly deviated due to interference, as stated in the following

Proposition 3.6. *Let us consider a two-components signal $f(t) = a_1\cos\phi_1(t) + a_2\cos\phi_2(t)$ with $a_1 = a_2$. Then the spectrogram center of mass in eq.(3.9) is the mean of its IFs, i.e.*

$$G(u) = \frac{\phi'_1(u) + \phi'_2(u)}{2}, \forall\, u.$$

Proof. Proof is in Appendix B. □

Remark 12. *The combination of Prop.3.5 and Prop.3.6 allows for ridge estimation in the interference region as follows*

$$\bar{\xi}(u) = G(u) \pm \frac{|\Delta\phi'(u)|}{2}. \tag{3.10}$$

3.1.1.1 Algorithm and some results

Eq.(3.10) can be exploited to partially correct the reassigned spectrogram obtained by the standard procedure in [59]. Given $f(t) = \cos\phi_1(t) + \cos\phi_2(t)$, the algorithm is described below, taking advantage of the illustrative example in Figs.3.6-3.7.

Step 1. Compute the STFT with a gaussian window g and the corresponding spectrogram $P(u,\xi)$—Fig.3.6(a).

Step 2. Estimate the energy function $\mathcal{E}_g(u)$ in eq.(3.1) as the sum along frequencies of the spectrogram.

Step 3. Estimate K in eq.(3.2) as a multiple of the window energy and set $f_{int}(u) = \mathcal{E}_g(u) - K$—Fig.3.6(c).

Step 4. Estimate the compact interference region Ω_{int} by retaining those points such that $\mathcal{E}_g(u)$ over-exceeds the 10% of its maximum value.

Step 5. Compute the STFT of $f_{int}(u)$—Fig.3.6(d-e).

Step 6. Compute the ratio in eq.(3.69) and —Fig.3.6(f) and estimate the frequencies $\Delta\phi'(u)$ according to (3.8)—Fig.3.7(a-b)

Step 7. Compute the center of mass $G(u)$ as in eq.(3.9) and its spline interpolation $\tilde{G}(u)$ —Fig.3.7(c-d)

Step 8. Reassign the estimated frequencies according to eq.(3.10) , $\forall\ u \in \Omega_{int}$—Fig.3.7(f).

Figs.3.6-3.7 show that the energy function $\mathcal{E}_g(u)$ localizes the interference between two crossing modes, as well as its translated version f_{int}. Its analysis allows to estimate the non-separability region Ω_{int} as in step 4. It is important to notice that the spectrogram of f_{int} is very concentrated, as shown in Figs.3.6(d). Only a section of the real part of the STFT of $f_{int}(u)$ is involved in

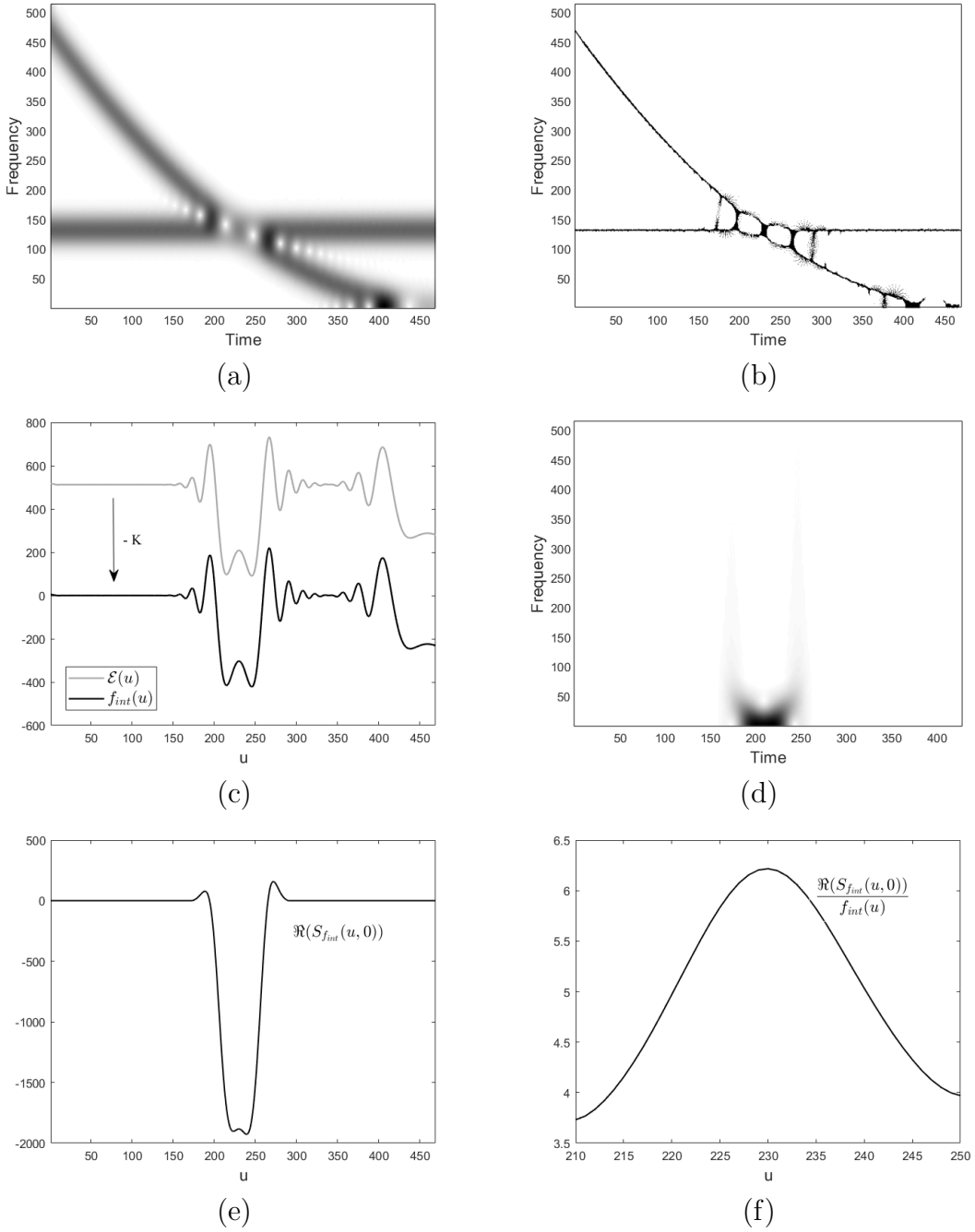

Figure 3.6: STFT-based method applied to a two-components signals having crossing modes. (a) Spectrogram; (b) Reassigned spectrogram; (c) Energy function in eq.(3.1) and its translated version $f_{int}(u) = \mathcal{E}(u) - K$, according to eq.(3.2); (d) $f_{int}(u)$ spectrogram; (e) $\Re(S_{f_{int}}(u,0))$ as in eq.(3.68); (f) Ratio between the section in (e) and f_{int} in (c) restricted to the detected interference region Ω_{int}.

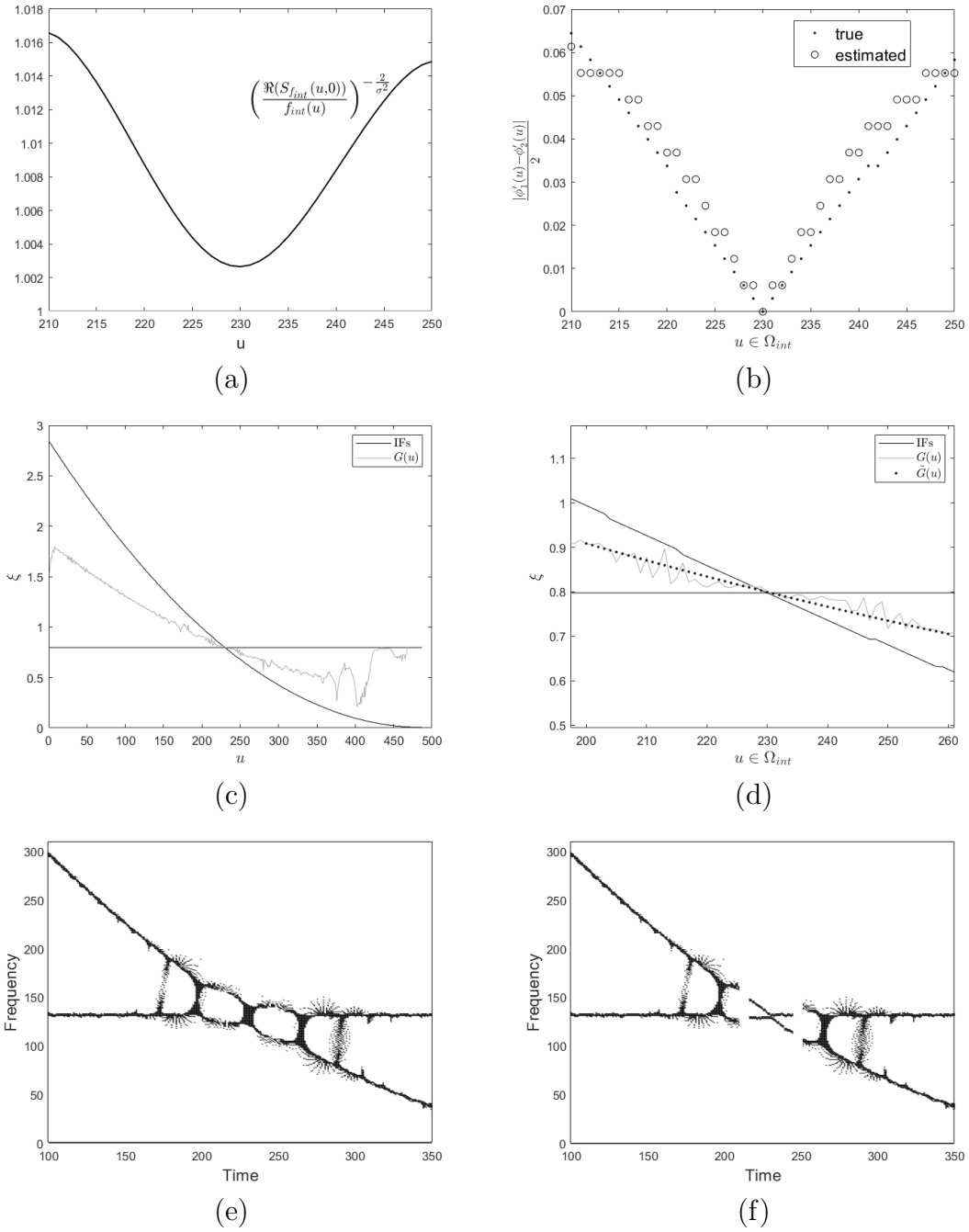

Figure 3.7: STFT-based method applied to a two-components signals having crossing modes. (a) Logarithm argument in eq.(3.71); (b) Estimated mean between $\phi_1'(u)$ and $\phi_2'(u)$; (c) True IFs laws and spectrogram center of mass estimated from the distribution in Fig.3.6(a); (d) Spline approximation of $G(u)$ at the interference region; (e) Reassigned spectrogram in Fig.3.6(b) zoomed at the interference region; (f) Result given by the proposed method.

the procedure (Fig.3.6(e)). As shown in Fig.3.6(f), the ratio between the section and f_{int} presents a gaussian profile, according to eq.(3.70). The difference between IFs is computed according to Prop.3.5, by computing the logarithm of the quantity depicted in Fig.3.7(a). Then, the spectrogram center of mass is computed and its spline interpolation is considered to prevent instabilities, as shown in Fig.3.7(c)-(d). Finally, TF points belonging to the detected interference region Ω_{int} are reassigned according to eq.(3.10). The comparison between Figs.3.7(e) and (d) shows that the presented method significantly improves reassigned spectrogram readability at the non-separability region.

Remark 13. *It is worth pointing out that the presented procedure is designed for MCS having quite comparable amplitudes and it has been preliminary applied only to two-components signals. Further in-depth studies are needed to make the method suitable for more general signals. Nevertheless, the proposed approach is a first attempt to recover the ridge curves in the most critical TF region, i.e. the one close to the intersection point, where the resolution of TF representations is commonly very poor.*

3.1.2 Gaussian interpolation for IFs recovery

Eq.(3) can be exploited to directly estimate IFs in the case of a gaussian analysis window, without computing the additional STFT required by the method proposed in the previous section. In this section, we only present the idea behind the approach.

Given two interfering modes f_k, f_j,

$$f_{int}(u) = \mathcal{E}_g(u) - K = A_{j,k}(u) \cos \Delta\phi_{k,j}(u),$$

and then

$$f_{int}(u) = A(u), \ \forall \ u : \cos \Delta\phi_{k,j}(u) = 1.$$

In particular, $f'_{int}(u) = A'_{k,j}(u) \cos \Delta\phi_{k,j}(u) - A_{k,j}(u)[\phi'_k(u) - \phi'_j(u)] \sin \Delta\phi_{k,j}(u)$; hence, if $\cos \Delta\phi_{k,j}(u) = 1$ and $|A'_{k,j}(u)| < \epsilon$, then $|f'_{int}(u)| < \epsilon$. In other words, some stationary points of f_{int} adjacent to the boundary of the support are approximately points belonging to the gaussian amplitude $A_{k,j}$, as depicted is Fig.3.8. As a result, $A_{k,j}$ can be interpolated over some extrema points in order to estimate $\Delta\phi'_{k,j}$ according to eq.(3). An illustrative and very preliminary

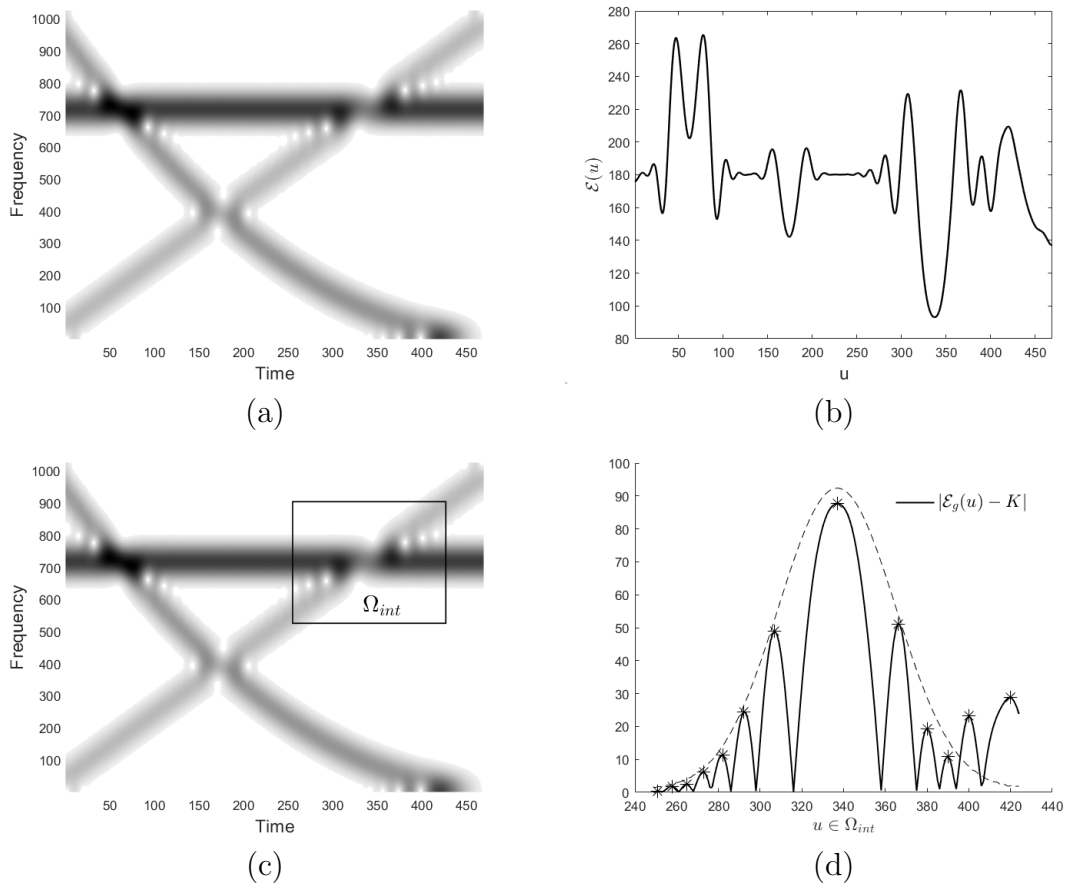

Figure 3.8: A three-components signal having solvable separability regions. (a) Spectrogram; (b) Energy function as in eq.(3.1); (c) A non-separable region Ω_{int} regarding the j-th and k-th modes; (d) Absolute value of the signal $\mathcal{E}_g(u) - K$ (solid line). The latter coincides to $|A_{k,j}(u)\cos(\phi_k(u) - \phi_j(u))|$ and the envelope of its maxima is close to the amplitude $A_{k,j}(u)$ (dashed line). As stated in Prop.3.3, since the STFT in (a) is computed by using a gaussian window, $A_{k,j}(u)$ still is gaussian.

example is shown in Fig.3.9, where the gaussian amplitude $A_{k,j}$ has been interpolated after a proper correction of the location of its center. As stated in Prop.3.6, if $a_1 = a_2$ the spectrogram center of mass provides the sum of the IFs, so that the ridge curve can be completely recovered. Fig.3.9(d) depicts the corrected reassigned spectrogram at the non-separability region following the procedure described above. The latter will be better formalized in future studies.

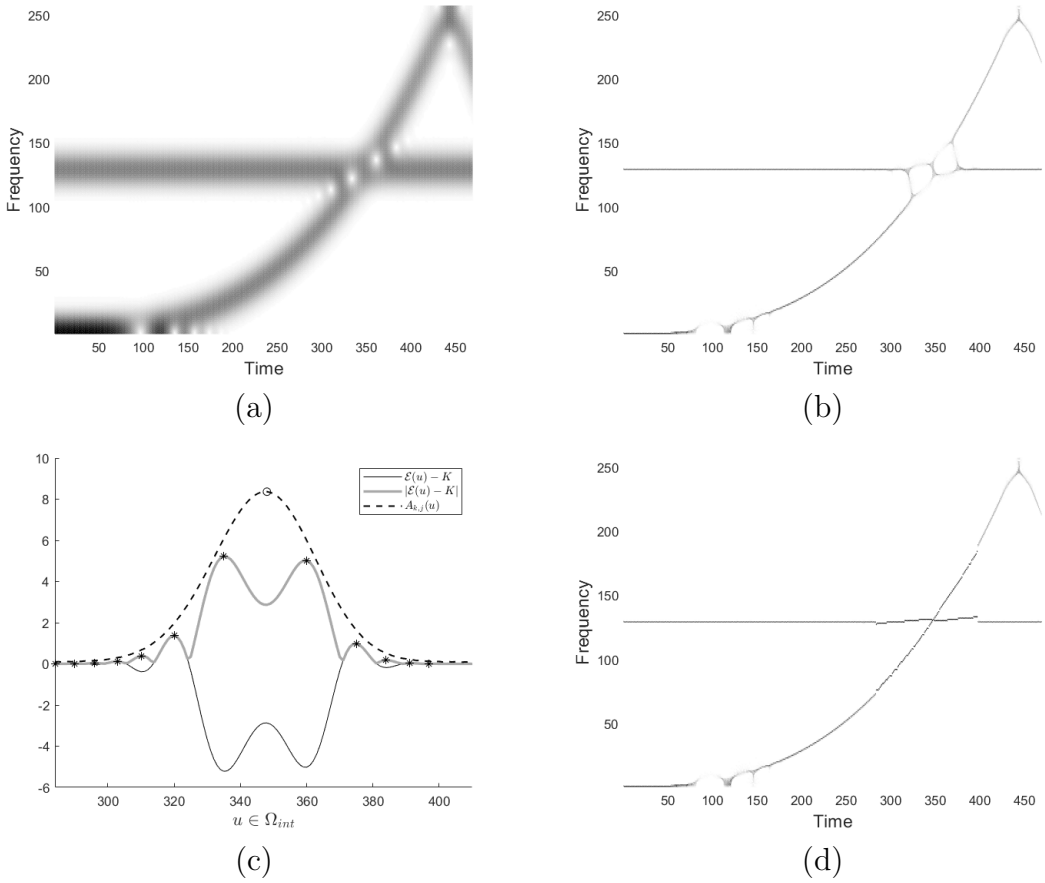

Figure 3.9: IFs estimation by gaussian interpolation. (a) Spectrogram; (b) Reassigned spectrogram; (c) Absolute value of the translated energy function $\mathcal{E}(u) - K$ at the non-separability region. The envelope of local maxima (asterisks) approximately fit the gaussian amplitude $A_{k,j}(u)$. In order to correctly interpolate it, the center should be relocated (o marker); (d) Reassigned spectrogram in (b) corrected at the non-separability region.

3.2 Two-dimensional energy for MCS analysis

The prior knowledge of TF regions interested by non-separability is very advantageous for methods dealing with overlapping MCS. Unfortunately, the automatic detection of interference region is nowadays an open problem. Another topic of great interest in FM signal processing is the detection of modes number, which is an unknown in practical applications as well. The latter problem is addressed, for instance, by Rényi entropy-based methods [109]. Interference region detection and modes countability are closely related and not trivially solvable without specific assumptions. By the analysis presented in Section 3.1,

it turns out that the spectrogram energy gives major information concerning the interaction between modes. In particular, in case of a constant amplitude signal, the energy function $\mathcal{E}_g(u)$ is constant in those regions where modes satisfy the separability condition, while significant oscillations occur at the interference region. This observation led to the STFT-based procedure presented in the previous section for IFs recovering. The goal becomes more complicated in case of MCS having more than two modes. In order to apply the presented method, it is necessary to first separate the non-separability regions. In other words, a new decomposition problem has to be solved, as the modes composing the energy function $\mathcal{E}_g(u)$ have to be separated too.

The knowledge of the energy evolution over time alone is not sufficient to deal with the problem. For this reason, a generalization of the energy function is considered.

Definition 17. *Given* $f(t) = \sum_{k=1}^{N} a_k \cos\phi_k(t)$*, let* $S_f^g(u,\xi)$ *be its STFT, with* $(u,\xi) \in \mathbb{R} \times \mathbb{R}^+$*, and for each fixed* u *let us consider*

$$\bar{S}_f^g(u,\xi) = \begin{cases} S_f^g(u,\xi) & \text{if } \exists\, i : |\xi - \phi_i'(u)| \leq \frac{\Delta\omega}{2} \\ 0 & \text{otherwise.} \end{cases} \tag{3.11}$$

The ***windowed energy function*** *(WEF) of* f *is then defined as*

$$W\mathcal{E}_g(u,\xi) = \int_0^{\xi} |\bar{S}_f^g(u,\xi')|^2 \, d\xi'. \tag{3.12}$$

Fig.3.10 depicts some examples of spectrogram and corresponding WEF. The latter is a sort of cumulative distribution of the spectrogram, as shown in Fig.3.11. Furthermore, by definition, WEF derivative presents points of discontinuity—a_1 and b_1 in Fig.3.11(c) and (d)— that localize signal energy in the TF plane. As it will be explained in details, those points will be involved for detecting the non-separability region between two overlapped modes. For a deeper understanding, we will first analyze the WEF of a single mode and then we will address the MCS case.

3.2.1 Monocomponent signals

It is interesting to notice that, in case of a single mode, WEF satisfies the evolution law in eq.(2.6), as stated below.

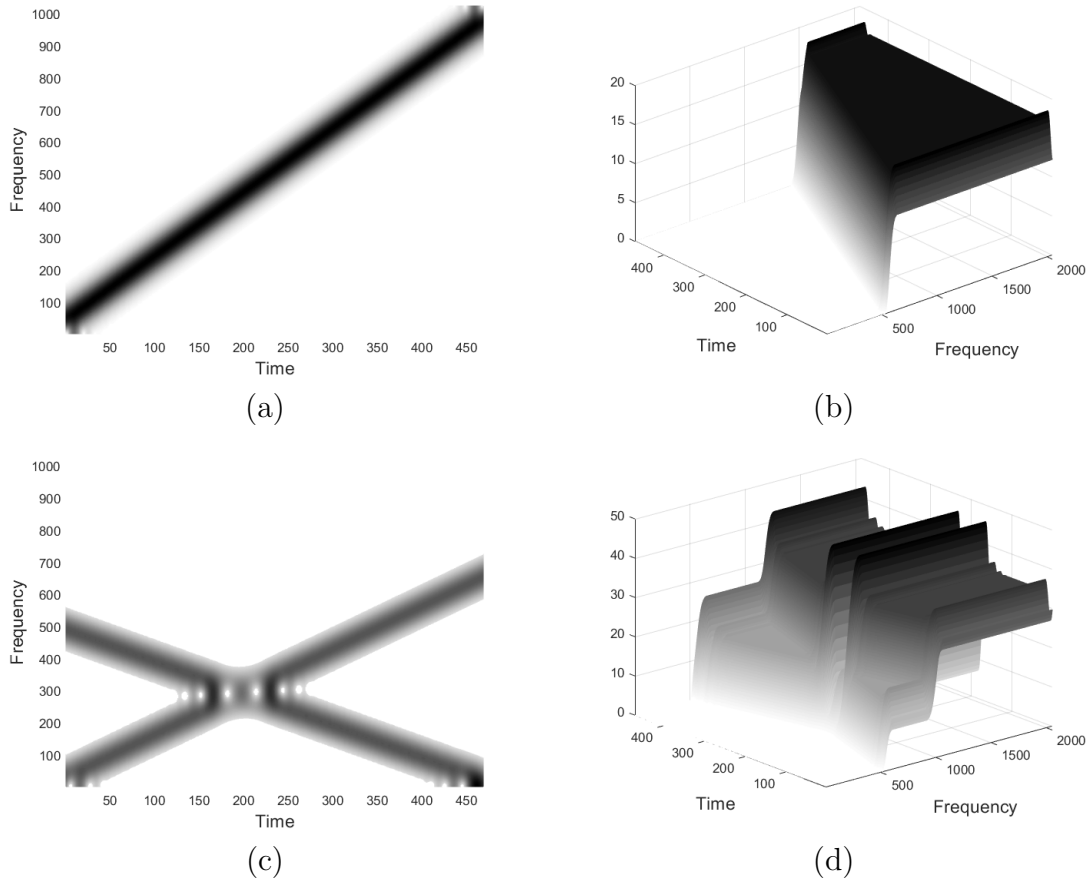

Figure 3.10: (a) Spectrogram of a linear chirp; (b) WEF of (a); (c) Spectrogram of a two-components signal with non-separable modes; (d) WEF of (c).

Proposition 3.7. *The WEF of a constant amplitude monocomponent FM signal* $f(t) = a\cos\phi(t)$ *satisfies the following evolution law*

$$\frac{\partial \mathcal{WE}_g(u,\xi)}{\partial u} + \phi''(u)\frac{\partial \mathcal{WE}_g(u,\xi)}{\partial \xi} = 0. \tag{3.13}$$

In addition, the characteristic curves $\mathcal{C}_{\phi,c}$ *of eq.*(3.13) *are* $\xi(u) = \phi'(u) + c$*, with* $c = \xi_0 - \phi'(u_0)$ *and* (u_0, ξ_0) *is a point in the TF plane.*

Proof. The thesis follows from eq.(2.6), indeed $\forall (u,\xi) \in supp\{\mathcal{WE}_g\}$,

$$\frac{\partial \mathcal{WE}_g(u,\xi)}{\partial u} = \int_0^{+\infty} P_u(u,\xi)\, d\xi = \int_0^{+\infty} -\phi''(u) P_\xi(u,\xi)\, d\xi = -\phi''(u)\frac{\partial \mathcal{WE}_g(u,\xi)}{\partial \xi}.$$

For the characteristic curves computation, we refer to the proof Prop.2.4. □

As a result, the following proposition holds true.

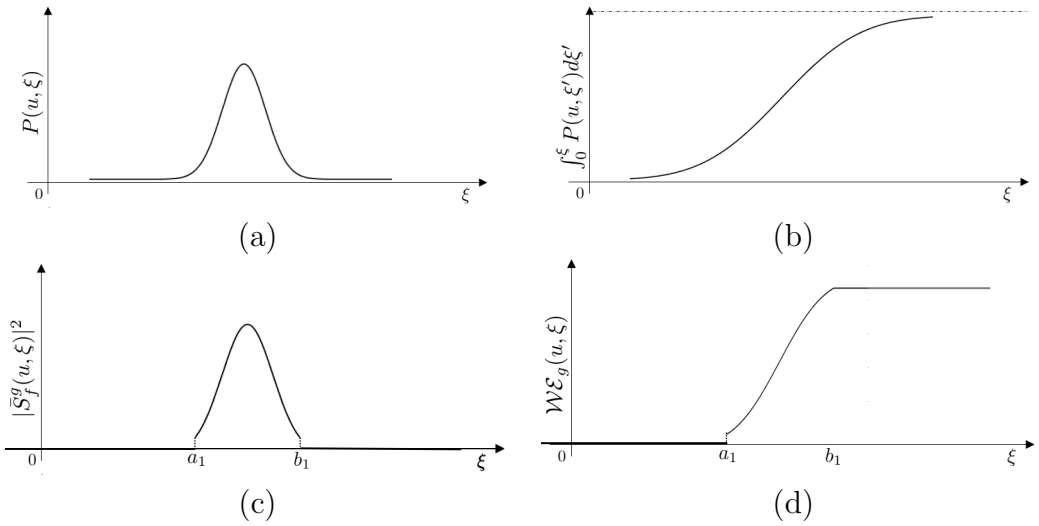

Figure 3.11: A monocomponent signal. (a) Spectrogram section; (b) Spectrogram cumulative function; (c) $|\bar{S}_f^g(u,\xi)|^2$ according to eq.(3.11); (d) WEF as defined in eq.(3.12).

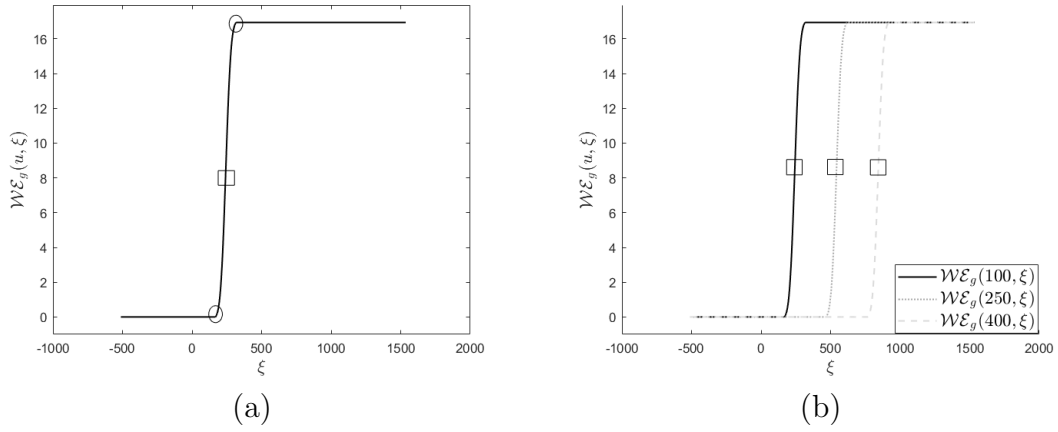

Figure 3.12: Section of the WEF in Fig.3.10(b). (a) $u = 100$: round markers denote the boundaries points of the interval where WEF is strictly increasing, i.e. $I(u) = [a_1(u), b_1(u)]$ and the rectangular marker denotes its middle point $m(u) = \frac{a_1(u)+b_1(u)}{2}$; (b) Sections at $u = 100, 250, 400$. As it can be observed, they are shifted copies of (a) and, in particular, at the middle point (rectangular marker) it holds $\mathcal{WE}_g(u, m(u)) = constant$.

Proposition 3.8. *The WEF of a constant amplitude monocomponent signal is constant along the characteristic curves of eq.*(3.13)*, i.e.*

$$\mathcal{WE}_g(u, \xi(u)) = constant,\ \xi(u) \in \mathcal{C}_{\phi,c},\ \forall\, u, \tag{3.14}$$

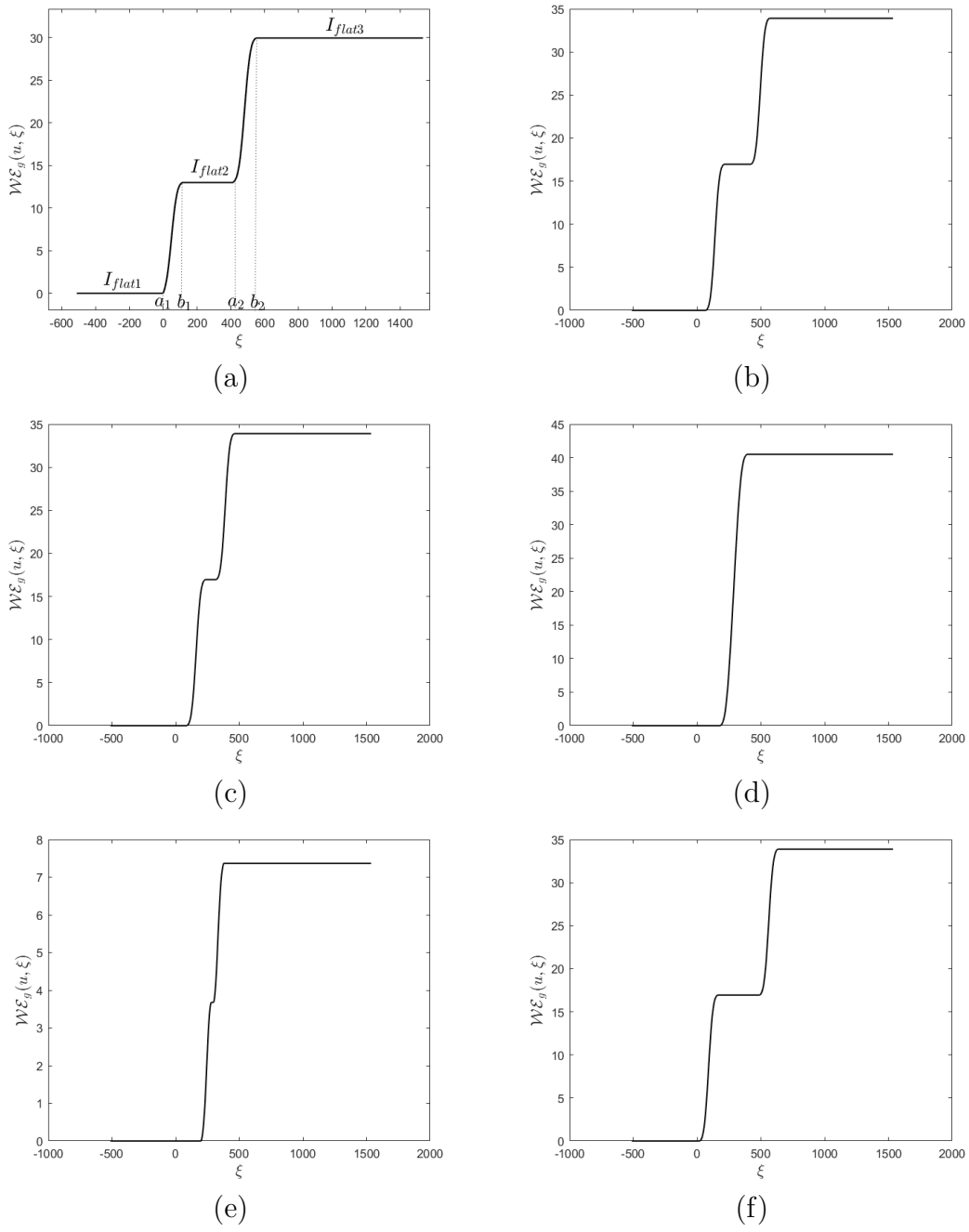

Figure 3.13: Sections of WEF in Fig.3.10(d) for different time instants u. (a) $u = 10$: modes are well separated in the TF plane, then WEF section presents three flat regions $I_{flat\,i}, i = 1, 2, 3$ and it strictly increases in $[a_1, b_1] \cup [a_2, b_2]$; (b)-(c) $u = 50, 100$: modes are separated but the internal flat region is reduced; (d) $u = 168$: u belongs to the non-separability region and only two flat regions are observed; (e) $u = 182$; (f) $u = 400$: modes are separated again.

Proof. The proof immediately follows from eq.(3.13). □

Fig.3.12 shows the transport phenomenon referred to the linear chirp in Fig.3.10(a). As it can be observed, for each fixed u, $\mathcal{WE}_g(u,\xi)$ increases over a compact interval I_1 whose boundary points depend on u, i.e. $I_1(u) = [a_1(u), b_1(u)]$, with

$$a_1(u) = \phi'(u) - \frac{\Delta\omega}{2} \text{ and } b_1(u) = \phi'(u) + \frac{\Delta\omega}{2}, \tag{3.15}$$

by definition. Formally, the following proposition holds true

Proposition 3.9. *For each fixed u, the WEF of a single mode is strictly increasing on the interval $I_1(u) = [a_1(u), b_1(u)]$, otherwise it is constant.*

Proof. $\bar{S}_f^g(u,\xi) \in L^1(\mathbb{R})$ with respect to ξ, then $W\mathcal{E}_g(u,\xi)$ is absolutely continuous and differentiable. By the Fundamental Theorem of Calculus for Lebesgue Integral it follows $\frac{\partial W\mathcal{E}_g(u,\xi)}{\partial\xi} = |\bar{S}_f^g(u,\xi)|^2$. Taking into account eq.(3.15), if $\xi : |\xi - \phi'(u)| > \frac{\Delta\omega}{2}$, then $\frac{\partial W\mathcal{E}_g(u,\xi)}{\partial\xi} = 0$ by definition. On the contrary, $\xi : |\xi - \phi'(u)| \leq \frac{\Delta\omega}{2} \Rightarrow |\bar{S}_f^g(u,\xi)| > 0$, i.e. $\frac{\partial W\mathcal{E}_g(u,\xi)}{\partial\xi} > 0$. □

Based on the theoretical results presented, we can list some important properties that apply to a monocomponent signal:

Property 1 For each fixed u, $\mathcal{WE}_g(u,\xi)$ striclty increases on $I_1(u) = [a_1(u), b_1(u)]$, with a_1 and b_1 such that

$$\lim_{\xi\to a_1(u)^-} \frac{\partial\mathcal{WE}_g(u,\xi)}{\partial\xi} = 0 \text{ and } \lim_{\xi\to a_1(u)^+} \frac{\partial\mathcal{WE}_g(u,\xi)}{\partial\xi} \neq 0 \tag{3.16}$$

$$\lim_{\xi\to b_1(u)^-} \frac{\partial\mathcal{WE}_g(u,\xi)}{\partial\xi} \neq 0 \text{ and } \lim_{\xi\to b_1(u)^+} \frac{\partial\mathcal{WE}_g(u,\xi)}{\partial\xi} = 0. \tag{3.17}$$

Proof. It follows from Prop.3.9, observing that $a_1(u), b_1(u)$ are discontinuity points for $\frac{\partial\mathcal{WE}_g(u,\xi)}{\partial\xi}$. □

Property 2 $I_1(u)$ has constant length.

Proof. Trivially, $b_1(u) - a_1(u) = \Delta\omega$, $\forall\, u$. □

Property 3 For each fixed u, the WEF of a single mode is constant over two disjoint compact intervals.

Proof. By Prop.(3.9), $\mathcal{WE}_g(u,\xi)$ is constant over each compact interval $I_K : I_K \subset (-\infty, a_1)\dot{\cup}(b_1, +\infty)$. □

Property 4

$$\mathcal{WE}_g(u,\xi(u)) = constant,\ \forall\, \xi(u) = (1-\lambda)\, a_1(u) + \lambda\, b_1(u), \text{with fixed } \lambda \in [0,1]. \tag{3.18}$$

Proof. By replacing eq.(3.15) in eq.(3.18), it follows $\xi(u) = \phi'(u) + \lambda\frac{\Delta\omega}{2}$. It thus belongs to the characteristic curve $\mathcal{C}_{\phi,c}$, with $c = \lambda\frac{\Delta\omega}{2}$ and the thesis follows from Prop.3.8. □

Property 1 characterizes the boundary points of the interval I_1. The latter has constant dimension, by Property 2. Property 3 tells us that the difference between the number of modes $N = 1$ and the number of disjoint flat regions in WEF section is always equal to 1—we will prove that this is true also for $N > 1$ well separated components. Finally, Property 4 can be visualized in Fig.3.12, showing that WEF is constant, for instance, at the middle point of I_1, i.e. $m_1(u) = \frac{a_1(u)+b_1(u)}{2}$.

Similarly to the discussion given in Chapter 2 concerning eq.(2.6), eq.(3.13) holds true also for MCS with well separated components. As a result, Properties 1–4 can be extended as well.

3.2.2 MCS

From now on, we will consider a MCS $f(t) = \sum_{k=1}^{N} f_k$ such that $supp\{f_k\} = [0,T]$, $T > 0$, $\forall\, k = 1, ..., N$.

In case of composite signals, WEF flat regions allow us to check if modes overlap with each other. For a comprehensive understanding, let us consider Fig.3.13 that depicts WEF sections of the two-components signal in Fig.3.10(c). (a)-(b)-(c) refer to increasing u in the separability region and, in this case, WEF is constant on $N + 1 = 3$ compact intervals, namely $I_{flat\,i}, i = 1, 2, 3$. Furthermore, WEF strictly increases over two compact disjoint intervals, with time-dependent boundary points a_1, b_1, a_2, b_2, as denoted in (a). The more the modes approach each other in the TF plane, the more $I_{flat\,2}$ reduces (c). At $\bar{u}$ belonging to the non-separability region (d), the window supports do overlap,

as $|\phi_1'(\bar{u}) - \phi_2'(\bar{u})| < \Delta\omega$, i.e. $[a_1(\bar{u}), b_1(\bar{u})] \cap [a_2(\bar{u}), b_2(\bar{u})] \neq \emptyset$. As a result, WEF presents only two flat disjoint regions and one interval where it strictly increases, i.e. $[a_1(\bar{u}), b_2(\bar{u})]$. While u increases, we exit the non-separability region (e)-(f) and we observe again $N+1=3$ flat disjoint regions. The above discussion can be generalized to $N \geq 2$ components, by means of the following proposition.

Proposition 3.10. *Let $f(t)$ be a MCS as defined in eq.(1.17) and let $\mathcal{WE}_g(u,\xi)$ be its WEF. Let us consider the set $I(u) = \cup_{k=1}^{N}[a_k(u), b_k(u)]$, where N denotes the number of modes and*

$$a_k(u) = \phi_k'(u) - \frac{\Delta\omega}{2}, \text{ and } b_k(u) = \phi_k'(u) + \frac{\Delta\omega}{2}, \forall\, k = 1, ..., N, \ \forall\, u \in \text{supp}\{f\}. \tag{3.19}$$

Then, the following properties hold true.

Property 1* *For each fixed u, $\mathcal{WE}_g(u,\xi)$ strictly increases over $I(u)$, whose boundary points are discontinuities of WEF derivative.*

Property 2* *$I(u)$ has constant length iff modes are well separated.*

Property 3* *If modes are well separated at time location u then $\mathcal{WE}_g(u,\xi)$ presents $N+1$ disjoint flat regions.*

Property 4* *If f_k is an isolated component, then*

$$\mathcal{WE}_g(u, \xi(u)) = constant, \forall\, \xi(u) = (1-\lambda)\, a_k(u) + \lambda\, b_k(u), \quad \text{with fixed } \lambda \in [0,1], \forall\, u. \tag{3.20}$$

Proof. **Property** 1*: $\bar{S}_f^g(u,\xi) \in L^1(\mathbb{R})$ with respect to ξ, then $W\mathcal{E}_g(u,\xi)$ is absolutely continuous and differentiable. By the Fundamental Theorem of Calculus for Lebesgue Integral it follows $\frac{\partial W\mathcal{E}_g(u,\xi)}{\partial \xi} = |\bar{S}_f^g(u,\xi)|^2$. Taking into account eq.(3.19), if $\xi : |\xi - \phi_k'(u)| > \frac{\Delta\omega}{2}$, $\forall\, k = 1, ..., N$, then $\frac{\partial W\mathcal{E}_g(u,\xi)}{\partial \xi} = 0$ by definition. On the contrary, if $|\xi - \phi_k'(u)| \leq \frac{\Delta\omega}{2}$ for some $k \in 1, ...N$ then $|\bar{S}_f^g(u,\xi)| > 0$, i.e. $\frac{\partial W\mathcal{E}_g(u,\xi)}{\partial \xi} > 0$, $\forall\, u \in [a_k(u), b_k(u)]$.

Property 2*: Modes are separable if $|\phi_k'(u) - \phi_j'(u)| > \Delta\omega$, $\forall\, k \neq j$, $\forall\, u \in$ *supp*$\{f\}$, then $[a_k(u), b_k(u)]$ are disjoint intervals. It follows $|I(u)| = \sum_{k=1}^{N}[b_k(u) - a_k(u)] = N\Delta\omega$. Conversely, if f_j and f_i are separable at u but do overlap at $\bar{u}$, then $[a_j(\bar{u}), b_j(\bar{u})] \cap [a_i(\bar{u}), b_i(\bar{u})] \neq \emptyset$ and $|I(\bar{u})| < |I(u)|$.

Property 3^*: Let $F : \phi'_k(u) + \frac{\Delta\omega}{2} < F$, $\forall\, k = 1, ..., N$, $\forall\, u \in supp\{f\}$. Since $\frac{\partial W\mathcal{E}_g(u,\xi)}{\partial\xi} = 0$, $\forall\, u \in [0, F] - \cup_{k=1}^{N}[a_k(u), b_k(u)]$, and $[a_k, b_k]$ are disjointed, then $W\mathcal{E}_g(u, \xi)$ is constant over the disjoint intervals $[0, a_1]$, $[b_k, a_{k+1}]$, $k = 1, ..., N-1$ and $[b_N, F]$.

Property 4^*: f_k is well separated from the other modes, $\forall\, u \in supp\{f\}$, then eq.(3.13) is satisfied $\forall\, \xi : |\xi - \phi'_k(u)| < \frac{\Delta\omega}{2}$ and Property 4^* holds true in $[a_k(u), b_k(u)]$, $\forall\, u$. □

3.2.2.1 Non-separability region localization

Based on Property 3^*, the non-separability region with respect to time can be defined as

$$\Omega_{int} = \{u : \max_u N_{flat}(u) < N + 1\}, \tag{3.21}$$

where $N_{flat}(u)$ is the number of compact and disjoint intervals such that $\mathcal{WE}_g(u, \xi)$ is constant and N is the number of modes. It is worth observing that if N is unknown, it can be operatively computed as $\max_u N_{flat}(u) - 1$.

If two modes are non-separable, then Property 2^* is not satisfied and the following proposition holds true.

Proposition 3.11. *Let $\mathcal{L}(u) = |I(u)|$ denote the length of $I(u) = \cup_{k=1}^{N}[a_k(u), b_k(u)]$ as in eq.(3.19). Then, for each couple of non-separable modes (f_k, f_j) there exists $u_{k,j} \in \arg\min \mathcal{L}(u)$. If modes do intersect with each other, then $(u_{k,j}, \phi'_j(u_{k,j}))$ is the crossing point between IFs curves.*

Proof. If f_k and f_j do overlap, then $[a_k(u), b_k(u)] \cap [a_j(u), b_j(u)] = I_{k,j} \neq \emptyset$, with $I_{k,j} = [a_k(u), b_j(u)]$ or $I_{k,j} = [a_j(u), b_k(u)]$. In addition, $\mathcal{L}$ is continuous and, since the non-separability regions of f are assumed separable, according to Def.15, there exists a compact interval $K \subset supp\{f\}$, such that

$$\mathcal{L}(u) = \sum_{i \neq k,j}(b_i(u) - a_i(u)) + |I_{k,j}(u)| = (N-2)\Delta\omega + |\phi'_j(u) - \phi'_k(u)|,\ \forall\, u \in K.$$

The thesis thus follows from Weierstrass Theorem, with $u_{k,j} := \min_{u\in K} \mathcal{L}(u) = \min_{u\in K} |\phi'_j(u) - \phi'_k(u)|$. If modes cross each other at u_0, i.e. $\phi'_k(u_0) = \phi'_j(u_0)$ then $u_{k,j} = u_0$. □

As a result, Ω_{int} can always be partitioned into disjoint subregions, i.e.

$$\Omega_{int} = \cup_{(k,j)}\Omega_{k,j},\ \text{with } \Omega_{k,j} \ni u_{k,j}, \tag{3.22}$$

assuming $\Omega_{i,j} = \emptyset$ if modes f_i and f_j are well separated.

Eq.(3.21) characterizes the non-separability region in time, but it does not provide any information concerning localization in frequency. Taking into account eq.(3.22), for each $u \in \Omega_{k,j}$, the discontinuity points of WEF derivative provide the region where WEF strictly increases, according to Property 1^*. As an example, let $u = 170$ belongs to the central non-separability region of the spectrogram in Fig.3.14(a). The corresponding WEF section, shown in Fig.3.14(c), increases over the disjoint intervals I_1 and I_2, whose boundary points are WEF derivative discontinuities. The first interval refers to the non-separability region—the one we are interested in— while the second is due to the contribution of the isolated constant chirp component, which has to be excluded, as depicted in Fig.3.14(d). Property 4^* offers a criterion for detecting (and then discarding) the isolated contribution. More precisely, the condition in eq.(3.14) can be checked both on I_1 and I_2, at the middle points m_1 and m_2, as denoted in Fig.3.14(e)-(f). The interval where the condition in eq.(3.20) is met is recognized as the isolated mode support and then discarded. As a result, the strip corresponding to interference is $\Omega_u = \{u\} \times I_{\bar{i}}(u)$, with $\bar{i} = 1$. The TF non-separability region is then defined as the union of the detected strips, i.e.

$$\mathbf{\Omega} = \bigcup_{u \in \Omega_{int}} \Omega_u.$$

The presented study can be applied to automatically detect the non-separability region of a MCS. The next section summarizes the whole procedure and provides some experimental results.

3.2.2.2 Algorithm and some results

WEF definition requires IFs knowledge, which is the unknown. A practical implementation of eq.(3.11) is possible by considering a spectrogram thresholding at level $\Theta > 0$, i.e.

$$\bar{P}(u,\xi) = \begin{cases} |S_f^g(u,\xi)|^2 & \text{if } |S_f^g(u,\xi)|^2 \geq \Theta \\ 0 & \text{otherwise;} \end{cases} \tag{3.23}$$

that provides a subset of characteristic curves of eq.(2.6), i.e. $\mathcal{C}_{\phi,c}$, with $c \leq \frac{\Delta\omega}{2}$. The threshold Θ can be set equal to the 10% of spectrogram maximum value.

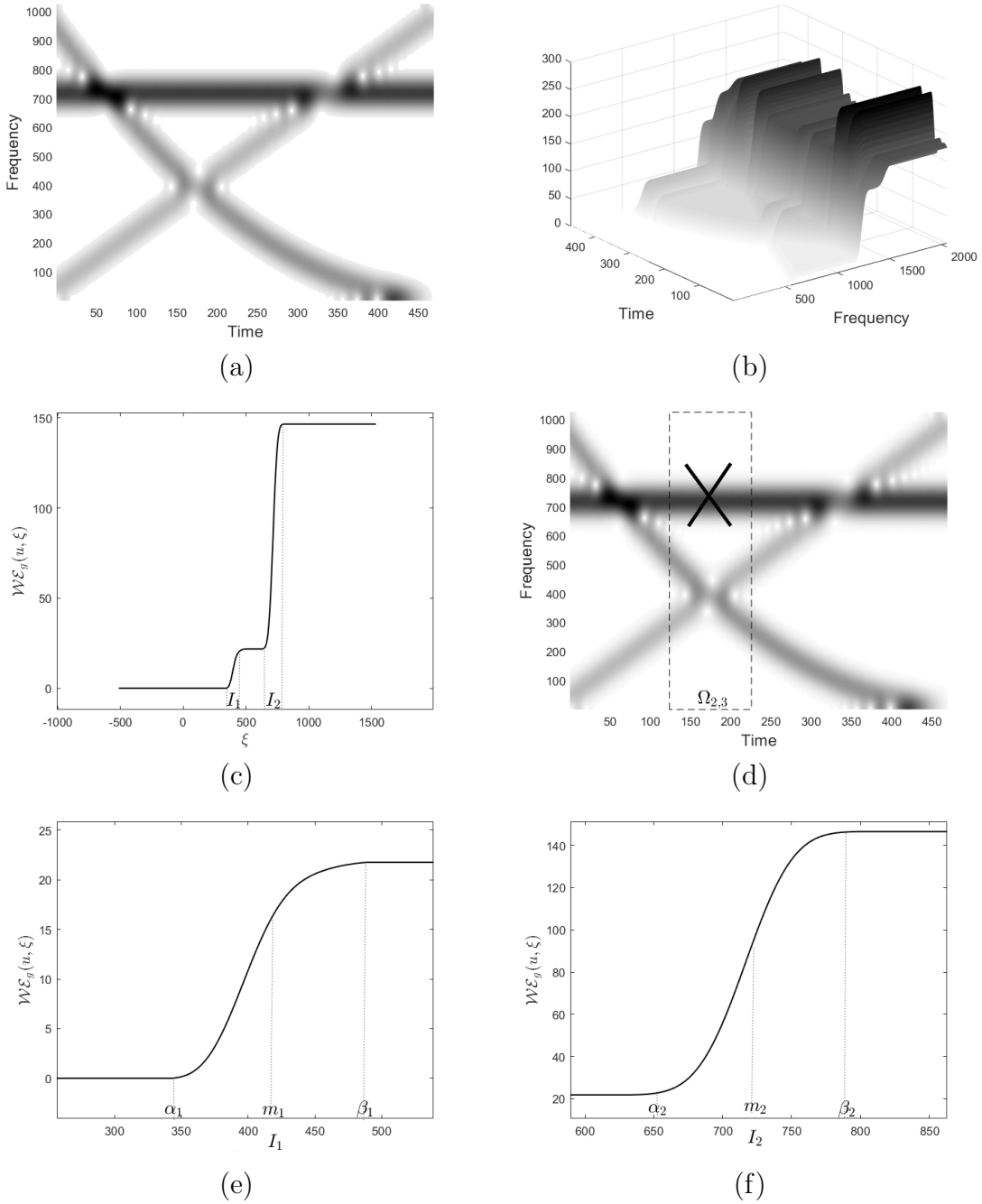

Figure 3.14: Three-components signal with non-separable modes and different constant amplitudes. (a) Spectrogram; (b) WEF; (c) WEF section at $u = 170$ belonging to a non-separability region; (d) The support of the linear chirp has to be excluded in non-separability region detection; (e)-(f) Section in (c) restricted to I_1 and I_2. Interval middle points are denoted by $m_i, i = 1, 2$.

WEF can be then computed as

$$\mathcal{WE}_g(u,\xi) = \int_0^{\xi} \bar{P}(u,\xi')d\xi'. \tag{3.24}$$

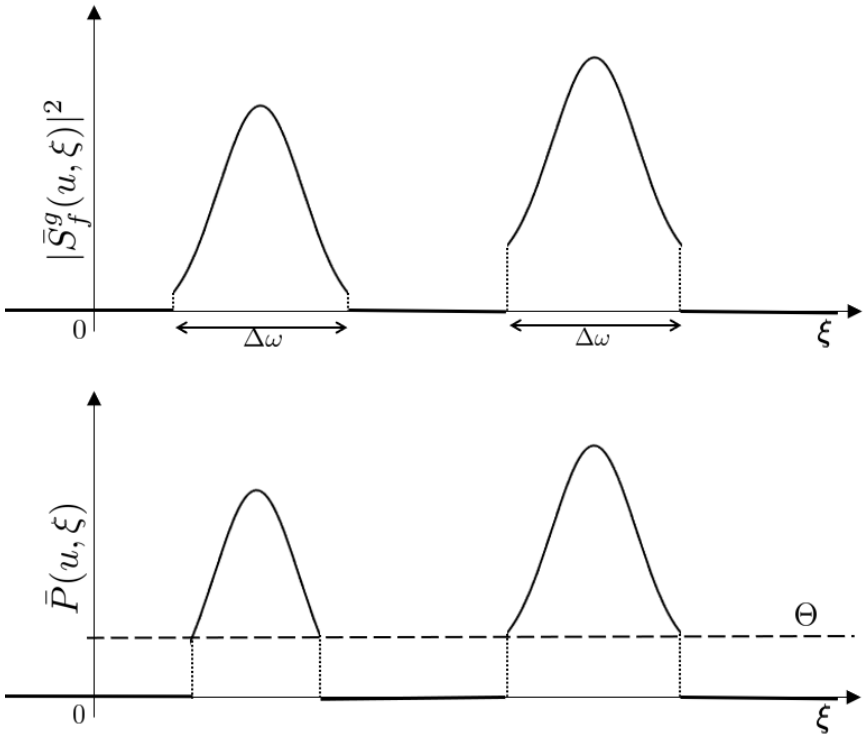

Figure 3.15: Practical WEF implementation, two-components signal: $|\bar{S}_f^g(u,\xi)|^2$ according to eq.(3.11) (top) and the thresholded spectrogram $\bar{P}(u,\xi)$ at level Θ, as in eq.(3.24) (bottom).

It is worth observing that using eqs.(3.23) and (3.24) is conceptually equivalent to set a smaller frequency bandwidth in WEF definition (see Fig.3.15) and then the results presented in the previous section remain valid. In particular, the boundary of the intervals where WEF strictly increases still characterizes the non-separability region in frequency, in fact they are discontinuity points of WEF derivative, i.e.

$$\lim_{\xi\to\alpha_i^-} \frac{\partial \mathcal{WE}_g(u,\xi)}{\partial\xi} = 0 \text{ and } \lim_{\xi\to\alpha_i^+} \frac{\partial \mathcal{WE}_g(u,\xi)}{\partial\xi} \neq 0 \tag{3.25}$$

$$\lim_{\xi\to\beta_i^-} \frac{\partial \mathcal{WE}_g(u,\xi)}{\partial\xi} \neq 0 \text{ and } \lim_{\xi\to\beta_i^+} \frac{\partial \mathcal{WE}_g(u,\xi)}{\partial\xi} = 0. \tag{3.26}$$

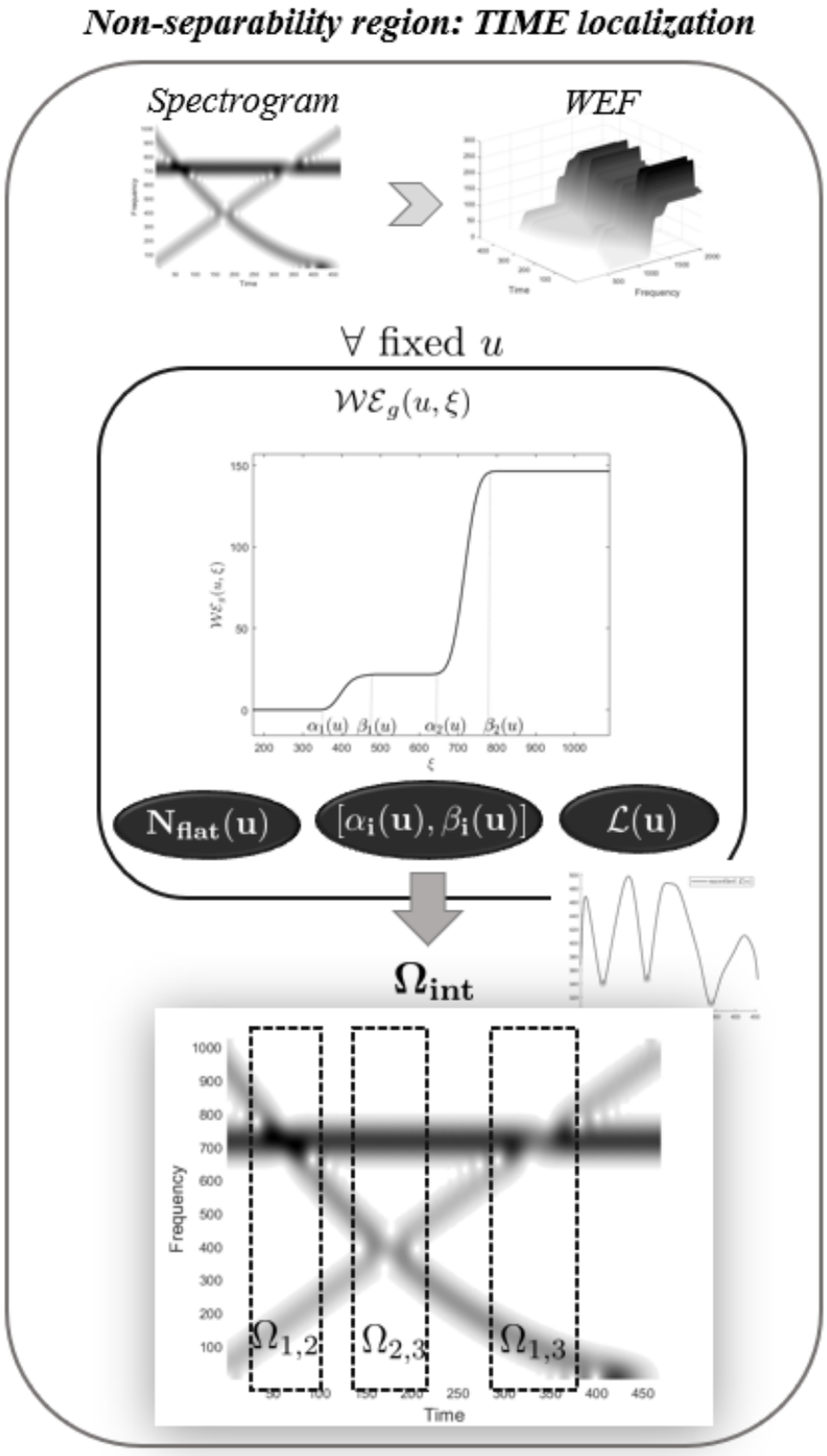

Figure 3.16: Non-separability region localization in time. WEF is analyzed section by section. For each fixed u, the number of flat regions $N_{flat}(u)$, the intervals $[\alpha_i(u), \beta_i(u)]$ where $\mathcal{WE}_g$ stricly increases and $\mathcal{L}(u) = \sum_i(\beta_i(u) - \alpha_i(u))$ are computed. Ω_{int} can be thus determined according to eq.(3.21) and partitioned by means of $\mathcal{L}(u)$ minima.

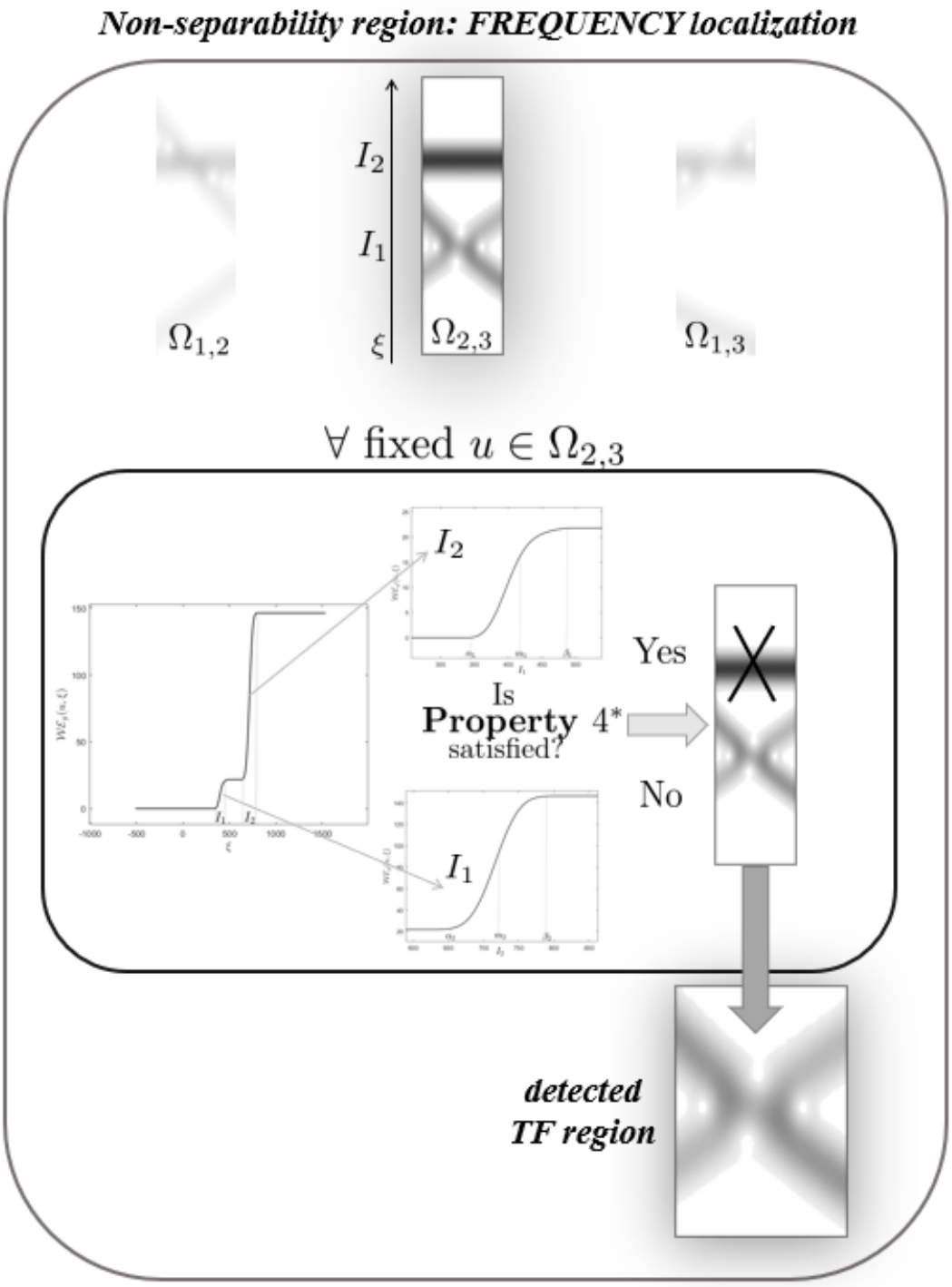

Figure 3.17: Non-separability region localization in frequency. The subregion $\Omega_{2,3}$ is considered. For each $u \in \Omega_{2,3}$, $\mathcal{WE}_g$ is analyzed for selecting the frequency interval corresponding to non-separable modes' support. Condition in eq.(3.20), with $\lambda = 0.5$, is checked both on I_1 and I_2. The latter is met on I_2— the constant chirp support— so that I_2 is discarded. The procedure has to be repeated on $\Omega_{1,2}$ and $\Omega_{1,3}$.

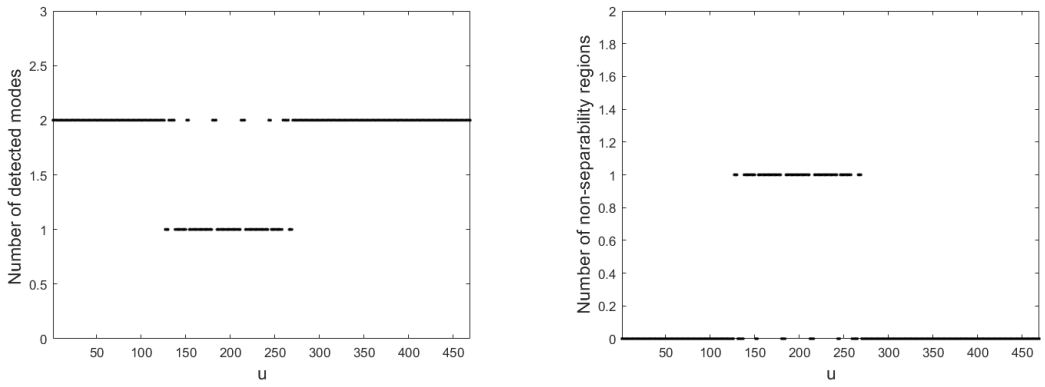

(a) (b)

Figure 3.18: (a) Number of detected components by the analysis of WEF in Fig.3.10(d) as a function of time u; (b) The non-separability region Ω_{int} is the time interval where the number of detected modes in (a) is less than 2, i.e. the maximum of observed components.

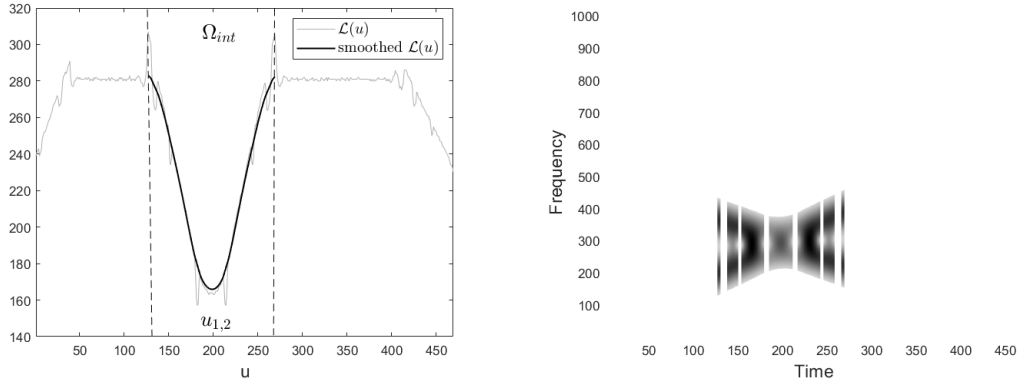

(a) (b)

Figure 3.19: Non-separability region detection. (a) Function $\mathcal{L}(u)$. The non-separability region in time Ω_{int} belongs to the intervals delimited by the dashed lines. The smoothed version of $\mathcal{L}(u)$ is minimum at $u_{1,2}$, that corresponds to the crossing point between modes; (b) Detected non-separability region $\mathbf{\Omega}$.

The step required by the proposed procedure are listed below. Fig.3.16 and Fig.3.17 provide a chart of the algorithm when applied to the three-components signal in Fig.3.14(a).

Detection in time (Fig.3.16)

1. Threshold the spectrogram and compute $\mathcal{WE}_g$ according to eq.(3.24);

2. $\forall\, u$, compute the number of plateaux $N_{flat}(u)$ of $\mathcal{WE}_g$ and set $N =$

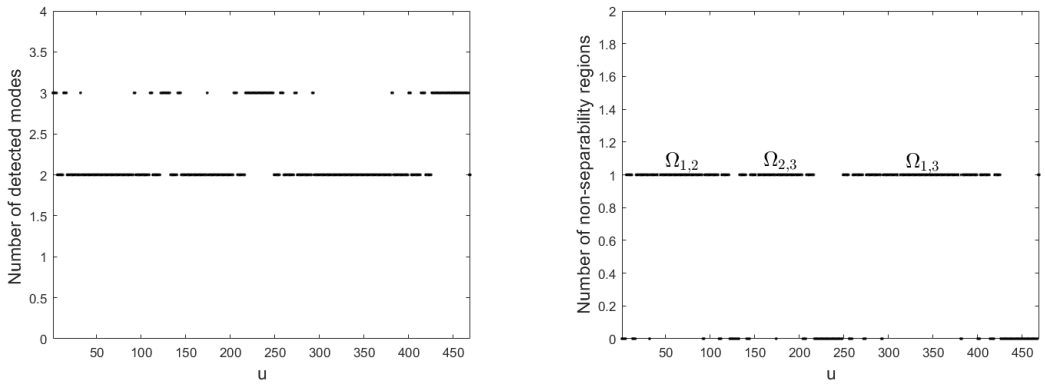

(a) (b)

Figure 3.20: (a) Number of detected components by the analysis of WEF in Fig.3.14(b) as a function of time u; (b) The non-separability region Ω_{int} is the time interval where the number of detected modes in (a) is less than the maximum of observed components. The latter is partitioned into the subregions $\Omega_{1,2}, \Omega_{2,3}, \Omega_{1,3}$.

$max_u N_{flat}(u) - 1$ as the number of modes;

3. determine the non-separability region in time Ω_{int} and its partition $\{\Omega_{k,j}\}_{(k,j)}$, according to eq.(3.21) and eq.(3.22);

4. $\forall\, u$, select $\{[\alpha_i(u), \beta_i(u)]\}_i$ according to eqs.(3.25)-(3.26), set $\mathcal{L}(u) = \sum_i (\beta_i(u) - \alpha_i(u))$ and compute its smoothing;

5. compute the minima $\{u_{k,j}\}_{(k,j)}$ of the smoothed $\mathcal{L}(u)$ and localize them in $\Omega_{k,j}$, determined in step 3.

Detection in frequency (Fig.3.17)

For each $(k, j) : \Omega_{k,j} \neq \emptyset$ in step 3

6. $\forall\, u \in \Omega_{k,j} \subset \Omega_{int}$,

   6.1 for each interval $[\alpha_i(u), \beta_i(u)], i = 1, 2, ..., N-1$, detected in step 4, compute the middle point $m_i = \frac{\alpha_i(u) + \beta_i(u)}{2}$;

   6.2 retain only the $\bar{i}$-th interval s.t. $\mathcal{WE}_g(t, m_{\bar{i}}) \neq constant$, with $t \in \Omega_{k,j}$;

   6.3 set $\mathbf{\Omega_u} = \{u\} \times [\alpha_{\bar{i}}, \beta_{\bar{i}}]$.

7. Set $\mathbf{\Omega} = \bigcup_u \mathbf{\Omega_u}$.

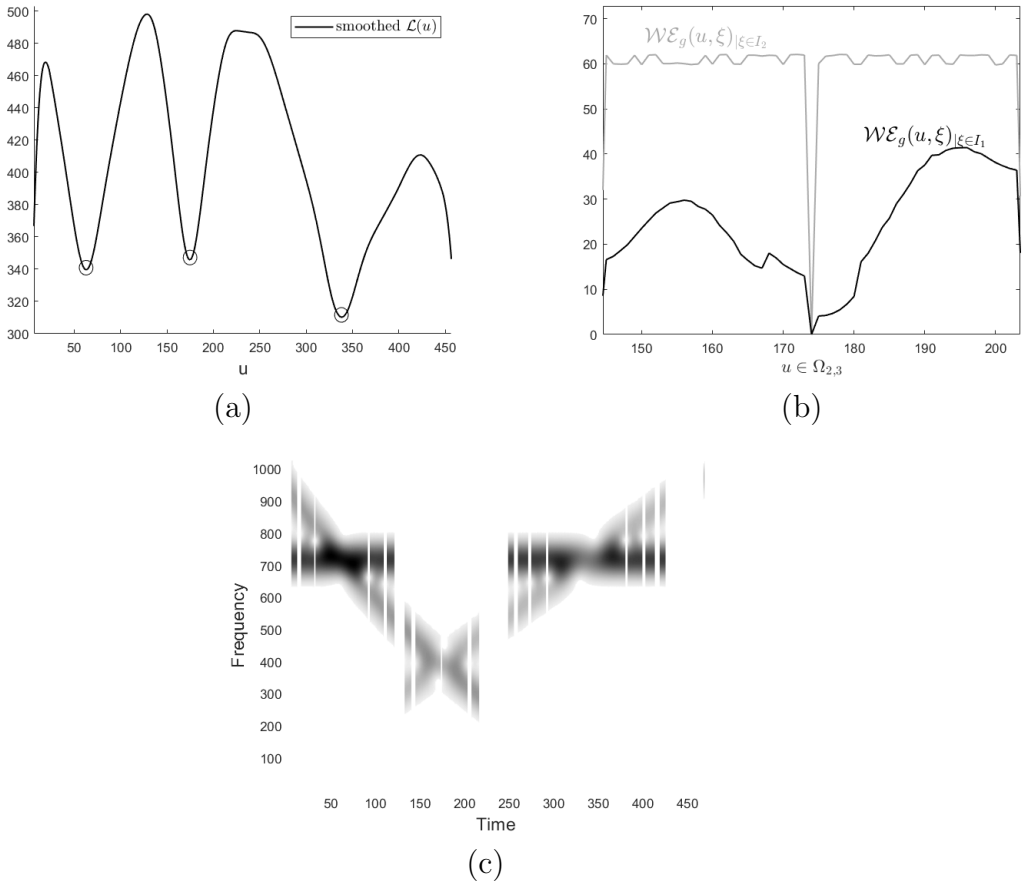

Figure 3.21: Non-separability region detection. (a) Smoothed $\mathcal{L}(u)$ whose minima identify crossing points between modes; (b) $\mathcal{WE}_g(u,\xi)$, with $u \in \Omega_{2,3}$. WEF strictly increases over the two intervals I_1 and I_2, as in Fig.3.14(c). Since the constant chirp is well separated from the other modes at $\Omega_{2,3}$, it holds $\mathcal{WE}_g(u,\xi)_{\xi\in|I_2} = constant$, while it significantly oscillates for $\xi \in I_1$; (c) Detected TF non-separability region $\mathbf{\Omega}$.

As first numerical example, let us consider the spectrogram of the two-components signal in Fig.3.10(c). WEF analysis allows to determine the number of modes and to localize the non-separability region in time, as shown in Fig.3.18. Fig.3.19(a) shows that $\mathcal{L}(u)$ realizes its minimum at the crossing point between modes, according to Prop.3.11. Finally, the region is localized in frequency by selecting only the interval where WEF stricly increases, as shown in Fig.3.19(b).

Fig.3.20 refers to the three-components signal in Fig.3.14(a). As it can be observed, Ω_{int} is partitioned into three subregions. Each of them corresponds to a minimum of the smoothed $\mathcal{L}(u)$, as shown in Fig.3.21(a). By processing each subregion separately, frequency localization is done by checking Property 4* at

the middle point of each interval where WEF strictly increases, namely $I_1(u)$ and $I_2(u)$ in this example. As shown in Fig.3.21(b), WEF is almost constant on the interval I_2, while it significantly oscillates on I_1. For this reason, only I_1 is retained. Fig.3.21(c) shows the final result. At this point, a reconstruction technique, as the one reviewed in Section 3.1.1, could be applied on each non-separability subregion to recover IFs curves.

3.2.2.3 Some remarks and conclusions

The presented method is a spectrogram-based technique which allows to automatically detect the eventual non-separability regions of a MCS. Actually, similar results are expected if a different TF density is used, provided it is smooth and concentrates the distribution along the ridge curve—for instance, the scalogram. As main advantage, the proposed method is able to deal with interfering modes having different frequency modulations and constant amplitudes, resulting in a powerful tool for IFs curves' reconstruction techniques. The application of the method to AM-FM MCS will be one of the main objectives of future studies.

3.3 Multidirectional energy analysis: Radon Spectrogram Distribution

Given a function F defined on the plane, its RT at (r, θ) is the integral of F along the line which is orthogonal to the direction identified by θ and located at distance r (with sign) to the origin. The energy function $\mathcal{E}_g(u)$ in eq.(3.1) can be thus understood as the RT of the spectrogram at points $(u, 0)$, with u varying in the signal support. In order to extend the energy-based approach presented in Section 3.1, we now consider the combination of spectrogram and RT, namely Radon Spectrogram Distribution (RSD), as depicted in Fig.3.22. First, Section 3.3.1 deepens the motivation for adopting RSD in crossing MCS' analysis; then Sections 3.3.2 and 3.3.3 contain some original theoretical results concerning the topic and, finally, Section 3.3.4 is devoted to an application of the presented study.

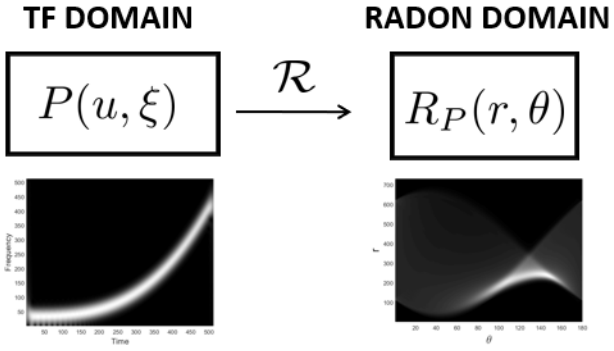

Figure 3.22: The RT of the spectrogram $P(u,\xi)$ results in the Radon Spectrogram Distribution $R_P(r,\theta)$ (RSD).

3.3.1 Separability in Radon domain

Fig.3.23 depicts the RT of the spectrogram of a constant amplitude LFM signal and the RT of a TF representation perfectly concentrated on the ridge curve. As it can be observed, both the distributions peak at the same point, that is (r_0, θ_0) identifying the ridge curve. Indeed, according to Prop.2.5, the spectrogram is constant along the characteristic curves of eq.(2.6). For linearly modulated signals, the latter are lines and since RT integrates along lines, it is the suitable tool to reveal the direction of the transport. If the number of components N is known in advance, the detection task turns into simply finding N peaks, that is why RT (as well as RW) is widely used as LFM signals detector in MCS analysis. On the contrary, non-linearly FM MCSs have more spread representations in Radon domain, as shown in Fig.3.24, making the detection task less trivial.

It is worth noticing that two well separated components in the TF plane are not guaranteed to be separable in Radon domain. For instance, the two parallel LFM signals in Fig.3.25(a) can not be easily disclosed in Radon domain as the RT in Fig.3.25(e) is influenced by artefacts. Although better concentrated, RW in Fig.3.25(f) is also ambiguous, as it still shows four peaks, instead of two. On the other hand, two modes that cross in TF plane, and thus do not satisfy the separability condition in Def.6, can appear separated in Radon domain, as in the case depicted in Fig.3.26. By summarizing, there exists a sort of duality between separability in TF and Radon domain; in addition the ability of RT in revealing crossing components makes it suitable for MCS analysis. As a matter of fact, Fig.3.27(b) better shows that there exist several isolevel curves

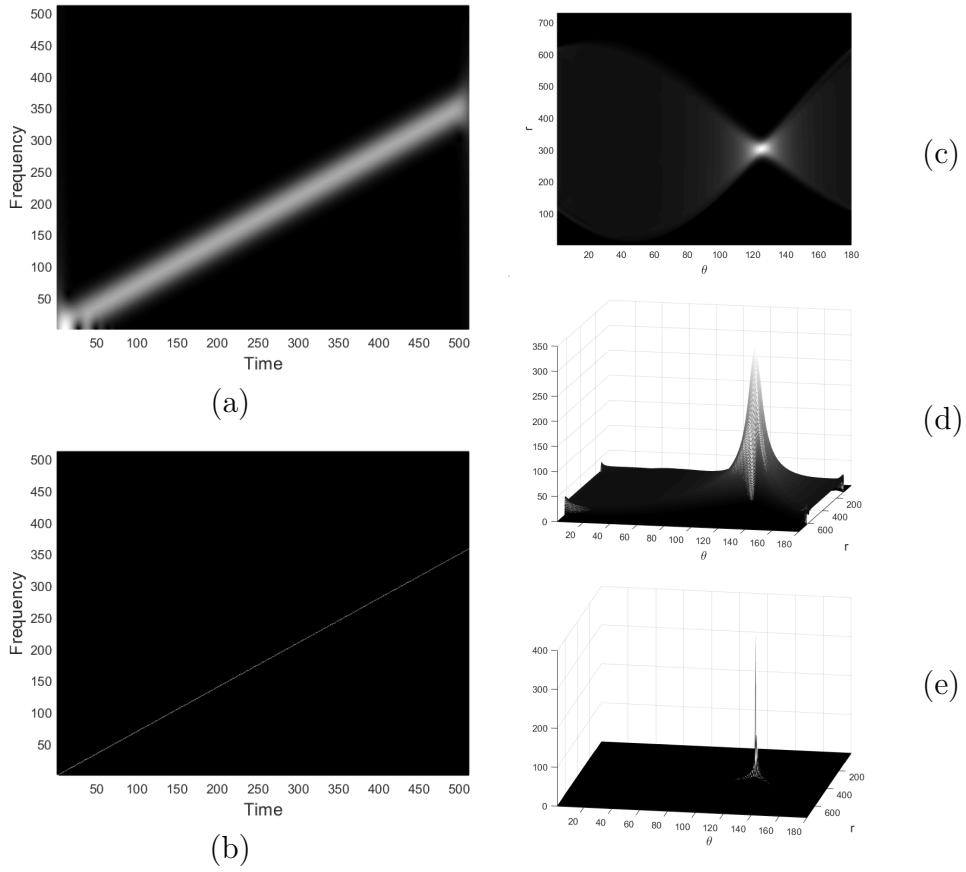

Figure 3.23: LFM signal. (a) Spectrogram; (b) Ideal TF representation located at the ridge curve; (c) RT of the spectrogram in (a), view from above; (d) 3d view of (c); (e) RT of (b), 3d view.

of separation and then, in this case, it is possible to disclose the two modes by choosing a proper threshold level. The latter observation can be exploited for defining a method for IFs discrimination, quite independent of the specific frequency modulation, as it will be explained in Section 3.3.4.

3.3.2 Ridge points representation

This section aims at investigating the relation between IF and RSD. As a starting point, the representation of ridge points in Radon domain is derived and a law with respect to r and θ describing IF curve is proposed.

To this aim, let us consider the ridge curve parametrization $(t, \phi'(t)), t \geq 0$

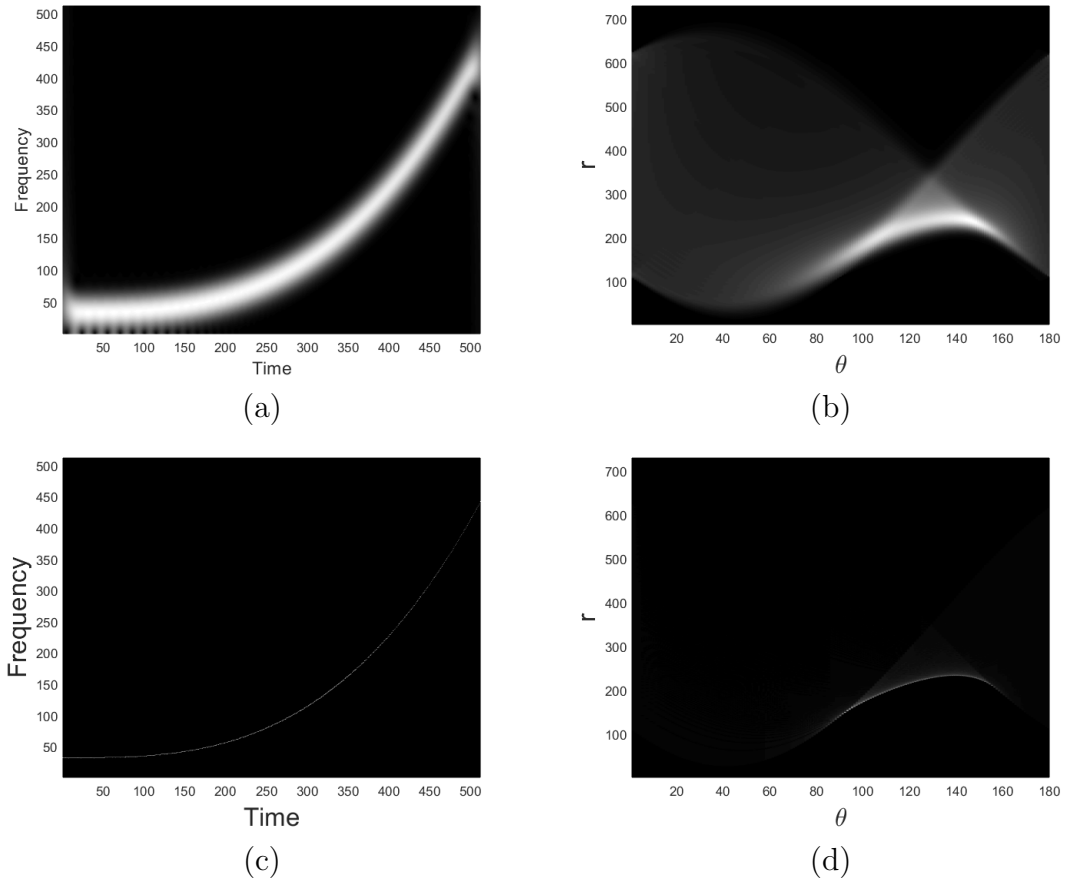

Figure 3.24: Non-linearly FM signal. (a) Spectrogram; (b) RT of the spectrogram in (a); (c) Ideal TF representation located at the ridge curve; (d) RT of (c).

and a TF representation perfectly localized on the ridge curve, i.e.

$$\rho(u,\xi) = \int_0^{+\infty} \delta(u-t)\delta(\xi - \phi'(t))\, dt,\ (u,\xi) \in \mathbb{R}^2,$$

then the following proposition provides the representation of the ridge curve in Radon domain.

Proposition 3.12. *The RT of* $\rho(u,\xi)$ *is*

$$R_\rho(r,\theta) = \int_0^{+\infty} \delta(r - t\,\cos\theta - \phi'(t)\,\sin\theta)\, dt. \tag{3.27}$$

Proof. The proof follows by first computing the RT of the delta function centered at the origin and then exploiting the shifting property, as follows. Let $\mathcal{R}$

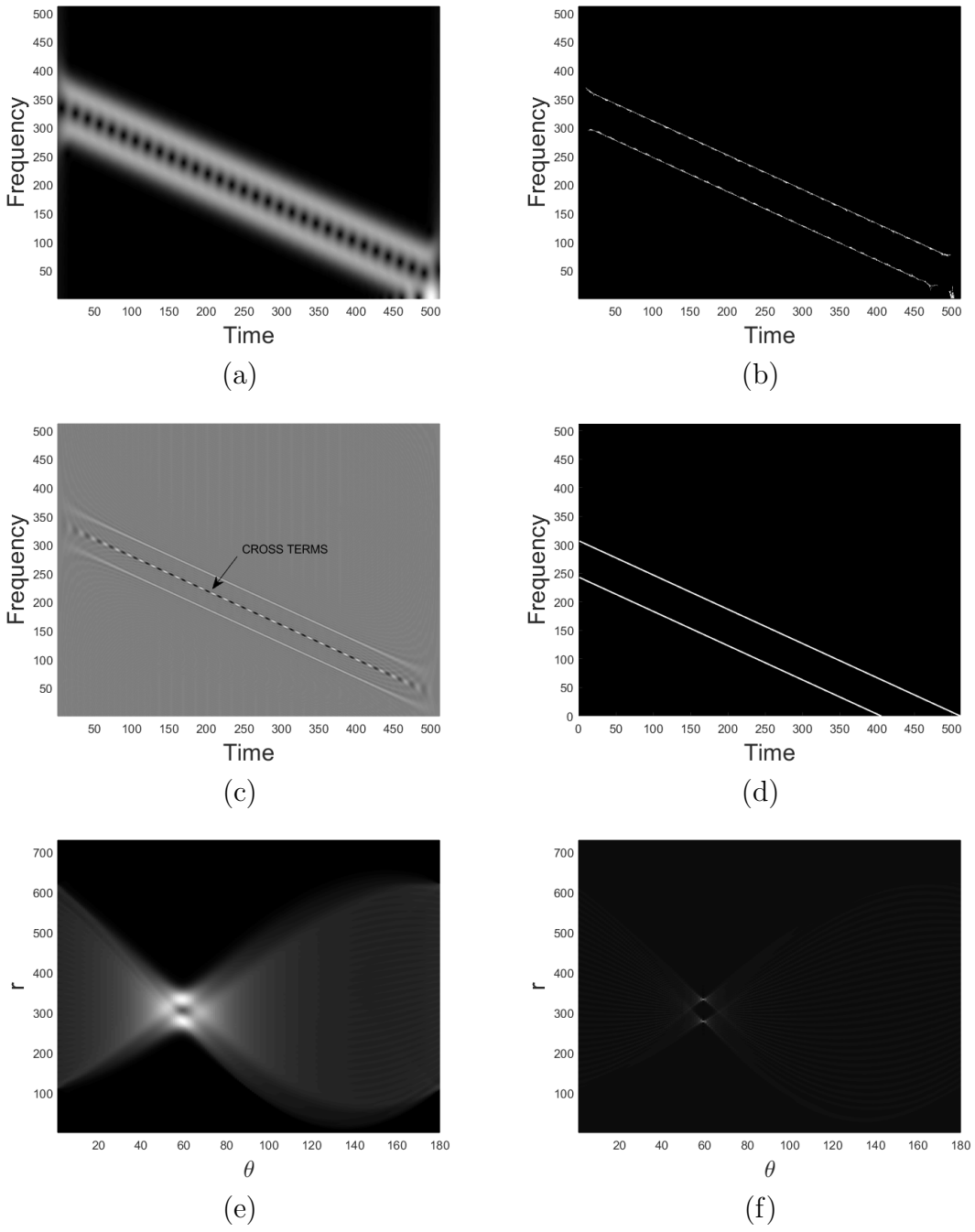

Figure 3.25: Separable components. (a) Spectrogram; (b) Reassigned spectrogram; (c) WVD; (d) Ideal TF representation perfectly concentrated on IF curves; (e) RT of the spectrogram in (a); (f) RT of the WVD in (c) [108].

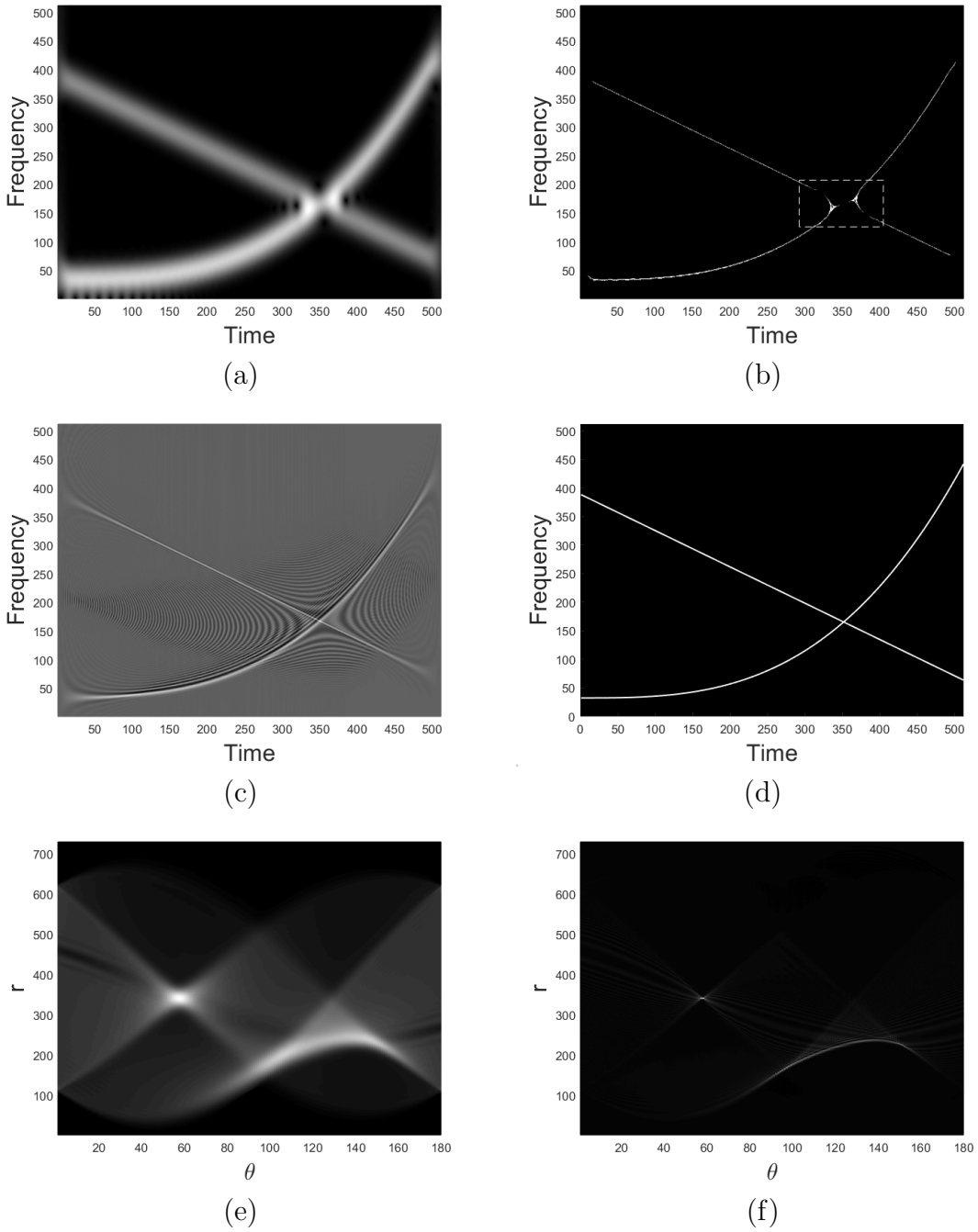

Figure 3.26: Overlapping components. (a) Spectrogram; (b) Reassigned spectrogram. The non-separability region is emphasized by the dashed box; (c) WVD; (d) Ideal TF representation perfectly concentrated on IF curves; (e) RT of the spectrogram in (a); (f) RT of the WVD in (c) [108].

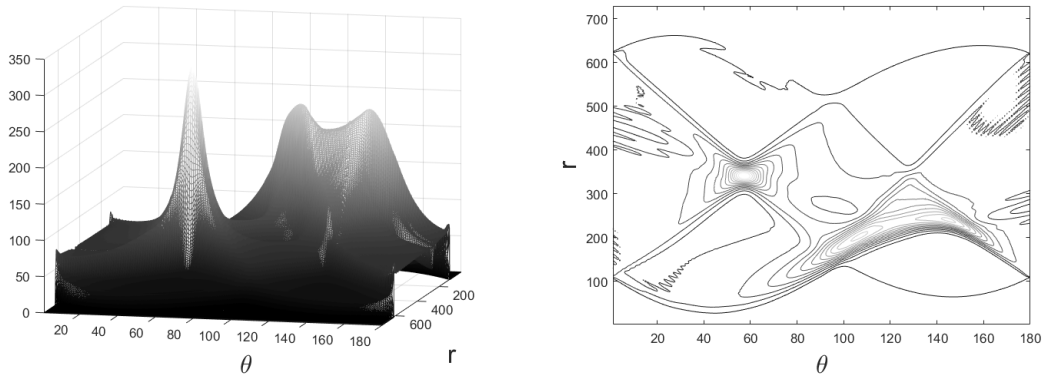

(a) (b)

Figure 3.27: (a) 3d view of RT in Fig.3.26(e) and its isolevel curves (b). As it can be observed, there exist several level sets in (b) that define two separated connected components.

be the Radon operator, then

$$\begin{aligned}\mathcal{R}[\delta(u,\xi)] &= \int_{\mathbb{R}} \delta(u,\xi)\delta(r-u\cos\theta-\xi\sin\theta)\,du\,d\xi \\ &= \frac{1}{2\pi}\int_{\mathbb{R}} \delta(u,\xi)\int_{\mathbb{R}} e^{-ik(r-u\cos\theta-\xi\sin\theta)}\,dk\,du\,d\xi\end{aligned}$$

$$= \frac{1}{2\pi}\int_{\mathbb{R}} e^{-ikr}\int_{\mathbb{R}} e^{ik(u\cos\theta+\xi\sin\theta)}\delta(u,\xi)\,du\,d\xi\,dk = \frac{1}{2\pi}\int_{\mathbb{R}} e^{-ikr}\,dk = \delta(r).$$

The shifting property gives us the RT of a single ridge point $(t,\phi'(t))$, i.e.

$$\mathcal{R}[\delta(u-t,\xi-\phi'(t))] = \delta(r-t\cos\theta-\phi'(t)\sin\theta).$$

Eq.(3.27) straightforward follows by integrating with respect to t. □

Definition 18. *The* ***mapped ridge curve*** $\mathcal{M}$ *is defined as the support of* $R_\rho(r,\theta)$*, i.e.*

$$\{(r,\theta) : r(t) = t\cos\theta+\phi'(t)\sin\theta,\ t\geq 0\} \subseteq \mathbb{R}\times\left(-\frac{\pi}{2},\frac{\pi}{2}\right]. \tag{3.28}$$

It is worth noticing that a single TF point is then mapped by RT to a curve in the Radon domain; therefore, the ridge curve is mapped into a set of curves, which is referred as $\mathcal{M}$, as depicted in Fig.3.28. For this reason, it is not

possible to directly define a curve $r(\theta)$ representing the ridge points in Radon domain. However, the goal is achieved by considering the envelope of the family of curves in the Radon domain. Indeed, as shown in Fig.3.29, curves belonging to $\mathcal{M}$ "accumulate" on a curve which appears to be tangent to $\mathcal{M}$. The latter is recognized as the envelope of $\mathcal{M}$, according to the following

Proposition 3.13. *Let $f(t) = a(t)\cos\phi(t)$. If $\phi''(t)$ is strictly monotone, the envelope of the mapped ridge curve $\mathcal{M}$ is the curve $(\theta_0, r(\theta_0))$, with $\theta_0 = -\arctan\frac{1}{\phi''(t)}$ and*

$$r(\theta_0) = \phi''^{-1}(\cot\theta_0)\cos\theta_0 + \phi'(\phi''^{-1}(\cot\theta_0))\sin\theta_0. \tag{3.29}$$

Proof. Proof is in Appendix B. □

Prop.3.13 provides the desired ridge point representation in Radon domain only depending on θ_0 and also a parametric representation, i.e.

$$\begin{cases} r(\theta_0) = t\cos\theta_0 + \phi'(t)\sin\theta_0 \\ \theta_0(t) = -\arctan\frac{1}{\phi''(t)}. \end{cases} \tag{3.30}$$

The knowledge of points belonging to the envelope in eq.(3.29) is sufficient to recover the ridge curve in the TF plane. Indeed, each fixed θ_0 defines the point $(r(\theta_0), \theta_0)$ representing the line $r(\theta_0) = u\cos\theta_0 + \xi\sin\theta_0$, i.e. the line passing through $(t_0, \phi'(t_0))$, with slope $\theta_0(t_0)$. By considering Lebesgue measure $\mathcal{L}$, we can say that the inverse RT should map a single point into a line—more precisely, a delta located in a single point should be mapped to a representation whose support is a line, i.e.

$$\mathcal{R}_{\mathcal{L}}^{-1}(\delta(r - r(\theta_0), \theta - \theta_0)) = \delta\left(t_0\cos\theta_0 + \phi'(t_0)\sin\theta_0 - u\cos\theta_0 - \xi\sin\theta_0\right), \tag{3.31}$$

whose support is the line

$$\xi(u) = t_0\frac{\cos\theta_0}{\sin\theta_0} + \phi'(t_0) - u\frac{\cos\theta_0}{\sin\theta_0},$$

such that $\frac{d\xi}{du} = -\cot\theta_0 = \phi''(u)$. For this reason, by associating each distribution $\mathcal{R}_{\mathcal{L}}^{-1}(r(\theta_0))$ to the corresponding support, we come up with a lines family whose envelope is the ridge curve. The procedure is sketched in Fig.3.30.

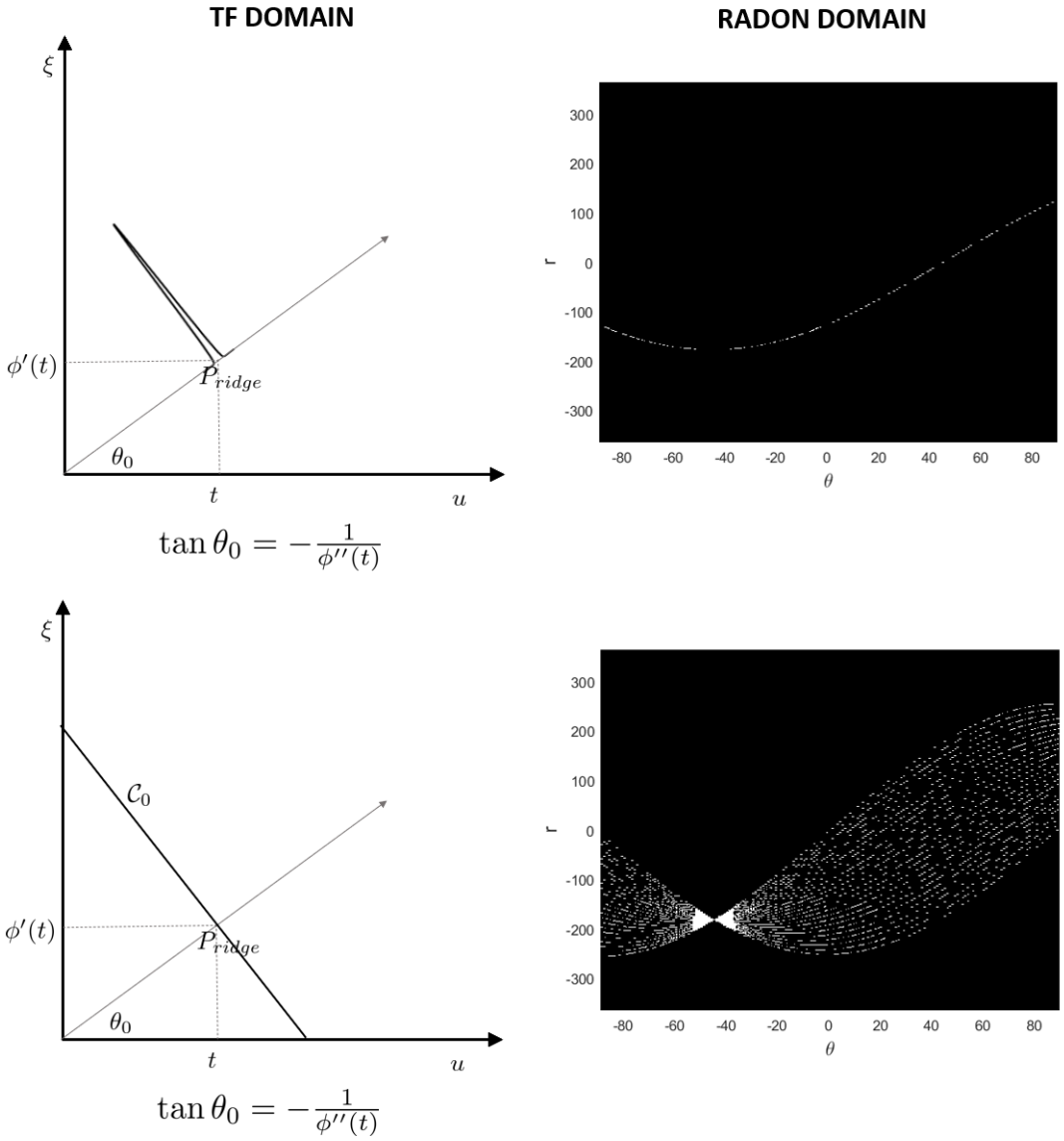

Figure 3.28: Top : RT of a delta function located at the ridge point $(t, \phi'(t))$. Bottom: RT of the ridge curve (linear case).

3.3.2.1 RW and RSD as mapped ridge curve detectors

It is well known that the Wigner Ville Transform of a monocomponent signal $f(t) = a\cos\phi(t)$ is concentrated on the IF curve of the signal. For this reason, we expect that the RT of WVD (i.e. the RW) provides a representation which is somehow close to the RT of the ridge curve R_ρ. Indeed, experimentally it turns out that the envelope of R_ρ is close to RW maxima along the radial direction,

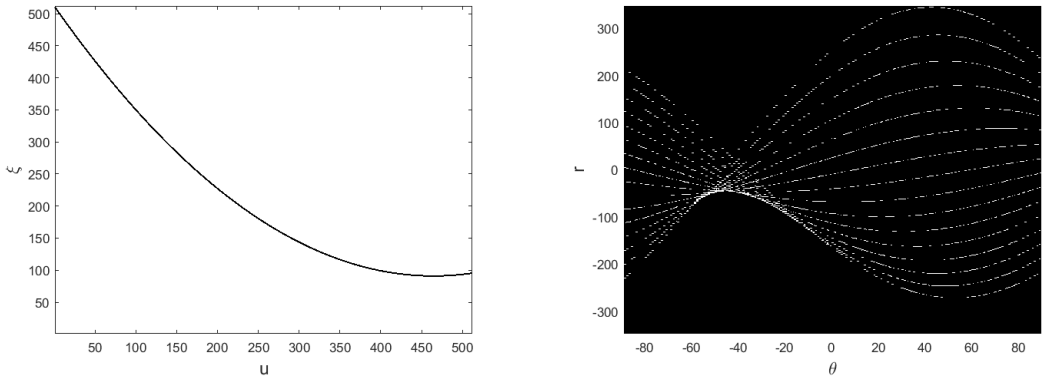

(a) (b)

Figure 3.29: Representation of the ridge curve in Radon domain. (a) TF representation perfectly localized on a non-linear ridge curve; (b) Support of the RT of (a), i.e. $\mathcal{M}$: the envelope of $\mathcal{M}$ consists in those points where the curves "accumulate".

i.e. the points realizing

$$\max_r RW(r,\theta),$$

as shown in Fig.3.31. Thanks to its high resolution properties, RW seems to be more suitable for ridge curve identification in Radon domain. Unfortunately, RW is very sharp, making the detection task unreliable for non-linearly modulated signals. On the contrary, RSD is smooth and its adoption allows to frame the detection problem in the context of the study proposed in Chapter 2. For this reason, RSD is preferable for our purpose.

Unfortunately, the maxima of the RSD, i.e. $\max_r R_P(r,\theta)$, appear shifted with respect to the ones observed in R_ρ, as depicted in Fig.3.32. In a first approximation, the latter is explained by the RT convolution property. Indeed, according to eq.(1.7), the spectrogram can be expressed as a smoothing of the WVD, i.e.

$$P(u,\xi) = \frac{1}{2\pi} WV_f(u,\xi) * *WV_g(u,\xi),$$

then

$$\mathcal{R}[P] = \frac{1}{2\pi}\mathcal{R}[WV_f] * \mathcal{R}[WV_g]. \tag{3.32}$$

A similar relation occurs by considering $P(u,\xi) = \frac{a^2}{2}\hat{g}(\xi - \phi'(u))$, as in Prop.1.1.

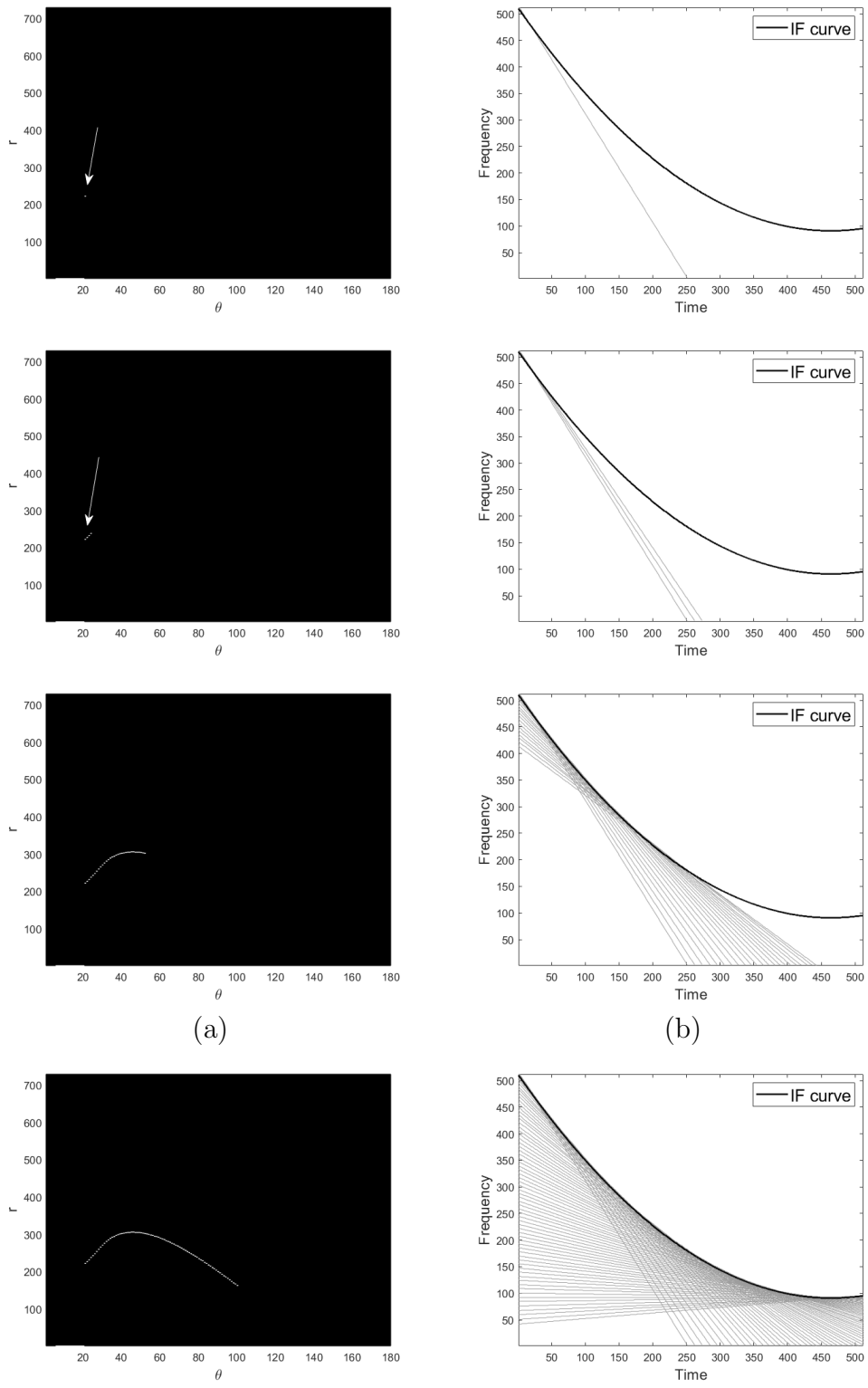

Figure 3.30: Each point of the envelope in eq.(3.30) is sequentially mapped according to eq.(3.31). (a) Points in Radon domain; (b) Superposition of the corresponding recovered lines (grey) in TF domain and IF curve (black).

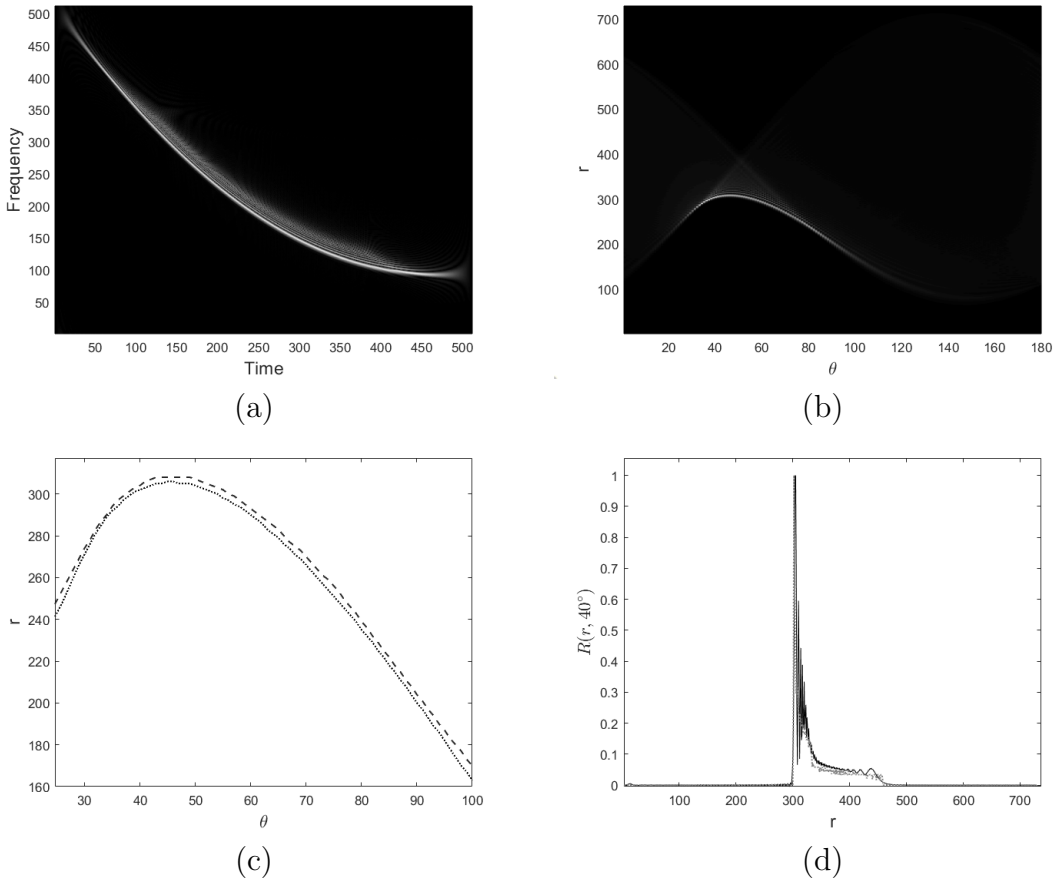

(a) (b) (c) (d)

Figure 3.31: Non-linearly modulated signal referred to Fig.3.29. (a) Absolute value of WVD; (b) RW; (c) Positions of RW maxima (dashed line) compared to the envelope in Fig.3.29 (dotted line); (d) Normalized sections at $\theta = 40°$, RW (black line) and R_ρ (gray line).

By setting $\hat{g}(u,\xi) = \hat{g}(\xi - \phi'(u))$, it can be expressed as

$$P(u,\xi) = \frac{a^2}{4} \iint \hat{g}(t,\omega)\delta(u-t, \omega - \phi'(u))\, dt\, d\omega = \frac{a^2}{4}\hat{g}(u,\xi) * *\delta(u, \phi'(u)),$$

and then

$$\mathcal{R}[P] = \frac{a^2}{4}\mathcal{R}[\hat{g}] * \mathcal{R}[\rho] = \frac{a^2}{4}\mathcal{R}[\hat{g}] * R_\rho. \tag{3.33}$$

Both eqs.(3.32) and (3.33) show a concentrated distribution in Radon which is blurred by the RT of the analysis window. Indeed, $\mathcal{R}[WV_f]$ is convolved with $\mathcal{R}[WV_g]$ in eq.(3.32) and R_ρ is convolved with $\mathcal{R}[\hat{g}]$ in eq.(3.33) and the above convolutions imply a shift in maxima positions. In this case, the reconstruction procedure based on eq.(3.31) results in the recovery of a characteristic curve

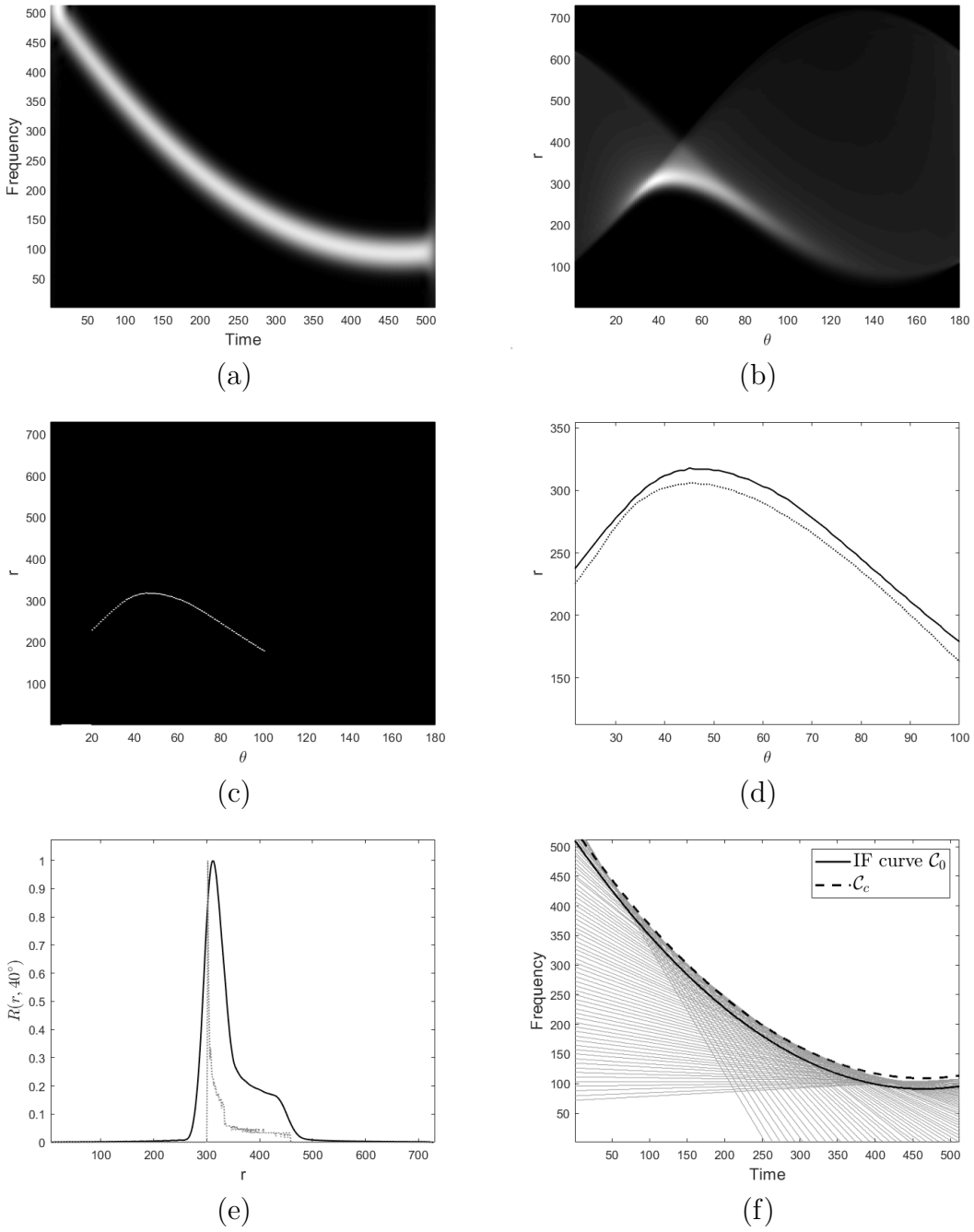

Figure 3.32: Non-linearly modulated signal referred to Fig.3.29. (a) Spectrogram; (b) RSD; (c) RSD evaluated on its maxima; (d) Positions of RSD maxima (solid line) compared to the ones of Radon ridge in Fig.3.30, (e) Normalized sections at $\theta = 40°$, RSD (black line) and R_ρ (gray line); (f) Lines family reconstructed by the radon spectrogram maxima. The shift observed in (d) causes the shifting on a different characteristic $\mathcal{C}_c : (u, \phi'(u) + c)$.

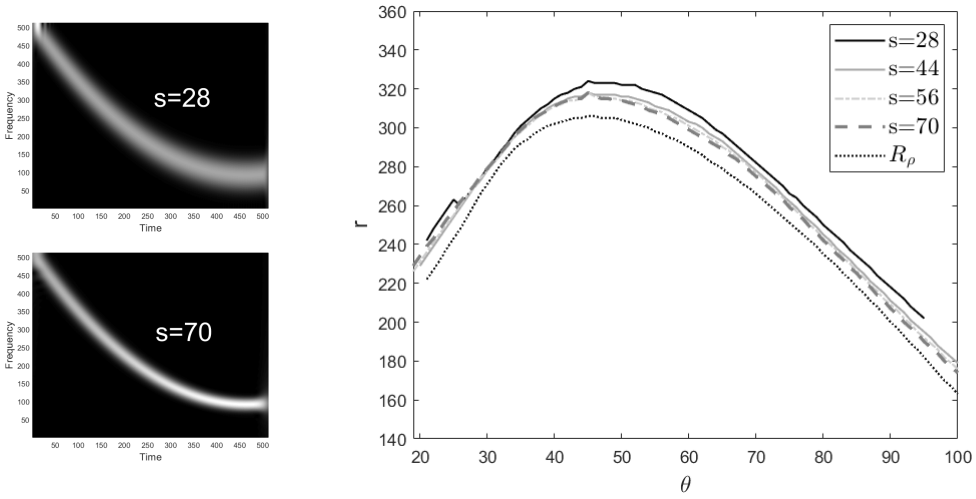

Figure 3.33: Non-linear chirp in Fig.3.32(a). Positions of RSD maxima in dependence on the analysis window size s, used in STFT computation, compared to the envelope of R_ρ (dotted line). As it can be observed, the smaller s, the closer the curves.

different from the ridge one, but still preserving IF information, according to Prop.2.4, as shown in Fig.3.32(f). In addition, the window size can be selected so that the radial shift becomes more negligible, as depicted in Fig.3.33. This topic will be better addressed in the next section.

3.3.3 A model for RSD

This section is aimed at defining a model for RSD that highlights its dependence on signal IF. Without loss of generality, in the sequel STFT modulus $p(u,\xi) := |S_f^g(u,\xi)|$ is referred as spectrogram and the corrective term in eq.(1.3) is assumed negligible, with $s = 1$.

Proposition 3.14. *The RT of the spectrogram $p(u,\xi)$ of a monocomponent signal $f(t) = a\cos\phi(t)$ is*

$$R(r,\theta) = \frac{a}{4\pi\sin\theta}\int \hat{g}\left(\frac{r - u\cos\theta - \phi'(u)\sin\theta}{\sin\theta}\right)du. \tag{3.34}$$

Proof. Proof is in Appendix B. □

Although general, eq.(3.34) does not directly provide information concerning IF. For getting a more meaningful expression of RSD, a special spectrogram

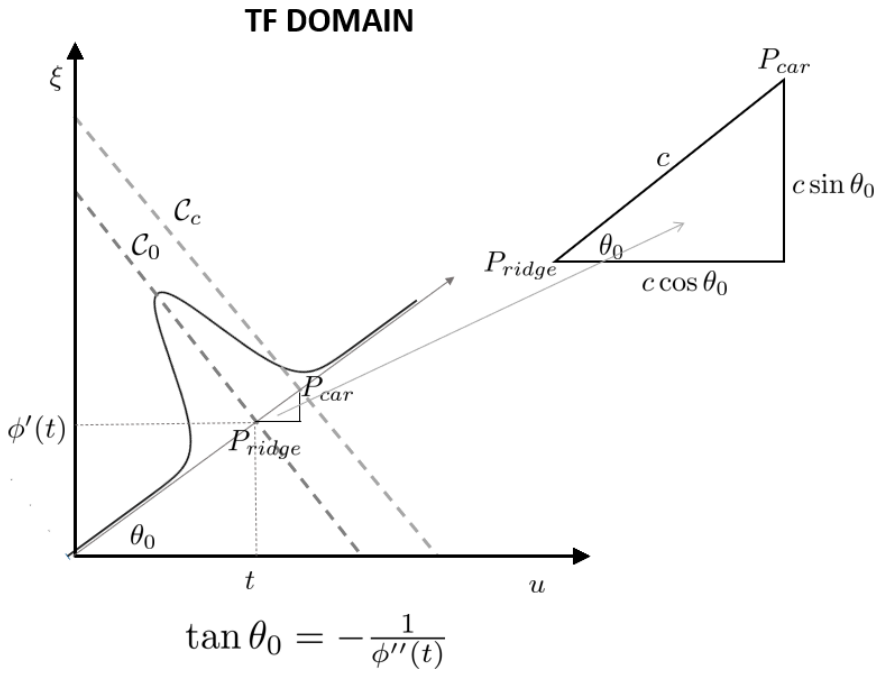

Figure 3.34: Spectrogram section $\tilde{p}(u,\xi)$ as defined in eq.(3.35) in the direction identified by $\theta = \theta_0 = -\arctan\left(\frac{1}{\phi''(t)}\right)$, which corresponds to the normal direction to the ridge. If $P_{ridge} = (t, \phi'(t))$ lies on the ridge curve $\mathcal{C}_0$, then $P_{car} = (t + c\cos\theta_0, \phi'(t) + c\sin\theta_0)$ belongs to the characteristic curve $\mathcal{C}_c$. $\tilde{p}(t,c)$ is then obtained by considering $c \in \left[-\frac{\Delta\omega}{2}, \frac{\Delta\omega}{2}\right]$.

decomposition that is based on the following model for a generic spectrogram section has to be considered, i.e.

$$\tilde{p}(t,c) = p(u(t),\xi(t)) = p(t + c\,\cos\theta(t), \phi'(t) + c\,\sin\theta(t)),\; c \in \left[-\frac{\Delta\omega}{2}, \frac{\Delta\omega}{2}\right]. \tag{3.35}$$

The latter is centered at the ridge point $(t, \phi'(t))$ and its orientation is identified by the angle θ. Fig.3.34 depicts $\tilde{p}(t,c)$, with θ_0 identifying the normal direction to the ridge, i.e. $\cot\theta_0(t) = -\phi''(t)$.

3.3.3.1 Spectrogram representation

Taking into account eq.(3.35), the evolution law in eq.(2.6) tells us that spectrogram is constant along the direction identified by $\theta = \frac{\pi}{2}$, so that it can be modelled as the ensemble of its sections at $\theta = \frac{\pi}{2}$, that are shifted copies of the analysis window. Actually, the same result holds true if we move along

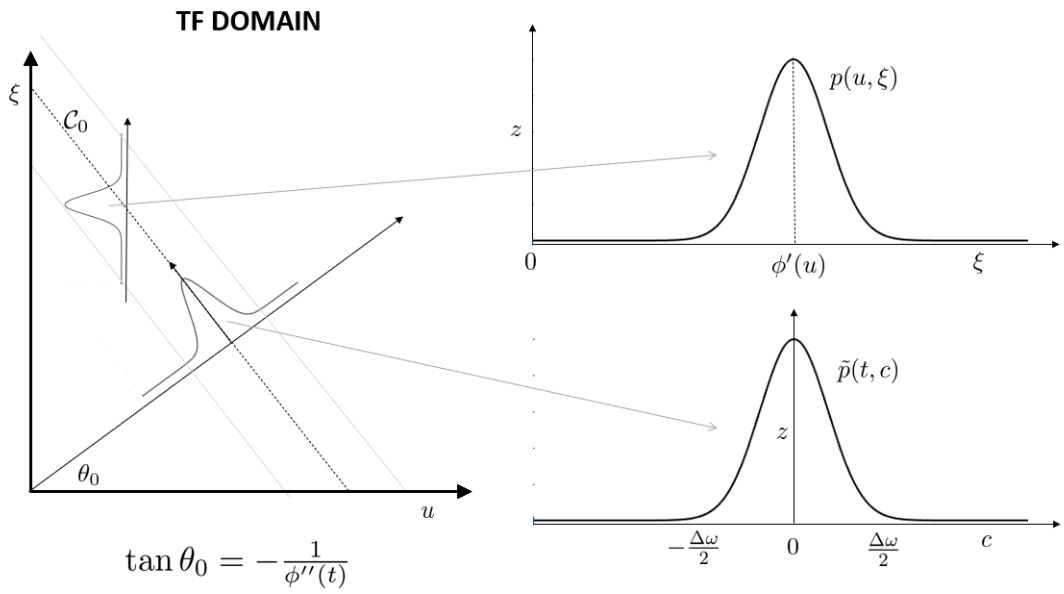

Figure 3.35: Sections of the spectrogram in the frequency direction, i.e., $\theta = \frac{\pi}{2}$, and in the normal direction to the ridge, i.e., $\theta = \theta_0$. In the first case (top), the spectrogram profile is a function of variable ξ (i.e. $p(u,\xi) = \hat{g}(\xi - \phi'(u))$, with fixed u). The second case (bottom) yields to a parametrization in the rotated system, depending on c, the same parameter describing the characteristic curves. For linear chirps, transport holds in both directions $\theta = \frac{\pi}{2}$ and $\theta = \theta_0$.

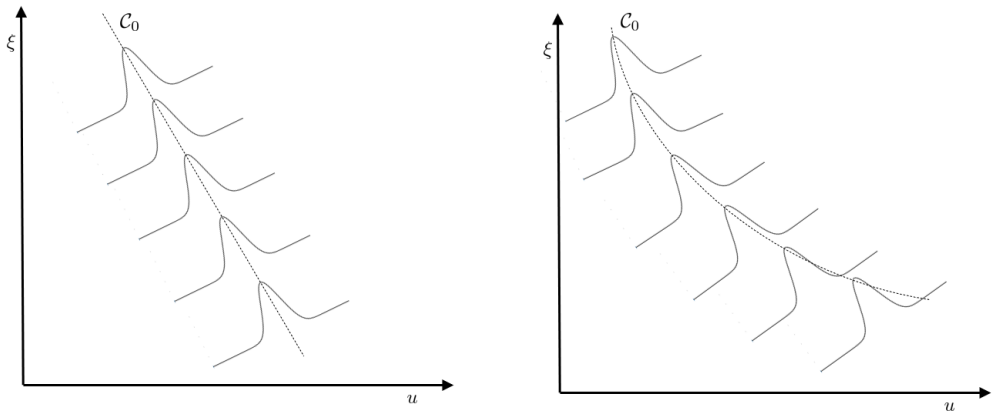

(a) (b)

Figure 3.36: Sections transported along the ridge direction. (a) linear case; (b) non linear case.

sections differently oriented, as shown in this section. The result is first proved for LFM signals and then extended to non-linearly FM signals, under specific assumptions.

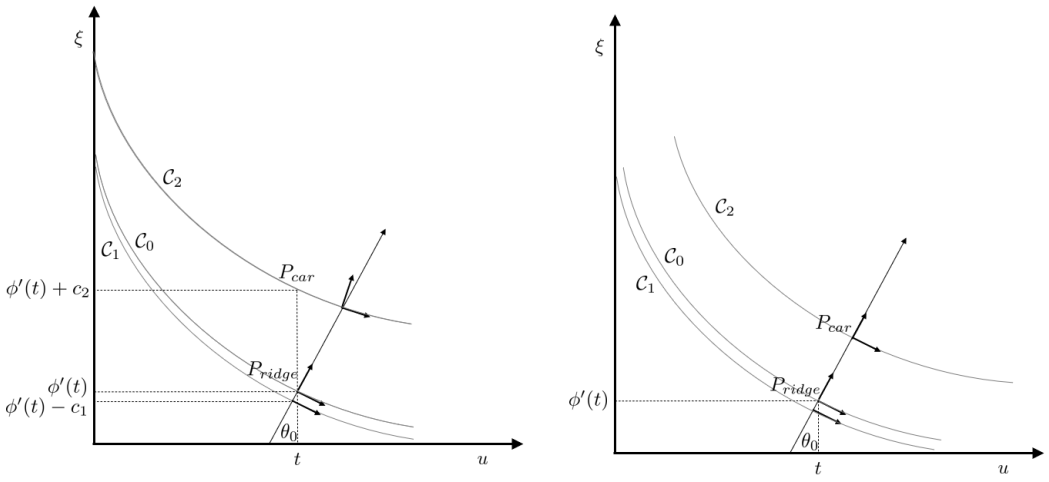

Figure 3.37: Geometry of characteristic curves. (a) Characteristic curves of eq.(2.6) detected in the normal direction to the ridge generally do not share the same tangent vector at the intersection point. The closer the characteristic is to the ridge, the more the normal direction is preserved; (b) Curves sharing the same tangent vector along the normal direction to the ridge at a fixed ridge point $(t, \phi'(t))$.

Proposition 3.15. *If $f(t) = a\cos\phi(t)$ is linearly modulated, i.e. $\phi''(t) = C =$ constant, then the function $\tilde{p}(t,c)$ in eq.*(3.35) *is constant along the characteristic curves of eq.*(2.6)*.*

Proof. The time derivative of $\tilde{p}$ is

$$\frac{d}{dt}\tilde{p}(t,c) = p_u(u(t),\xi(t))\dot{u} + p_\xi(u(t),\xi(t))\dot{\xi} = p_u(u(t),\xi(t)) + \phi''(t)p_\xi(u(t),\xi(t)), \tag{3.36}$$

which is zero by eq.(2.6), as $\phi''(t)$ is constant. □

As a consequence, in the linear case it is possible to choose a different and more convenient orientation for sections composing the spectrogram, preserving the total energy, as stated in the following

Proposition 3.16. *Let $f(t) = a\cos\phi(t)$ be a linearly FM signal and let us consider $\tilde{p}(t,c)$ as in eq.*(3.35)*, with $\theta_0 = -\arctan\frac{1}{\phi''(t)} = -\arctan\frac{1}{C}$. Then,*

$$\iint p^2(u,\xi)\,du\,d\xi = \iint \tilde{p}^2(t,c)\,dc\,dt.$$

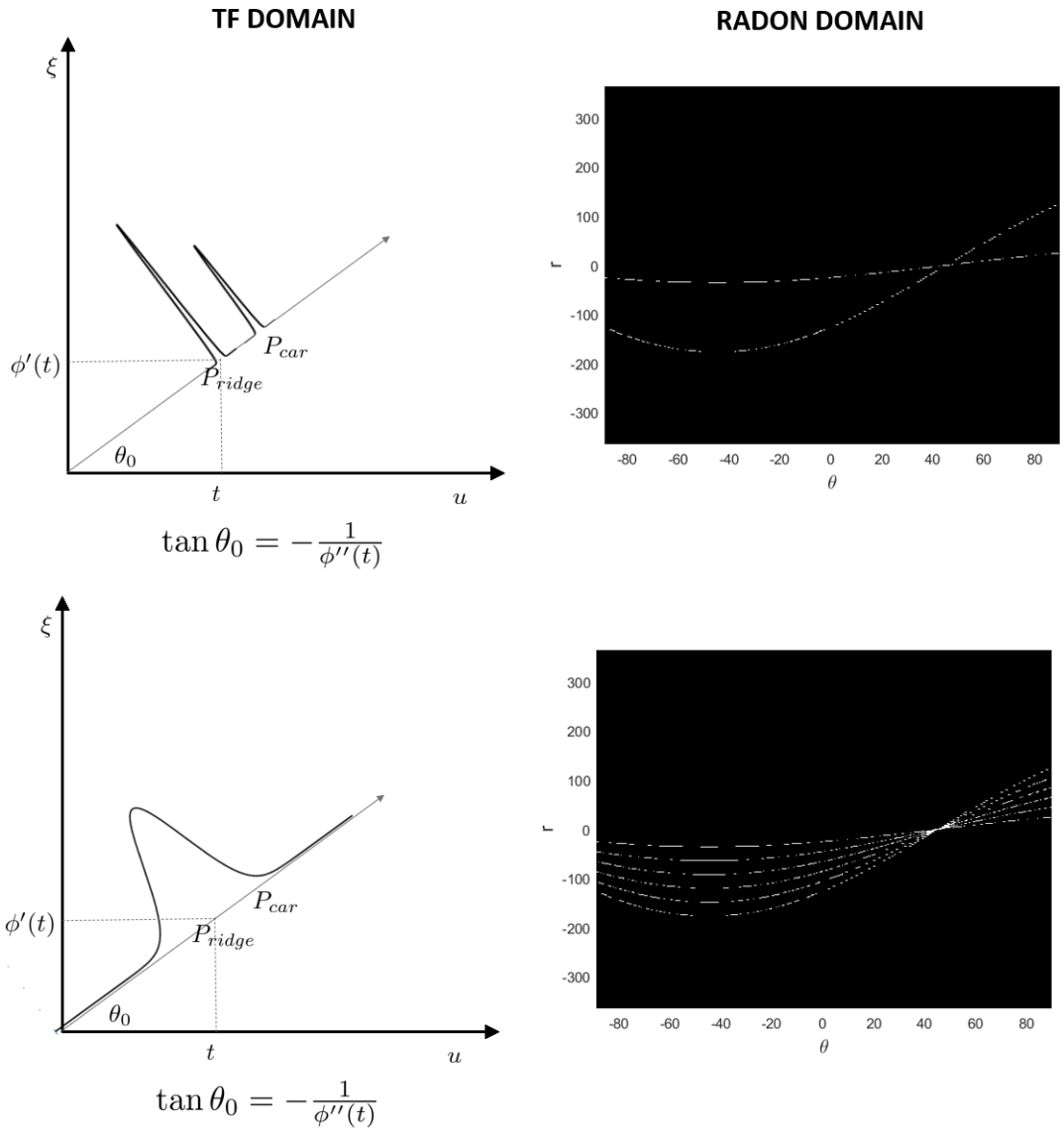

Figure 3.38: Top : RT of two modulated delta functions respectively located at the ridge point P_{ridge} and at the point P_{car} belonging to the characteristic curve detected in the normal direction to the ridge. Bottom: RT of the analysis window orientated in the normal direction to the ridge.

Proof. Proof can be found in Appendix B. □

Prop.3.15 allows us to model the spectrogram of a LFM signal as the ensemble of its sections in an arbitrary direction, different from the one parallel to the frequency axis, as depicted in Fig.3.35. In addition, Prop.3.16 states that the total energy is preserved along the normal direction to the ridge, i.e. the one identified by $\theta = \theta_0$. It is worth observing that sections in eq.(3.35) share

the same maximum, therefore the smaller the area the higher the concentration. The proposition below shows that θ_0 also provides the direction along with the spectrogram is more concentrated.

Proposition 3.17. *Let $\tilde{p}(t,c)$ be as in eq.*(3.35) *for a fixed t, with $\theta \in [0,\pi) - \{\arctan C\}$. The minimum of the area of $\tilde{p}(t,c)$ is realized at $\theta = \theta_0$.*

Proof. Proof can be found in Appendix B. □

The preliminary study on LFM signals allows us to deal with general FM signals. In particular, similar results obtained for LFM can be derived in the non-linear case by involving only characteristic curves sufficiently close to the ridge, as assumed in the sequel.

Proposition 3.18. *Let $f(t) = a\cos\phi(t)$ be a FM signal let $p(u,\xi)$ be its normalized spectrogram satisfying one of the following conditions:*

Hp 1) $f(t)$ is linearly or constantly modulated, i.e. $\phi'''(t) = 0$ or $\phi''(t) = 0$, $\forall\, t$

Hp 2) $0 < |\phi''(t)| < L_1$, $|\phi'''(t)| \geq L_2 > 0$ and $p(u,\xi)$ is computed with an analysis window such that $\Delta\omega \leq \frac{1+L_1^2}{L_2}$.

Then the function $\tilde{p}(t,c)$ in eq.(3.35) *is constant along the characteristic curves of eq.*(2.6).

Proof. Proof is in Appendix B. □

Prop.3.18 states that Prop.3.15 can be generalized to non-linearly FM signals, provided that the window size is sufficiently small to guarantee a moderate spread, so that the characteristic curves of eq.(2.6) are sufficiently close to the ridge and $Hp\,2$ is satisfied. Fig.3.36(a) shows that the window profile is perfectly transported in the direction of the ridge in the linear case, while for non-linearly frequency modulation the transport holds true for those points locally around the ridge curve, as depicted in Fig.3.36(b). In the present approach, we consider a different geometry for the characteristics, as a set of curves approximately parallel in the normal direction to the ridge, as sketched in Fig.3.37.

3.3.3.2 RT of a spectrogram section

Prop.3.18 allows us to model the spectrogram as the ensemble of its sections normal to the ridge direction, also in the non-linear case. Under this assumption, by RT linearity, RSD can be formally expressed as the ensemble of spectrogram sections' RT. To this aim, the following proposition provides the RT of the spectrogram section in eq.(3.35)

Proposition 3.19. *Let $f(t) = a\cos\phi(t)$ satisfies $Hp\,1$ or $Hp\,2$ as in Prop.3.18. Let us assume $\hat{g}$ is compactly supported and symmetric and let define $\theta_0 = \theta_0(t) = -\arctan\left(\frac{1}{\phi''(t)}\right)$. Then, the RT of $\tilde{p}(t,c)$, as in eq.(3.78), is*

$$R(r,\theta,t) = \frac{1}{2\pi\cos(\theta-\theta_0)}\,\hat{g}\left(\frac{r - t\cos\theta - \phi'(t)\sin\theta}{\cos(\theta-\theta_0)}\right), \qquad (3.37)$$
$$t \geq 0,\ \forall\,\theta\ :\ |\theta-\theta_0| \in \left[0, \frac{\pi}{2}\right).$$

Proof. Proof can be found in Appendix B. □

An example of the RT of a spectrogram section $R(r,\theta,t)$ is provided in Fig.3.38(Bottom).

The following proposition highlights the relation between signal IF and $R(r,\theta,t)$. Indeed, the latter reaches its maximum on the mapped ridge curve $\mathcal{M}$.

Proposition 3.20. *For each fixed $\theta : |\theta-\theta_0(t)| \in [0, \frac{\pi}{2})$, $\mathcal{M} : r(t) = t\cos\theta + \phi'(t)\sin\theta$ satisfies $r(t) \in arg\max_r R(r,\theta,t)$.*

Proof. Proof is in Appendix B. □

3.3.3.3 An evolution law for $R(r,\theta,t)$

The proposition below provides a family of pdes depending on the parameter t.

Proposition 3.21. *For each fixed $t \geq 0$, $\forall\,\theta : |\theta-\theta_0(t)| \in [0, \frac{\pi}{2})$, $R^t := R(r,\theta,t)$ in eq.(3.37) satisfies the following evolution law*

$$\cos(\theta-\theta_0)\cdot R^t_\theta + [\phi'(t)\cos\theta_0 - t\sin\theta_0 - r\sin(\theta-\theta_0)]\cdot R^t_r - \sin(\theta-\theta_0)R^t = 0. \quad (3.38)$$

Proof. Proof can be found in Appendix B. □

For each fixed t, the characteristic curves of eq.(3.38) are related to the mapped ridge curve, as follows from Prop.3.22 and Prop.3.23.

Proposition 3.22. *The characteristic curves of eq.(3.38) are*

$$r(\theta) = c(t) \cdot \cos(\theta - \theta_0) + \sin(\theta - \theta_0)(\phi'(t)\cos\theta_0 - t\sin\theta_0), \tag{3.39}$$

with $c(t) = k(-t\sin\theta_0 + \phi'(t)\cos\theta_0)$, $k \in \mathbb{R}$ *and* $\theta \in [0, \pi) - \{\theta_0 + \frac{\pi}{2}\}$.

Proof. Proof is in Appendix B. □

Proposition 3.23. *The mapped ridge curve lies on the characteristic curves of eq.*(3.38).

Proof. Proof can be found in Appendix B. □

Prop.3.20 and Prop.3.23 clarify the role of the IF curve in Radon domain: each ridge point P_{ridge} is mapped to a curve in Radon domain passing through the maximum of the spectrogram section RT — the one centered at P_{ridge} — which is as well a characteristic curves of eq.(3.37). We can finally derive the expression for RSD.

3.3.3.4 RSD model

RT linearity allows us to introduce a model for RSD, as stated in the following

Proposition 3.24. *In the assumption* $Hp1$ *or* $Hp2$*, the Radon Spectrogram of* $f(t) = a\cos\phi(t)$ *is*

$$R(r,\theta) = \int R(r,\theta,t)\,dt - \int \frac{\phi'''(t)\sin^2\theta_0}{\cos(\theta-\theta_0)}(r - t\cos\theta - \phi'(t)\sin\theta)\,R(r,\theta,t)\,dt. \tag{3.40}$$

Proof. Proof is in Appendix B. □

It is worth observing that Prop.3.20 states that, in case of LFM signals, maxima curve lies on the mapped ridge curve $r(\theta)$. In addition, Prop.3.24 shows that RSD peaks at the angle corresponding to the normal direction to the ridge curve. In fact, for LFM signals, it holds $\phi'''(t) = 0$ and then it follows

$$R_r(r,\theta) = \int R_r(r,\theta,t)dt, \tag{3.41}$$

and

$$R_\theta(r,\theta) = \int R_\theta(r,\theta,t)dt, \tag{3.42}$$

Both eq.(3.41) and eq.(3.42) are zero when evaluated at $r(\theta_0)$. As a result, IF can be easily detected in the linear case.

Remark 14. *Unfortunately, in the non-linear case, maxima do not lay on the mapped ridge curve $\mathcal{M} : (\theta, r(\theta))$, as*

$$R_r(r(\theta),\theta) = \int \frac{\phi'''(t)\sin^2\theta_0}{\cos(\theta-\theta_0(t))}\,\hat{g}\,(0)\,dt \neq 0. \tag{3.43}$$

However, if the analysis window can be selected to strongly meet $Hp\,2$, i.e.

$$\Delta\omega << \frac{1+L_1^2}{L_3}, \tag{3.44}$$

then the term in eq.(3.43) is negligible and the linear model better fits the non-linear one. It turns out that $R(r,\theta) \approx \iint R(r,\theta,t)\,dt$ and $\theta = \theta_0(t)$ realizes the maximum value for each t in the signal support. In this case, RSD maxima provide the IF signature in Radon domain which can be easily extracted and processed to disclose IF curves. This is the topic of the next section.

3.3.4 RSD-based method for modes separation

Based on the study provided in Section 3.3.3, a method for IFs curve separation in Radon domain can be defined, as presented in the sequel.

3.3.4.1 The algorithm

Given a constant amplitude MCS $f(t)$ as defined in eq.(1.17), with crossing modes and comparable amplitudes, the contribution of each component can be isolated in Radon domain by a simple thresholding. The Radon domain is then partitioned into connected components R_i, $i = 1, ..., N$, where N is the number of modes. The latter is assumed to be known or it can be estimated by a counting procedure as the one proposed in [109] or the one described in Section 3.1.3. For each θ belonging to the support of R_i, the maxima points are selected as a signature of IF curve in Radon domain, according to Prop.3.20 and Remark 14. The latter are involved in RT inversion. This results in N separated TF representations IR_i, whose sparsity is promoted by selecting the

local centers of mass (i.e. the centers of mass around the maxima points along the vertical direction). The whole procedure is illustrated by the flow-chart in Fig.3.39 and it can be summarized as follows:

Step 1. compute the spectrogram p of the input signal f;

Step 2. compute RT of the spectrogram, i.e. RSD R_p;

Step 3. compute the threshold value $thr = \mu + 2\sigma^2$, where μ and σ respectively denote the mean and the standard deviation of R_p;

Step 4. determine the set $\mathcal{U} = \{(r,\theta)|R_p(r,\theta) > thr\}$ and set $\bar{R}(r,\theta) = R(r,\theta)$, $\forall\,(r,\theta) \in \mathcal{U}$ and $\bar{R} = 0$ otherwise;

Step 5. identify the connected components R_i of $\bar{R}$, i.e. the sets satisfying $\bar{R} = \cup_{i=1}^{P} R_i$;

Step 6. for each R_i

6.1 extract the signature: for each fixed θ, set $r_\theta = \arg\max_r(R_i(r,\theta))$ and set $R_i(r,\theta) = 0\,\forall\, r \neq r_\theta$;

6.2 compute $IR_i(u,\xi)$ as the inverse RT of R_i according to eq.(1.15);

6.3 for each u, select $\xi_u = \arg\max_\xi(IR_i(u,\xi))$ and the center of mass c_u around ξ_u;

6.4 the curve (u, c_u), for all considered u, is the separated IF curve corresponding to the i-th mode.

3.3.4.2 Experimental results

In this section, we present some experimental results obtained by applying the procedure sketched in Fig.3.39, concerning MCS having different frequency modulations. The robustness with respect to noise is also investigated, as signals embedded in white gaussian noise at SNR levels ranging from 5dB to 10dB are considered. In all simulations, the considered signal has length $N = 512$ and the STFT is computed by a gaussian window with variance equal to 1.37 and length $L = 44$. The set threshold is $thr = \mu + 2\sigma$, where μ and σ respectively denote the mean and the standard deviation of the considered RSD and all points (r,θ) satisfying $R_p(r,\theta) > thr$ are involved in the inversion. This choice corresponds

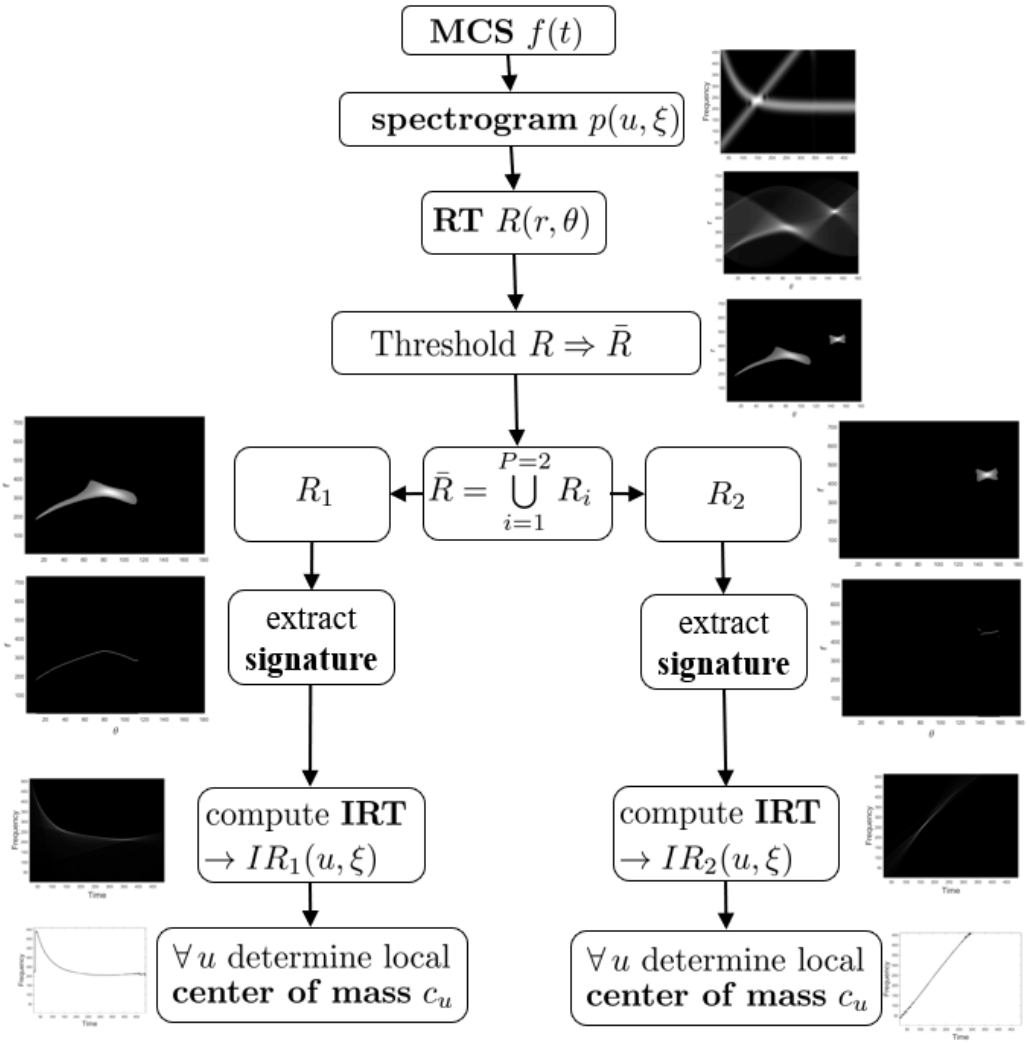

Figure 3.39: Flow-chart of the proposed method. A two-components signal is considered as illustrative example [107].

to selecting the points that do not belong to the confidence interval at 95% of the Radon distribution. In Fig.3.40, the result for a single quadratic chirp is depicted. As it can be observed, RSD maxima, for each fixed θ, provide a compact representation whose inverse gives TF signal representation sparser than spectrogram, as shown in Fig.3.40(e). In order to improve resolution and to compensate the eventual shift with respect to the radial components r (Section 3.3.2.1), the center of mass c_u of points close to each maximum has been considered, i.e.

$$c_u = \frac{\int_{\xi_u-\delta}^{\xi_u-\delta} \xi\, IR(u,\xi)\, d\xi}{\int_{\xi_u-\delta}^{\xi_u-\delta} IR(u,\xi)\, d\xi}$$

where $\xi_u = \arg\max_\xi IR(u,\xi)$ and $\delta \in [\frac{\Delta\omega}{2}, \Delta\omega]$. c_u is then the candidate separated ridge curve, as shown in Fig.3.40(f). In case of MCS, the processing of RSD is done separately on each component provided by the thresholding operation. Fig.3.41 depicts the result obtained for a two components signal composed of an hyperbolic and a linear mode, embedded in white gaussian noise. Each step of the algorithm is illustrated and the recovered IF curves are provided in Fig.3.41(i)-(l). In Fig.3.42 the result for a linear combination of polynomial chirps having constant unitary amplitudes is shown. As it can been observed, the reconstructed curves (dashed lines) approximate IF laws (solid lines). Although some instabilities at the boundaries, the method is able to recover the missing information in the non separability regions and the result is quite stable even in the presence of noise. Figs.3.43-3.44 respectively refer to the sum of a linear and a hyperbolic chirp and a linear combination of a quadratic and logarithmic chirp. In both cases, the proposed approach disentangles the single modes for those TF points belonging to the non-separability region and it is robust to noise.

3.3.4.3 Some observations

The procedure presented has been further refined by adopting the advanced technique in [29] for the extraction of informative content from noisy distributions, as preprocessing for the modes separation algorithm. As a result, the overall procedure in [108] is proven to be more robust to noise.

As a main drawback, the method presented in this section and the one in [108] are essentially based on thresholding, and then suitable only for MSC having comparable amplitudes. A more advanced technique should be able to adapt the threshold level in dependence on the amplitudes behaviour. The theoretical results in Section 3.2.3 suggest that RSD maxima could guide thresholding. Indeed, Prop.3.20 can be operatively used in order to detect the envelope in eq.(3.29) and separate each mode contribution in Radon domain. As shown in Fig.3.45, Radon sections corresponding to slopes $\theta_0(t)$ have a strict maximum, while sections apart present a plateau. In other words, the region of interest (ROI) in θ is the overall of Radon sections showing a strict global maximum. ROI support length thus depends on the specific IF law and it is minimum in case of linear modulation. A similar strategy could adopted for AM-MCS. The above-mentioned issues will be investigated in future studies.

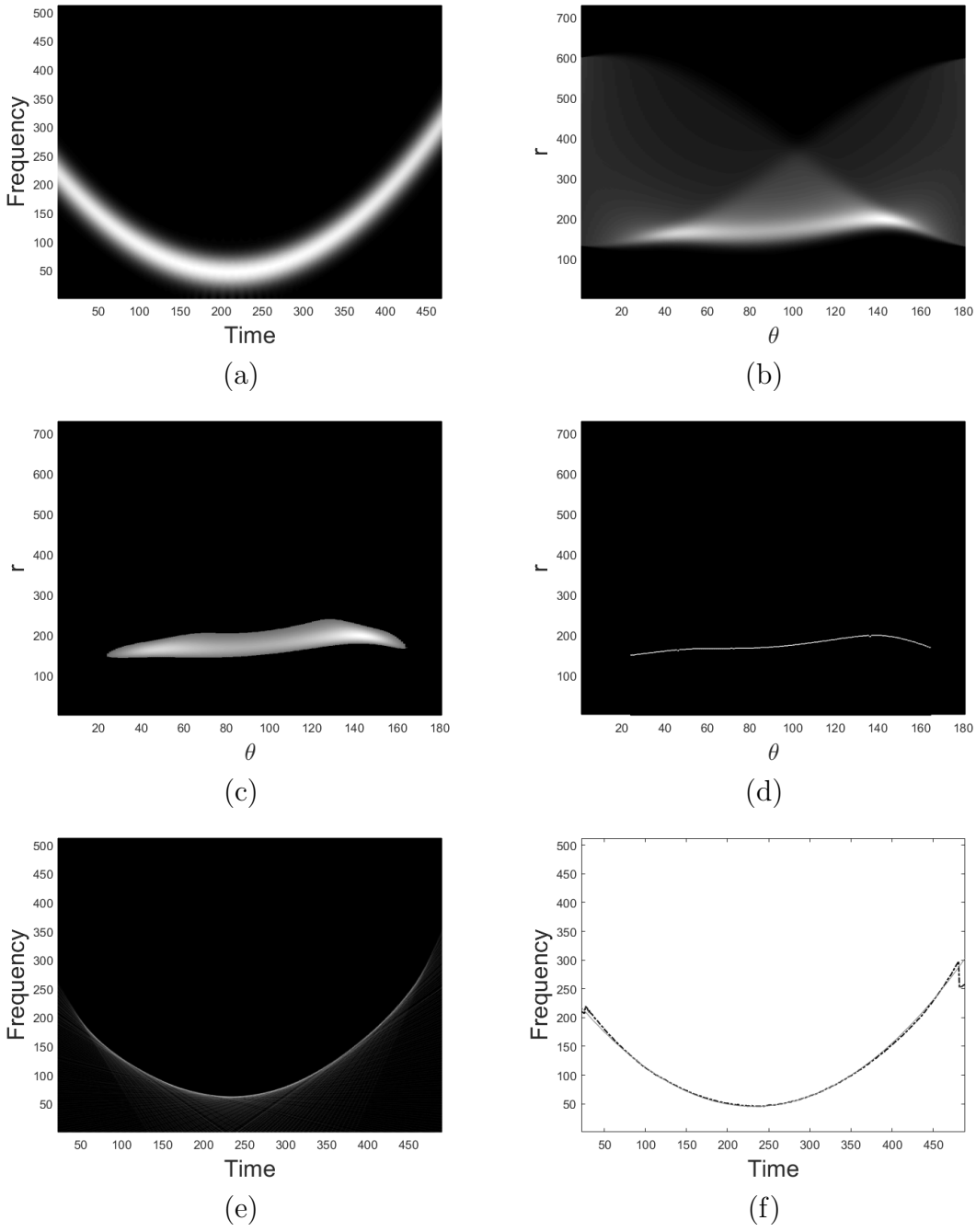

Figure 3.40: Quadratic chirp signal. (a) Spectrogram of the signal; (b) RT of the spectrogram in (a), i.e. RSD; (c) Mask obtained by thresholding RSD in (b); (d) Maxima points of (c) along the vertical direction (signature); (e) Inversion of (d) according to backprojection formula in (1.15); (f) Local center of mass (dotted line) of (e) compared to the exact IF law (solid grey line) [107].

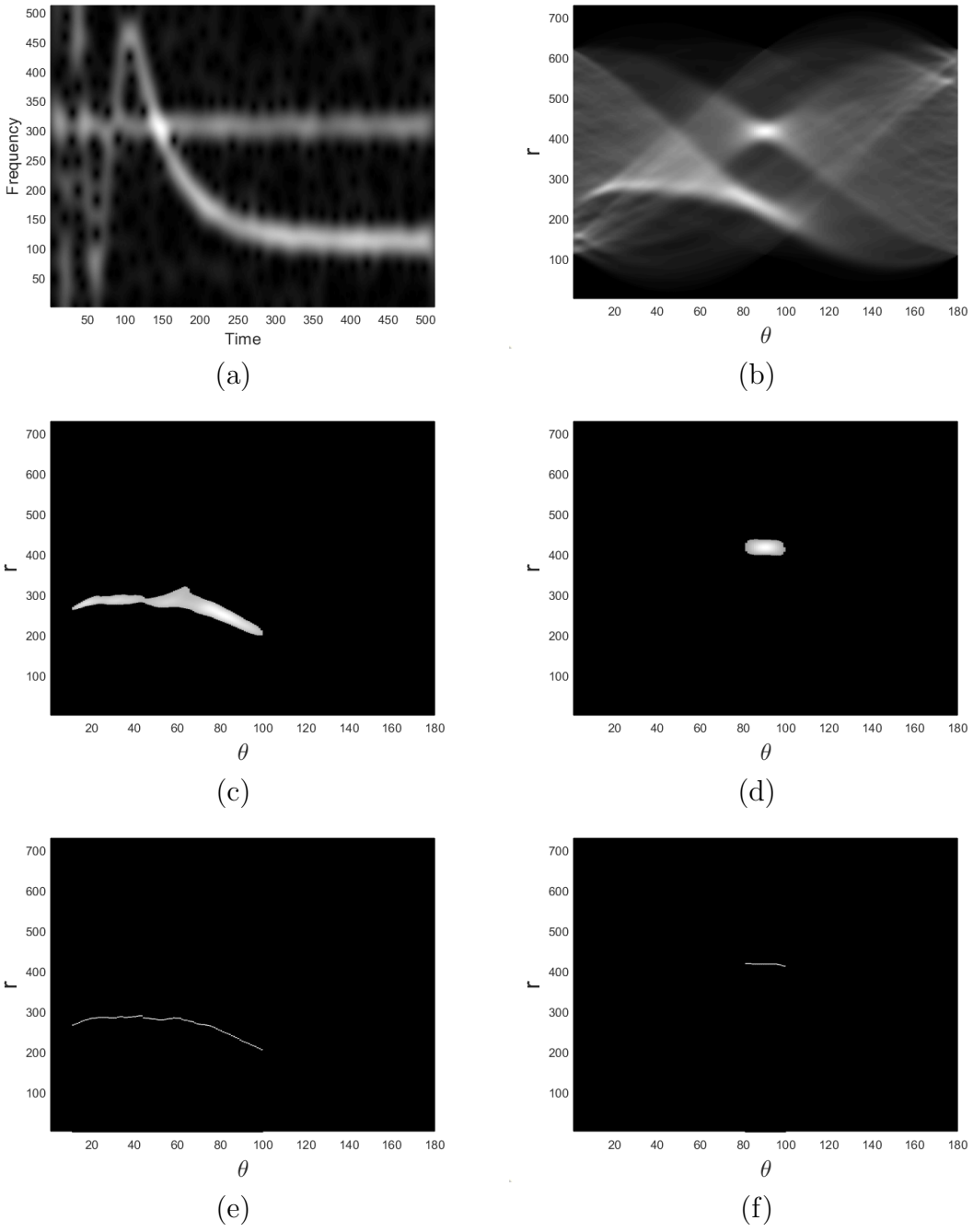

Figure 3.41: Two components signal composed of a linear and a hyperbolic chirp embedded in AWN at SNR level equal to 5 dB. (a) Spectrogram of the signal; (b) RT of the spectrogram in (a), i.e. RSD; (c)-(d) Components obtained by thresholding RSD in (b); (e)-(f) Signatures given by maxima points selection along the vertical direction respectively of (c) and (d) — Figure continued on the next page.

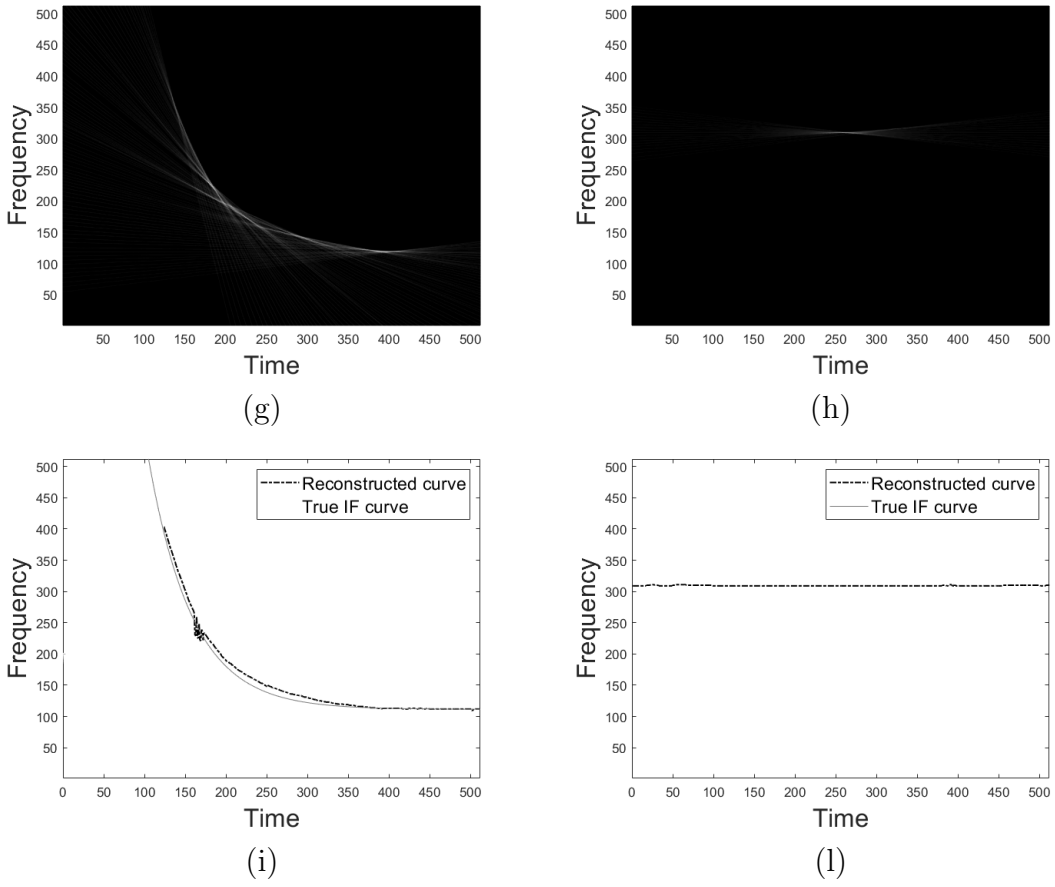

Figure 3.41: (g)-(h) Inverse RT respectively applied to (e) and (f); (i) Recovered hyperbolic curve (solid line) compared to the true IF (dashed grey lines); (l) Recovered linear curve (solid line) compared to the true IF (dashed grey lines).

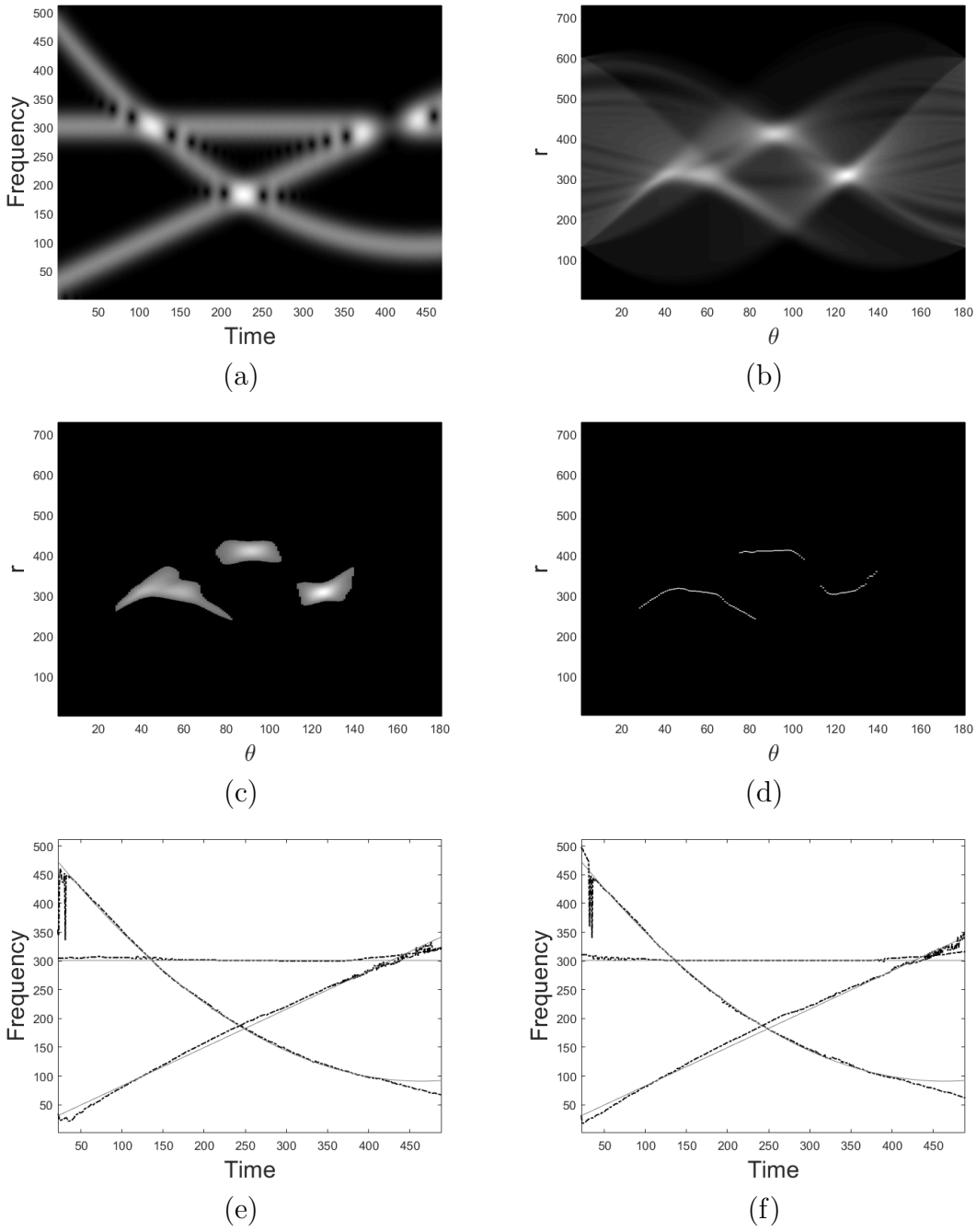

Figure 3.42: Three components polynomial chirp having non separable modes: (a) Spectrogram of the signal; (b) RSD; (c) Mask obtained by thresholding RSD in (b); (d) Signatures given by maxima points selection along the vertical direction; (e) Result (solid line) compared to the IF laws (dashed grey lines); (f) Result in the noisy case, SNR=9dB [107].

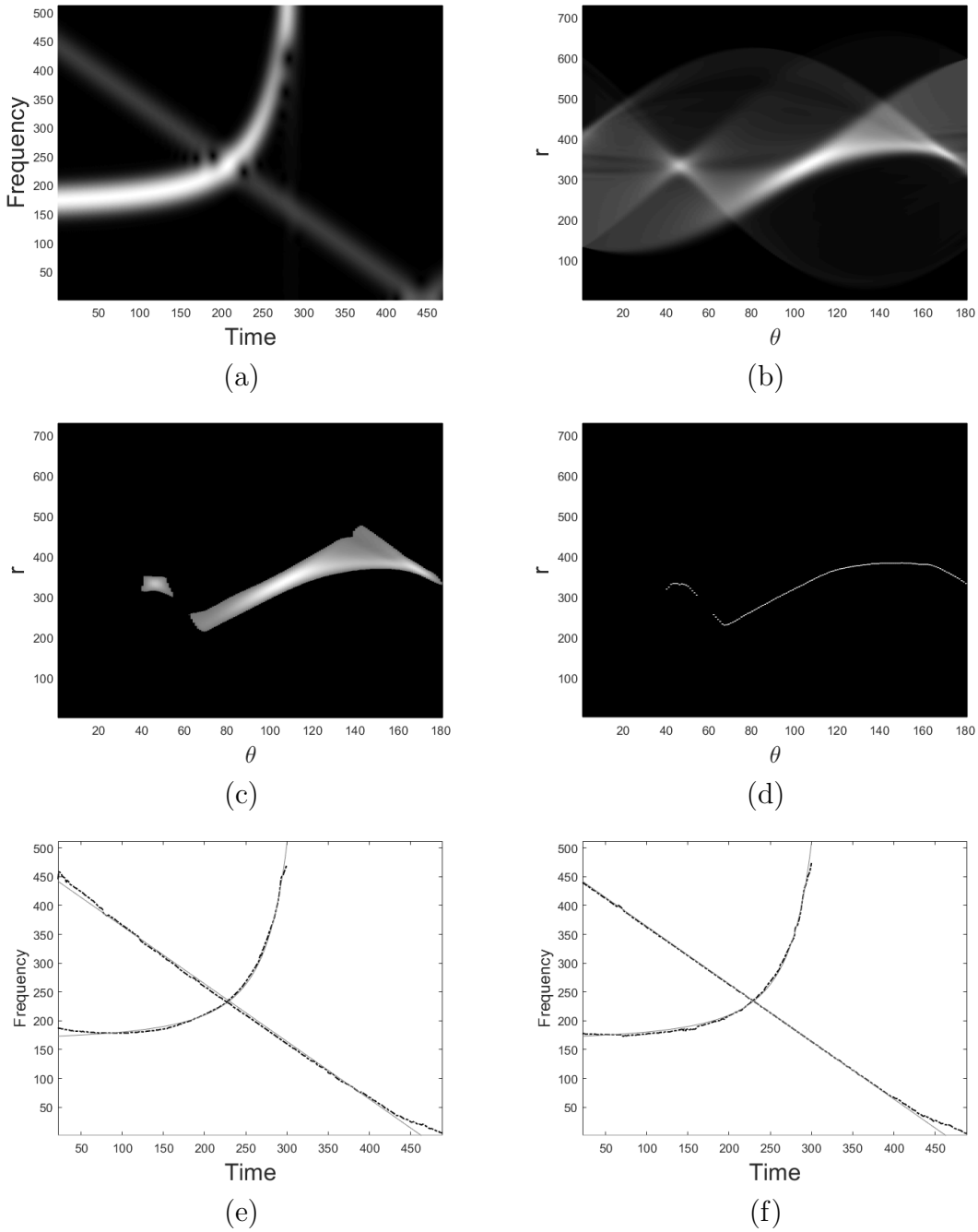

Figure 3.43: Two components signal composed of a linear and a hyperbolic chirp: (a) Spectrogram of the signal; (b) RSD; (c) Mask obtained by thresholding RSD in (b); (d) Signatures given by maxima points selection along the vertical direction; (e) Result (solid line) compared to the IF laws (dashed grey lines); (f) Result in the noisy case, SNR=5dB [107].

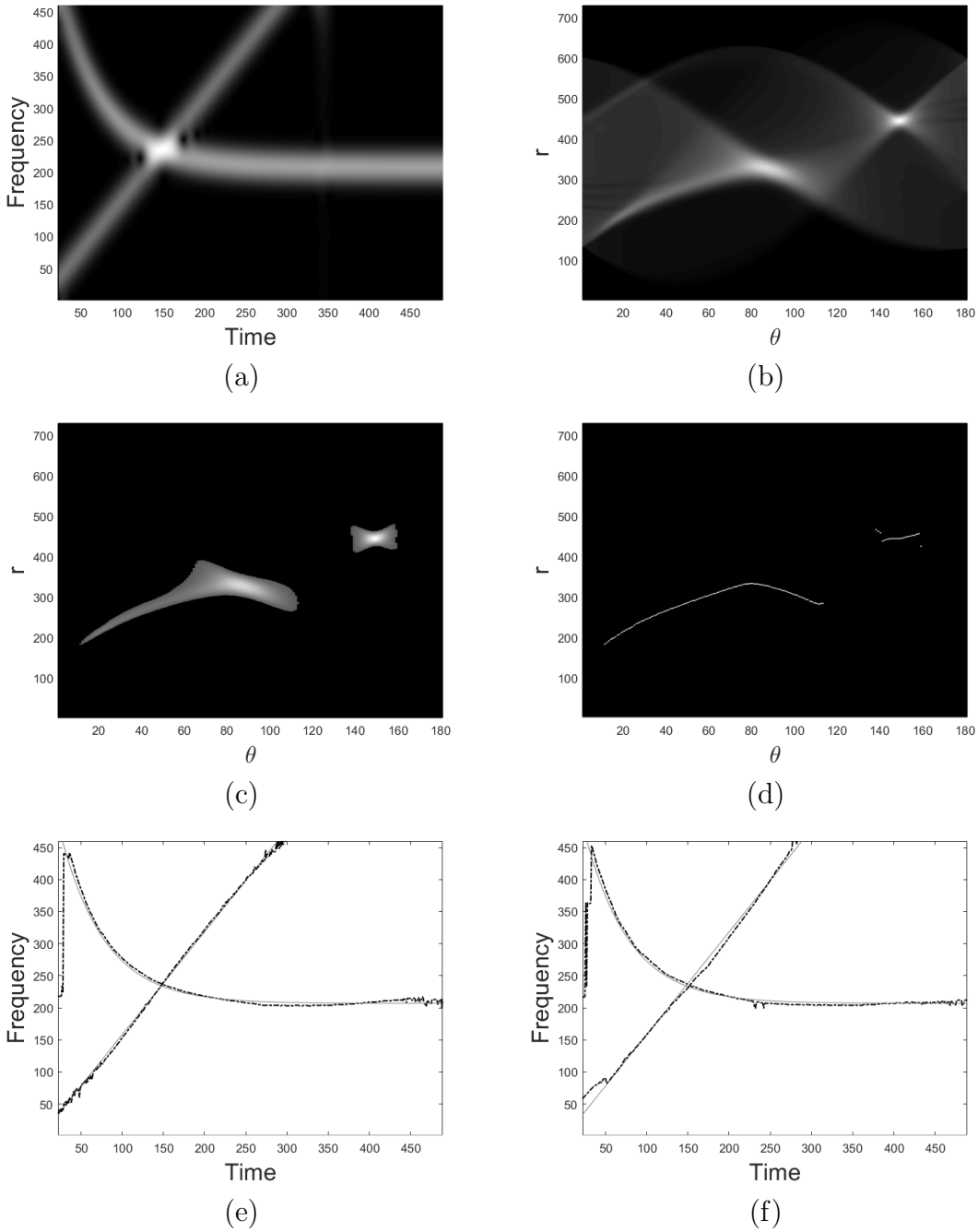

Figure 3.44: Two components signal composed of a linear and a logarithmic chirp: (a) Spectrogram of the signal; (b) RSD; (c) Mask obtained by thresholding RSD in (b); (d) Signatures given by maxima points selection along the vertical direction; (e) Result (solid line) compared to the IF laws (dashed grey lines); (f) Result in the noisy case, SNR=10dB [107].

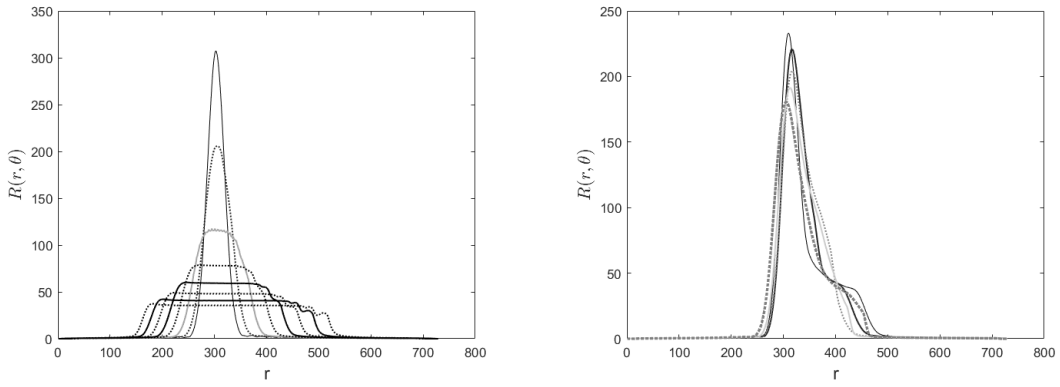

(a) (b)

Figure 3.45: RSD $R_p(r,\theta)$ for different $\theta \in [\theta_{max}, \theta_{max} + \Delta\theta]$, $\theta_{max} = \arg\max R_p(r,\theta)$, $\Delta\theta > 0$. (a) Linear case in Fig.3.23(c): sections lose the strict maximum, as the envelope in eq.(3.30) is composed of only a point; (b) Non-linear case in Fig.3.24(b): the strict maximum is preserved as long as $t \in supp\{f\}$ so that $\theta = \theta_0(t)$.

3.4 Conclusions

This chapter presented an energy approach for MCS analysis. Contrary to existing methods that recover IF curves by fitting procedures, the presented study is aimed at exploiting as far as possible the available information. Indeed, the spectrogram energy of a MCS, computed in the frequency direction, contains much information concerning the original IFs, especially at the non-separability region. In addition, the windowed energy function allows to monitor modes interaction and then to detect the eventual interference region. Finally, RSD seems to compensate for the lack of resolution at the non-separability region, providing an advantageous tool for overlapped MCS processing. Since the joint use of TF analysis and energy transforms has proven to be convenient for MCS decomposition, future work will be devoted to more advanced studies in this framework, in order to further extend the results presented in this chapter.

Conclusions

This thesis deepened the problem of frequency modulated multicomponent signals (FM-MCS) decomposition, in the general context of interfering modes. Both theoretical and applied aspects have been taken into account. Starting from an exhaustive analysis of the current state of the art, the presented work addressed the problem following two main approaches, respectively described in Chapter 2 and 3.

The first one is aimed at enhancing signal resolution in the time-frequency (TF) domain, and especially in the so-called non-separability regions, where standard methods fail in disclosing components. Based on the introduction of a spectrogram model, robust iterative reallocation procedures have been defined, studied and applied to provide sparse signal TF representations, and it has been shown that they are able to better disclose signal modes with respect to standard reassignment method. As a further advantage, the methods presented in Chapter 2 are convenient from the computational point of view.

The second approach is based on the combination of linear TF transforms and energy-based non-linear ones, such as Radon Transform. Contrary to existing strategies that ignore regions affected by interference and approximate the missing target by interpolation, the proposed one takes into account all the available information in the TF distribution (TFD) and exploits it to recover and separate instantaneous frequencies curves. Signal embedded with noise have been also considered in the experimental tests. Furthermore, a method for the automatic detection of the non-separability regions have been introduced.

It is worth observing that the proposed methods have the advantage of being non-parametric, as they do not require specific assumptions on the signal class. Experimental results concerning synthetic constant-amplitude MCS have confirmed both their effectiveness, with a consequent improvement of the state of the art, and their potential in solving a challenging problem in TF analysis

of FM-MCS. In particular, although MCS resolution has been improved significantly in TF non-separability regions, an additional effort is needed for applying the presented study to amplitude modulated MCS and non-monotonic IFs, which are recurrent features in real-world signals. Furthermore, even though the presented thesis focused on a specific TFD, namely spectrogram, study and results are expected to adapt to different TFDs, making the applicability to real-life signals more viable.

Appendix A

Proof of Proposition 2.1. Let us recall $P(u,\xi) = |S_f^g(u,\xi)|^2 = Re^2(S_f^g) + Im^2(S_f^g)$, with

$$Re(S_f^g) = \frac{1}{\sqrt{s}} \int_{-\infty}^{-\infty} f(t) g\left(\frac{t-u}{s}\right) \cos(\xi t)\, dt,$$

$$Im(S_f^g) = -\frac{1}{\sqrt{s}} \int_{-\infty}^{-\infty} f(t) g\left(\frac{t-u}{s}\right) \sin(\xi t)\, dt.$$

Let us first prove the following expressions for the derivatives:

$$\frac{\partial P}{\partial u} = -\frac{2}{s} Re(S_f^{g'}(S_f^g)^*), \tag{3.45}$$

$$\frac{\partial P}{\partial \xi} = 2\, s\, Im(S_f^{tg}(S_f^g)^*). \tag{3.46}$$

By deriving P with respect to variable u, we obtain

$$\begin{aligned}
\frac{\partial P}{\partial u} &= 2Re(S_f^g)\frac{\partial}{\partial u} Re(S_f^g) + 2Im(S_f^g)\frac{\partial}{\partial u} Im(S_f^g) \\
&= 2Re(S_f^g)\frac{1}{\sqrt{s}} \int_{-\infty}^{-\infty} f(t) g'\left(\frac{t-u}{s}\right) \cdot \left(-\frac{1}{s}\right) \cos(\xi t)\, dt \\
&- 2Im(S_f^g)\frac{1}{\sqrt{s}} \int_{-\infty}^{-\infty} f(t) g'\left(\frac{t-u}{s}\right) \cdot \left(-\frac{1}{s}\right) \sin(\xi t)\, dt \\
&= -\frac{2}{s} Re(S_f^g) Re(S_f^{g'}) - \frac{2}{s} Im(S_f^g) Im(S_f^{g'}) = -\frac{2}{s} Re(S_f^{g'}(S_f^g)^*),
\end{aligned}$$

thus eq.(3.45) holds true. The derivation with respect to ξ gives

$$\begin{aligned}
\frac{\partial P}{\partial \xi} &= 2Re(S_f^g)\frac{\partial}{\partial \xi}Re(S_f^g) + 2Im(S_f^g)\frac{\partial}{\partial \xi}Im(S_f^g) \\
&= 2Re(S_f^g)\frac{1}{\sqrt{s}}\int_{-\infty}^{-\infty} f(t)g\left(\frac{t-u}{s}\right)\cdot(-t)\sin(\xi t)\,dt \\
&- 2Im(S_f^g)\frac{1}{\sqrt{s}}\int_{-\infty}^{-\infty} f(t)g\left(\frac{t-u}{s}\right)\cdot t\cos(\xi t)\,dt \\
&= -2Re(S_f^g)\frac{s}{\sqrt{s}}\int_{-\infty}^{-\infty} f(t)g\left(\frac{t-u}{s}\right)\cdot\left(\frac{t-u}{s}\right)\sin(\xi t)\,dt \\
&- 2Re(S_f^g)\frac{s}{\sqrt{s}}\int_{-\infty}^{-\infty} f(t)g\left(\frac{t-u}{s}\right)\cdot\left(\frac{u}{s}\right)\sin(\xi t)\,dt \\
&- 2Im(S_f^g)\frac{1}{\sqrt{s}}\int_{-\infty}^{-\infty} f(t)g\left(\frac{t-u}{s}\right)\cdot t\cos(\xi t)\,dt \\
&= 2sRe(S_f^g)Im(S_f^{tg}) + 2uRe(S_f^g)Im(S_f^g) - 2sIm(S_f^g)Re(S_f^{tg}) \\
&- 2uIm(S_f^g)Re(S_f^g) = 2sIm((S_f^g)^* S_f^{tg}),
\end{aligned}$$

which proves eq.(3.46). Eq.(2.3) follows by comparing eq.(3.45) and eq.(3.46).

Taking into account eqs.(3.45) and (3.46), it follows

$$\frac{s^2}{2}Re(S_f^{tg}(S_f^g)^*)\frac{\partial P}{\partial u} + \frac{1}{2}Im(S_f^{g'}(S_f^g)^*)\frac{\partial P}{\partial \xi} = \tag{3.47}$$

$$\begin{aligned}
&= -sRe(S_f^{tg}(S_f^g)^*)Re(S_f^{g'}(S_f^g)^*) + sIm(S_f^{g'}(S_f^g)^*)Im(S_f^{tg}(S_f^g)^*) \\
&= -sRe(S_f^{g'}(S_f^g)^* S_f^{tg}(S_f^g)^*) \\
&= -sRe(S_f^{g'}\frac{P}{S_f^g}S_f^{tg}\frac{P}{S_f^g}) \\
&= -sP^2 Re\left(\frac{S_f^{g'}}{S_f^g}\frac{S_f^{tg}}{S_f^g}\right) \qquad (3.48) \\
&= -sP^2\left[Re\left(\frac{S_f^{g'}}{S_f^g}\right)Re\left(\frac{S_f^{tg}}{S_f^g}\right) - Im\left(\frac{S_f^{g'}}{S_f^g}\right)Im\left(\frac{S_f^{tg}}{S_f^g}\right)\right] \\
&= -sP^2\left(\Delta_u Re\left(\frac{S_f^{g'}}{S_f^g}\right) + \Delta_\xi Im\left(\frac{S_f^{tg}}{S_f^g}\right)\right)
\end{aligned}$$

then it follows

$$s^2\Delta_u\frac{\partial P}{\partial u}-\Delta_\xi\frac{\partial P}{\partial \xi}=-2sP\left(\Delta_u Re\left(\frac{S_f^{g'}}{S_f^g}\right)+\Delta_\xi Im\left(\frac{S_f^{tg}}{S_f^g}\right)\right). \tag{3.49}$$

or equivalently, according to eq.(3.48),

$$s^2\Delta_u\frac{\partial P}{\partial u}-\Delta_\xi\frac{\partial P}{\partial \xi}=-2sP\cdot Re\left(\frac{S_f^{g'}}{S_f^g}\frac{S_f^{tg}}{S_f^g}\right). \tag{3.50}$$

Proof of Proposition 2.4 Let us consider the parametric curve

$$\begin{cases} u=u(\tau) \\ \xi=\xi(\tau),\ \tau\in\mathbf{R}. \end{cases}$$

The derivative of $P(u(\tau),\xi(\tau))$ with respect to τ is

$$\frac{d}{d\tau}P(u(\tau),\xi(\tau))=\frac{\partial P}{\partial u}\dot{u}+\frac{\partial P}{\partial \xi}\dot{\xi}, \tag{3.51}$$

where $\dot{u}=\frac{du}{d\tau}$ and $\dot{\xi}=\frac{d\xi}{d\tau}$. Eq.(2.6) implies

$$\frac{d}{d\tau}P(u(\tau),\xi(\tau))=0 \tag{3.52}$$

if

$$\begin{cases} \dot{u}=1 \\ \dot{\xi}=\phi''(u). \end{cases} \tag{3.53}$$

Finally, the proof follows by solving the system of ordinary differential equations in eq.(3.53).

Proof of Proposition 2.6 Let us consider the spectrogram of a two-components signal in eq.(2.1), then for a fixed u

$$P(u,\xi)\approx|Sf_1(u,\xi)|^2,\quad\forall\,\xi:|\xi-\phi_2'(u)|\geq\Delta\omega.$$

More in general, for fixed u the following inequality holds:

$$0 \leq \frac{P(u,\xi)}{max_\xi P(u,\xi)} = \frac{P(u,\xi)}{\hat{g}^2(0)(a_1^2+a_2^2)} \leq \frac{(\sqrt{P_1(u,\xi)}+\sqrt{P_2(u,\xi)})^2}{\hat{g}^2(0)(a_1^2+a_2^2)} = \\ = \frac{(a_1\hat{g}([\xi-\phi_1'(u)])+a_2\hat{g}([\xi-\phi_2'(u)]))^2}{\hat{g}^2(0)(a_1^2+a_2^2)}. \tag{3.54}$$

Let ξ_1 : $\frac{\hat{g}(\xi_1-\phi_1'(u))}{\hat{g}(0)} = \frac{1}{H}$, and $\frac{\hat{g}(\xi_1-\phi_2'(u))}{\hat{g}(0)} = \frac{1}{K}$, with $\hat{g}$ symmetric and monotonically decreasing window function; if $\hat{g}(|\xi_1-\phi_2'(u)|) << 1$ and $\xi_1 < \phi_1'(u) < \phi_2'(u)$, then $\hat{g}(|\xi_1-\phi_2'(u)|) < \hat{g}(|\xi_1-\phi_1'(u)|)$, i.e., $H < K$, and then the inequality in eq.(3.54) becomes

$$0 \leq \frac{P(u,\xi)}{max_\xi P(u,\xi)} \leq \frac{\left(\frac{a_1}{H}+\frac{a_2}{K}\right)^2}{(a_1^2+a_2^2)} < \frac{(a_1+a_2)^2}{H^2(a_1^2+a_2^2)} < \frac{2}{H^2}.$$

Taking into account Definition 5, which defines the window bandwidth, previous inequality is not trivial for $H < \sqrt{2}$, i.e., for $|\xi_1 - \phi_1'(u)| < \frac{\Delta\omega}{2}$. Hence, TF points (u,ξ) such that

$$\frac{P(u,\xi)}{max_\xi P(u,\xi)} << \Theta = \frac{1}{2},$$

with high probability satisfy the WSC in Definition 11.

Proof of Equation (2.11). By eq.(**??**), it follows

$$p(u,\xi) = \frac{|S_f(u,\xi)|}{\frac{a_1\sqrt{s}}{2}\hat{g}(0)} = \frac{1}{a_1\hat{g}(0)}\Big[a_1^2\hat{g}_1^2 + a_2^2\hat{g}_2^2 + 2a_1a_2\hat{g}_1\hat{g}_2\cos\Delta\phi\Big]^{\frac{1}{2}}.$$

Denoting by $G = G(u,\xi) = \Big[a_1^2\hat{g}_1^2 + a_2^2\hat{g}_2^2 + 2a_1a_2\hat{g}_1\hat{g}_2\cos\Delta\phi\Big]^{\frac{1}{2}}$, the partial derivatives of $p(u,\xi)$ with respect to variables ξ and u are

$$\frac{\partial p}{\partial \xi} = \frac{s}{a_1\hat{g}(0)G}\Big(a_1^2\hat{g}_1\hat{g}_1' + a_2^2\hat{g}_2\hat{g}_2' + a_2a_1\cos(\phi_2-\phi_1)(\hat{g}_1'\hat{g}_2+\hat{g}_2'\hat{g}_1)\Big), \tag{3.55}$$

$$\frac{\partial p}{\partial u} = \frac{s}{a_1\hat{g}(0)G}\Big(-\phi_1''a_1^2\hat{g}_1\hat{g}_1' - \phi_2''a_2^2\hat{g}_2\hat{g}_2' + a_2a_1\cos(\phi_2-\phi_1)(-\phi_1''\hat{g}_1'\hat{g}_2 - \phi_2''\hat{g}_2'\hat{g}_1) \\ - \frac{a_1a_2}{s}\hat{g}_1\hat{g}_2\sin\Delta\phi\Delta\phi'\Big). \tag{3.56}$$

where $\hat{g}_i'$ denotes the derivative of $\hat{g}_i$ with respect to its argument. It follows

$$
\begin{aligned}
-\phi_1''(u)\frac{\partial p}{\partial \xi} &= \frac{\partial p}{\partial u} - \frac{s}{a_1\hat{g}(0)G}\Big(- \phi_2'' a_2^2 \hat{g}_2\hat{g}_2' + a_2 a_1 \cos(\phi_2-\phi_1)(-\phi_1''\hat{g}_1'\hat{g}_2 - \phi_2''\hat{g}_2'\hat{g}_1) \\
&\quad - \frac{a_1 a_2}{s}\hat{g}_1\hat{g}_2 \sin\Delta\phi\Delta\phi'\Big) \\
&\quad + \frac{s}{a_1\hat{g}(0)G}\Big(- \phi_1'' a_2^2 \hat{g}_2\hat{g}_2' - \phi_1'' a_2 a_1 \cos(\phi_2-\phi_1)(\hat{g}_1'\hat{g}_2 + \hat{g}_2'\hat{g}_1)\Big)
\end{aligned}
$$

$$
= \frac{\partial p}{\partial u} + \frac{a_2}{\hat{g}(0)G}\hat{g}_1\hat{g}_2 \sin\Delta\phi\Delta\phi' + \frac{s}{a_1\hat{g}(0)G}\Big[a_2^2\hat{g}_2\hat{g}_2'\Delta\phi'' + a_1 a_2 \cos\Delta\phi\hat{g}_2'\hat{g}_1\Delta\phi''\Big]
$$

$$
= \frac{\partial p}{\partial u} + \frac{a_2}{\hat{g}(0)G}\hat{g}_1\hat{g}_2 \sin\Delta\phi\Delta\phi' + \frac{s\,\Delta\phi''}{a_1\hat{g}(0)G}\Big[a_2^2\hat{g}_2\hat{g}_2' + a_1 a_2 \cos\Delta\phi\hat{g}_2'\hat{g}_1\Big].
$$

Observing that $p(u,\xi) = \frac{\frac{\sqrt{s}}{2}G(u,\xi)}{\frac{\sqrt{s}}{2}a_1\hat{g}(0)} = \frac{G(u,\xi)}{a_1\hat{g}(0)}$, we finally obtain

$$
\begin{aligned}
-\phi_1''(u)\frac{\partial p}{\partial \xi} &= \frac{\partial p}{\partial u} + \frac{a_2}{a_1\hat{g}^2(0)\,p}\hat{g}_1\hat{g}_2 \sin\Delta\phi\Delta\phi' \\
&\quad + \frac{s\,\Delta\phi''}{a_1^2\hat{g}^2(0)\,p}\Big[a_2^2\hat{g}_2\hat{g}_2' + a_1 a_2 \cos\Delta\phi\hat{g}_2'\hat{g}_1\Big],
\end{aligned}
$$

and eq.(2.11) holds true.

Proof of Proposition 2.8 Let define $C = \alpha\frac{p(u,\phi'(u))}{|p''(u,\phi'(u))|}$ and $R(\tau) = \frac{p(u,\tau+\phi'(u))}{p(u,\phi'(u))}$, so that $\Delta\tau = \sqrt{C(1-R(\tau))}$. Reminding that $p(u,\tau+\phi'(u)) = a\hat{g}(\tau)$, then $\tau = 0$ is a fixed point of the function $\varphi(\tau)$. In addition, it is unique whenever $\hat{g}$ is positive, symmetric with respect to 0 and monotonically decreasing away from 0, as it is the case of the analysis window used for the computation of the spectrogram. Hence, the convergence of τ_n to 0 can be proved using the fixed-point convergence theorems.

$\varphi(\tau)$ is a continuous function as well as $\varphi'(\tau)$. In fact,

$$
\varphi'(\tau) = 1 + \begin{cases} \frac{d\Delta\tau}{d\tau}, & \tau < 0 \\ -\frac{d\Delta\tau}{d\tau}, & \tau > 0 \end{cases} \tag{3.57}
$$

where $\frac{d\Delta\tau}{d\tau} = -\frac{\sqrt{C}}{2\sqrt{1-R(\tau)}}\frac{\hat{g}'(\tau)}{\hat{g}(0)}$ and $\varphi'(0) = 1 - \frac{\sqrt{\alpha}}{\sqrt{2}}$. In fact, reminding that

$sign(\tau\hat{g}'(\tau)) < 0$ and $\hat{g}''(0) < 0$,

$$\lim_{\tau\to 0^-}\frac{d\Delta\tau}{d\tau} = \lim_{\tau\to 0^-} -\frac{\sqrt{C}}{2\hat{g}(0)}\sqrt{\frac{\hat{g}'^2(\tau)}{1-R(\tau)}} = -\frac{\sqrt{\alpha}}{2\sqrt{|\hat{g}''(0)|}}\sqrt{\lim_{\tau\to 0^-}\frac{2\hat{g}'(\tau)\hat{g}''(\tau)}{-\hat{g}'(\tau)}} =$$

$$-\frac{\sqrt{\alpha|\hat{g}''(0)|}}{\sqrt{2|\hat{g}''(0)|}} = -\frac{\sqrt{\alpha}}{\sqrt{2}},$$

and similarly, $\lim_{\tau\to 0^+}\frac{d\Delta\tau}{d\tau} = \frac{\sqrt{\alpha}}{\sqrt{2}}$.

In addition, since $0 \leq \varphi'(0) < 1$, $\exists\ I_0 = [-\delta, \delta]$, with $\delta > 0$, such that $\forall\ \tau_0 \in I_0$, the sequence τ_{n+1} monotonically converges to 0. The convergence is linear for $\alpha < 2$.

It is worth observing that

$$\varphi''(\tau) = \begin{cases} \frac{d^2\Delta\tau}{d\tau^2}, & \tau < 0 \\ -\frac{d^2\Delta\tau}{d\tau^2}, & \tau > 0 \end{cases} \tag{3.58}$$

with

$$\frac{d^2\Delta\tau}{d\tau^2} = -\frac{\sqrt{C}}{2\hat{g}(0)}\frac{2\hat{g}''(\tau)(1-R(\tau)) + \hat{g}'(\tau)R'(\tau)}{(1-R(\tau))^{\frac{3}{2}}}.$$

and $\lim_{\tau\to 0^-}\frac{d^2\Delta\tau}{d\tau^2} = \lim_{\tau\to 0^+}\frac{d^2\Delta\tau}{d\tau^2} = 0$.

However,

$$\varphi''(\tau) = 0 \Leftrightarrow (\hat{g}'(\tau))^2 = 2\hat{g}(0)\hat{g}''(\tau)(1-R(\tau)). \tag{3.59}$$

Hence, $\tau = \bar{\tau}$ satisfies previous equation if $\bar{\tau} = 0$ or $\hat{g}''(\bar{\tau}) > 0$.

It turns out that if $\bar{\tau}$ is a zero for $\varphi''(\tau)$ and $\bar{\tau} \neq 0$, then $\varphi'(\bar{\tau}) = 1 + sign(\bar{\tau})\frac{\sqrt{C}}{2\hat{g}(0)}\sqrt{2\hat{g}(0)|\hat{g}''(\tau)|} = 1 + sign(\bar{\tau}\hat{g}'(\tau))\sqrt{\frac{\alpha\hat{g}''(\tau)}{2|\hat{g}''(0)|}}$. By observing that $0 = argmax_\tau|\hat{g}''(\tau)|$ for the considered analysis windows and $\bar{\tau} \neq 0$, we have

$$0 < \sqrt{\alpha\frac{\hat{g}''(\bar{\tau})}{2|\hat{g}''(0)|}} < 1$$

and then, since $sign(\tau\hat{g}'(\tau)) < 0$, $|\varphi'(\bar{\tau})| < 1, \quad \forall\ \bar{\tau} \neq 0$.

Finally, since $\bar{\tau}$ is a relative extreme point for $\varphi'(\tau)$, then

$$|\varphi'(\tau)| \leq max_{\bar{\tau}}|\varphi'(\bar{\tau})| < 1.$$

On the other hand, for $\bar{\tau} = 0$, $\varphi'(\bar{\tau}) = 1 - \sqrt{\frac{\alpha}{2}} < 1$. Hence, the convergence of τ_n is guaranteed $\forall\ \tau_0 \in supp\{\hat{g}\}$, i.e., $\tau_0 \in \left[-\frac{\Delta\omega}{2}, \frac{\Delta\omega}{2}\right]$.

Proof of Proposition 2.9. (i) Let us consider the fixed-point method [102] for equation $p_\xi(\xi) = 0$ using $F(\xi) = \xi - \frac{p_\xi(\xi)}{p_{\xi\xi}(\xi_R)}$ as iteration function. From eq.(1.6), $F(\xi) = \xi - \frac{\hat{g}'(\xi - \xi_R)}{\hat{g}''(0)}$. In addition, by observing $\hat{g}''(0) < 0$, $|F'(\xi)| < 1$ is exactly eq.(2.23).
(ii) Using Taylor approximation of the function p_ξ around ξ_R and eq.(1.3), up to $o((\xi_k - \xi_R)^4)$, we get

$$\xi_{k+1} - \xi_R = -\frac{p^{(4)}(\xi_R)}{p_{\xi\xi}(\xi_R)} \cdot \frac{1}{6}(\xi_k - \xi_R)^3 = -\frac{1}{6}\frac{\hat{g}''(\xi_k - \xi_R)}{\hat{g}''(0)}(\xi_k - \xi_R)^3 .$$

By setting $e_k = \xi_R - \xi_k$, $\exists\, \bar{k}$: $\left|\frac{e_{k+1}}{e_k^3}\right| \approx \frac{1}{6}\left|\frac{\hat{g}^{(4)}(0)}{\hat{g}^{(2)}(0)}\right|$, $\forall k > \bar{k}$.

Proof of Proposition 2.11. According to eq.(2.10) and assuming $\hat{g}(0) = 1$, $p(u, \xi) = \hat{g}(\xi - \phi'(u)) = e^{-\frac{1}{2}\sigma^2(\xi - \phi'(u))^2}$ and $\hat{g}''(0) = -\sigma^2$. Let $\xi_0 > \xi_R$ and set $p_0 = p(\xi_0)$. Let ξ_1 be defined as in eq.(2.24), then

$$0 < \xi_1 - \xi_R = \xi_1 - \xi_0 + \xi_0 - \xi_R = -\frac{1}{\sigma}\sqrt{1 - p(\xi_0)} + \xi_0 - \xi_R.$$

By setting $x = \xi_0 - \xi_R$, then ξ_1 belongs to the convergence interval of Method I if $\xi_1 - \xi_R < 1/\sigma$, i.e. if $-\sqrt{1 - e^{-\frac{1}{2}\sigma^2 x^2}} < 1 - \sigma x$. In the non trivial case $x > 1/\sigma$, this is equivalent to require

$$f(x) = 1 - e^{-\frac{1}{2}\sigma^2 x^2} > (\sigma x - 1)^2 = g(x).$$

The latter condition is satisfied, for instance, $\forall\, x \in [1/\sigma, 1.91/\sigma]$, since f and g are respectively strictly concave and convex. Therefore, the thesis holds $\forall p_0 \geq 0.16$.

Proof of Proposition 2.12. The scheme

$$\xi_{k+1} = \xi_k + sign(p_\xi(\xi_k))\sqrt{\frac{p(\xi_{k+1}) - p(\xi_k)}{|\hat{g}''(0)|}}, \quad k \geq 0$$

defines an implicit method having ξ_R as fixed point, where the value of $p(\xi_{k+1})$ is predicted by the linear method according to eq.(2.24). In the sequel, $(*)'$ indicates the derivative of function $(*)$ with respect to the frequency variable.

Set $\mu = sign(p_\xi(\xi))$, ξ_R is a fixed point for the function $\psi(\xi) = \xi + \alpha\,\mu\sqrt{\frac{p(\varphi(\xi))-p(\xi)}{|\hat{g}''(0)|}}$. $\psi(\xi)$ is continuous since p and φ are continuous. In order to prove the continuity of

$$\psi'(\xi) = 1 + \frac{\alpha\mu}{2\sqrt{|\hat{g}''(0)|}}\frac{p'(\varphi(\xi))\varphi'(\xi) - p'(\xi)}{\sqrt{p(\varphi(\xi)) - p(\xi)}} \tag{3.60}$$

it is necessary to prove that it is continuous in $\xi = \xi_R$. To this aim, using Taylor approximation of $p(\xi) = \hat{g}(\xi - \xi_R)$ in ξ_R and in $\varphi(\xi)$, we have respectively

$$\varphi(\xi) - \xi = \frac{\mu}{\sqrt{|\hat{g}''(0)|}}\sqrt{-\frac{\hat{g}''(0)(\xi - \xi_R)^2}{2} + o((\xi - \xi_R)^2)} = \frac{\mu}{\sqrt{2}}|\xi - \xi_R| + o(\xi - \xi_R)$$

and

$$\begin{aligned} p'(\varphi(\xi))\varphi'(\xi) - \varphi'(\xi) &= p'(\xi)(\varphi'(\xi) - 1) + p''(\xi)\varphi'(\xi)(\varphi(\xi) - \xi) + o(\varphi(\xi) - \xi) \\ &= -\mu|\hat{g}''(0)|\left(\sqrt{2} - \frac{1}{2}\right)|\xi - \xi_R| + o(\xi - \xi_R), \end{aligned}$$

where we used $\lim_{\xi \to \xi_R} \varphi'(\xi) = 1 - \frac{1}{\sqrt{2}}$; similarly

$$\begin{aligned} \sqrt{p(\varphi(\xi)) - p(\xi)} &= \sqrt{p'(\xi)(\varphi(\xi) - \xi) + \frac{p''(\xi)}{2}(\varphi(\xi) - \xi)^2 + o((\xi - \xi_R))^2} \\ &= \sqrt{-\hat{g}''(0)\frac{1}{\sqrt{2}}(\xi - \xi_R)^2 - \frac{\hat{g}''(0)}{2}\frac{1}{2}(\xi - \xi_R)^2 + o((\xi - \xi_R))^2} \\ &= \sqrt{|\hat{g}''(0)|}\sqrt{\frac{1}{\sqrt{2}} - \frac{1}{4}}\,|\xi - \xi_R| + o(\xi - \xi_R). \end{aligned}$$

By assuming $sign(\hat{g}'(\xi))sign(\xi - \xi_R) < 0$, it follows

$$\lim_{\xi \to \xi_R} \psi'(\xi) = 1 - \alpha \sqrt{\frac{1}{\sqrt{2}} - \frac{1}{4}}$$

and then ψ' is continuous.

By selecting $\alpha = \left(\frac{1}{\sqrt{2}} - \frac{1}{4}\right)^{-\frac{1}{2}}$, $\psi'(\xi_R) = 0$. Hence, the convergence order is greater than 1.

Eq.(3.60) provides the following necessary condition for convergence

$$sign(p'(\xi)) \cdot sign(p'(\varphi(\xi))\varphi'(\xi) - p'(\xi)) < 0, \tag{3.61}$$

which is equivalent to $|p'(\varphi(\xi))\varphi'(\xi)| < |p'(\xi)|$. Since $\varphi'(\xi) \in (0,1) \, \forall \, \xi$, we can conclude that the necessary condition in eq. (3.61) is satisfied if $|p'(\varphi(\xi))| < |p'(\xi)|$, which holds if $p''(\xi) < 0$ (and consequently $p''(\varphi(\xi)) < 0$), i.e. ξ is "sufficiently close" to the ridge point. Under this assumption, eq.(3.60) becomes

$$\psi'(\xi) = 1 - \frac{\alpha}{2\sqrt{|\hat{g}''(0)|}} \frac{|p'(\varphi(\xi))\varphi'(\xi) - p'(\xi)|}{\sqrt{p(\varphi(\xi)) - p(\xi)}}$$

and the convergence is assured if $|\psi'(\xi)| < 1$, which is equivalent to

$$\frac{\alpha}{2\sqrt{|\hat{g}''(0)|}} \frac{|p'(\varphi(\xi))\varphi'(\xi) - p'(\xi)|}{\sqrt{p(\varphi(\xi)) - p(\xi)}} < 2, \quad \text{with } \alpha > 0.$$

From eq.(2.24), we have $p(\xi) = 1 - (\varphi(\xi) - \xi)^2 |\hat{g}''(0)|$, then

$$p(\varphi(\xi)) = 1 - (\varphi(\varphi(\xi)) - \varphi(\xi))^2 |\hat{g}''(0)|, \text{and}$$

$$\begin{aligned} &p'(\varphi(\xi))\varphi'(\xi) - p'(\xi) = \\ &2|\hat{g}''(0)| \left[(\varphi(\xi) - \xi)(\varphi'(\xi) - 1) - \varphi'(\xi)(\varphi'(\varphi(\xi)) - 1)(\varphi(\varphi(\xi)) - \varphi(\xi)) \right]. \end{aligned} \tag{3.62}$$

Since $\varphi(\varphi(\xi)) - \varphi(\xi) = \varphi'(\tau)(\varphi(\xi) - \xi)$, $\tau \in (\xi, \varphi(\xi))$or $\in (\varphi(\xi), \xi)$, eq.(3.62) can be replaced by

$$2|\hat{g}''(0)|(\varphi(\xi) - \xi)(\varphi'(\xi) - 1 - \varphi'(\tau)\varphi'(\xi)(\varphi'(\varphi(\xi)) - 1).$$

Furthermore, $p(\varphi(\xi) - p(\xi)) =$

$$|\hat{g}''(0)|[(\varphi(\xi) - \xi)^2 - (\varphi(\varphi(\xi)) - \varphi(\xi))^2] = |\hat{g}''(0)|(\varphi(\xi) - \xi)^2(1 - \varphi'^2(\tau))$$

then

$$\frac{\alpha}{2\sqrt{|\hat{g}''(0)|}} \frac{|p'(\varphi(\xi))\varphi'(\xi) - p'(\xi)|}{\sqrt{p(\varphi(\xi)) - p(\xi)}} =$$

$$\frac{\alpha}{2\sqrt{1 - \varphi'^2(\tau)}} |[1 - \varphi'(\varphi(\xi))]\varphi'(\tau)\varphi'(\xi) - [1 - \varphi'(\xi)]|.$$

The quantity in squared brackets is in $(-1, 1)$ as it is the difference between two positive numbers in the interval $(0, 1)$. Hence, if

$$\frac{\alpha}{\sqrt{1 - \varphi'^2(\tau)}} < 2 \tag{3.63}$$

then $|\psi'(\xi)| < 1$ and

$$\varphi'(\tau) < \beta = \sqrt{1 - 1/(2\sqrt{2} - 1)} \approx 0.67,$$

whenever $\alpha \in (0, 2\sqrt{1 - \varphi'^2(\tau)})$. As a result, the convergence is assured $\forall\, \xi$: $\varphi'(\xi) < \beta$.

Remark: It is easy to verify that $\varphi'(\xi) = 1 - \frac{|\hat{g}'(\xi - \xi_R)|}{2\sqrt{|\hat{g}''(0)|(1 - \hat{g}(\xi - \xi_R))}}$ and all its extrema points satisfy [98]

$$(\hat{g}'(\xi - \xi_R))^2 = -2\hat{g}''(\xi - \xi_R)(1 - \hat{g}(\xi - \xi_R)),$$

then, condition in eq.(3.4) is satisfied if $1 - \frac{1}{\sqrt{2}} \sqrt{\frac{\hat{g}''(\xi - \xi_R)}{\hat{g}''(0)}} < \beta$, i.e.,

$$\frac{\hat{g}''(\xi - \xi_R)}{\hat{g}''(0)} > 2(1 - \beta)^2 \approx 0.22.$$

In the gaussian case, $\forall \xi : |\xi - \xi_R| < 1/\sigma$ we have $\varphi'(\xi) < \varphi'(\xi_R) = 1 - 1/\sqrt{2} \approx 0.29 < \beta$ and the convergence of Method II is then proved for these points.

Proof of Proposition 2.13. It holds

$$\tilde{p}(\tilde{\omega_1}) - \tilde{p}(\xi_0) = p(\omega_1) - p(\xi_0) + \delta_1 p'(\tau_1) + \epsilon_1 - \epsilon_0, \quad \tau_1 \in (\omega_1, \omega_1 + \delta_1).$$

Since

$$(\xi_1 - \xi_0)^2 = \frac{\alpha^2}{|\hat{g}''(0)|}(p(\omega_1) - p(\xi_0)),$$

$$(\tilde{\xi_1} - \xi_0)^2 = \frac{\alpha^2}{|\hat{g}''(0)|}(\tilde{p}(\tilde{\omega_1}) - \tilde{p}(\xi_0)),$$

by subtraction, it follows

$$(\tilde{\xi_1} - \xi_0)^2 - (\xi_1 - \xi_0)^2 = \frac{\alpha^2}{|\hat{g}''(0)|}(\delta_1 p'(\tau_1) + \epsilon_1 - \epsilon_0), \tag{3.64}$$

which yields to

$$(\tilde{\xi_1} - \xi_1)^2 + 2(\xi_1 - \xi_0)(\tilde{\xi_1} - \xi_1) - \frac{\alpha^2}{|\hat{g}''(0)|}(\delta_1 p'(\tau_1) + \epsilon_1 - \epsilon_0) = 0.$$

$\tilde{\xi_1} - \xi_1$ is a solution of the second order equation $x^2 + 2(\xi_1 - \xi_0)x - e = 0$, with $e = \frac{\alpha^2}{|\hat{g}''(0)|}(\delta_1 p'(\tau_1) + \epsilon_1 - \epsilon_0)$. Since $\tilde{\xi_1} - \xi_1$ must be zero when $e = 0$, by setting $\beta = sign(\xi_1 - \xi_0)$ it follows

$$\tilde{\xi_1} - \xi_1 = -\beta|\xi_1 - \xi_0| \left(-1 + \sqrt{1 + \frac{e}{(\xi_1 - \xi_0)^2}}\right),$$

and then

$$|\tilde{\xi_1} - \xi_1| \leq \frac{e}{2|\xi_1 - \xi_0|}, \tag{3.65}$$

where a first-order Taylor approximation has been used. Eq.(3.65) is exactly eq.(2.26).

Let now derive bounds for errors ϵ_1, and δ_1.

Bound for ϵ_1: Using the same notation adopted in Prop.2.2,

$$p(u, \xi)^2 = \hat{g}_1^2 + \frac{a_2^2}{a_1^2}\hat{g}_2^2 + 2\frac{a_2}{a_1}\hat{g}_1\hat{g}_2 \cos(\phi_2 - \phi_1)$$

and, without loss of generality, let consider the case $\Delta\phi'(u) = \phi_2'(u) - \phi_1'(u) > 0$ and $a_2 \geq a_1$. It holds

$$(\hat{g}_1 - \frac{a_2}{a_1}\hat{g}_2)^2 \leq p^2(u, \xi) \leq (\hat{g}_1 + \frac{a_2}{a_1}\hat{g}_2)^2 \Leftrightarrow$$

$$|\hat{g}_1 - \frac{a_2}{a_1}\hat{g}_2| \leq p(u, \xi) \leq \hat{g}_1 + \frac{a_2}{a_1}\hat{g}_2.$$

Let set $\hat{g}_1(\xi) = \hat{g}(\bar{\xi})$, with $\bar{\xi} = \xi - \phi_1'(u)$, then $\hat{g}_2(\bar{\xi}) = \hat{g}(\bar{\xi} + \Delta\phi'(u)) \approx \hat{g}(\bar{\xi}) + \hat{g}'(\bar{\xi})\Delta\phi'$, provided $\hat{g}(\bar{\xi}) + \hat{g}'(\bar{\xi})\Delta\phi' > 0$. Hence,

$$\hat{g}(\bar{\xi})\left(1 - \frac{a_2}{a_1}\right) - \frac{a_2}{a_1}|\hat{g}'(\bar{\xi})\Delta\phi'| \leq p(u,\xi) \leq \hat{g}(\bar{\xi})\left(1 + \frac{a_2}{a_1}\right) + \frac{a_2}{a_1}|\hat{g}'(\bar{\xi})\Delta\phi'| \Leftrightarrow$$

$$-\frac{a_2}{a_1}\hat{g}(\bar{\xi}) - \frac{a_2}{a_1}|\hat{g}'(\bar{\xi})\Delta\phi'| \leq p(u,\xi) - \hat{g}(\bar{\xi}) \leq \frac{a_2}{a_1}\hat{g}(\bar{\xi}) + \frac{a_2}{a_1}|\hat{g}'(\bar{\xi})\Delta\phi'| \Rightarrow$$

$$|\epsilon_1| = |p(u,\xi) - \hat{g}_1(\xi)| \leq \frac{a_2}{a_1}\left(1 + |\Delta\phi'(u)| \cdot \max_{\xi}|\hat{g}'(\xi)|\right).$$

Bound for δ_1: Let define $\Delta_1 = \sqrt{1 - p(\xi_0)}$ and $\tilde{\Delta}_1 = \sqrt{1 - \tilde{p}(\xi_0)}$, then $\tilde{\Delta}_1^2 = \Delta_1^2 - \epsilon_0$, where ϵ_0 is the error on the initial data, and

$$\delta_1 = |\Delta_1|\left(\sqrt{1 - \frac{\epsilon_0}{\Delta_1^2}} - 1\right) \approx -\frac{1}{2}|\Delta_1|\frac{\epsilon_0}{\Delta_1^2} \Rightarrow |\delta_1| < \frac{\epsilon_0}{2|\Delta_1|} < \frac{\epsilon_0}{\Delta\omega}.$$

Appendix B

Proof of Proposition 3.1. Setting $s = 1$ in eq.(1.3), it follows

$$S^g_{f_k}(u,\xi) = \frac{a_k(u)}{2}\, e^{i(\phi_k(u)-\xi\cdot u)}\left(\hat{g}(\xi-\phi'(u)) + \epsilon_k(u,\xi)\right), \forall\, k = 1, ...N,$$

with ϵ_k negligible. Assuming solvable non-separability regions, by STFT linearity we obtain

$$|S^g_f(u,\xi)|^2 = \sum_{k=1}^{N} |S^g_{f_k}(u,\xi)|^2 + 2\sum_{k\neq j}\cos\theta_{k,j}(u)|S^g_{f_k}(u,\xi)|\cdot|S^g_{f_j}(u,\xi)|, \quad (3.66)$$

where $\theta_{i,j} = \phi_k(u) - \phi_j(u)$ is the angle between $S^g_{f_k}(u,\xi)$ and $S^g_{f_j}(u,\xi)$. Since $|S_{f_k}(u,\xi)| = \frac{a_k(u)}{2}\hat{g}(\xi-\phi'_k(u))$ and $\theta_{k,j}$ is independent of ξ, by substitution in eq.(3.66), it follows

$$\int_{-\infty}^{+\infty} |S^g_f(u,\xi)|^2 d\xi = \sum_k \frac{a_k(u)^2}{4}\int_{-\infty}^{+\infty}\hat{g}^2(\xi-\phi'_k(u))d\xi$$
$$+\frac{a_k(u)a_j(u)}{2}\cos\theta_{i,j}(u)\sum_{k\neq j}\int_{-\infty}^{+\infty}\hat{g}(\xi-\phi'_k(u))\hat{g}(\xi-\phi'_j(u))d\xi\,. \quad (3.67)$$

Finally, the proof follows by applying Plancharel formula, i.e.

$$\int_{-\infty}^{+\infty}\hat{g}^2(\xi-\phi'_k(u))d\xi = ||\hat{g}||_{L^2(\mathbb{R})} = 2\pi\int_{-\infty}^{+\infty} g(t)^2 dt,\ \forall\, k$$

and setting $K(u) = \sum_k \frac{a_k^2(u)}{4}||\hat{g}||_{L^2(\mathbb{R})} = \frac{\pi}{2}\sum_k a_k^2(u)\int_{-\infty}^{+\infty} g(t)^2 dt$.

Proof of Proposition 3.3. Window FT is $\hat{g}(\xi) = \int_{-\infty}^{+\infty} g(t)e^{-i\xi t}\,d\xi = \exp(-\frac{1}{2}\sigma^2\xi^2)$, then by replacing it in eq.(3.3), $\forall\, u : a_k(u)a_j(u) > 0$, we get

$$\begin{aligned}\frac{2A_{k,j}(u)}{a_k(u)a_j(u)} &= \int_{-\infty}^{+\infty} \exp\left(-\frac{\sigma^2}{2}[(\xi-\phi'_k(u))^2 + (\xi-\phi'_j(u))^2]\right)\,d\xi \\ &= \int_{-\infty}^{+\infty} \exp\left(-\frac{\sigma^2}{2}[2\xi^2 - 2(\phi'_k(u)+\phi'_j(u))\cdot\xi + \phi'_k(u)^2 + \phi'_j(u)^2]\right)\,d\xi.\end{aligned}$$

The argument of the exponential can be rewritten as

$$\begin{aligned}&-\sigma^2\left[\xi^2 - (\phi'_k(u)+\phi'_j(u))\xi + \frac{\phi'_k(u)^2+\phi'_j(u)^2}{2}\right] \\ =&-\sigma^2\left[\xi^2 - (\phi'_k(u)+\phi'_j(u))\xi + 2\frac{\phi'_k(u)^2+\phi'_j(u)^2}{4} + 2\frac{\phi'_k\phi'_j}{4} - 2\frac{\phi'_k\phi'_j}{4}\right] \\ =&-\sigma^2\left[\left(\xi - \frac{\phi'_k(u)+\phi'_j(u)}{2}\right)^2 + \frac{\phi'_k(u)^2+\phi'_j(u)^2}{4} - 2\frac{\phi'_k\phi'_j}{4}\right] \\ =&-\sigma^2\left[\left(\xi - \frac{\phi'_k(u)+\phi'_j(u)}{2}\right)^2 + \frac{(\phi'_k(u)-\phi'_j(u))^2}{4}\right].\end{aligned}$$

By a change of variables, it follows

$$\begin{aligned}\frac{2A_{k,j}(u)}{a_k(u)a_j(u)} &= \frac{1}{\sigma}\exp\left(-\frac{\sigma^2}{4}(\phi'_k(u)-\phi'_j(u))^2\right)\int_{-\infty}^{+\infty}\exp\left(-\xi^2\right)d\xi \\ &= \frac{\sqrt{\pi}}{\sigma}\exp\left(-\frac{\sigma^2}{4}(\phi'_k(u)-\phi'_j(u))^2\right),\end{aligned}$$

which gives eq.(3).

Proof of Proposition 3.5. By Prop.3.1, $f_{int}(u) = A_{1,2}\cos\Delta\phi_{1,2}$, with $\Delta\phi_{1,2} = \phi_1(u) - \phi_2(u)$. From eq.(1.3) with $\epsilon(u,\xi)$ negligible and $s = 1$ we get

$$\Re(S^g_{f_{int}}(u,\xi)) = \frac{A_{1,2}(u)}{2}\hat{g}(\xi - |\Delta\phi'(u)|)\cos\Delta\phi_{1,2}(u)\,. \tag{3.68}$$

It is worth observing that the previous model holds true for time instants u such that $\Re(S^g_{f_{int}}(u,\xi))$ and $f_{int}(u)$ have the same sign. In this case, for all u

belonging to the support of f_{int}, we consider the ratio

$$\frac{\Re(S_{f_{int}}(u,\xi))}{f_{int}(u)} = \frac{1}{2}\hat{g}(\xi - |\Delta\phi'(u)|)\,. \tag{3.69}$$

Since $\hat{g}(\xi) = \int_{-\infty}^{+\infty} g(t)e^{-i\xi t}\,d\xi = \exp(-\frac{1}{2}\sigma^2\xi^2)$, by evaluating eq.(3.69) at $\xi = 0$, we get

$$\exp\left(-\frac{1}{2}\sigma^2\Delta\phi'^2(u)\right) = \frac{2\Re(S^g_{f_{int}}(u,0))}{f_{int}(u)}, \tag{3.70}$$

and then

$$\Delta\phi'^2(u) = -\frac{2}{\sigma^2}\ln\left(\frac{2\Re(S^g_{f_{int}}(u,0))}{f_{int}(u)}\right) = \ln\left[\left(\frac{2\Re(S^g_{f_{int}}(u,0))}{f_{int}(u)}\right)^{-\frac{2}{\sigma^2}}\right], \tag{3.71}$$

for all $u \in supp\{f_{int}\} : \ln\left(\frac{2\Re(S^g_{f_{int}}(u,0))}{f_{int}(u)}\right) \leq 0$, i.e. $\frac{2\Re(S^g_{f_{int}}(u,0))}{f_{int}(u)} \leq 1$.

Proof of Proposition 3.6.

Recalling the spectrogram model

$$P(u,\xi) = \frac{a_1^2}{4}\hat{g}_1^2 + \frac{a_2^2}{4}\hat{g}_2^2 + \frac{a_1a_2}{2}\cos\Delta\phi_{1,2}(u)\hat{g}_1\hat{g}_2,\ \hat{g}_i = \hat{g}(\xi - \phi_i'(u)), \tag{3.72}$$

$\Delta\phi(u) = \Delta\phi_{1,2}(u) = \phi_1(u) - \phi_2(u)$, let us compute the numerator of eq.(3.9) for a real and even window g. First, we observe that

$$\int_{-\infty}^{+\infty} \xi\,\hat{g}^2(\xi - \phi_i')\,d\xi = \int_{-\infty}^{+\infty} \xi\,\hat{g}^2(\xi)\,d\xi + \phi_i'(u)\int_{-\infty}^{+\infty} \hat{g}^2(\xi)\,d\xi = \phi_i'(u)\cdot||\hat{g}||_{L^2(\mathbb{R})}. \tag{3.73}$$

In addition,

$$\begin{aligned}
&\frac{a_1a_2}{2}\int_{-\infty}^{+\infty} \xi\,\hat{g}(\xi - \phi_1')\hat{g}(\xi - \phi_2')\,d\xi \\
&= \frac{a_1a_2}{2}\int_{-\infty}^{+\infty}\left(\omega + \frac{\phi_1' + \phi_2'}{2}\right)\hat{g}\left(\omega + \frac{\Delta\phi'}{2}\right)\hat{g}\left(\omega - \frac{\Delta\phi'}{2}\right)\,d\omega \\
&= \frac{a_1a_2}{2}\int_{-\infty}^{+\infty}\omega\,\hat{g}\left(\omega + \frac{\Delta\phi'}{2}\right)\hat{g}\left(\omega - \frac{\Delta\phi'}{2}\right)\,d\omega + \frac{\phi_1' + \phi_2'}{2}A_{1,2}(u)
\end{aligned}$$

$$= \frac{a_1 a_2}{2} \underbrace{\int_{-\infty}^{+\infty} \omega\, \hat{g}^2(\omega)\, d\omega}_{=0} + \frac{\phi_1' + \phi_2'}{2} A_{1,2}(u).$$

Hence,

$$\int_{-\infty}^{+\infty} \xi \cdot P(u,\xi)\, d\xi = ||\hat{g}||_{L^2(\mathbb{R})} \left(\frac{a_1^2}{4}\phi_1'(u) + \frac{a_2^2}{4}\phi_2'(u) \right) + \frac{\phi_1' + \phi_2'}{2} \cos\Delta\phi(u) A_{1,2}(u), \tag{3.74}$$

where eqs.(3.72), (3.73) and (3.74) have been accounted for. On the other hand, using the same equations,

$$\mathcal{E}_g(u) = ||\hat{g}||_{L^2(\mathbb{R})} \left(\frac{a_1^2}{4} + \frac{a_2^2}{4} \right) + A_{1,2}(u) \cos\Delta\phi(u),$$

and eq.(3.9) becomes

$$\begin{aligned} G(u) =& \frac{||\hat{g}||_{L^2(\mathbb{R})} \left(\frac{a_1^2}{4}\phi_1'(u) + \frac{a_2^2}{4}\phi_2'(u) \right) + \frac{\phi_1'+\phi_2'}{2} \cos\Delta\phi(u) A_{1,2}(u)}{||\hat{g}||_{L^2(\mathbb{R})} \left(\frac{a_1^2}{4} + \frac{a_2^2}{4} \right) + A_{1,2}(u) \cos\Delta\phi(u)} \\ =& \frac{||\hat{g}||_{L^2(\mathbb{R})} \frac{a_1^2}{4} \left(\phi_1'(u) + \frac{a_2^2}{a_1^2}\phi_2'(u) \right) + \frac{\phi_1'+\phi_2'}{2} \cos\Delta\phi(u) A_{1,2}(u)}{||\hat{g}||_{L^2(\mathbb{R})} \frac{a_1^2}{4} \left(1 + \frac{a_2^2}{a_1^2} \right) + A_{1,2}(u) \cos\Delta\phi(u)} \end{aligned}$$

$$= \frac{\phi_1'(u) + \frac{a_2^2}{a_1^2}\phi_2'(u)}{1 + \frac{a_2^2}{a_1^2}} \underbrace{\frac{1 + \frac{2(\phi_1'+\phi_2')}{||\hat{g}||_{L^2(\mathbb{R})} \left(\phi_1'(u) + \frac{a_2^2}{a_1^2}\phi_2'(u) \right)} \cos\Delta\phi(u) A_{1,2}(u)}{1 + \frac{4A_{1,2}(u)\cos\Delta\phi(u)}{\left(1+\frac{a_2^2}{a_1^2}\right)||\hat{g}||_{L^2(\mathbb{R})}}}}_{(*)}.$$

If the signal amplitudes are comparable, i.e. $\frac{a_1}{a_2} \approx 1$, then

$$\frac{(\phi_1' + \phi_2')}{2} \approx \frac{\left(\phi_1'(u) + \frac{a_2^2}{a_1^2}\phi_2'(u) \right)}{\left(1 + \frac{a_2^2}{a_1^2} \right)},$$

and

$$\frac{2(\phi_1' + \phi_2')}{\left(\phi_1'(u) + \frac{a_2^2}{a_1^2}\phi_2'(u)\right)} \approx \frac{4}{\left(1 + \frac{a_2^2}{a_1^2}\right)}.$$

Hence, $(*) \approx 1$ and then

$$G(u) \approx \frac{\phi_1'(u) + \phi_2'(u)}{2},$$

where the equality holds for $a_1 = a_2$.

Proof of Proposition 3.13. Let us define $F(r, \theta, t) = r - t\cos\theta - \phi'(t)\sin\theta$, then $\mathcal{M}$ is implicitly given by

$$F(r, \theta, t) = 0, \tag{3.75}$$

and $F_t(r, \theta, t) = 0 \Leftrightarrow -\cos\theta - \phi''(t)\sin\theta = 0 \Leftrightarrow \cot\theta = -\phi''(t)$. It follows that

$$\begin{cases} r(\theta_0) = t\cos\theta_0 + \phi'(t)\sin\theta_0 \\ \theta_0(t) = -\arctan\frac{1}{\phi''(t)} \end{cases} \tag{3.76}$$

satisfies $F(r(\theta_0(t)), \theta_0(t)) = 0$ and $F_t(r(\theta_0(t)), \theta_0(t)) = 0$. If $\phi''(t)$ is strictly monotone, eq.(3.76) defines $t_0 = \phi''^{-1}(\cot\theta_0)$. Finally, by replacing t with t_0 and θ with θ_0 in eq.(3.75), we obtain the function of variables (r, θ_0)

$$G(r, \theta_0) = r - t_0\cos\theta_0 - \phi'(t_0)\sin\theta_0, \tag{3.77}$$

and the envelope is implicitly given by $G(r, \theta_0) = 0$.

Proof of Proposition 3.14.

$$\begin{aligned} R(r, \theta) &= \iint p(u, \xi)\delta(r - u\cos\theta - \xi\sin\theta)du\, d\xi \\ &= \frac{a}{2}\iint \hat{g}(\xi - \phi'(u))\delta(r - u\cos\theta - \xi\sin\theta)du\, d\xi \\ &= \frac{a}{4\pi}\iint \hat{g}(\xi - \phi'(u)) \int e^{-ik(r - u\cos\theta - \xi\sin\theta)}dk\, du\, d\xi, \end{aligned}$$

that by the change of variable $k = \frac{k'}{\sin\theta}$ becomes

$$
\begin{aligned}
&= \frac{a}{4\pi \sin\theta} \iint dk'\, du\, e^{-\frac{ik'r}{\sin\theta}} e^{ik'u\cot\theta} \int \hat{g}(\xi - \phi'(u)) e^{ik'\xi} d\xi \\
&= \frac{a}{4\pi \sin\theta} \iint e^{-\frac{ik'}{\sin\theta}} e^{ik'\cot\theta} g(k) e^{ik'\phi'(u)} dk'\, du \\
&= \frac{a}{4\pi \sin\theta} \iint g(k') e^{-\frac{ik'}{\sin\theta}(r - u\cos\theta - \phi'(u)\sin\theta)} dk'\, du \\
&= \frac{a}{4\pi \sin\theta} \int \hat{g}\left(\frac{r - u\cos\theta - \phi'(u)\sin\theta}{\sin\theta}\right) du.
\end{aligned}
$$

Proof of Proposition 3.16. Let us consider the change of variables

$$
\begin{cases}
u = t + c\,\cos\theta \\
\xi = \phi'(t) + c\,\sin\theta,
\end{cases}
$$

with $t \in [0, +\infty)$ and $\theta \in [0, \pi)$. The corresponding jacobian is

$$
J(t, c) = \det \begin{pmatrix} 1 & \cos\theta \\ \phi''(t) & \sin\theta \end{pmatrix} = \sin\theta - \phi''(t)\cos\theta,
$$

which is non-zero $\forall\, \theta \neq \arctan\phi''(t)$, therefore eq.(3.35) well-defines a new parametrization of the spectrogram, $\forall\, \theta \in [0, \pi) - \{\arctan\phi''(t)\}$.

Furthermore,

$$
\iint p(u, \xi)^2\, du, d\xi = \iint \tilde{p}^2(t, c)\, |\sin\theta - \phi''(t)\cos\theta|\, dc\, dt,
$$

and the thesis follows by observing that θ_0 identifies the direction $(\cos\theta_0, \sin\theta_0) = \left(-\frac{\phi''(t)}{1+\phi''^2(t)}, \frac{1}{1+\phi''^2(t)}\right)$, so that $\sin\theta_0 - \phi''(t)\cos\theta_0 = 1$.

Proof of Proposition 3.17. For each fixed t, the area of the spectrogram section identified by θ is

$$
Area(\theta) = \int \tilde{p}(t, c)\, dc = \int p(t + c\,\cos\theta, \phi'(t) + c\,\sin\theta)\, dc,
$$

and then

$$\frac{dArea}{d\theta} = \int -c\,p_u \sin\theta + c\,p_\xi \cos\theta\, dc = \int c\,p_\xi \cdot (\phi''(t)\sin\theta + \cos\theta)\, dc;$$

since $(\cos\theta_0, \sin\theta_0) = \left(\frac{-\phi''(t)}{1+\phi''^2(t)}, \frac{1}{1+\phi''^2(t)}\right)$, then $\frac{d}{d\theta}Area(\theta_0) = 0$. Furthermore,

$$\left.\frac{d^2Area}{d\theta^2}\right|_{\theta=\theta_0} = \int c\,p_\xi \cdot (\phi''(t)\cos\theta_0 - \sin\theta_0) dc = -\int c\,p_\xi \cdot \underbrace{(-\phi''(t)\cos\theta_0 + \sin\theta_0)}_{=1}\, dc$$

$$= -\int c\,p_c\, dc = \left[-c\,p + \int p\, dc\right] = \int p\, dc.$$

It follows that assuming $\hat{g}$ to be compactly supported or rapidly decreasing to zero we obtain $\left.\frac{d^2Area}{d\theta^2}\right|_{\theta=\theta_0} > 0$ and then θ_0 is a minimum of $Area$.

Proof of Proposition 3.18. Let us consider the section of the spectrogram centered in $(t, \phi'(t))$ and normal to the ridge direction identified by $\theta_0(t) = -\arctan\frac{1}{\phi''(t)}$ for a fixed t, i.e.

$$\tilde{p}(t,c) = p(u(t),\xi(t)) = p(t + c\,\cos\theta_0(t), \phi'(t) + c\,\sin\theta_0(t)),\ c \in \left[-\frac{\Delta\omega}{2}, \frac{\Delta\omega}{2}\right]. \tag{3.78}$$

If $t \in [0, +\infty)$, eq.(3.78) provides a new parametrization for the spectrogram, through the change of variables

$$\begin{cases} u = t + c\,\cos\theta_0(t) \\ \xi = \phi'(t) + c\,\sin\theta_0(t), \end{cases} \tag{3.79}$$

whose jacobian is

$$J(t,c) = \det\begin{pmatrix} 1 - c\frac{\phi'''}{1+\phi''^2(t)}\sin\theta_0(t) & \cos\theta_0(t) \\ \phi''(t) + c\frac{\phi'''}{1+\phi''^2(t)}\cos\theta_0(t) & \sin\theta_0(t) \end{pmatrix}$$
$$= \sin\theta_0 - \phi''(t)\cos\theta_0 - c\,\frac{\phi'''}{1+\phi''^2(t)} = 1 - c\,\frac{\phi'''(t)}{1+\phi''^2(t)},$$

which is equal to 1 if $\phi'''(t) = 0$ or both ϕ'' and ϕ''' are zero ($Hp\,1$). $|c| < \frac{1+\phi''^2(t)}{\phi'''(t)}$ guarantees that $J(t,c) \neq 0$, $\forall\, t$. The latter condition is met if the bandwidth of

the analysis window satisfies $\Delta\omega \leq \frac{1+L_1^2}{L_2}$. According to eq.(3.35),

$$\tilde{p}(t,c) = p(t+c\,\cos\theta_0(t), \phi'(t)+c\,\sin\theta_0(t)) = \hat{g}(\phi'(t)+c\,\sin\theta_0(t)-\phi'(t+c\,\cos\theta_0(t))),$$

that reduces to

$$\tilde{p}(t,c) = \hat{g}(c\,(-\phi''(t)\cos\theta_0 + \sin\theta_0(t))o(c)),$$

whenever c is close to 0. By recalling $(-\phi''(t)\cos\theta_0 + \sin\theta_0(t)) = 1$ and neglecting the error in Taylor approximation, it holds

$$\tilde{p}(t,c) = \hat{g}\,(c)\,.$$

and then $\frac{d}{dt}\tilde{p}(t,c) = 0$.

Proof of Proposition 3.19. A generic characteristic curve can be parametrized as

$$(t - c\cdot\cos\theta_0, \phi'(t) - c\cdot\sin\theta_0), t \geq 0,$$

where $\theta_0 = \theta_0(t) = -\arctan\left(\frac{1}{\phi''(t)}\right)$ and $c \in [-\frac{\Delta\omega}{2}, \frac{\Delta\omega}{2}]$ — see Fig.3.34. Let us suppose $\hat{g}$ to be compactly supported, symmetric and positive.

It is worth observing that the spectrogram value at a point belonging to a characteristic curve can be obtained by considering the spectrogram section, i.e. $\tilde{p}(t,c) = \hat{g}(c)$. In addition, the shifting property, $R[f(x-a, y-b)](r,\theta) = R[f](r - a\cos\theta - b\sin\theta, \theta)$ allows to write the parametric RT of a TF representation which is perfectly localized on a point P_{car} on a generic characteristic, i.e.

$$\begin{aligned} R_{P_{car}}(r,\theta,t) &= \hat{g}(c)\,\delta(r - c\cos\theta_0\cos\theta - c\sin\theta_0\sin\theta - t\,\cos\theta - \phi'(t)\,\sin\theta) \\ &= \hat{g}(c)\,\delta(r - t\cos\theta - \phi'(t)\sin\theta - c\cos(\theta-\theta_0)). \end{aligned} \tag{3.80}$$

The RT of $\tilde{p}(t,c)$ is obtained by integrating eq.(3.80) over c, $R(r,\theta,t) =$

$\int R_{P_{car}}(r,\theta,t)\,dc$, i.e.

$$\begin{aligned} R(r,\theta,t) &= \int_{\mathbb{R}} \hat{g}(c)\,(r - t\cos\theta - \phi'(t)\sin\theta - c\cos(\theta-\theta_0))\,dc \\ &= \frac{1}{2\pi}\int_{\mathbb{R}} dc\,\hat{g}(c)\int_{\mathbb{R}} e^{-ik[r-t\cos\theta-\phi'(t\sin\theta)-c\,\cos(\theta-\theta_0)]}\,dk \\ &= \frac{1}{2\pi}\int_{\mathbb{R}} dk\,e^{-ik(r-t\cos\theta-\phi'(t)\sin\theta)}\int_{\mathbb{R}} \hat{g}(c)e^{ikc\,\cos(\theta-\theta_0)}dc. \end{aligned}$$

Therefore,

$$R(r,\theta,t) = \frac{1}{2\pi}\int_{\mathbb{R}} g\,(k\cos(\theta-\theta_0))\,e^{-ik(r-t\cos\theta-\phi'(t)\sin\theta)}\,dk,$$

and the change of variable $k\cos(\theta-\theta_0) = k'$ finally gives

$$R(r,\theta,t) = \frac{1}{2\pi\cos(\theta-\theta_0)}\hat{g}\left(\frac{r - t\cos\theta - \phi'(t)\sin\theta}{\cos(\theta-\theta_0)}\right),\ \forall\,\theta : |\theta-\theta_0| \in \left[0,\frac{\pi}{2}\right).$$

Proof of Proposition 3.20. Let us take $R(r,\theta,t)$ derivatives with respect to variable r, at fixed θ.

$$2\pi R_r(r,\theta,t) = \frac{1}{\cos^2(\theta-\theta_0)}\,\hat{g}'\left(\frac{r - t\cos\theta - \phi'(t)\sin\theta}{\cos(\theta-\theta_0)}\right),$$

$$2\pi R_{rr}(r,\theta,t) = \frac{1}{\cos^3(\theta-\theta_0)}\,\hat{g}''\left(\frac{r - t\cos\theta - \phi'(t)\sin\theta}{\cos(\theta-\theta_0)}\right).$$

It follows

$$\begin{cases} R_r(r(t),\theta,t) = \frac{1}{2\pi\cos^2(\theta-\theta_0)}\,\hat{g}'(0) = 0 \\ R_{rr}(r(t),\theta,t) = \frac{1}{2\pi\cos^3(\theta-\theta_0)}\,\hat{g}''(0) < 0, \quad \forall\,\theta \neq 0. \end{cases}$$

Proof of Proposition 3.21. Let us compute $R(r,\theta,t)$ derivatives with respect variable r and θ.

$$R_r(r,\theta,t) = \frac{1}{2\pi\cos^2(\theta-\theta_0)}\hat{g}'\left(\frac{r - t\cos\theta - \phi'(t)\sin\theta}{\cos(\theta-\theta_0)}\right),$$

$$
\begin{aligned}
R_\theta(r,\theta,t) &= \frac{\sin(\theta-\theta_0)}{2\pi(\cos(\theta-\theta_0))^2}\hat{g}\left(\frac{r-t\cos\theta-\phi'(t)\sin\theta}{\cos(\theta-\theta_0)}\right)\\
&+\frac{1}{2\pi\cos(\theta-\theta_0)}\hat{g}'\left(\frac{(r-t\cos\theta-\phi'(t)\sin\theta)}{\cos(\theta-\theta_0)}\right)\cdot\\
&\cdot\frac{\cos(\theta-\theta_0)(t\sin\theta-\phi'(t)\cos\theta)+\sin(\theta-\theta_0)(r-t\cos\theta-\phi'(t)\sin\theta)}{\cos^2(\theta-\theta_0)}\\
&=\frac{\sin(\theta-\theta_0)}{\cos(\theta-\theta_0)}R(r,\theta,t)+\frac{-\phi'(t)\cos\theta_0+t\sin\theta_0+r\sin(\theta-\theta_0)}{\cos(\theta-\theta_0)}R_r(r,\theta,t);
\end{aligned}
$$

it follows

$$
\cos(\theta-\theta_0)R_\theta+(\phi'(t)\cos\theta_0-t\sin\theta_0-r\sin(\theta-\theta_0))R_r(r,\theta,t)=\sin(\theta-\theta_0)R.
$$

Proof of Proposition 3.22. The characteristic curves of eq.(3.38) are the solution of the following system of odes

$$
\begin{cases}
\dot{\theta}(\tau)=1\\
\dot{r}(\tau)=-r(\tau)\tan(\theta(\tau)-\theta_0)+\frac{-t\sin\theta_0+\phi'(t)\cos\theta_0}{\cos(\theta(\tau)-\theta_0)},
\end{cases}
$$

that is equivalent to the following equation

$$
\dot{r}(\theta)+r(\theta)\tan(\theta-\theta_0)=\frac{1}{\cos(\theta-\theta_0)}(-t\sin\theta_0+\phi'(t)\cos\theta_0),
$$

whose solution is

$$
\begin{aligned}
r(\theta)&=\cos(\theta-\theta_0)(-t\sin\theta_0+\phi'(t)\cos\theta_0)\left(\int\frac{1}{\cos^2(\theta'-\theta_0)}d\theta'+c\right)=\\
&=\cos(\theta-\theta_0)(-t\sin\theta_0+\phi'(t)\cos\theta_0)\left(\tan(\theta-\theta_0)+k\right)\\
&=k(-t\sin\theta_0+\phi'(t)\cos\theta_0)\cdot\cos(\theta-\theta_0)|+\sin(\theta-\theta_0)(\phi'(t)\cos\theta_0-t\sin\theta_0),
\end{aligned}
$$

which proves eq.(3.39).

Proof of Proposition 3.23. By assuming $\frac{\phi'(t)}{t}\approx\phi''(t)$, the support of the RT of a characteristic curve as in eq.(3.80) can be expressed as

$$
\delta\left(r-t\sqrt{1+\cot^2\theta_0}\sin(\theta-\theta_0)-c\cos(\theta-\theta_0)\right),
$$

while eq.(3.39) becomes

$$\delta\left(r - t\sqrt{1+\cot^2\theta_0}\,\sin(\theta-\theta_0) + k\,t\,\sqrt{1+\cot^2\theta_0}\cos(\theta-\theta_0)\right).$$

They are equivalent if $c = k\,t\sqrt{1+\cot^2\theta_0} \Leftrightarrow k = \frac{c}{t\sqrt{1+\cot^2\theta_0}} = \frac{c\,|\sin\theta_0|}{t}, t > 0$. In particular, $k = 0$ corresponds to the mapped ridge curve.

Proof of Proposition 3.24. The change of variables in eq.(3.79) gives $du\,d\xi = \left|1 - c\,\frac{\phi'''}{1+\phi''^2(t)}\right| dt\,dc$ with $\left(1 - c\,\frac{\phi'''}{1+\phi''^2(t)}\right) > 0$ by hypothesis; it follows

$$R(r,\theta) = \iint \left[\tilde{p}(t,c)\cdot\left(1 - \frac{c\,\phi'''}{1+\phi''^2(t)}\right)\cdot \right.$$
$$\left. \delta(r - t\cos\theta - \phi'(t)\sin\theta - c\cos(\theta-\theta_0))\right] dt\,dc,$$

that is

$$R(r,\theta) = \iint R(r,\theta,t)\,dt \tag{3.81}$$
$$- \iint c\,\hat{g}\,(c)\,\frac{\phi'''(t)}{1+\phi''^2(t)}\delta(r - t\cos\theta - \phi'(t)\sin\theta - c\cos(\theta-\theta_0))\,dt\,dc. \tag{3.82}$$

Eq.(3.82) is equal to

$$-\frac{1}{2\pi}\iint dt\,dc\frac{\phi'''(t)}{1+\phi''^2(t)}\,c\,\hat{g}\,(c)\int e^{-ik(r-t\cos\theta-\phi'(t)\sin\theta-c\,\cos(\theta-\theta_0))}\,dk$$
$$= -\frac{1}{2\pi}\iint dt\,\frac{\phi'''(t)}{1+\phi''^2(t)}\,e^{-ik(r-t\cos\theta-\phi'(t)\sin\theta)}\int c\,\hat{g}\,(c)\,e^{ikc\,\cos(\theta-\theta_0))}\,dc\,dk$$
$$= \frac{i}{2\pi}\iint \frac{\phi'''(t)}{1+\phi''^2(t)}\,e^{-ik(r-t\cos\theta-\phi'(t)\sin\theta)}\int ic\,\hat{g}\,(c)\,e^{ikc\,\cos(\theta-\theta_0}\,dc\,dk\,dt;$$

and by applying FT properties to the last integral, we obtain

$$= \frac{i}{2\pi}\iint \frac{\phi'''(t)}{1+\phi''^2(t)}\,e^{-ik(r-t\cos\theta-\phi'(t)\sin\theta)}g'\,(k\cos(\theta-\theta_0))\,dk\,dt.$$

By applying the change of variable $k\cos(\theta-\theta_0) = k'$, the previous equation can

be written as

$$= \frac{i}{2\pi} \iint \frac{\phi'''(t)}{\cos(\theta - \theta_0)(1 + \phi''^2(t))} \, e^{-\frac{ik'(r - t\cos\theta - \phi'(t)\sin\theta)}{\cos(\theta - \theta_0)}} g'(k') \, dk' \, dt$$

$$= -\frac{1}{2\pi} \int \frac{\phi'''(t)}{1 + \phi''^2(t)} \frac{r - t\cos\theta - \phi'(t)\sin\theta}{\cos^2(\theta - \theta_0)} \, \hat{g}\left(\frac{r - t\cos\theta - \phi'(t)\sin\theta)}{\cos(\theta - \theta_0)}\right) dt. \tag{3.83}$$

Since $1 + \phi''^2(t) = 1 + \cot\theta_0^2(t) = 1/\sin^2\theta_0$, then eq.(3.83) is

$$= -\frac{1}{2\pi} \int \phi'''(t)\sin^2\theta_0 \frac{r - t\cos\theta - \phi'(t)\sin\theta}{\cos^2(\theta - \theta_0)} \, \hat{g}\left(\frac{r - t\cos\theta - \phi'(t)\sin\theta)}{\cos(\theta - \theta_0)}\right) dt,$$

and from eq.(3.37) it results

$$= -\int \frac{\phi'''(t)\sin^2\theta_0}{\cos(\theta - \theta_0)} (r - t\cos\theta - \phi'(t)\sin\theta) \, R(r, \theta, t) \, dt. \tag{3.84}$$

Finally, eq.(3.40) follows by replacing eq.(3.84) in eq.(3.82).

Bibliography

[1] Yaqian Shi, Da Zhang, Hu Ji, and Rui Dai. Application of synchrosqueezed wavelet transform in microseismic monitoring of mines. In *IOP Conference Series: Earth and Environmental Science*, volume 384, page 012075. IOP Publishing, 2019.

[2] Hyewon Lee, Tae Hyun Kim, Jun Won Choi, and Sunghyun Choi. Chirp signal-based aerial acoustic communication for smart devices. In *2015 IEEE Conference on Computer Communications (INFOCOM)*, pages 2407–2415, 2015.

[3] Irena Orović and Srdjan Stanković. Time-frequency-based speech regions characterization and eigenvalue decomposition applied to speech watermarking. *EURASIP Journal on Advances in Signal Processing*, 2010:4, 2010.

[4] Duong-Hung Pham and Sylvain Meignen. High-order synchrosqueezing transform for multicomponent signals analysis with an application to gravitational-wave signal. *IEEE Transactions on Signal Processing*, 65(12):3168–3178, 2017.

[5] Jonathan S Smith. The local mean decomposition and its application to eeg perception data. *Journal of the Royal Society Interface*, 2(5):443–454, 2005.

[6] Gang Wang, Chaolin Teng, Kuo Li, Zhonglin Zhang, and Xiangguo Yan. The removal of eog artifacts from eeg signals using independent component analysis and multivariate empirical mode decomposition. *IEEE journal of biomedical and health informatics*, 20(5):1301–1308, 2015.

[7] Cornel Ioana, Cédric Gervaise, Yann Stéphan, and Jerôme I Mars. Analysis of underwater mammal vocalisations using time–frequency-phase tracker. *Applied Acoustics*, 71(11):1070–1080, 2010.

[8] Victor C Chen, Fayin Li, S-S Ho, and Harry Wechsler. Micro-doppler effect in radar: phenomenon, model, and simulation study. *IEEE Transactions on Aerospace and electronic systems*, 42(1):2–21, 2006.

[9] Daniel L Stevens and Stephanie A Schuckers. Detection and parameter extraction of low probability of intercept radar signals using the hough transform. *Global Journal of Research In Engineering*, 2016.

[10] Takuya Sakamoto, Toru Sato, Pascal J Aubry, and Alexander G Yarovoy. Texture-based automatic separation of echoes from distributed moving targets in uwb radar signals. *IEEE Transactions on Geoscience and Remote Sensing*, 53(1):352–361, 2014.

[11] Bastien Lyonnet, Cornel Ioana, and Moeness G Amin. Human gait classification using microdoppler time-frequency signal representations. In *2010 IEEE Radar Conference*, pages 915–919. IEEE, 2010.

[12] Yipeng Ding and Jingtian Tang. Micro-doppler trajectory estimation of pedestrians using a continuous-wave radar. *IEEE Transactions on Geoscience and Remote Sensing*, 52(9):5807–5819, 2014.

[13] G Lopez-Risueno, J Grajal, and O Yeste-Ojeda. Atomic decomposition-based radar complex signal interception. *IEE Proceedings-Radar, Sonar and Navigation*, 150(4):323–331, 2003.

[14] Patrick Flandrin. Time frequency and chirps. In *Wavelet Applications VIII*, volume 4391, pages 161–175. International Society for Optics and Photonics, 2001.

[15] B. Boashash. *Time-Frequency Signal Analysis and Processing: A Comprehensive Reference*. 2015.

[16] V. Bruni, B. Piccoli, S. Marconi, and D. Vitulano. Instantaneous frequency detection via ridge neighbor tracking. *Proceedings of the 2nd International Workshop on Cognitive Information Processing,Elba,Italy*, June 2010.

[17] R. A. Carmona, W. L. Hwang, and B. Torresani. Characterization of signals by the ridges of their wavelet transform. *IEEE Transactions on Signal Processing*, 45(10):2586–2590, October 1997.

[18] Nabeel Ali Khan and Boualem Boashash. Multi-component instantaneous frequency estimation using locally adaptive directional time frequency distributions. *International Journal of Adaptive Control and Signal Processing*, 30(3):429–442, 2016.

[19] Luke Rankine, Mostefa Mesbah, and Boualem Boashash. If estimation for multicomponent signals using image processing techniques in the time–frequency domain. *Signal Processing*, 87(6):1234–1250, 2007.

[20] LJubiša Stankovic, Igor Djurovic, Akira Ohsumi, and Hiroshi Ijima. Instantaneous frequency estimation by using wigner distribution and viterbi algorithm. In *2003 IEEE International Conference on Acoustics, Speech, and Signal Processing, 2003. Proceedings.(ICASSP'03).*, volume 6, pages VI–121. IEEE, 2003.

[21] Jonatan Lerga and Victor Sucic. An instantaneous frequency estimation method based on the improved sliding pair-wise ici rule. In *10th International Conference on Information Science, Signal Processing and their Applications (ISSPA 2010)*, pages 161–164. IEEE, 2010.

[22] Jonatan Lerga, Victor Sucic, and Boualem Boashash. An efficient algorithm for instantaneous frequency estimation of nonstationary multicomponent signals in low snr. *EURASIP Journal on Advances in Signal Processing*, 2011(1):725189, 2011.

[23] Jonatan Lerga, Victor Sucic, and Boualem Boashash. An improved method for nonstationary signals components extraction based on the ici rule. In *International Workshop on Systems, Signal Processing and their Applications, WOSSPA*, pages 307–310. IEEE, 2011.

[24] Jonatan Lerga, Nicoletta Saulig, Vladimir Mozetic, and Rebeka Lerga. Number of eeg signal components estimated using the short-term rényi entropy. In *2016 International Multidisciplinary Conference on Computer and Energy Science (SpliTech)*, pages 1–6. IEEE, 2016.

[25] Jonatan Lerga, Nicoletta Saulig, and Vladimir Mozetič. Algorithm based on the short-term rényi entropy and if estimation for noisy eeg signals analysis. *Computers in biology and medicine*, 80:1–13, 2017.

[26] Jonatan Lerga, Nicoletta Saulig, Rebeka Lerga, and Željka Milanović. Effects of tfd thresholding on eeg signal analysis based on the local rényi entropy. In *2017 2nd International Multidisciplinary Conference on Computer and Energy Science (SpliTech)*, pages 1–6. IEEE, 2017.

[27] Jonatan Lerga, Nicoletta Saulig, Rebeka Lerga, and Ivan Štajduhar. Tfd thresholding in estimating the number of eeg components and the dominant if using the short-term rényi entropy. In *Proceedings of the 10th International Symposium on Image and Signal Processing and Analysis*, pages 80–85. IEEE, 2017.

[28] Nicoletta Saulig, Jonatan Lerga, Zlatko Baracskai, and Miloš Daković. Adaptive thresholding in extracting useful information from noisy time-frequency distributions. In *2019 11th International Symposium on Image and Signal Processing and Analysis (ISPA)*, pages 329–334. IEEE, 2019.

[29] Nicoletta Saulig, Jonatan Lerga, Željka Milanović, and Cornel Ioana. Extraction of useful information content from noisy signals based on structural affinity of clustered tfds' coefficients. *IEEE Transactions on Signal Processing*, 67(12):3154–3167, 2019.

[30] Patrick Flandrin. *Time-frequency/time-scale analysis*, volume 10. Academic press, 1998.

[31] I. Daubechies, J. Lu, and H. T. Wu. Synchrosqueezed wavelet transforms: an empirical mode decomposition-like tool. *Applied and Computational Harmonic Analysis*, 30(2):243–261, 2011.

[32] Z. Průša, P. L. Søndergaard, N. Holighaus, Ch. Wiesmeyr, and P. Balazs. The Large Time-Frequency Analysis Toolbox 2.0. In *Sound, Music, and Motion*, LNCS, pages 419–442. Springer International Publishing, 2014.

[33] MATLAB. *9.6.0.1099231 (R2019a) Update 1*. The MathWorks Inc., Natick, Massachusetts, 2019.

[34] Scott. Example of doppler radar signal processing. *https://www.mathworks.com/matlabcentral/fileexchange/49014-example-of-doppler-radar-signal-processing), MATLAB Central File Exchange*, August 2020.

[35] Stéphane Mallat. *A wavelet tour of signal processing*. Elsevier (1999).

[36] Sylvain Meignen, Marcelo Colominas, and Duong-Hung Pham. On the use of rényi entropy for optimal window size computation in the short-time fourier transform. In *ICASSP 2020-2020 IEEE International Conference on Acoustics, Speech and Signal Processing (ICASSP)*, pages 5830–5834. IEEE, 2020.

[37] H-I Choi and William J Williams. Improved time-frequency representation of multicomponent signals using exponential kernels. *IEEE Transactions on Acoustics, Speech, and Signal Processing*, 37(6):862–871, 1989.

[38] Ram Bilas Pachori and Pradip Sircar. A new technique to reduce cross terms in the wigner distribution. *Digital Signal Processing*, 17(2):466–474, 2007.

[39] Yong-sheng Yan, Carmen CY Poon, and Yuan-ting Zhang. Reduction of motion artifact in pulse oximetry by smoothed pseudo wigner-ville distribution. *Journal of NeuroEngineering and Rehabilitation*, 2(1):1–9, 2005.

[40] LJubisa Stankovic. A method for time-frequency analysis. *IEEE Transactions on Signal Processing*, 42(1):225–229, 1994.

[41] LJubisa Stankovic, Thayananthan Thayaparan, and Milos Dakovic. Signal decomposition by using the s-method with application to the analysis of hf radar signals in sea-clutter. *IEEE Transactions on Signal Processing*, 54(11):4332–4342, 2006.

[42] Stanley R Deans. *The Radon transform and some of its applications*. Courier Corporation (2007).

[43] Stanley R Deans. Radon and abel transforms. *The transforms and applications handbook*, 2, 2000.

[44] Stanley R Deans. *The Radon transform and some of its applications*. Courier Corporation, 2007.

[45] Ervin Sejdić, Igor Djurović, and LJubiša Stanković. Fractional fourier transform as a signal processing tool: An overview of recent developments. *Signal Processing*, 91(6):1351–1369, 2011.

[46] Victor Namias. The fractional order fourier transform and its application to quantum mechanics. *IMA Journal of Applied Mathematics*, 25(3):241–265, 1980.

[47] AC McBride and FH Kerr. On namias's fractional fourier transforms. *IMA Journal of applied mathematics*, 39(2):159–175, 1987.

[48] John C Wood and Daniel T Barry. Tomographic time-frequency analysis and its application toward time-varying filtering and adaptive kernel design for multicomponent linear-fm signals. *IEEE transactions on signal processing*, 42(8):2094–2104, 1994.

[49] LJubiša Stanković, Tatiana Alieva, and Martin J Bastiaans. Time–frequency signal analysis based on the windowed fractional fourier transform. *Signal processing*, 83(11):2459–2468, 2003.

[50] Tatiana Alieva and Martin J Bastiaans. On fractional fourier transform moments. *IEEE signal processing letters*, 7(11):320–323, 2000.

[51] Shiqian Chen, Xingjian Dong, Guanpei Xing, Zhike Peng, Wenming Zhang, and Guang Meng. Separation of overlapped non-stationary signals by ridge path regrouping and intrinsic chirp component decomposition. *IEEE Sensors Journal*, 17(18):5994–6005, 2017.

[52] Norden E Huang, Zheng Shen, Steven R Long, Manli C Wu, Hsing H Shih, Quanan Zheng, Nai-Chyuan Yen, Chi Chao Tung, and Henry H Liu. The empirical mode decomposition and the hilbert spectrum for nonlinear and non-stationary time series analysis. *Proceedings of the Royal Society of London. Series A: Mathematical, Physical and Engineering Sciences*, 454(1971):903–995, 1998.

[53] Zhaohua Wu and Norden E Huang. Ensemble empirical mode decomposition: a noise-assisted data analysis method. *Advances in adaptive data analysis*, 1(01):1–41, 2009.

[54] Luan Lin, Yang Wang, and Haomin Zhou. Iterative filtering as an alternative algorithm for empirical mode decomposition. *Advances in Adaptive Data Analysis*, 1(04):543–560, 2009.

[55] Antonio Cicone. Nonstationary signal decomposition for dummies. In *Advances in Mathematical Methods and High Performance Computing*, pages 69–82. Springer, 2019.

[56] Naveed Rehman and Danilo P Mandic. Multivariate empirical mode decomposition. *Proceedings of the Royal Society A: Mathematical, Physical and Engineering Sciences*, 466(2117):1291–1302, 2009.

[57] Danilo P Mandic, Naveed ur Rehman, Zhaohua Wu, and Norden E Huang. Empirical mode decomposition-based time-frequency analysis of multivariate signals: The power of adaptive data analysis. *IEEE signal processing magazine*, 30(6):74–86, 2013.

[58] Kunihiko Kodera, Roger Gendrin, and C de Villedary. Analysis of time-varying signals with small bt values. *IEEE Transactions on Acoustics, Speech, and Signal Processing*, 26(1):64–76, 1978.

[59] F. Auger and P. Flandrin. Improving the readability of time-frequency and time-scale representations by the reassignment method. *IEEE Transactions on Signal Processing*, 43:1068–1089, May 1995.

[60] F. Flandrin, F. Auger, and E. Chassandre-Mottin. Time-frequency reassignment: From principles to algorithms. *Applications in Time Frequency Signal Processing,CRC Press: Boca Raton, FL, USA, Chapter 5*, pages 179–193, 2003.

[61] I Djurovic, L Stankovic, and Martin J Bastiaans. Multidimensional reassignment method. In *5th International Conference on Telecommunications in Modern Satellite, Cable and Broadcasting Service. TELSIKS 2001. Proceedings of Papers (Cat. No. 01EX517)*, volume 1, pages 13–16. IEEE, 2001.

[62] Ingrid Daubechies. A nonlinear squeezing of the continuous wavelet transform based on auditory nerve models. *Wavelets in medicine and biology*, pages 527–546, 1996.

[63] F. Auger, P. Flandrin, Y. Lin, S. Mclaughlin, S. Meignen, and et al. Time-frequency reassignment and synchrosqueezing: an overview. *IEEE Signal Processing Magazine*, 30(6):32–41, 2013.

[64] T. Oberlin, S. Meignen, and V. Perrier. Second-order synchrosqueezing transform of invertible reassignment towards ideal time-frequency representations. *IEEE Transactions Signal Processing*, 63:1335–1344, 2015.

[65] R. Behera, S. Meignen, and T. Oberlin. Theoretical analysis of the second-order synchrosqueezing transform. *Applied and Computational Harmonic Analysis*, 45:379–404, 2016.

[66] Franz Hlawatsch. Interference terms in the wigner distribution. *Proc. Dig. Sig. Proc.*, 363, 1984.

[67] Mokhtar Mohammadi, Ali Akbar Pouyan, Nabeel Ali Khan, and Vahid Abolghasemi. Locally optimized adaptive directional time–frequency distributions. *Circuits, Systems, and Signal Processing*, 37(8):3154–3174, 2018.

[68] Shiying Dong, Boualem Boashash, Ghasem Azemi, Barbara E Lingwood, and Paul B Colditz. Automated detection of perinatal hypoxia using time–frequency-based heart rate variability features. *Medical & biological engineering & computing*, 52(2):183–191, 2014.

[69] Boualem Boashash, Ghasem Azemi, and Nabeel Ali Khan. Principles of time–frequency feature extraction for change detection in non-stationary signals: Applications to newborn eeg abnormality detection. *Pattern Recognition*, 48(3):616–627, 2015.

[70] Igor Djurovic and L Stankoic. Influence of high noise on the instantaneous frequency estimation using quadratic time-frequency distributions. *IEEE Signal Processing Letters*, 7(11):317–319, 2000.

[71] Igor Djurović and LJubiša Stanković. An algorithm for the wigner distribution based instantaneous frequency estimation in a high noise environment. *Signal Processing*, 84(3):631–643, 2004.

[72] Nabeel Ali Khan, Mokhtar Mohammadi, and Igor Djurović. A modified viterbi algorithm-based if estimation algorithm for adaptive directional

time–frequency distributions. *Circuits, Systems, and Signal Processing*, 38(5):2227–2244, 2019.

[73] Po Li and Qing-Hai Zhang. An improved viterbi algorithm for if extraction of multicomponent signals. *Signal, Image and Video Processing*, 12(1):171–179, 2018.

[74] Nabeel Ali Khan, Mokhtar Mohammadi, and Sadiq Ali. Instantaneous frequency estimation of intersecting and close multi-component signals with varying amplitudes. *Signal, Image and Video Processing*, 13(3):517–524, 2019.

[75] Xingjian Dong, Shiqian Chen, Guanpei Xing, Zhike Peng, Wenming Zhang, and Guang Meng. Doppler frequency estimation by parameterized time-frequency transform and phase compensation technique. *IEEE Sensors Journal*, 18(9):3734–3744, 2018.

[76] Haijian Zhang, Guoan Bi, Wen Yang, Sirajudeen Gulam Razul, and Chong Meng Samson See. If estimation of fm signals based on time-frequency image. *IEEE Transactions on Aerospace and Electronic Systems*, 51(1):326–343, 2015.

[77] Shiqian Chen, Yang Yang, Kexiang Wei, Xingjian Dong, Zhike Peng, and Wenming Zhang. Time-varying frequency-modulated component extraction based on parameterized demodulation and singular value decomposition. *IEEE Transactions on Instrumentation and Measurement*, 65(2):276–285, 2015.

[78] Yang Yang, Xingjian Dong, Zhike Peng, Wenming Zhang, and Guang Meng. Component extraction for non-stationary multi-component signal using parameterized de-chirping and band-pass filter. *IEEE Signal Processing Letters*, 22(9):1373–1377, 2014.

[79] Yang Yang, Zhike Peng, Xingjian Dong, Wenming Zhang, and Guang Meng. Application of parameterized time-frequency analysis on multi-component frequency modulated signals. *IEEE Transactions on Instrumentation and Measurement*, 63(12):3169–3180, 2014.

[80] Cornel Ioana, Arnaud Jarrot, Cédric Gervaise, Yann Stéphan, and André Quinquis. Localization in underwater dispersive channels using the time-frequency-phase continuity of signals. *IEEE Transactions on Signal Processing*, 58(8):4093–4107, 2010.

[81] Shiqian Chen, Xingjian Dong, Yang Yang, Wenming Zhang, Zhike Peng, and Guang Meng. Chirplet path fusion for the analysis of time-varying frequency-modulated signals. *IEEE Transactions on Industrial Electronics*, 64(2):1370–1380, 2016.

[82] Johan Swärd, Johan Brynolfsson, Andreas Jakobsson, and Maria Hansson-Sandsten. Sparse semi-parametric estimation of harmonic chirp signals. *IEEE Transactions on Signal Processing*, 64(7):1798–1807, 2015.

[83] Ljubisa Stankovic, Milos Dakovic, Thayananthan Thayaparan, and Vesna Popovic-Bugarin. Inverse radon transform–based micro-doppler analysis from a reduced set of observations. *IEEE Transactions on Aerospace and Electronic Systems*, 51(2):1155–1169, 2015.

[84] Qun Zhang, Tat Soon Yeo, Hwee Siang Tan, and Ying Luo. Imaging of a moving target with rotating parts based on the hough transform. *IEEE transactions on geoscience and remote sensing*, 46(1):291–299, 2007.

[85] Shiqian Chen, Zhike Peng, Yang Yang, Xingjian Dong, and Wenming Zhang. Intrinsic chirp component decomposition by using fourier series representation. *Signal Processing*, 137:319–327, 2017.

[86] Yaron Doweck, Alon Amar, and Israel Cohen. Joint model order selection and parameter estimation of chirps with harmonic components. *IEEE Transactions on Signal Processing*, 63(7):1765–1778, 2015.

[87] Zhipeng Feng, Fulei Chu, and Ming J Zuo. Time–frequency analysis of time-varying modulated signals based on improved energy separation by iterative generalized demodulation. *Journal of Sound and Vibration*, 330(6):1225–1243, 2011.

[88] Igor Djurović and Ljubiša Stanković. Quasi-maximum-likelihood estimator of polynomial phase signals. *IET Signal Processing*, 8(4):347–359, 2013.

[89] Igor Djurović. Quasi ml algorithm for 2-d pps estimation. *Multidimensional Systems and Signal Processing*, 28(2):371–387, 2017.

[90] Igor Djurović. Qml-ransac: Pps and fm signals estimation in heavy noise environments. *Signal Processing*, 130:142–151, 2017.

[91] Igor Djurović. Qml-ransac instantaneous frequency estimator for overlapping multicomponent signals in the time-frequency plane. *IEEE Signal Processing Letters*, 25(3):447–451, 2018.

[92] Tatiana Alieva, Martin J Bastiaans, and Ljubisa Stankovic. Signal reconstruction from two close fractional fourier power spectra. *IEEE Transactions on Signal Processing*, 51(1):112–123, 2003.

[93] Po Li, De-Chun Wang, and Jin-Li Chen. Parameter estimation for micro-doppler signals based on cubic phase function. *Signal, Image and Video Processing*, 7(6):1239–1249, 2013.

[94] Peng Yang, Zheng Liu, and Wen-Li Jiang. Parameter estimation of multicomponent chirp signals based on discrete chirp fourier transform and population monte carlo. *Signal, Image and Video Processing*, 9(5):1137–1149, 2015.

[95] Abdelkhalek Bouchikhi, Abdel-Ouahab Boudraa, Jean-Christophe Cexus, and Thierry Chonavel. Analysis of multicomponent lfm signals by teager huang-hough transform. *IEEE Transactions on Aerospace and Electronic Systems*, 50(2):1222–1233, 2014.

[96] Shan Luo, Xiaolei Lv, and Guoan Bi. Lv's distribution for time-frequency analysis. In *Proc. 2011 Int. Conf. Circuits, Systems, Control, Signals*, pages 110–115, 2011.

[97] Ljubiša Stanković, Danilo Mandić, Miloš Daković, and Miloš Brajović. Time-frequency decomposition of multivariate multicomponent signals. *Signal Processing*, 142:468–479, 2018.

[98] Vittoria Bruni, Michela Tartaglione, and Domenico Vitulano. A fast and robust spectrogram reassignment method. *Mathematics MDPI*, 7(4):360, 2019.

[99] Vittoria Bruni, Michela Tartaglione, and Domenico Vitulano. An iterative spectrogram reassignment of frequency modulated multicomponent signals. In *MASCOT2018-15th Meeting On Applied Scientific Computing and Tools*, 2018.

[100] Vittoria Bruni, Michela Tartaglione, and Domenico Vitulano. An iterative approach for spectrogram reassignment of frequency modulated multicomponent signals. *Mathematics and Computers in Simulation*, 2019.

[101] V. Bruni, S. Marconi, B. Piccoli, and D. Vitulano. Instantaneous frequency estimation of interfering fm signals through time-scale isolevel curves. *Signal Processing*, 93:882–896, 2013.

[102] A. Quarteroni, A. Sacco, and F. Saleri. *Numerical mathematics*. Springer Science & Business Media, 2010.

[103] I. Daubechies, Y. Wang, and H.T. Wu. Conceft: Concentration of frequency and time via a multitapered synchrosqueezed transform. *Philosophical Transactions of the Royal Society A: Mathematical, Physical and Engineering Sciences*, 374(2065):20150193, 2015.

[104] Luigi Ambrosio, Nicola Gigli, and Giuseppe Savare. Gradient flows in metric spaces and in the wasserstein space of probability measures, 2005.

[105] Ludger Rüschendorf. The wasserstein distance and approximation theorems. *Probability Theory and Related Fields*, 70(1):117–129, 1985.

[106] Vittoria Bruni, Michela Tartaglione, and Domenico Vitulano. On the time-frequency reassignment of interfering modes in multicomponent fm signals. In *2018 26th European Signal Processing Conference (EUSIPCO)*, pages 722–726. IEEE, 2018.

[107] Vittoria Bruni, Michela Tartaglione, and Domenico Vitulano. Instantaneous frequency modes separation via a spectrogram-radon based approach. In *2019 11th International Symposium on Image and Signal Processing and Analysis (ISPA)*, pages 347–351. IEEE, 2019.

[108] Vittoria Bruni, Michela Tartaglione, and Domenico Vitulano. Radon spectrogram-based approach for automatic ifs separation. *EURASIP Journal on Advances in Signal Processing*, 2020(1):1–21, 2020.

[109] Victor Sucic, Nicoletta Saulig, and Boualem Boashash. Estimating the number of components of a multicomponent nonstationary signal using the short-term time-frequency rényi entropy. *EURASIP Journal on Advances in Signal Processing*, 2011(1):125, 2011.